

Permanent Deformation of Asphalt Mixtures

Blijvende Vormverandering van Asfaltmengsels

Proefschrift

ter verkrijging van de graad van doctor
aan de Technische Universiteit Delft
op gezag van de Rector Magnificus prof. dr.ir. J.T. Fokkema
voorzitter van het College voor Promoties,
in het openbaar te verdedigen op 5 juni 2007 om 10:00 uur

door

Patrick Mwangi MURAYA

Master of Science in Road Engineering, IHE/TU Delft, The Netherlands
geboren te Nyandarua, Kenya

Dit proefschrift is goedgekeurd door de promotor:
Prof. dr. ir. A.A.A. Molenaar

Toegevoegd promotor
Ir. M.F.C. van de Ven

Samenstelling promotiecommissie:

Rector Magnificus, Technische Universiteit Delft, voorzitter
Prof. dr. ir. A.A.A. Molenaar, Technische Universiteit Delft, promotor
Ir. M.F.C. van de Ven, Technische Universiteit Delft, toegevoegd promotor
Prof. A. C. Collop, BEng., PhD., DSc., University of Nottingham
Prof. K. J. Jenkins, BSc., MSc., PhD., University of Stellenbosch
Prof. dr. ir. K. van Breugel, Technische Universiteit Delft
H. Al-Khalid, BSc., MSc., PhD., Senior Lecturer, University of Liverpool
Dr. P. Stienstra, Rijkswaterstaat Dienst Weg- en Waterbouwkunde

Prof. dr. ir. F. Molenkamp, Technische Universiteit Delft, reserve lid

Published and distributed by:

P.M. Muraya
E-mail: P.M.Muraya@tudelft.nl; pmmuraya@hotmail.com

Section of Road and Railway Engineering
Faculty of Civil Engineering and Geosciences
Delft University of Technology
P.O. Box 5048
2600 GA Delft
The Netherlands

ISBN-13: 978-90-9021895-3

Key words: permanent deformation, asphalt mixture, skeleton, mastic.

© 2007 by Patrick Mwangi Muraya

All rights reserved. No part of the material protected by this copyright notice may be reproduced or utilised in any form or by any means, electronic or mechanical, including photocopying, recording or by any information storage and retrieval system, without written consent from the publisher.

Printed in The Netherlands

I dedicate this dissertation to my family especially Liz who spiced my writing with her inquisitive questions and Charles who always kept a smile.

ACKNOWLEDGEMENTS

A PhD dissertation is like an asphalt mixture ...to some extent.

The research presented in this dissertation was conducted at the Road and Railway Engineering section in the Faculty of Civil Engineering and Geo-Sciences at the Delft University of Technology. The research was funded by the University and the Dr. ir. Cornelis Lely Stichting (CLS) organization. In addition, part of the material testing was performed at the Road and Hydraulic Engineering Division of the Dutch Ministry of Transport, Public Works and Water Management. I wish to extend my gratitude to these organizations for the support.

The preparation of a PhD dissertation is to some extent like the preparation of an asphalt mixture. A PhD dissertation is a mixture of many components that are contributed by different people. My work has been made possible by many people who have contributed tirelessly and this dissertation cannot be complete without appreciating their support. My heart goes to all of them.

I wish to extend my appreciation to Lambert Houben and Arthur van Dommelen for their support during pavement analysis. I could always pop in to Houben's office with all kinds of questions and he always had answers.

A word of thanks goes to Abdol Miradi for project administration, Robin van Dijk and Mark Gonesh for managerial and technical support. I am especially grateful to Robin van Dijk. His efforts were instrumental in the completion of most of the laboratory work within one year.

The support offered by Marco Poot, Jan-Willem Bientjes, Jan Moraal, Jacqueline Barnhoorn and Sonja van de Bos is greatly appreciated. I am particularly grateful to Marco Poot. His extensive experience of the test equipment ensured the production of appropriate test signals.

The assistance provided by Huub Wakkarij, Dave van Vliet and Jan Voskuilen is also appreciated. Their assistance made me familiar with the mix design stipulations of the Dutch pavement specifications.

I wish to thank my family for emotional support. Especially my daughter Liz who paid keen attention to my dressing habits. I had two pairs of similar jeans. I kept interchanging the two pairs of jeans for several months. She concluded I was under my teacher's instructions to wear only one pair of jeans to school.

SUMMARY

This research is focused on the separate characterization of the components of asphalt mixtures in relation to their contribution towards resistance to permanent deformation. This is a pioneering approach in the characterization of permanent deformation behaviour of asphalt mixtures. Towards this end, extensive laboratory material testing was performed on porous asphalt concrete (PAC), stone mastic asphalt (SMA) and dense asphalt mixtures (DAC). Prior to identification and testing, a Marshall mixture design was performed for the three asphalt mixtures with the aim of obtaining mixtures that meet pavement specifications.

An identification process was developed to determine the composition of the components. This process involved the identification of the composition of the skeleton and the bituminous mortar. The identification of the aggregate skeleton was performed on the basis of aggregate grid interlock between the different aggregate fractions. Aggregate fractions that fell through the aggregate grid interlock were omitted from the composition of the aggregate skeleton. In order to identify this grid interlock, aggregate fractions were mixed together without bitumen and visually observed during the mixing and compaction process. The bituminous mortar was identified as the composition of the aggregates smaller than the minimum aggregate size in the skeleton and the bitumen.

For purposes of fabricating specimens with reasonable compaction homogeneity, elaborate specimen preparation protocols were developed for the aggregate skeleton as well as the asphalt mixture. The development of these protocols included investigation of the compaction homogeneity in the aggregate skeleton and asphalt mixture specimens by means X-ray tomography.

The characterization was performed with the aim of applying a plasticity model to describe the separate role played by each component in the different types of mixtures considered in this research. The characterization involved different types of tests for the asphalt mixture and the different components. The total asphalt mixture was characterized by indirect tension tests, compression failure tests and tension failure tests. The aggregate skeleton was characterized by triaxial compression and triaxial permanent-resilient deformation tests. The mortar was characterized by Dynamic Shear Rheometer (DSR) and tension failure tests, while the bitumen was characterized by DSR tests.

The research provided a good insight into the contribution of the components of an asphalt mixture towards resistance to permanent deformation. The research clearly emphasized the importance of the aggregate skeleton as well as the degree of compaction on the resistance to permanent deformation of stone skeleton asphalt mixtures such as PAC and SMA asphalt mixtures. The test results showed that SMA provides excellent resistance to permanent deformation even at very high stress levels and that the PAC provided a good rut resistant mixture. The test

results also underscored the importance of the contribution of the mastic in the DAC.

A Desai type plasticity model that included effects of temperature, loading rates and confinement was used to describe the resistance to permanent deformation of the investigated mixtures. This approach was selected because a study on the applicability of linear visco-elastic models showed that they were not sufficient for purposes of describing the permanent deformation in asphalt pavements.

In order to demonstrate the implications of this research, the permanent deformation in two test pavements was analyzed. The two test pavements were part of the LINTRACK accelerated test program and were subjected to test conditions that are prone to permanent deformation. This analysis showed that the permanent deformation in these pavements could be explained fairly well by the approach developed in this research.

SAMENVATTING

Het onderzoek is gericht op de karakterisering van de afzonderlijke componenten in asfaltmengsels met betrekking tot hun bijdrage aan de weerstand tegen blijvende vormverandering. Het is een nieuwe benadering van de karakterisering van de weerstand tegen blijvende vormverandering van asfaltmengsels. Uitgebreid laboratoriumonderzoek is daarom uitgevoerd op zeer open asfaltbeton (ZOAB), steenmastiekasfalt (SMA) en dichtasfaltbeton (DAB). Voorafgaand aan het testprogramma is, m.b.v. de Marshall methode, een onderzoek naar de mengselsamenstellingen gedaan om zeker te stellen dat de te onderzoeken mengsels aan de daaraan gestelde eisen voldoen.

Een identificatiemethode is ontwikkeld om de samenstelling van de componenten te bepalen. Hierbij werd bepaald wat de samenstelling van het steenskelet en van de bitumineuze mortel is. De identificatie van het steenskelet kwam neer op het bepalen van de aggregaatfracties die een samenhangend skelet vormden en van de fracties die door dat skelet vielen. Deze laatste fracties werden geacht niet tot het skelet te behoren. Om dit steenskelet te bepalen werden de verschillende fracties met elkaar gemengd zonder toevoeging van bitumen en visueel beoordeeld tijdens menging en verdichting. De bitumineuze mortel werd geïdentificeerd als dat deel van het aggregaat dat kleiner is dan de kleinste steenmaat in het skelet tezamen met het bitumen.

Teneinde proefstukken te kunnen maken met een redelijk homogene dichtheid zijn uitgebreide protocollen opgesteld voor het vervaardigen van proefstukken van zowel het steenskelet als het asfaltmengsel. Bij het opstellen van deze protocollen is de homogeniteit van de dichtheid van zowel de steenskeletproefstukken als de asfaltproefstukken bepaald m.b.v. X-ray tomography technieken.

De karakterisering is uitgevoerd met het doel een plasticiteitsmodel toe te kunnen passen voor het beschrijven van de bijdrage van de afzonderlijke componenten in de beschouwde asfaltmengsels. Deze karakterisering behelsde verschillende typen proeven voor de asfaltmengsels en de afzonderlijke componenten. De asfaltmengsels zijn gekarakteriseerd met de indirecte trekproef, en met druk- en trekproeven tot bezwijken. De steenskeletten zijn gekarakteriseerd met triaxiaalproeven tot bezwijken en met triaxiaalproeven met herhaalde belasting ter bepaling van het elastische en blijvende vervormingsgedrag. De bitumineuze mortel is gekarakteriseerd met de Dynamic Shear Rheometer (DSR) proef en trekproeven tot bezwijken. De DSR proef is ook gebruikt voor de karakterisering van het bitumen.

Het onderzoek heeft een goed inzicht verschaft in de bijdrage van de verschillende componenten in een asfaltmengsel aan de weerstand tegen blijvende vormverandering. Het onderzoek heeft overduidelijk het belang aangetoond van het steenskelet en de verdichtingsgraad op de weerstand tegen blijvende vormverandering van steenskeletmengsels als ZOAB en SMA. De proefresultaten

toonden dat SMA een zeer goede vervormingsweerstand heeft, ook bij hoge spanningsniveaus, en ZOAB een goede. De proeven onderstreepten ook het belang aan van de bijdrage van de mastiek aan de weerstand tegen blijvende vormverandering van DAB.

Een Desai type plasticiteitsmodel, inclusief de effecten van temperatuur, belastingsnelheid en zijdelingse opsluiting, is gebruikt om de weerstand tegen blijvende vormverandering van de onderzochte mengsels te beschrijven. Dit type model is gebruikt omdat aangetoond is dat lineair visco-elastische modellen niet goed genoeg zijn om de blijvende vormverandering van asfaltverhardingen te kunnen beschrijven.

Teneinde de implicaties van het onderzoek aan te tonen, is het blijvend vervormingsgedrag van twee proefvakken geanalyseerd. Deze proefvakken maakten deel uit van het met de LINTRACK uitgevoerde spoorvormingsonderzoek. Hierbij werden de proefvakken aan condities blootgesteld waarbij spoorvorming versneld optrad. Deze analyse toonde aan dat de gemeten blijvende vormverandering van deze proefvakken behoorlijk goed met de in dit onderzoek ontwikkelde benadering kon worden voorspeld.

Table of Contents

1	Introduction.....	1
1.1	Definition of Asphalt Mixtures.....	2
1.2	Aim of the Research	2
1.3	Organisation of this Dissertation	3
1.4	References.....	4
2	Background, Literature Review and Test Program	5
2.1	Introduction.....	5
2.2	Factors Affecting Permanent Deformation Behaviour	5
2.2.1	Contact Stress Distribution	5
2.2.2	Pavement Structure	7
2.3	General Concept	8
2.3.1	Mixture Composition.....	10
2.3.2	Voids in the Asphalt Mixture.....	15
2.3.3	Compaction.....	15
2.4	Modelling of Permanent Deformation.....	16
2.4.1	Hybrid Models	17
2.4.2	Visco-Elastic Models.....	18
2.5	Prediction of Permanent Deformation based on Visco-elastic and Hybrid Models	19
2.6	Influence of Asphalt Mixture Components on Permanent Deformation Behaviour.....	28
2.7	Models Used in this Research.....	30
2.7.1	Desai Model.....	32
2.7.2	Unified Model.....	34
2.8	Test Program and Permanent Deformation Analyses.....	35
2.8.1	Test Program.....	36
2.8.2	Permanent Deformation Analyses	37
2.9	Conclusions.....	38
2.10	References.....	38
3	Material Procurement and Mixture Design	43
3.1	Introduction.....	43
3.2	Material Procurement	43
3.3	Material Sieving.....	44
3.4	Mixture Design	45
3.4.1	Porous Asphalt Concrete (PAC 0/16) Mixture Design.....	47
3.4.2	Stone Mastic Asphalt Mixture (SMA 0/11) Design	48
3.4.3	Dense Asphalt Concrete (DAC) Mixture Design	49
3.4.4	Composition Determination for PAC 0/16 and SMA 0/11.....	50
3.5	Summary.....	50
3.6	Conclusions.....	52
3.7	References.....	52
4	Aggregate Skeleton	53
4.1	Introduction.....	53
4.2	Triaxial Testing.....	53
4.2.1	Test Set-Up	53
4.3	Identification of Aggregate Skeleton	54

4.3.1	Introduction.....	54
4.3.2	PAC aggregate skeleton.....	56
4.3.3	SMA Aggregate Skeleton.....	56
4.3.4	DAC Aggregate Skeleton.....	57
4.3.5	X-Ray Tomography.....	58
4.3.6	Aggregate Skeleton Summary.....	60
4.4	Preparation of Aggregate Skeleton Specimens.....	61
4.5	Test Conditions.....	63
4.5.1	Displacement Controlled Monotonic Constant Confinement Failure Tests (DCMCC).....	63
4.5.2	Permanent Deformation (PD) Tests.....	64
4.6	Test results.....	67
4.6.1	Displacement Controlled Monotonic Constant Confinement Failure Test (DCMCC).....	67
4.7	Flow Surface.....	76
4.7.1	Model Parameters.....	77
4.7.2	Flow Surfaces.....	77
4.7.3	Permanent Deformation.....	78
4.8	Conclusions.....	95
4.9	References.....	95
5	Total Asphalt Mixture.....	97
5.1	Introduction.....	97
5.2	Specimen Preparation Procedure.....	98
5.2.1	Introduction.....	98
5.2.2	Specimen Preparation.....	100
5.2.3	Air-void Distribution.....	102
5.2.4	X-ray Tomography Analysis.....	102
5.2.5	Standard Laboratory Procedures.....	106
5.2.6	Results.....	106
5.2.7	Gyratory Specimen Compaction to Reference Marshall Density.....	108
5.2.8	Test Specimens.....	114
5.3	Test Equipment.....	118
5.3.1	Resilient Modulus Indirect Tensile Test (RMIT).....	118
5.3.2	Displacement Controlled Monotonic Compression Test (DCMC).....	118
5.3.3	Displacement Controlled Monotonic Tension Test (DCMT).....	119
5.4	Test Conditions.....	120
5.4.1	Experimental Design.....	120
5.5	Test Results.....	123
5.5.1	Resilient Modulus Indirect Tensile Test (RMIT).....	123
5.5.2	Displacement Controlled Monotonic Compression and Tension Tests (DCMC and DCMT).....	132
5.5.3	DCMC and DCMT Tests.....	145
5.6	Flow Surface.....	154
5.6.1	Model Parameter γ , R and n.....	155
5.6.2	Flow Surfaces.....	158
5.7	Conclusions.....	160
5.7.1	Specimen Preparation Procedure.....	160
5.7.2	RMIT, DCMC and DCMT Tests.....	160

5.8	References.....	161
6	Mastic and Bitumen.....	163
6.1	Introduction.....	163
6.1.1	Determination Indicative Tensile Stress in the Mastic/Mortar....	166
6.1.2	Indicative Tensile Stress in the Mastic/Mortar.....	170
6.1.3	Mastic Characterization.....	171
6.2	Ageing Test.....	172
6.3	Preparation of Mastic Specimens.....	174
6.4	DSR Test Set Up.....	175
6.5	DSR Test Conditions.....	175
6.6	DTT Test Set Up.....	176
6.7	DTT Specimen Fabrication.....	177
6.7.1	DTT specimen Fabrication Summary.....	178
6.8	DTT Test Conditions for DAC Mastic.....	178
6.9	DSR Test Results.....	179
6.9.1	Modelling of Complex Modulus and Phase Angle.....	183
6.9.2	Comparison of the Measured Complex Modulus to the Shell Relationship for Dynamic Stiffness.....	186
6.10	DTT Test Results.....	187
6.11	Modelling of DTT Test Results.....	190
6.12	Conclusions.....	192
6.13	References.....	193
7	Failure and Permanent Deformation of the Components and Asphalt Mixtures.....	195
7.1	Introduction.....	195
7.2	Pavement Strains.....	195
7.3	Triaxial Stress and Strain Conditions.....	196
7.3.1	Determination of Vertical Triaxial Strain Rate.....	197
7.4	Equivalency Principle to Analyze Permanent Deformation.....	199
7.5	Compressive and Tensile Strengths of the PAC, SMA and DAC Total Asphalt Mixtures.....	200
7.6	Compressive Strength and Stress at Initiation of Dilatation of the PAC, SMA and DAC Total Asphalt Mixtures.....	201
7.7	Strength at Failure of DAC Total mixture and Tensile Strength of the DAC Mastic.....	202
7.8	Ultimate Surfaces of the Total Asphalt Mixture and the Aggregate Skeleton.....	203
7.9	Comparison of the Test Results to Pavement Stress and Strain Conditions.....	207
7.9.1	PAC (Third) Test Pavement.....	207
7.9.2	DAC (Second) Test Pavement.....	209
7.10	Comparison of PD Tests to Pavement Stress Conditions.....	210
7.11	Conclusions.....	212
8	Conclusions and Recommendations.....	213
8.1	Conclusions.....	213
8.1.1	Main Highlights.....	213
8.1.2	Related to Practice.....	215
8.2	Recommendations.....	216
8.2.1	Related to Chapter 2 and 4.....	216

8.2.2	Related to Chapter 5	216
8.2.3	Related to Chapter 2 and 7.....	216
Annex 1 - VEROAD Visco-Elastic Analysis.....		217
A1.1	Test Pavements	217
A1.2	Measurement of Pavement Response	218
A1.3	Laboratory Characterization of the Pavement Materials	220
A1.4	Visco-Elastic Analysis	226
A1.5	Manual Fitting of the Burger's Parameters.....	232
A1.6	Measured and Calculated Rut Depths.....	235
A1.7	References.....	236
Annex 2 - Influence of Model Parameters on the Desai Model and Unified Model.....		239
A2.1	Desai Model	239
A2.2	Unified Model	241
Annex 3 - MATLAB Code.....		243
A3.1	Step 1: Sorting Out the Slides.....	243
A3.2	Step 2: Exclusion of Empty Slides	243
A3.3	Step 3: Location of Centre of Area.....	245
A3.4	Step 4: Determination of Material Boundaries	246
A3.5	Step 5: Elimination of the Air Surrounding the Specimen	247
A3.6	Step 6: Coring and Determination of Air Content in the Cores.....	248
Annex 4 - Determination of Tangent Stiffness and Poisson's Ratios.....		253

List of Frequently Used Symbols and Abbreviations

Symbols

I_1	first stress invariant
J_2	the second deviatoric stress invariant
J_3	the third deviatoric stress invariant
p	isotropic stress
s_i	i^{th} principal deviator stress
α, γ, n, R	Desai model parameters
P	property under consideration
P_{high}, P_{low}	limiting values of the property P
u_r	time derivative
u_0	a reference value of the time derivative
T_s	temperature susceptibility factor
T_0	reference temperature
T	temperature
λ	unified model parameter
τ	shear strength
c	cohesion
σ	normal stress
ϕ	angle of internal friction
C_{agg}	cumulative percentage of the aggregate fraction in the total mixture by weight
x	mix component
V_x	volumetric composition of component x
M_x	weight of component x
ρ	density
P_x	percentage by weight of component x
V_T	total volume
M_T	total weight
VTM	air voids in the total asphalt mixture
τ	shear stress
D	distance
v	velocity
E	stiffness
ν	Poisson's ratio
M_r	resilient modulus
ε	strain

Abbreviations

PAC	porous asphalt concrete
SMA	stone mastic asphalt concrete
DAC	dense asphalt concrete

EXCEL	computer package
MATLAB	computer package
cSt	centistokes
EVT	temperature at which the viscosity of the bitumen = 170 cSt
DSR	dynamic shear rheometer
DCMT	displacement controlled monotonic tension failure tests
DCMC	displacement controlled monotonic compression failure tests
DCMCC	displacement controlled constant confinement failure tests
ITT	indirect tension test
PD	permanent deformation tests
LVDT	linear variable differential transducers
kPa	kilopascals
MPa	megapascals
MPa.s	megapascals second

1 Introduction

“Gūtīrī ũndũ ũtarī kīhumo” *All things have a beginning*

- Kikuyu saying

Transportation of goods, people and services from one point to another plays an important role in our daily lives. Road transportation creates a vital link in transportation networks. The ability of roads or pavements to deliver goods, people and services within acceptable costs in terms of comfort, time and safety is governed by the pavement life. Permanent deformation or rutting is one of the most important failure modes in asphalt pavements (Barksdale 1967) that affects the pavement life. Permanent deformation in asphalt mixtures can be defined as the unrecoverable cumulative deformation that occurs mainly at high temperatures in the wheel paths as a result of repeated traffic loading as shown in Figure 1.1. The deformation results in depressions on the pavement surface along the wheel tracks relative to other points on the surface. The depressions are as a result of downwards and lateral movement of the asphalt mixture. The downward movement is mainly due to compaction while the lateral movement occurs as a result of shear failure.



Figure 1.1 *Definition of permanent deformation (source WAPA)*

In order to offer acceptable pavement life, several factors place great demands on the permanent deformation resistance of asphalt mixtures. These factors include pressure to decrease maintenance related traffic delays and influence of economic and environmental considerations. In order to increase pavement life and consequently decrease maintenance related traffic delays, great demands are placed on permanent deformation resistance of asphalt mixtures. Great demands are also placed on the permanent deformation resistance by the increase in axle loads as a result of economic and environmental factors. Economic factors such as tendency to transport goods in larger units and reduction of rolling resistance lead to the placement of heavier axle loads on fewer tyres. Environmental pressure to reduce the number of scrap tyres also means more pressure to decrease the

number of tyres. The heavier axle loads on fewer tyres increases the contact stresses leading to increase in permanent deformation.

The preceding discussion emphasizes the need for materials with improved characteristics to cater for the great demands that are placed on the permanent deformation resistance of asphalt mixtures. Unfortunately, the knowledge of permanent deformation is mainly empirical and is suitable for the materials and conditions under which the knowledge was attained. Empirical knowledge does not provide insights in the contribution of the different material characteristics that are otherwise known to affect the permanent deformation behaviour.

In addition, most of the studies carried out in permanent deformation consider the asphalt mixture as one homogenous material. This has also led to permanent deformation models that do not provide insight in the contribution of the different material characteristics that are otherwise known to affect the permanent deformation behaviour of asphalt mixtures. It is the aim of this research to address the contribution of different material characteristics towards resistance to permanent deformation.

1.1 Definition of Asphalt Mixtures

Asphalt mixtures are composed of aggregates, sand, filler, bitumen and air. The contents of any of these constituents may vary depending on the type of asphalt mixture. Asphalt mixtures can generally be classified as dense (continuously graded) or gap-graded asphalt mixtures.

Dense asphalt concrete mixtures are characterised by low air void contents and can be divided into the widely known traditional dense asphalt mixture (DAC) and the stone skeleton asphalt mixtures such as the stone mastic asphalt concrete (SMA). Mixtures such as the DAC are continuously graded and derive their stability from the packing of the aggregates and the cohesion provided by the bitumen. On the other hand SMA is a gap-graded asphalt mixture that maximizes both the bitumen content and the coarse aggregate fraction. The coarse aggregate provides a stable stone-on-stone skeleton that is held together by a rich mixture of bitumen, filler, and stabilizing agent (Brown and Cooley 1999). Another example of a stone skeleton mixture is porous asphalt concrete (PAC). Porous asphalt can be defined as a gap-graded mixture in which the amount of mortar provides sufficient coating for the aggregate skeleton and allows a high void content in the mixture. PAC mixtures derive their stability from the stone-on-stone skeleton.

1.2 Aim of the Research

The main aim of this dissertation is to provide more insight into the contribution of the different components in asphalt mixtures towards resistance to permanent deformation. In order to meet this aim it is necessary to investigate the separate contribution of the different components in asphalt mixtures towards resistance to permanent deformation. As mentioned before, the asphalt mixture is a composition of aggregates, filler, bitumen and air voids. The behaviour of individual components needs to be characterized for purposes of understanding

the permanent deformation behaviour. This means that the different effect of the components of the asphalt mixture have to be identified and characterized with suitable tests. Based on this aim the objectives were to:

1. Investigate the contribution of the aggregate skeleton towards resistance to permanent deformation of asphalt mixtures.
2. Investigate the contribution of the bituminous mortar towards resistance to permanent deformation of asphalt mixtures.
3. Evaluate the relative influence of the two components in stone skeleton mastic and dense asphalt concrete mixtures.
4. Design a test program capable of achieving objectives 1, 2 and 3.
5. Identify a suitable model for the analysis of permanent deformation in asphalt mixtures. In this regard, examine the applicability of a linear visco-elastic model, (e.g. VEROAD), in the prediction of permanent deformation in asphalt pavements.

1.3 Organisation of this Dissertation

Chapter 2 provides a background and literature review on permanent deformation of asphalt mixtures. The chapter entails a brief discussion of the various issues related to permanent deformation of asphalt mixtures. The general concept is also offered in the context of the widely used dense asphalt mixtures and the stone skeleton asphalt mixtures. Special attention is paid to the influence of the different components in the asphalt mixture on the permanent deformation behaviour. An outline of the modelling of permanent deformation and a visco-elastic analysis of asphalt test pavements is also offered. In addition to this the test program and permanent deformation analyses is discussed.

Chapter 3 is dedicated to material procurement and mixture design. The objective of the mixture design was to compose different types of asphalt mixtures with similar mineralogical compositions that meet pavement mixture specifications. Mixtures with similar mineralogical composition would allow the comparison of the different mixtures without the influence of the aggregate mineralogical composition.

Chapter 4 offers the characterization of the aggregate skeleton. The objective of the tests performed on the aggregate was to characterize the influence of the aggregate skeleton in the permanent deformation of asphalt mixtures. The characterization of the aggregate skeleton was performed by means of triaxial testing. The triaxial testing involved displacement controlled tests and permanent deformation tests conducted under cyclic and constant confinement. Prior to laboratory testing, the skeleton components were identified for the purposes of fabricating the specimens.

Chapter 5 presents the characterization of the total asphalt mixture. The characterization involved extensive laboratory tests performed in relation to the failure behaviour of the asphalt mixtures. Since specimen preparation plays a crucial role on mixture properties, an elaborate specimen preparation procedure was developed. The preparation procedure was developed for the purposes of fabricating specimens with reasonable compaction homogeneity over both the height and the width of the test specimens. Apart from compaction homogeneity,

the other aim of the specimen preparation procedure was to compact the test specimen to a similar density level as determined in the Marshall mixture design.

Chapter 6 details the characterization of the bituminous binder. The characterization of the bituminous binder was performed in relation to the tensile strength. A comparison of the extent of dilation in the aggregate skeleton and in total asphalt mixture is also presented in Chapter 6.

The influence of the different components in the asphalt mixture is presented in Chapter 7 using flow surfaces. In addition, the chapter presents the implication of the test results on the permanent deformation of actual pavements.

The conclusions and the recommendations are presented in Chapter 8. The conclusion and the recommendations focus on the main highlights and conclusions related to practice.

1.4 References

- Barksdale R.D., (1967), *Predicting Performance of Bituminous Surfaced Pavements*, Proceedings of the Second International Conference Structural Design of Asphalt Pavements, pp. 321-340, University of Michigan Ann Arbor, United States of America.
- Brown E.R. and Cooley L.A., (1999), *Designing Stone Matrix Asphalt Mixtures for Rut-Resistant Pavements*, TRB, National Research Council, Washington D.C.
- WAPA, Washington Asphalt Pavement Association,
http://training.ce.washington.edu/WSDOT/Modules/09_pavement_evaluation/09-7_body.htm

2 Background, Literature Review and Test Program

Research, just like life is all about developing ideas from the known to the unknown. The background and literature review attempts to reveal the extent of the known and furnishes a route plan of travelling from the known to the unknown.

2.1 Introduction

This chapter offers a brief discussion of various issues related to permanent deformation. In this chapter, several factors that influence the permanent deformation behaviour of asphalt mixtures are presented. The general concept is also offered in the context of the various asphalt mixtures that have been considered in this research. In addition to this, a brief discussion on the influence of the different components in an asphalt mixture and an outline on the modelling of permanent deformation are presented. Apart from this, a description of the models used in this research as well as an overview of the testing program is offered.

2.2 Factors Affecting Permanent Deformation Behaviour

It is generally accepted that permanent deformation that is observed at the pavement surface in the wheel tracks is influenced by the stress conditions and the properties of the pavement layers. The stress conditions in the pavement layers are strongly influenced by the contact stress distributions as well as the stiffness and thickness of the various pavement layers. The stiffness and resistance to permanent deformation of asphalt mixtures strongly depends on the mixture composition, degree of compaction, rate of loading and temperature. The influence of these factors will be offered in the following sections.

2.2.1 Contact Stress Distribution

The wheel load generates non-uniform vertical, longitudinal and lateral contact stresses. The contact stresses are a function of tyre pressure, wheel load, type of tyre and pavement surface texture depth. Himeno et al (1997) studied the effects of speed, vehicle load and tyre inflation pressure on the vertical contact stress distribution. They concluded that the distribution of the vertical contact stress was complex and that the relationship between the average vertical contact stress and the wheel load is almost independent of the inflation tyre pressure and vehicle speed. Knowledge on average contact stresses is however not sufficient to analyze permanent deformation in detail and more detailed information on the distribution of the contact stresses is needed. This can be retrieved from the work done by De Beer et al (1997). In their research, De Beer et al carefully measured the contact stress distribution of a free rolling wheel at slow speed using a sophisticated measuring system known as Vehicle Road Surface Pressure Transducer Array (VRSPTA) that is shown in Figure 2.1. They found the contact stresses to consist of three dimensional vertical, lateral and longitudinal contact stresses and that the contact stresses depend on the tyre inflation pressure, the type of tyre and the wheel load. An illustration of the contact stress distributions measured by De Beer

et al is shown in Figure 2.2. Groenendijk et al (1997) investigated the effect of tyre inflation pressure, tyre load and speed on the contact stress using two different types of tyres. They found that the vertical, lateral and longitudinal contact stresses are influenced by the tyre inflation pressure and tyre load but only to a small extent by the speed. It should be noted however that the speed could only be varied between 0.32 to 4 m/s. De Beer et al and Groenendijk showed that peak contact stresses that can result in significant rutting can be avoided if wheel load and tyre pressure are balanced with respect to each other. Woodside et al (1992) studied the effect of the surface texture depth on contact stresses. The surface texture depth in this study was simulated by varying the height of the transducer protruding from a simulated road surface. The findings from this study indicated that a surface chipping of 1 mm macro-texture endured a contact force of twice that induced on a chipping at zero texture depth.

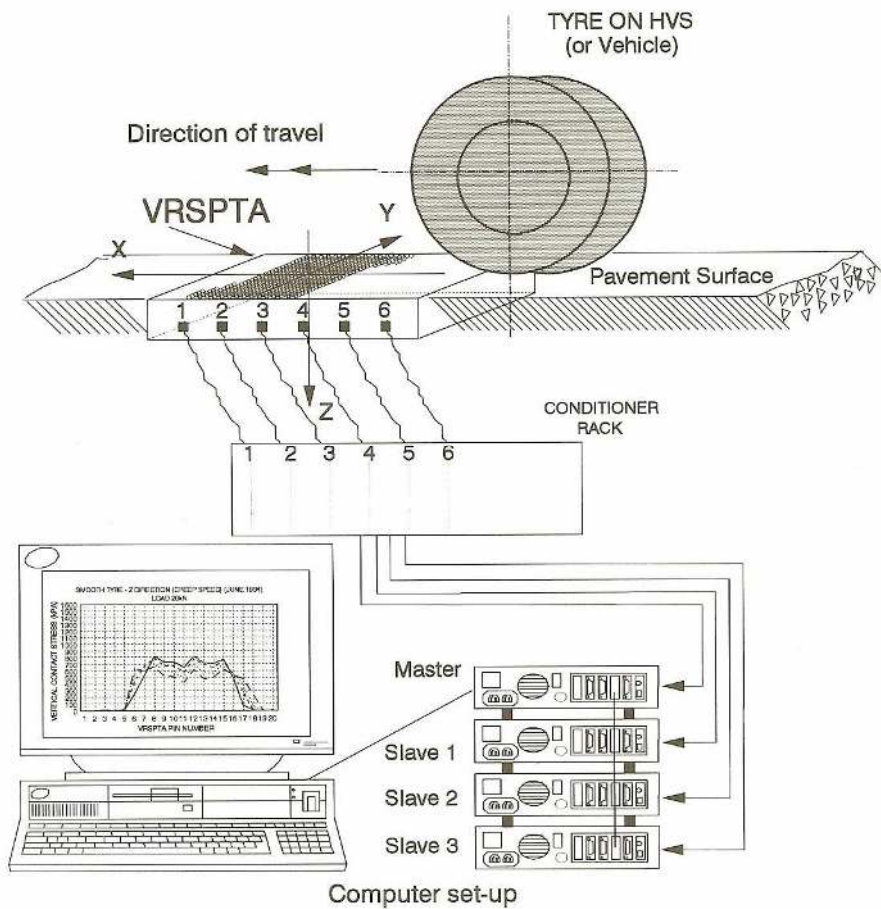


Figure 2.1 An illustration of the VRSPTA system (De Beer et al 1997)

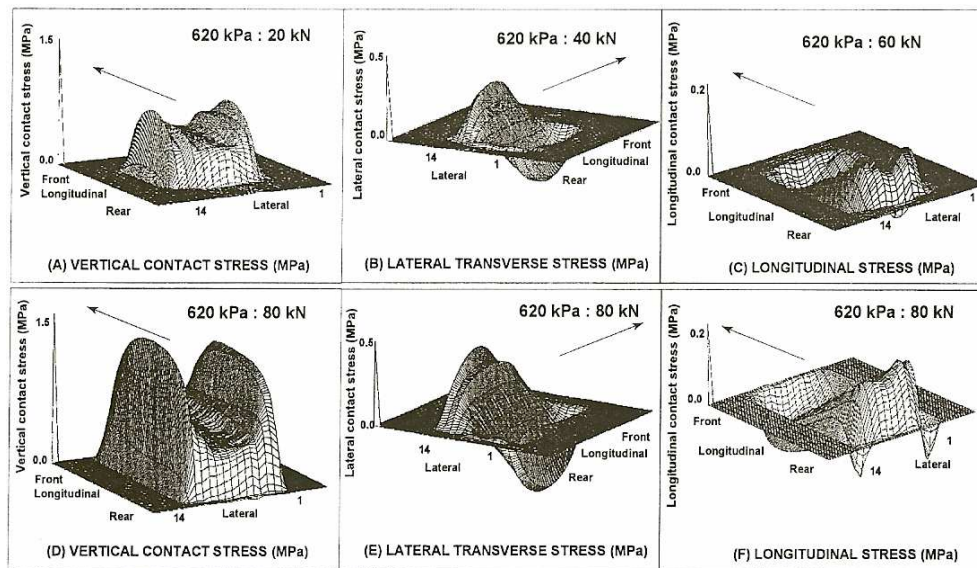


Figure 2.2 3-D contact stresses for a slow moving (1.2 m/s) single truck tyre (Goodyear) (De Beer et al 1997)

Many pavement analysis methods assume that a uniform vertical contact stress is sufficient to characterise the contact stress arising from the wheel load. Using a multi-layer linear elastic approach, Verstraeten (1967) demonstrated that serious errors could be made in the magnitudes and distributions of stresses in the upper pavement layers (depth to contact radius ratio ≤ 0.5) if the shear stresses on the surface of the pavement are ignored. In addition he illustrated that the failure conditions cannot be simply characterised by only one point in a three-dimensional system but by a particular surface at which the stress combinations become critical to the strength of the material.

Heavy slow moving vehicles are known to cause considerable rutting on inclined sections of asphalt pavements as demonstrated by a report compiled by Harun and Jones (1992). At first sight, it may appear as if this considerable rutting is caused by the slow speed of the vehicles. However, this considerable rutting can be associated with the increase in longitudinal and lateral contact stresses. The increase in these stresses results from the increase in the component of the wheel load acting on the inclined surface.

2.2.2 Pavement Structure

A typical asphalt pavement structure consists of a top layer, base, subbase and subgrade as shown in Figure 2.3 (Huang 1993). The distribution of stresses in the pavement depends on the stiffness, Poisson's ratio and thickness of the pavement layers. Similar to granular materials, the resistance to permanent deformation of asphalt mixtures is to a large extent dependent on the magnitude of the confining stresses that result from the wheel load. Generally, an increase in confinement enhances the resistance to permanent deformation. By smartly stacking the pavement layers, significant confinement levels can be generated leading to enhanced resistance to permanent deformation. Such a stacking mostly involves a layer with a high modulus below the asphalt top layers.

top layer	75 – 150 mm
base	100 – 300 mm
subbase	100 – 300 mm
subgrade	

Figure 2.3 Typical asphalt pavement structure (Huang 1993)

Typical examples of such a pavement are the LINTRACK¹ test pavements that were tested in the accelerated permanent deformation program carried out by the Ministry of Transport and Delft University of Technology in the Netherlands. Table 2.1 shows the pavement structure of some of the LINTRACK test pavements. Since the permanent deformation tests were performed at elevated temperatures ($\approx 40^{\circ}\text{C}$), the stiffness of the asphalt top layers was significantly lower than that of the cement treated AGRAC base. Despite of the low stiffness of the asphalt layers, significant horizontal confinement stresses were induced in the asphalt layers. This was proven by means of an extensive visco-elastic analysis (Muraya et al 2002).

Table 2.1 Pavement structure of some of the LINTRACK test pavements

top layer - 40 mm asphalt layer
second layer - 60 mm asphalt
third layer - 80 mm asphalt layer
fourth layer - 90 mm asphalt layer
base layer - 250 mm cement bound asphalt aggregate (AGRAC) layer
subgrade

2.3 General Concept

Asphalt mixtures share many similarities with soil mixtures. Figure 2.4 shows the physical states of soil mixtures. Figure 2.5 shows X-ray tomography images of porous asphalt concrete (PAC), stone mastic asphalt concrete (SMA) and dense asphalt concrete that were fabricated in the course of this research. By comparing the two figures, similarity between the asphalt mixtures and the soil mixtures can be observed.

The soil mixture shown in Figure 2.4 (a) is similar to the PAC. At first sight, the mixture gives the impression that the stone skeleton held together by the mortar plays an important role in offering resistance to permanent deformation. Initially

¹ LINTRACK is an accelerated pavement testing facility which simulates the traffic of heavy vehicles. It is jointly owned by the Delft University of Technology and the Road and Hydraulic Division (RHED) of the Dutch Ministry of Transport, Public Works and Water Management (Groenendijk 1998).

the friction forces generated in the contact points carry the loads applied to the skeleton and the skeleton will only show a limited amount of deformation. If however the load becomes too high, deformations will occur and because the skeleton is so well compacted it will not show a decrease in volume but an increase as a result of dilation. When dilation occurs, the mortar is subjected to tension hence underlining the importance of the adhesive characteristics of the mortar to the aggregate and the tensile characteristics of the mortar.

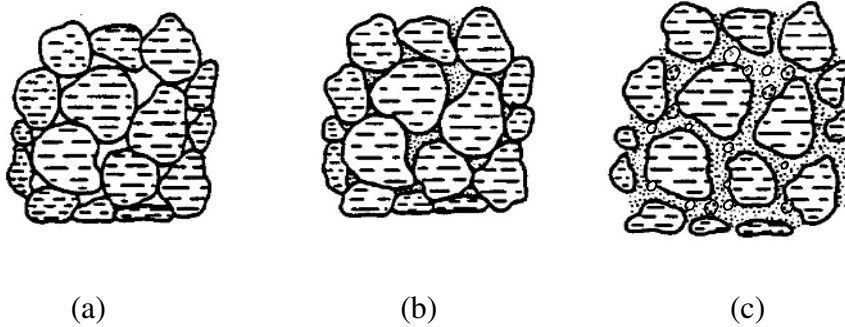


Figure 2.4 Physical states of soil mixtures, source (Yoder 1959).

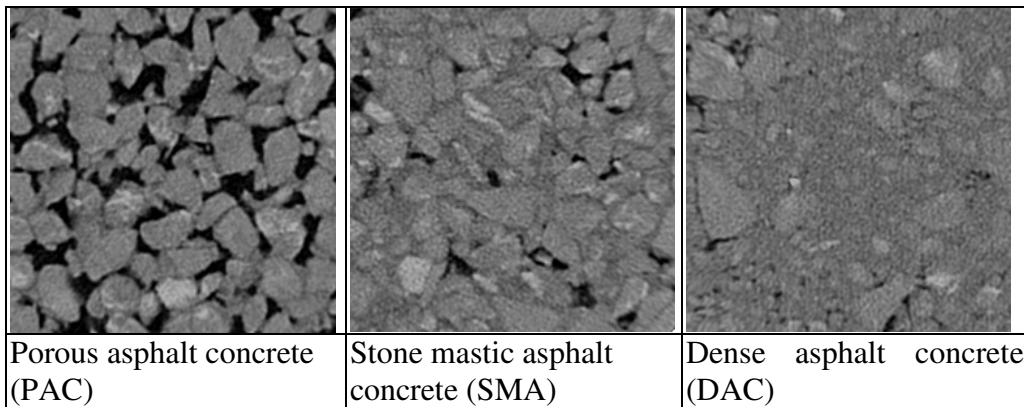


Figure 2.5 X-ray tomography images of porous asphalt concrete (PAC), stone mastic asphalt concrete (SMA) and dense asphalt concrete (DAC)

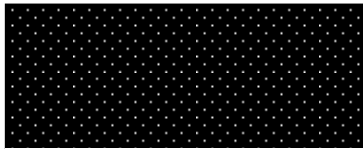
The soil mixture shown in Figure 2.4 (b) bears good resemblance to the SMA. In this case, the resistance to permanent deformation relies on both the skeleton and the mortar. If the void content is low, pore pressures as observed in saturated soils might develop resulting in instability in the mixture. Furthermore the tensile characteristics of the mortar and the adhesive characteristics of the mortar-aggregate interface become important if dilation occurs.

The soil mixture shown in Figure 2.4 (c) is comparable to the DAC. In such a mixture, the large stone aggregates do not really form a skeleton but more or less float in the mortar. The large aggregate particles do not play a role in providing resistance to permanent deformation. This resistance must be provided by the mortar thus emphasizing the importance of the visco-elastic properties in such a mixture. The type of bitumen, type of filler and the amount of bitumen and filler mainly determines these properties. If the void content is too low, pore pressure effects as observed in saturated soils may occur resulting in instability of the mixture.

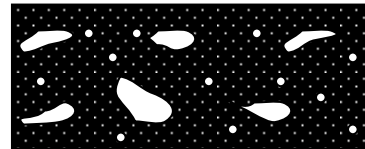
The preceding discussion shows that asphalt mixtures share many similarities with soil mixtures and it also demonstrates that the skeleton and the mortar play specific roles. The discussion also underscores the importance of the adhesive and tensile characteristics of the mortar. Therefore it is important to understand and characterize the contribution of the different components of an asphalt mixture in the development of its resistance to permanent deformation.

2.3.1 Mixture Composition

The influence of the mixture composition will be discussed in relation to the aggregate skeleton, the mortar or the mastic and the voids in the asphalt mixture. Different definitions of mastic and mortar exist in literature. In this research, the mortar is defined as a mixture of bitumen and any other aggregates below a certain aggregate size and the mastic as a mixture of bitumen and filler only as shown in Figure 2.6. This will be discussed in more detail in section 4.3.



Mastic = filler + bitumen



Mortar = aggregates smaller than a certain aggregate size + filler + bitumen

Figure 2.6 Definition of mastic and mortar

The mineralogy and amount of the filler influences the behaviour of the mastic and the mortar and consequently the behaviour of the asphalt mixture. In addition the influence of the mixture characteristics depends on the gradation and the surface texture of the aggregates.

2.3.1.1 Gradation

Gradation is the particle size distribution in an aggregate mixture and is determined in terms of the percentage passing or retained on each of the sieves. Gradations are specified to ensure acceptable pavement performance. For example, Superpave specifies gradations within designated control points (Roberts et al 1996) as illustrated in Figure 2.7. Gradations passing through the restricted zone are thought to have low resistance to permanent deformation but this has been disapproved in some studies as will be presented in the following paragraphs.

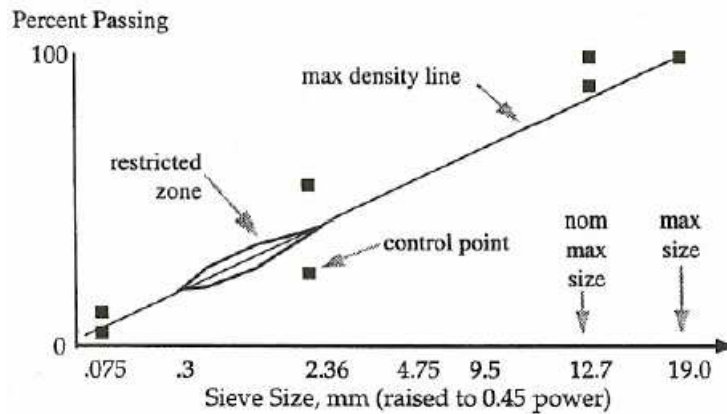


Figure 2.7 Superpave gradation for 12.7 mm nominal maximum size (Kett 1998)

Gradation influences the permanent deformation in asphalt mixtures. Asphalt mixtures composed of different gradations but of similar mineralogical composition exhibit significantly different permanent deformation behaviour. This was shown in a study conducted by Kandhal and Mallick (1999, 2001) in which the effect of gradation on the permanent deformation behaviour of Superpave dense asphalt mixtures was evaluated. The study involved different gradations with similar mineralogical composition and similar gradations with different mineralogical composition. The asphalt mixtures were composed of granite, limestone and gravel gradations passing above, through and below the restricted zone. The results of this study showed significant gradation effects on the permanent deformation behaviour of the asphalt mixtures. For granite and limestone mixtures, the gradations passing below the restricted zone exhibited highest amount of rutting, gradations passing through showed the lowest amount of rutting and the gradations passing above showed intermediate amount of rutting. For gravel mixtures, the gradation passing below the restricted zone exhibited the lowest amount of rutting, the gradations above showed the highest amount of rutting and the gradations passing through showed an intermediate amount of rutting.

The perception that gradations passing through the restricted zone offer low resistance to permanent deformation was also disapproved in a study conducted by Ven van de et al (1997). The study considered dense asphalt mixtures composed from different gradations but with similar mineralogical composition. Part of the study involved the evaluation of rutting resistance of the asphalt mixtures. The evaluation suggested that the restricted zone does not necessarily influence the rutting resistance of asphalt mixtures.

2.3.1.2 Type of Aggregate Surface Texture

The type of aggregate surface texture depends on hardness, grain size, pore characteristics of the parent rock as well as the extent to which forces acting on the particle surface have smoothed or roughened the surface (Su 1996). The type of aggregate surface texture is categorized by shape features such as angular, rounded, smooth or rough. The aggregate surface texture affects the aggregate interlock. Durable angular aggregates with a rough surface texture are normally considered to offer good aggregate interlock.

The type of aggregate surface texture influences the permanent deformation performance of aggregate mixtures. This was shown by Kalcheff and Tunnicliff (1982) who investigated the effects of crushed stone aggregate size and shape on asphalt mixture properties. They concluded that mixtures containing crushed coarse and fine aggregates with or without high proportions of mineral filler should be more resistant to permanent deformation resulting from repeated traffic loadings. They also found that these asphalt mixtures were much less susceptible to the effects of temperature and high initial void content than comparable mixtures containing natural sand. However this is countered by Célard (1977) who showed that mixtures containing a large fraction of rounded aggregates could exhibit better dynamic creep behaviour than the same composition made up of crushed aggregates only.

A relatively similar finding was made by Coree and Hislop (2001) who conducted their investigations at constant compaction but using different gradations of continuously graded mixtures. They defined the critical voids in the mineral aggregates (VMA_c) as the VMA at which a mixture transits from sound to unsound permanent deformation behaviour i.e. the VMA below which excessive permanent deformation initiates. They found this critical VMA to be directly related to the proportion of crushed coarse and fine aggregates and to the fineness modulus².

2.3.1.3 Influence of the Filler

In the composition of asphalt mixtures, fillers are used to meet specifications for the aggregate gradation, to increase stability, and to improve the bond between the mortar/mastic and the aggregates. In a literature review conducted by Anderson et al (1982) it was reported that part of the filler is embedded in the bitumen while the other part fills the voids in the aggregate mixture. The part that fills the aggregate voids provides contact points between larger aggregate particles. The embedded part of the filler may act as a bitumen extender or serve to stiffen the bitumen. The review also reported that the rheological behaviour of the bitumen was influenced by the size of the filler particles. The type of bitumen and mineralogy of the filler had a very large effect on the rheological behaviour of the mastic. Stiffening effects of fine mineral powders on filler/bitumen mixtures were relatively small at short loading times or low temperatures but were large at higher temperatures and long loading times. The same review also reported that in a research carried out by Craus and Ishai (1978), it was concluded that the strength of the filler-bitumen bond increased with increase in adsorption intensity, geometric irregularities (shape, angularity and surface texture) and the selective adsorption potential of the fillers.

The effect of the filler on the mixture composition has also been documented by other researchers. Bolk et al (1982) conducted a study on the effect of filler on the mechanical properties of dense asphalt concrete. The study considered fillers based on limestone powder (Wigro and Rhecal 60) and fillers based on fly-ash (Vulcom 40 and Vulcom 60). Results from static creep tests performed at 40⁰C and at a stress of 10⁵ N/m² for a period of 1 hour showed that the filler affected

² Fineness modulus is defined as the sum of cumulative percentages retained on sieves 150µm, 300 µm, 600 µm, 1.18 µm, 2.36 µm, 4.75 µm, 9.5 µm, 19 µm, 37.5 µm and larger increasing in the ratio of 2 to 1, divided by 100 (ASTM C136-96a).

the creep stiffness but the bitumen content had a much greater effect as shown in Figure 2.8.

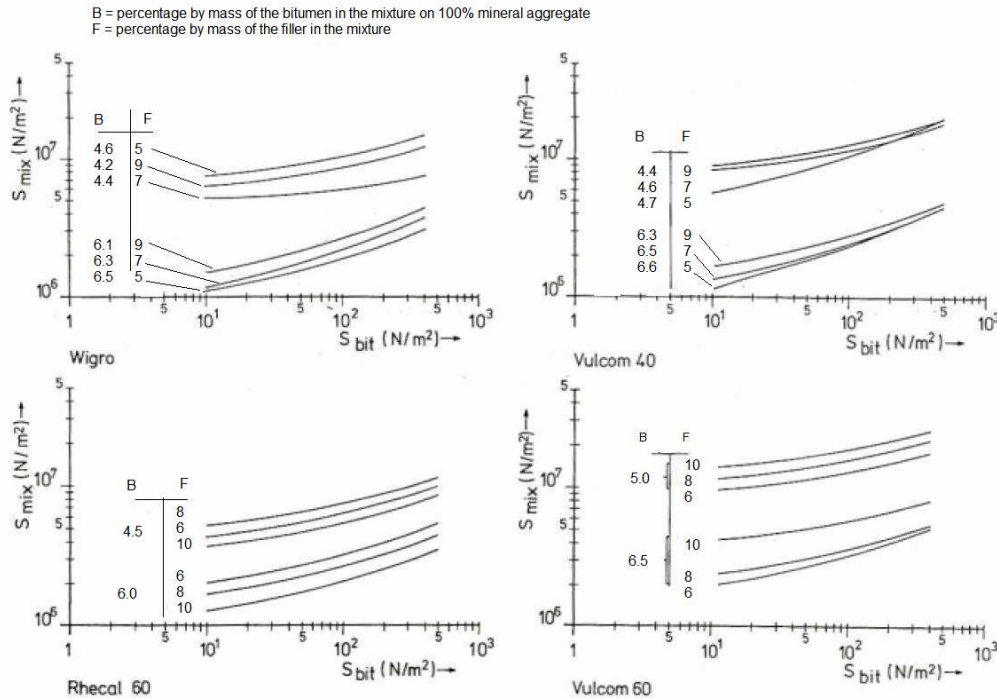


Figure 2.8 Effect of type of filler, filler content and bitumen content on creep stiffness (Bolk et al 1982)

Since the mortar/mastic is composed of bitumen and aggregate particles, change in bitumen properties influences the behaviour of the mortar/mastic. Studies performed by Shell researchers (Heukelom and Wijga 1973) suggest that the stiffness of the mastic and asphalt concrete is influenced by the stiffness of the bitumen and the content of filler and bitumen. As evident from Figure 2.9, increase in the stiffness of bitumen increases the stiffness of mastic and the asphalt concrete. A similar trend in the stiffness of the mastic is observed when the content of filler is increased. Apart from increasing the stiffness of the mastic and the asphalt concrete, increase in bitumen stiffness particularly at high temperatures has also been shown to decrease the amount of permanent deformation in asphalt mixtures. A recent study performed by Ghile (2006) showed that modification of the bitumen can enhance the bitumen stiffness and the rutting behaviour of the asphalt mixture. The study conducted by Ghile involved dense asphalt mixtures composed of unmodified and modified bitumen. The bitumen was modified by a special type of nanoclay. The study found that the modified bitumen not only improved the stiffness of the bitumen at high temperatures but also enhanced the resistance to permanent deformation of the dense mixtures in unconfined repeated load compression tests.

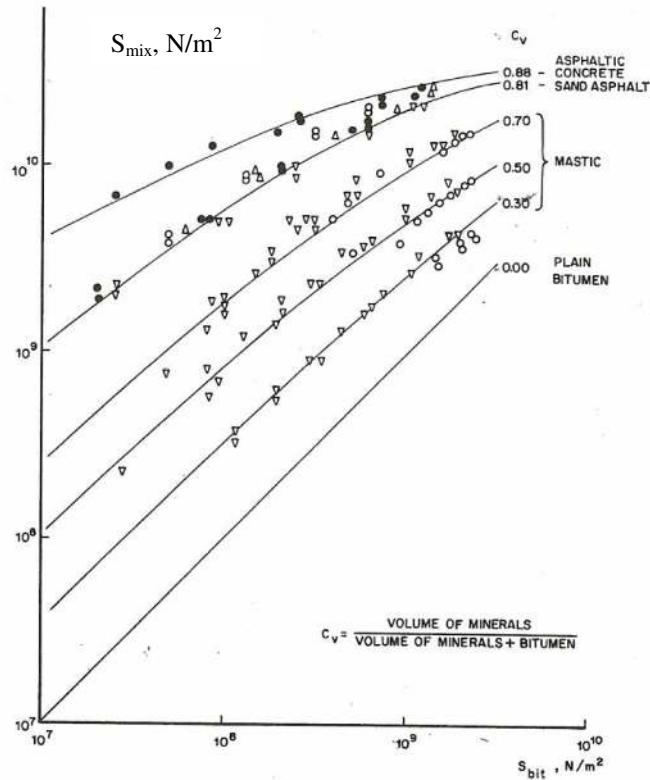


Figure 2.9 Influence of stiffness bitumen on mastic and asphalt concrete (Heukelom and Wijga 1973)

The amount of viscous deformation in bitumen depends on the stiffness and the penetration index of the bitumen as evident from Shell bitumen testing (Heukelom and Wijga 1973). Figure 2.9 shows that the amount of viscous deformation in the bitumen is influenced by both the stiffness and the penetration index. Increase of both the stiffness and the penetration index decreases the amount of viscous deformation in the bitumen relative to the delayed-elastic and elastic deformation thereby leading to increased resistance to permanent deformation.

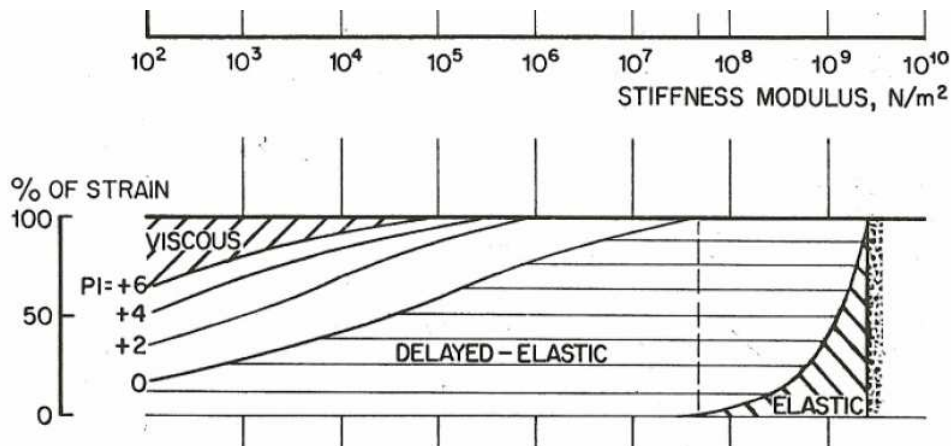


Figure 2.10 Influence of penetration index and stiffness on the viscous deformation in bitumen (Heukelom and Wijga 1973)

2.3.2 Voids in the Asphalt Mixture

With regard to the asphalt mixture, air voids and the voids in the aggregate skeleton filled with bitumen play a significant role in the resistance to permanent deformation. Some asphalt mixture design specifications prescribe air voids and voids filled with bitumen as part of the acceptance criteria for asphalt mixtures. For example, the Dutch mixture design specifications (CROW 2000) prescribe a maximum amount of air voids content of 4-6 % and a maximum voids filled with bitumen of 87-80%. The purpose of this provision is to prevent overfilling that may occur as a result of extension of the volume of bitumen at high temperatures. The amount of voids filled with bitumen has been shown to influence the stiffness of the asphalt mixture. During the study performed by Bolk et al (1982), the creep stiffness was found to decrease with increase in the voids filled with bitumen as illustrated in Figure 2.11.

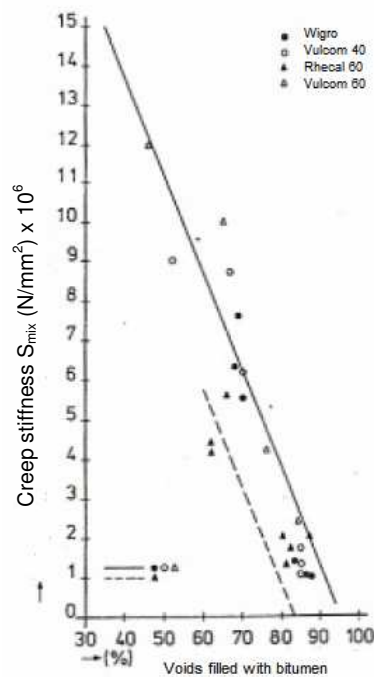


Figure 2.11 Effect of voids filled with bitumen on static creep stiffness (Bolk et al 1982)

The content of air voids in asphalt mixtures also affects the permanent deformation behaviour. In their literature survey on types of density specifications, Roberts et al (1996) concluded that too low air void contents (<3%) could lead to rutting and shoving in dense graded asphalt mixtures. May and Witczak (1992) found that rapid or plastic flow dominates the permanent deformation behaviour of HMA mixtures with less than 3% air voids.

2.3.3 Compaction

The purpose of compaction in asphalt mixtures is to stabilize and enhance the mechanical properties of asphalt mixtures. Linden and Van der Heide (1987) investigated the influence of compaction in asphalt mixtures. They concluded that the degree of compaction was a dominant quality parameter in asphalt mixtures especially when the mixture is critically designed with a low bitumen content to deliver high resistance to permanent deformation in mixtures such as dense

asphalt concrete. The level of compaction achieved in the field is also influenced by the method of compaction. Different modes of compaction and efforts are applied depending on field conditions. In the Marshall mixture design, the compactive effort is selected in such a way to attain optimum bitumen content and to produce a density in the laboratory equivalent to that ultimately obtained in the pavement under traffic (Roberts et al 1996). Typically a compaction effort of 35, 50 or 75 blows is applied in the Marshall mixture design depending on the anticipated traffic loading.

In soils, the compaction density is influenced by the compaction effort and the water content. Similar to soils, the compaction density of the asphalt mixture is affected by the compaction effort and bitumen content. The density of the asphalt mixture increases with increase in the bitumen content reaching the maximum density at optimum content after which it decreases as illustrated in Figure 2.12.

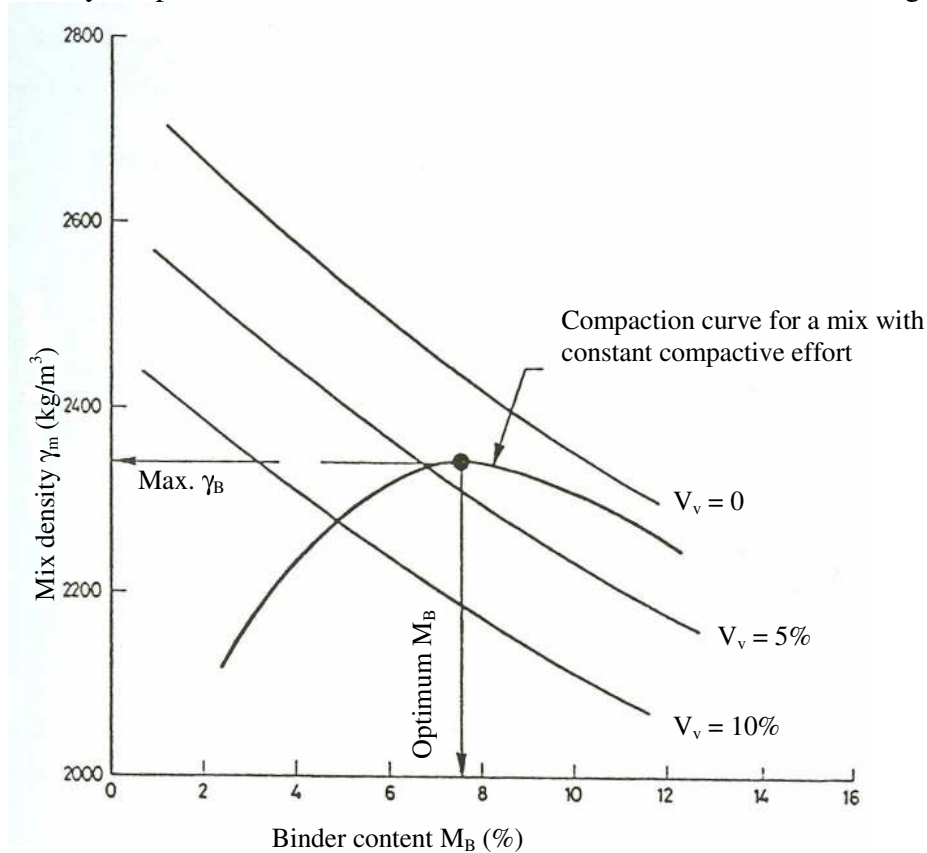


Figure 2.12 Effect of bitumen content on the density of the asphalt mixture (Brown 1992)

2.4 Modelling of Permanent Deformation

Linear elastic multi-layer analysis in combination with laboratory based permanent deformation relationships and visco-elastic methods are some of the methods that are currently used to describe the development of permanent deformation in asphalt mixtures. The term “hybrid models” will be used to describe models that are a combination of elastic multi-layer analysis and laboratory based permanent deformation relationships. On the other hand, visco-

elastic methods use time-dependent material properties that are defined in terms of Maxwell or Kelvin elements.

Although many pavement models assume the properties within the pavement layers to remain constant irrespective of the stress distribution, stress dependency of pavement layers has been reported in literature. Several researchers have shown that the behaviour of unbound pavement materials and bound pavement materials such as asphalt mixtures is stress dependent (Sweere 1990, Huurman 1997, Antes 2002, Parajuli 2002). The consequence of this stress dependent behaviour is that material properties such as stiffness and Poisson's ratio are not constant but vary as a function of the stresses at a particular point in the layer.

2.4.1 Hybrid Models

In hybrid models, the development of permanent deformation in asphalt mixtures is modelled as illustrated in Figure 2.13. The stresses or strains calculated from linear elastic multi-layer analysis are used in laboratory based permanent deformation relationships to predict permanent deformation. The laboratory based permanent deformation relationships are developed by means of laboratory tests such as creep, repeated load, uniaxial or triaxial tests.

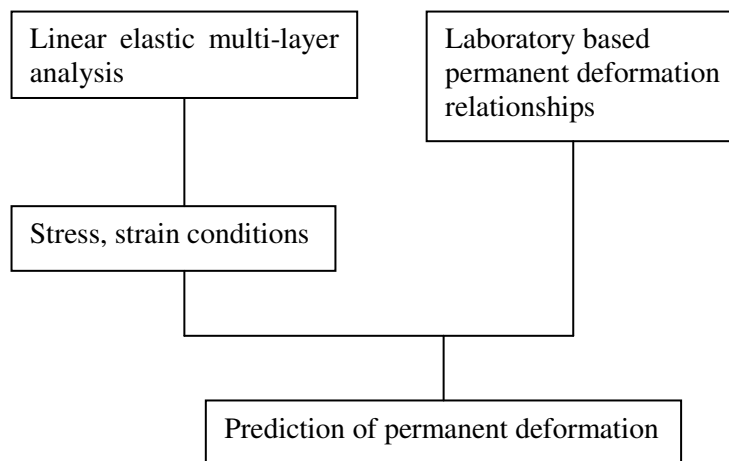


Figure 2.13 Hybrid Models

2.4.1.1 Linear Elastic Multi-Layer Analysis

In 1885 Boussinesq developed a theory for the calculation of stresses and displacements based on a concentrated load applied on an elastic half-space (Huang 1993). In his theory the stresses were dependent on the load, depth and distance while the displacements were a function of load, depth, distance, Poisson's ratio and elastic modulus. Alvin and Ulery extended Boussinesq theory to allow for the determination of stress, strain and deflection at any point in a homogenous half space subjected to a vertical circular load of uniform pressure. Odemark developed the equivalent layer thickness theory for application of the Boussinesq theory to multi-layer systems with varying elastic moduli. However, the combined Odemark and Boussinesq theory could not predict horizontal tensile stresses that can be generated if a stiff bound layer is applied on a relatively softer layer (Molenaar 1998). Since the occurrence of tensile stresses has been identified among the causes of failure in asphalt layers founded on unbound materials, researchers such as Nijboer (1955) and Huang (1993) have come up with

procedures to determine the tensile stresses occurring at the bottom of the bound layers based on a circular uniformly distributed vertical contact stress. Burmister developed the linear elastic multi-layered theory, which is considered to give reasonable estimates of the stresses and strains occurring in bound materials (Molenaar 1998).

Hybrid models characterise the pavement layers with elastic material properties. In these models, each layer is characterised by a single elastic and Poisson's ratio parameter and the stresses in the pavement layers are calculated by means of elastic analysis. The single elastic parameters do not account for the stress dependency nor do they account for time-dependent visco-elastic material properties in the asphalt layers. The wheel load is represented as a static load and the contact stress distribution is generally considered to be uniformly distributed over a regular (mostly circular) contact area.

2.4.1.2 Laboratory Based Permanent Deformation Relationships

One example of a hybrid model is the ESSO (Eckmann 1987) method. In this method, the permanent deformation is determined as a function of the pavement stresses and permanent deformation relationships as developed from repeated load triaxial tests. The permanent deformation in the pavement is calculated based on Equations 2.1 and 2.2.

$$\varepsilon_i = \alpha t_i^\beta \quad 2.1$$

$$\varepsilon = \varepsilon_i + \dot{\varepsilon} \Delta t \quad 2.2$$

Where:

ε_i	=	initial permanent deformation,
α, β	=	regression parameters dependent on type of mixture and test conditions,
t_i	=	initial loading time,
ε	=	permanent deformation,
$\dot{\varepsilon}$	=	rate of permanent deformation dependent on type of mixture and test conditions,
Δt	=	change in loading time.

The hybrid model approach is attractive because of its simplicity and straightforwardness. However, literature review suggests that the agreement between the predicted and the actual permanent deformation varies from very good to very poor (Eckmann 1987, Sousa et al 1991). The application of the hybrid models in the prediction of permanent deformation was further examined in this research and will be presented in section 2.5.

2.4.2 Visco-Elastic Models

The main difference between the elastic and visco-elastic approach is that in the elastic theory the material is visualised to have fixed time-independent stress to strain ratios whereas in the visco-elastic approach, the material is characterised by time-dependent stress to strain ratios (Ashton and Moavenzadeh 1967). The time-dependent material properties in the visco-elastic approach are defined in terms of

Maxwell or Kelvin elements. It is suggested in literature that, under small strains, asphalt mixtures exhibit a linear visco-elastic behaviour and that the visco-elastic theory may give a better prediction than the elastic theory for predicting displacements in asphalt pavements (Huang 1967). An important advantage of this approach is that moving wheel loads can be considered directly. This results in the correct time-rate of loading to be applied to each material element. While nonlinear visco-elastic response characteristics may provide a more realistic estimate of pavement response, the associated mathematical complexities have limited past analyses (Sousa et al 1991).

One of the better known earlier visco-elastic models is VESYS (Kenis et al 1982, Kenis 1977). VESYS is a visco-elastic probabilistic computer program for predicting pavement performance in terms of rutting, roughness, and crack damage. In the VESYS model, the pavement layers are described by elastic or visco-elastic properties and the material properties are assumed to be isotropic.

The permanent deformation is calculated based on the laboratory determined permanent deformation expression (Equation 2.3) that relates the resilient modulus and the recoverable strain to permanent deformation.

$$\Delta e_p(N) = e\mu N^{-\alpha} \quad 2.3$$

Where:

Δe_p	=	vertical permanent deformation at the N^{th} load repetition,
N	=	number of load repetitions,
e	=	peak strain for a haversine load pulse of duration 0.01 sec measured on the 200 th repetition,
μ, α	=	model parameters.

Apart from VESYS, VEROAD (Visco Elastic ROad Analysis Delft) was also considered. In VEROAD, pavement materials are modelled using linear visco-elasticity. This enables VEROAD to account for the time retardation between the applied load and the generated response (Hopman et al 1997).

2.5 Prediction of Permanent Deformation based on Visco-elastic and Hybrid Models

As part of this research an extensive visco-elastic analysis was performed using the VEROAD visco-elastic model. The main aim of this analysis was to evaluate the applicability of such a model in the prediction of permanent deformation occurring in asphalt pavements. The use of the hybrid models in prediction of permanent deformation was also considered. In addition, the applicability of these models in the prediction of strains occurring in the pavement was evaluated as well.

The analysis involved the back calculation of measured pavement response in two LINTRACK test pavements using laboratory developed relationships. In this section, a brief description of the analysis will be presented. A summary of this process can be found in Annex 1 and a complete report on this topic can be found in Muraya et al (2002).

Table 2.2 shows the details and the test conditions of two of the four LINTRACK test pavements that were considered in the analysis presented in this section. The two test pavements consisted of four asphalt layers and a cement bound asphalt granulate base layer constructed on a well compacted sand subgrade. During testing, the test section was sheltered from climatic influences such as rain and sunshine by a housing hall measuring 23 m long, 6 m wide and 5 m high, which covers the entire installation. The temperature of the test pavement was controlled through an infrared heating system. The strain in the asphalt layers was measured by means of strain transducers while the permanent deformation on the pavement surface was measured using a transverse profilometer. The strain transducers were placed at a depth of 180 mm in one test pavement and 190 mm in the other test pavement (i.e. at the bottom of STAC 2 layer). The typical rutting profile consisted of heaves and depressions indicating the presence of shear failure.

Table 2.2 Second and third LINTRACK test pavements³

Layer	Test pavement	
	second	third
top layer	DAC-45/60 40 mm thick	PAC 50 mm thick
second layer	OAC2 60 mm thick	STAC3 60 mm thick
third layer	STAC2 80 mm thick	
fourth layer	STAC1 90 mm thick	
fifth layer	AGRAC 250 mm thick	
subgrade	WCS over 5 m thick	
wheel load characteristics	standard wide based tyre 45 kN load, 0.9 MPa tyre pressure, 0.123 m contact radius, 20 km/h speed	
temperature	between 38 - 40 ⁰ C at the top of the pavement and 32 - 34 ⁰ C at the top of the base	
abbreviation	Material description	
DAC-45/60	Dense asphalt concrete	
OAC2	Open asphalt concrete	
STAC1,2,3	Stone asphalt concrete	
AGRAC	Cement bound asphalt aggregate base	
WCS	Well compacted sand	

The back calculation was performed on the basis of models developed from laboratory tests. The laboratory tests involved extensive triaxial tests that were conducted on specimens cored from material sections that were constructed at the same time and in the same manner as the test pavements (Parajuli 2002, Antes 2002 and Houben et al 2003). All test samples had a diameter of 101.6 mm and a height between 110 and 120 mm. The triaxial tests consisted of resilient and permanent deformation tests that were performed using a vertical haversine stress signal and constant confinement. From these triaxial tests, the models for resilient modulus, Burger's parameters and permanent deformation behaviour were obtained. The results from the resilient deformation tests showed that the Burger's parameters were highly non-linear and were dependent on temperature, stress

³ The two test pavements are referred to as second and third test pavements to make the terminology for the two test pavements in this dissertation consistent with the complete report on the visco-elastic analysis (Muraya et al 2002).

conditions and loading duration (Parajuli 2002, Antes 2002). The resilient modulus and the Burger's parameters were modelled based on work done by Pellinen and Witzak (2002) while the permanent deformation was modelled in relation to the bulk stress and the deviator stress (Houben 2003, Muraya et al 2003).

The back calculation of measured pavement response was performed using BISAR and VEROAD computer packages. BISAR is a linear elastic pavement model and was used to calculate strains in the pavement and to estimate the initial VEROAD input parameters. The VEROAD model was used in the calculation of both strains in the pavement and the rut depths on the pavement surface.

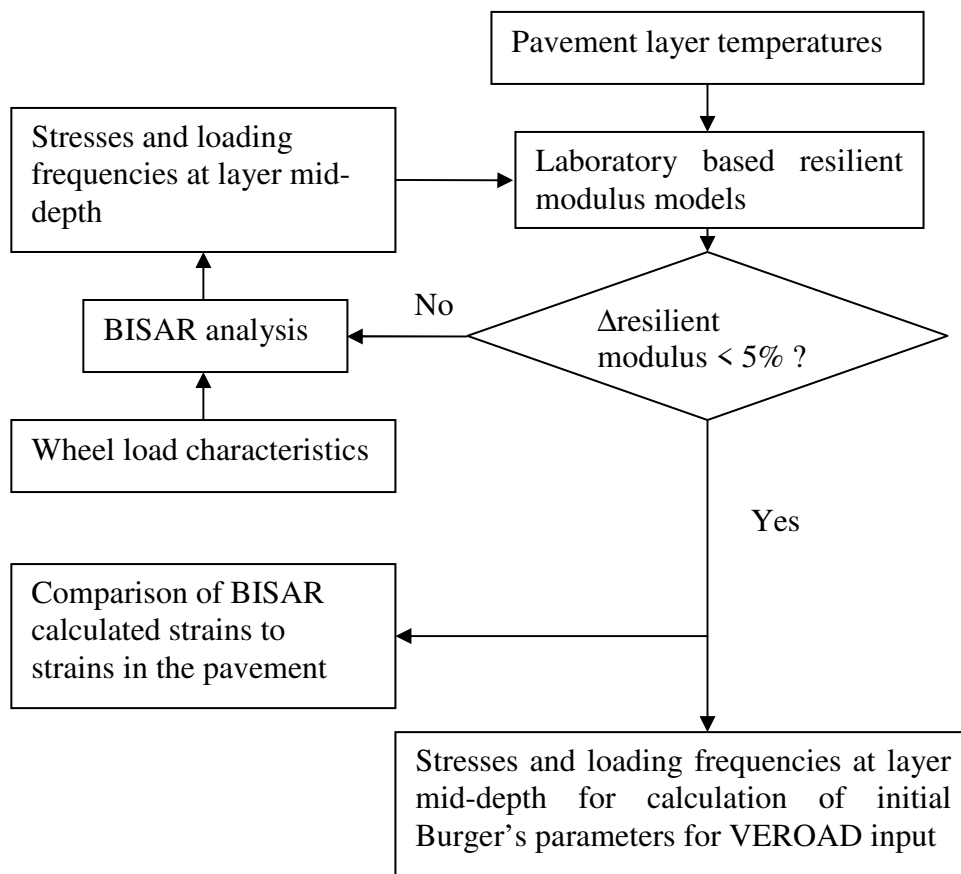


Figure 2.14 BISAR linear elastic analysis

Figure 2.14 shows the process that was applied in the BISAR back calculation. The initial resilient modulus was roughly estimated from resilient modulus charts obtained from the triaxial tests. The initial moduli values together with the wheel load characteristics were then used to calculate the stresses from which the frequencies at the layers mid-depth were obtained. These stresses, frequencies and the measured layer temperatures were then applied in the resilient modulus models to estimate the next set of resilient moduli for the different pavement layers. This process was repeated until the change in resilient moduli was less or equal to 5%. The calculated strains in the pavement at this stage were then compared to the measured strains.

The initial Burger's parameters for the VEROAD analysis were estimated from the final stresses and frequencies obtained in BISAR analysis. The stresses were then processed to obtain the loading frequencies occurring at the mid-depth of each pavement layer. The next set of Burger's parameters was determined from these stresses, frequencies and layer temperatures. This process was repeated until the change in Burger's parameters was less or equal to 5% after which the calculated strains in the pavement were compared to the measured strains as illustrated in Figure 2.15.

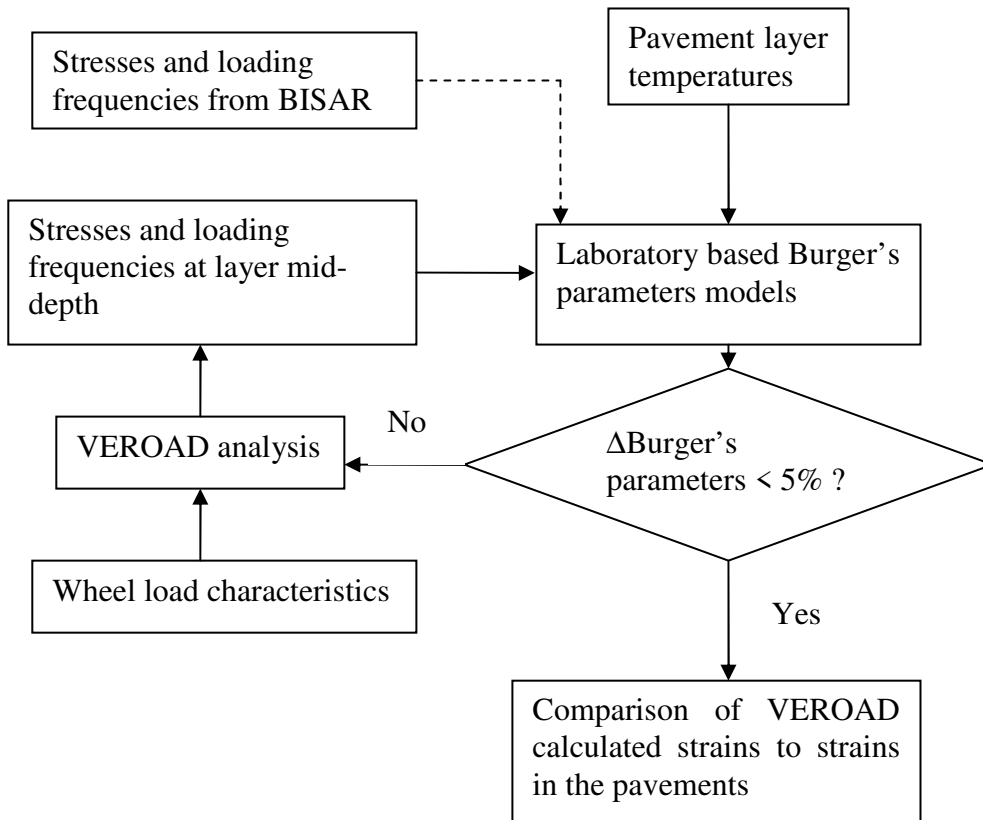


Figure 2.15 VEROAD linear elastic analysis

Figure 2.16 and Figure 2.17 show the stresses determined using the BISAR and the VEROAD analysis in the top two layers of the second and the third test pavements. The figures show that the stresses in the top layers calculated using the linear elastic approach in BISAR and the linear visco-elastic analysis in VEROAD compare reasonably well. The stresses are virtually the same.

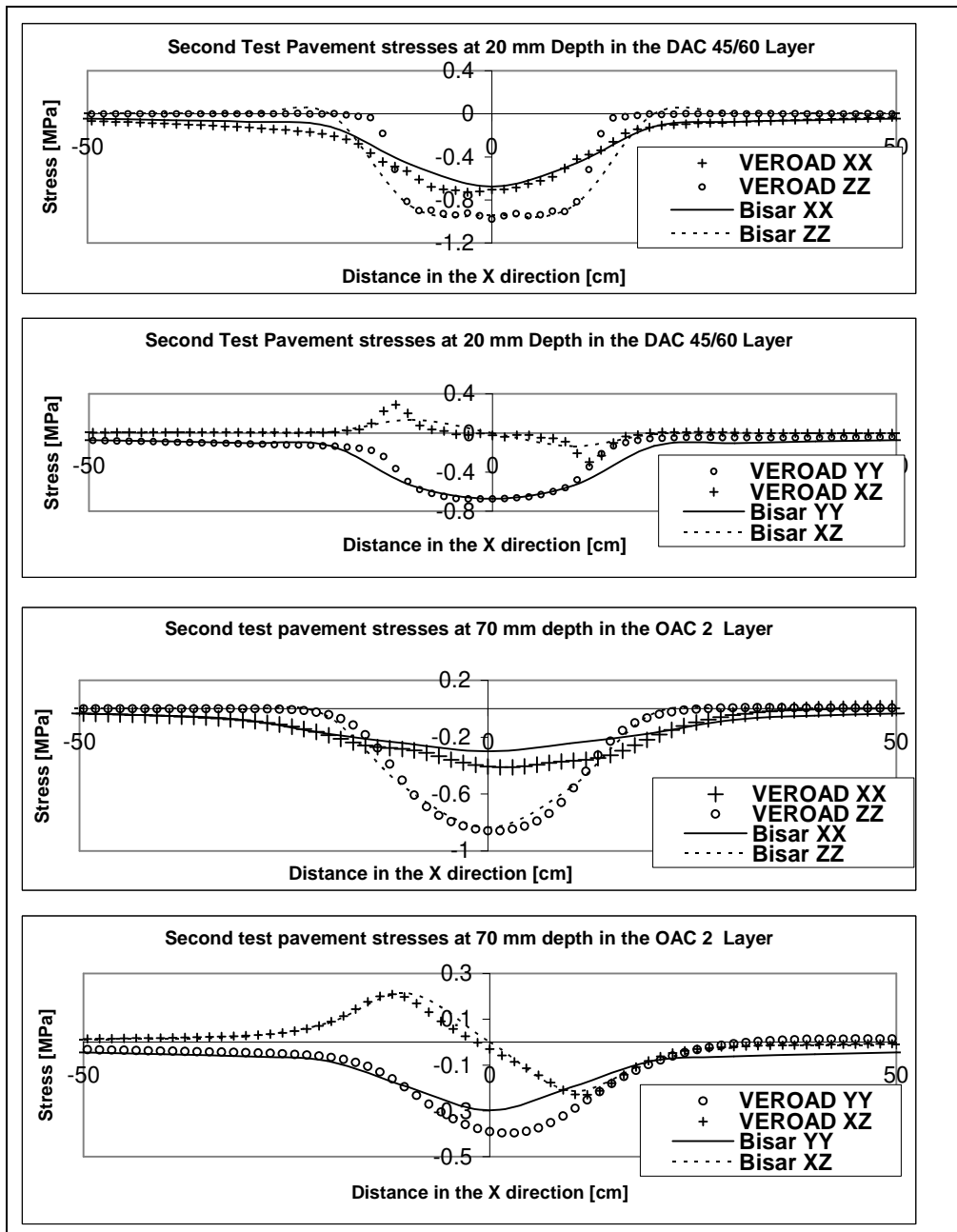


Figure 2.16 BISAR and VEROAD Stresses in the top two layers of the second test pavement (DAC 45/60 and OAC 2)

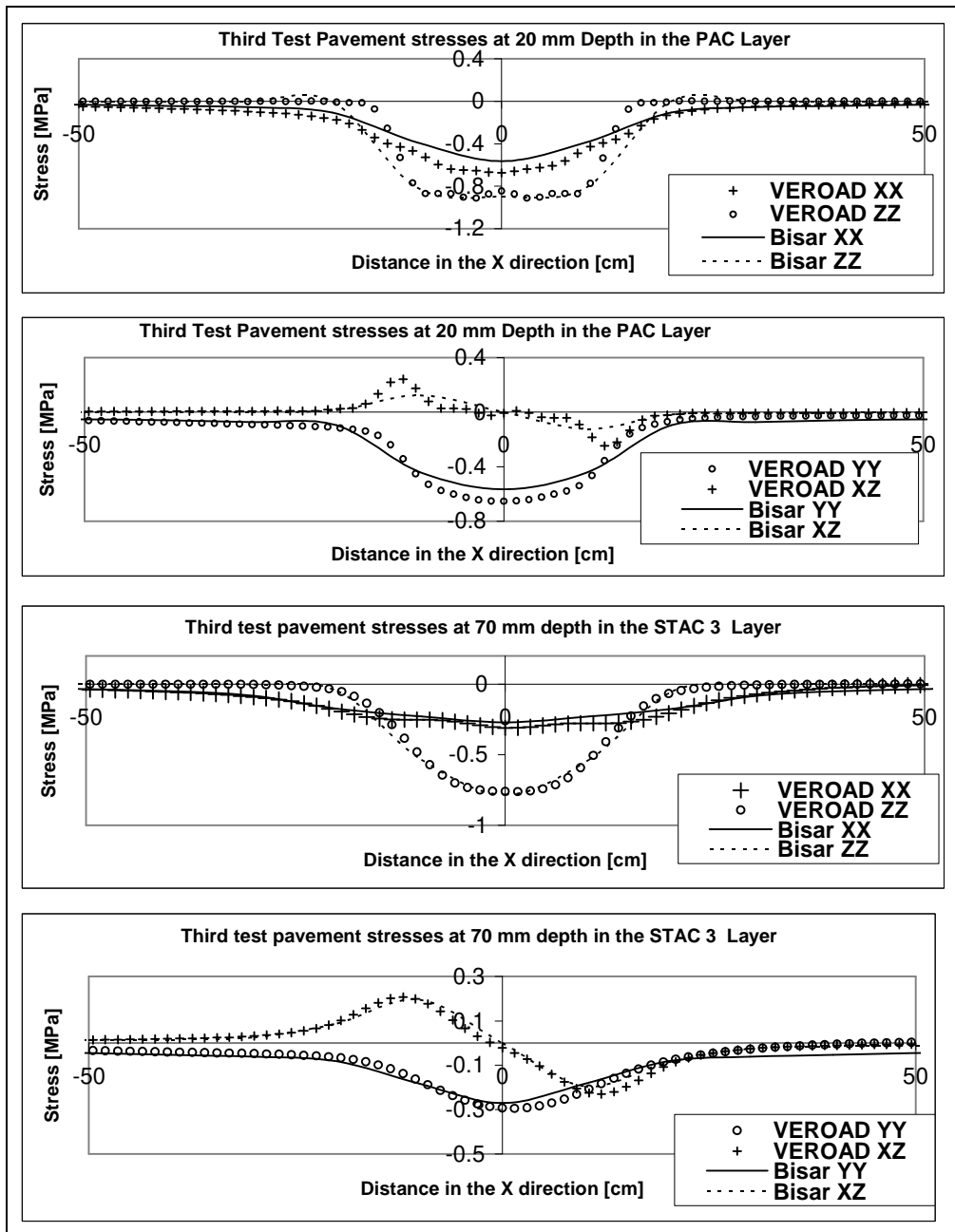


Figure 2.17 BISAR and VEROAD Stresses in the top two layers of the third test pavement (PAC and STAC 3)

The BISAR and VEROAD analysis resulted in strains that were much lower in comparison to the measured strains in the pavement. Figure 2.18 and Figure 2.19 show the measured strains at $N = 100$ and calculated strains in the asphalt layer at 180 mm depth and at 190 mm depth for the second and the third test pavement respectively. These figures show that the calculated strains using both BISAR and VEROAD were much lower and out phase relative to the measured strains. The figures also show that both the transverse and longitudinal VEROAD strains were of the same shape as the measured strains. On the other hand, the shape of the longitudinal BISAR strain and the measured longitudinal strain was similar but the shape of the BISAR transverse strain was different to the measured transverse strain.

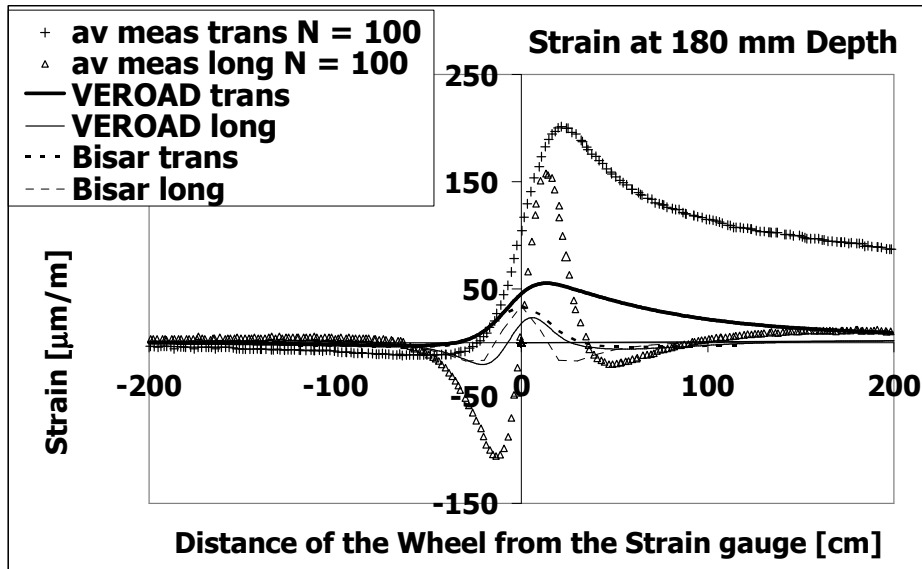


Figure 2.18 Measured strain signals at $N = 100$ and calculated strains (based on triaxial resilient deformation tests) in the asphalt layer for the second test pavement at 180 mm depth.

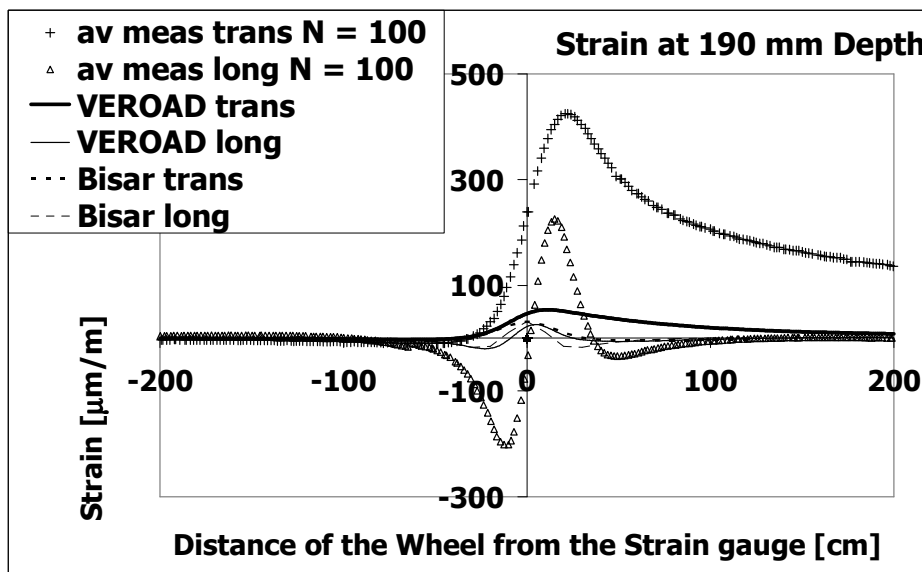


Figure 2.19 Measured strain signals at $N = 100$ and calculated strains (based on triaxial resilient deformation tests) in the asphalt layer for the third test pavement at 190 mm depth.

An alternative manual process shown in Figure 2.20 was therefore adopted to fit the Burger's parameters on the measured pavements strain, in order to calculate realistic stresses for back calculation of permanent deformation based on the triaxial permanent deformation tests. In this manual process, the η_1 was first fitted on the measured practical rut depth while accounting for the effect of lateral wander through the Twinwheels package (Van Dommelen 2000). This was followed by the fitting of the other Burger's parameters on the measured strains in the pavement. The manually fitted Burger's parameters were then used to calculate the stresses occurring in the test pavements. The triaxial vertical and

triaxial confining stresses in the two test pavements calculated from the fitted Burger's parameters exhibited little variation irrespective of the number of load repetitions. Consequently representative Burger's parameters and pavement stresses were adopted from load repetition #4000 in the second test pavement and from load repetition #3000 in the third test pavement (Muraya et al 2002).

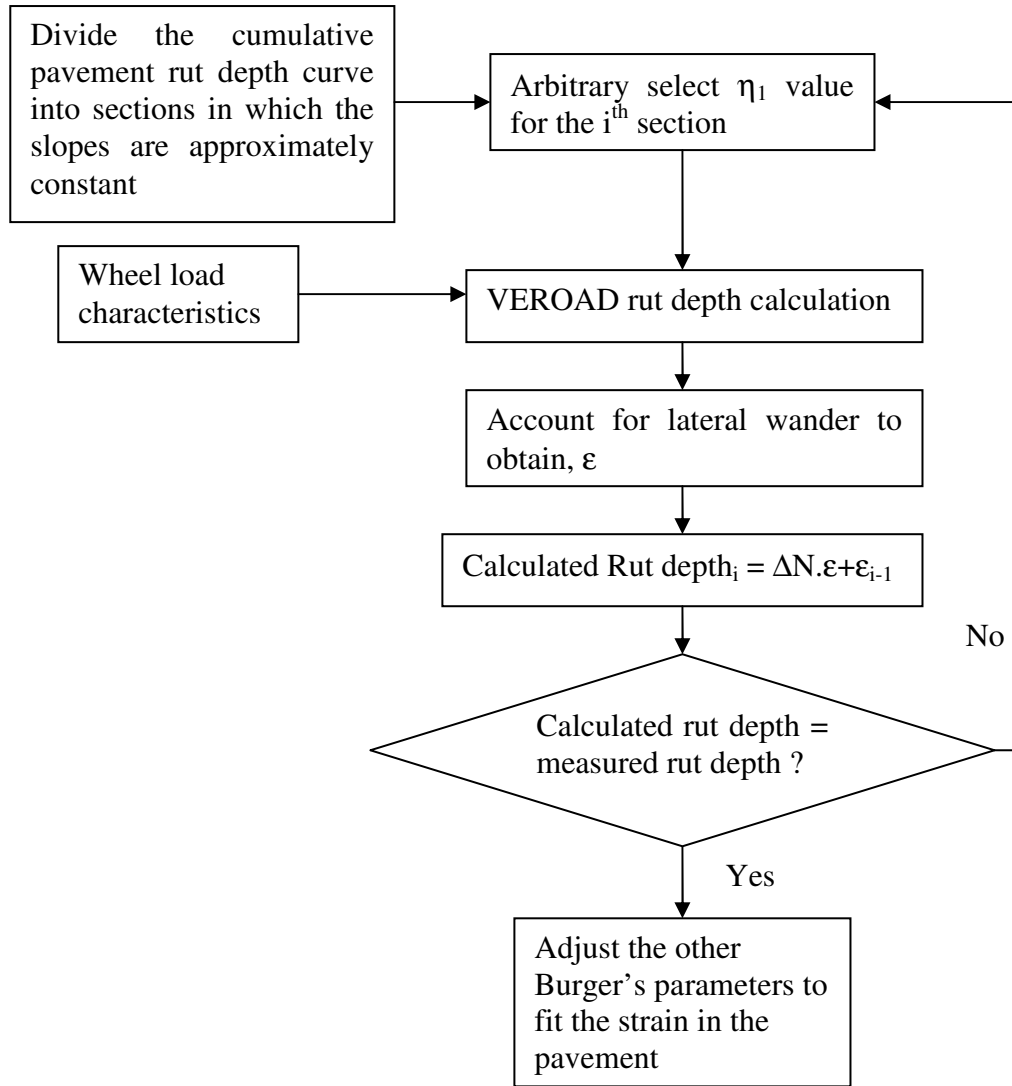


Figure 2.20 Manual fitting of Burger's parameters

The permanent deformation in the test pavement was back calculated using two methods namely the η_1 method and direct method. In the η_1 method, the permanent deformation was calculated using VEROAD and η_1 values derived from the triaxial test permanent deformation model. The direct method involved the direct application of the triaxial test permanent deformation model. In this method, the stresses occurring at the axis of load symmetry in the various layers were directly applied on the triaxial permanent deformation model. Figure 2.21 shows the results of the visco-elastic analysis. As evident from this figure, the calculated rut depths using the η_1 and the direct method were much smaller than the measured rut depths.

The permanent deformation in hybrid models is determined on the basis of laboratory based relationships and linear elastic multi-layer analysis. The hybrid approach can be envisaged by the use of BISAR stresses in the direct method. Since the BISAR and VEROAD stresses were virtually the same (refer to Figure 2.16 and Figure 2.17), hybrid model would have resulted in rut depths similar to those calculated using the direct method.

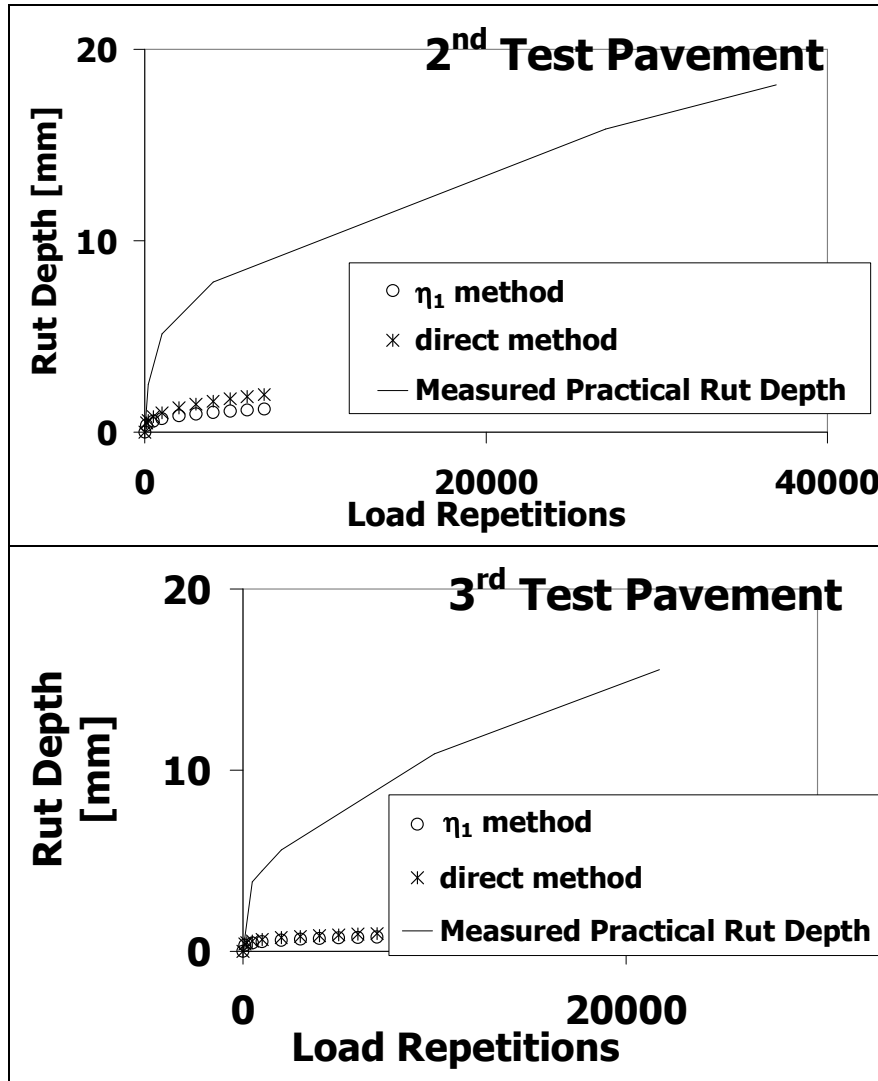


Figure 2.21 A comparison of rut depths calculated using VEROAD and measured rut depths in the second and the third LINTRACK test pavements

The inability by the VEROAD analysis and hybrid models in predicting the permanent deformation could be attributed to the following reasons:

- The Burger's parameters and resilient modulus were determined from constant confinement tests. However, the stresses in the pavement vary depending on the position of the wheel load. This approach of measuring the Burger's parameters and resilient modulus may not be sufficient and variation of the confinement during laboratory tests may be necessary. The necessity of confinement variation will be further discussed in section 4.5.

- The shear failure observed in the rut depth profiles suggests the need for shear strength tests. This type of deformation cannot be explained by means of a linear visco-elastic or the linear elastic approach.
- The Burger's parameters and resilient moduli were highly non-linear and dependent on stress conditions and loading duration. VEROAD and BISAR are linear models that do not incorporate non-linearity in stress dependency or in loading durations.

2.6 Influence of Asphalt Mixture Components on Permanent Deformation Behaviour

It is a well known fact that higher permanent deformation occurs in asphalt mixtures at high temperatures compared to low temperatures. Brown and Snaith (1974) suggested that the increase in deformation is related to the decrease in binder viscosity at high temperatures (40°C), thereby leading to a lower interlock between the aggregates. The contribution of the aggregate skeleton towards the behaviour of the mixture becomes more significant at higher temperatures. For example, Pellinen and Witczak (2002) found the aggregate influence to be more dominant than the influence of the binder on the modulus at high temperatures and the binder influence to be more dominant over the aggregate influence at low temperatures. At high temperatures the effects of confining stresses play a significant role in the permanent deformation of the mixture. Awad (1972) and Morris (1973) found that the effect of confining stresses on elastic and permanent deformation strains respectively was more important at high temperatures than at low temperatures.

The foregoing discussion demonstrates that both the aggregates and the mortar play a crucial role towards the resistance to permanent deformation in asphalt mixtures. Especially at high temperatures where the role of the aggregate skeleton becomes dominant, asphalt mixtures have many similarities with unbound materials. It is therefore reasonable to assume that failure mechanisms that are applicable to unbound materials are valid for asphalt mixtures as well. The Mohr-Coulomb criterion is widely used to describe the shear characteristics of unbound materials and asphalt materials (Molenaar 1993). Plasticity models such as the Mohr-Coulomb yield criterion describe the response of a material in relation to an ultimate surface beyond which no stresses are permitted to occur. If the state of stress is inside the ultimate surface, the deformations are purely elastic and plastic deformation occurs at states of stress on the ultimate surface.

The Mohr-Coulomb failure criterion expressed in Equation 2.4 provides an elegant means of demonstrating the effect of both aggregates and the mortar on the permanent deformation behaviour (FHWA). Figure 2.22 illustrates the effect of the aggregates and the mortar on the failure behaviour of asphalt mixtures. For simplicity purposes, the cohesive strength is considered to be wholly influenced by the mortar while the angle of internal friction is influenced entirely by the aggregates. If the binder has a high cohesion at high temperatures, then it will provide better resistance to permanent deformation than a binder with a lower cohesion. Similarly aggregates with a higher internal angle of friction can be

expected to provide a better resistance to permanent deformation than similar aggregates with a lower angle of internal friction.

$$\tau = c + \sigma \tan \phi \quad 2.4$$

Where:

τ	=	shear strength,
c	=	cohesion,
σ	=	normal stress,
ϕ	=	angle of internal friction.

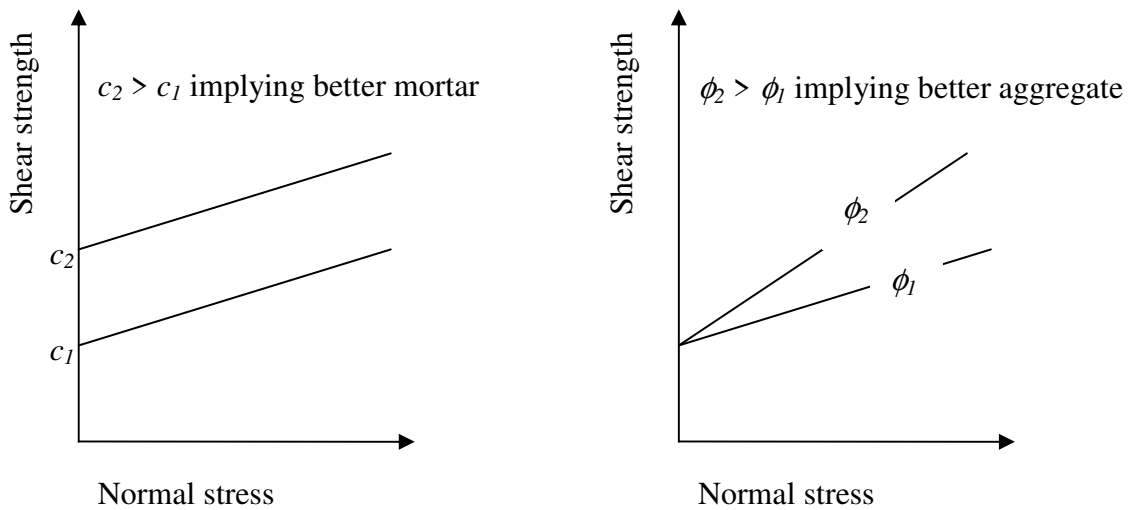


Figure 2.22 Effect of aggregate and mortar on the failure behaviour of asphalt mixtures

However, it must be emphasized that this is a very simple idealization of the asphalt mixture. The cohesion strength of the mortar is dependent on strain rate as well as temperature. It may well be that one mortar may seem to be better at a given strain rate and temperature but the opposite can be true at a different set of strain rate and temperature in comparison to another mortar. Another reason is that permanent deformation may involve rotation of aggregate particles, a fact that cannot be represented by the internal angle of friction.

These simple examples illustrate that both the mortar and the aggregate skeleton play a role in the resistance to permanent deformation. The extent of the role they play depends on the type of mixture and loading conditions. For a good understanding of the permanent deformation behaviour it is important to understand the role of the material components. However, little or no quantitative information is available on how the various components of an asphalt mixture contribute towards the resistance to permanent deformation and as a result this item will form one of the main topics in this research.

2.7 Models Used in this Research

The preceding discussion on elastic models and the extensive visco-elastic analysis that was performed during the course of this research demonstrate that elastic and visco-elastic models are not sufficient for purposes of describing the permanent deformation of asphalt mixtures.

Plasticity models may provide a better description of the permanent deformation in asphalt mixtures. This can be attested by a recent research performed by Medani (2006) at the Delft University of Technology. Medani conducted an extensive investigation into the behaviour of surfacings on orthotropic steel bridge decks. Part of the research involved numerical simulation of damage and cracking in ITT test specimens using the ACR_e (Erkens 2002) plasticity model. He found a remarkable agreement between the simulation and the observed experimental response as is evident from his damage evolution (Figure 2.23), crack evolution (Figure 2.24) and the test observation (Figure 2.25). The research projects conducted by Erkens and Medani were inspired by Desai's plasticity model (Desai et al 1986).

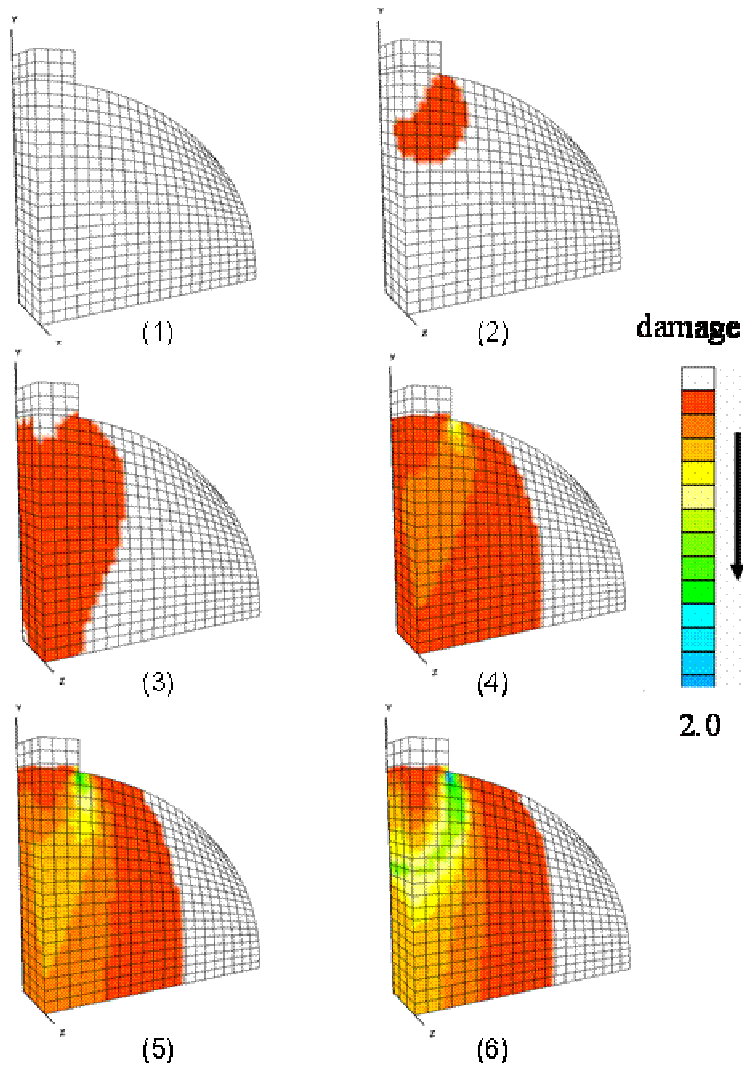


Figure 2.23 Evolution of damage in an ITT test specimen (Medani 2006)

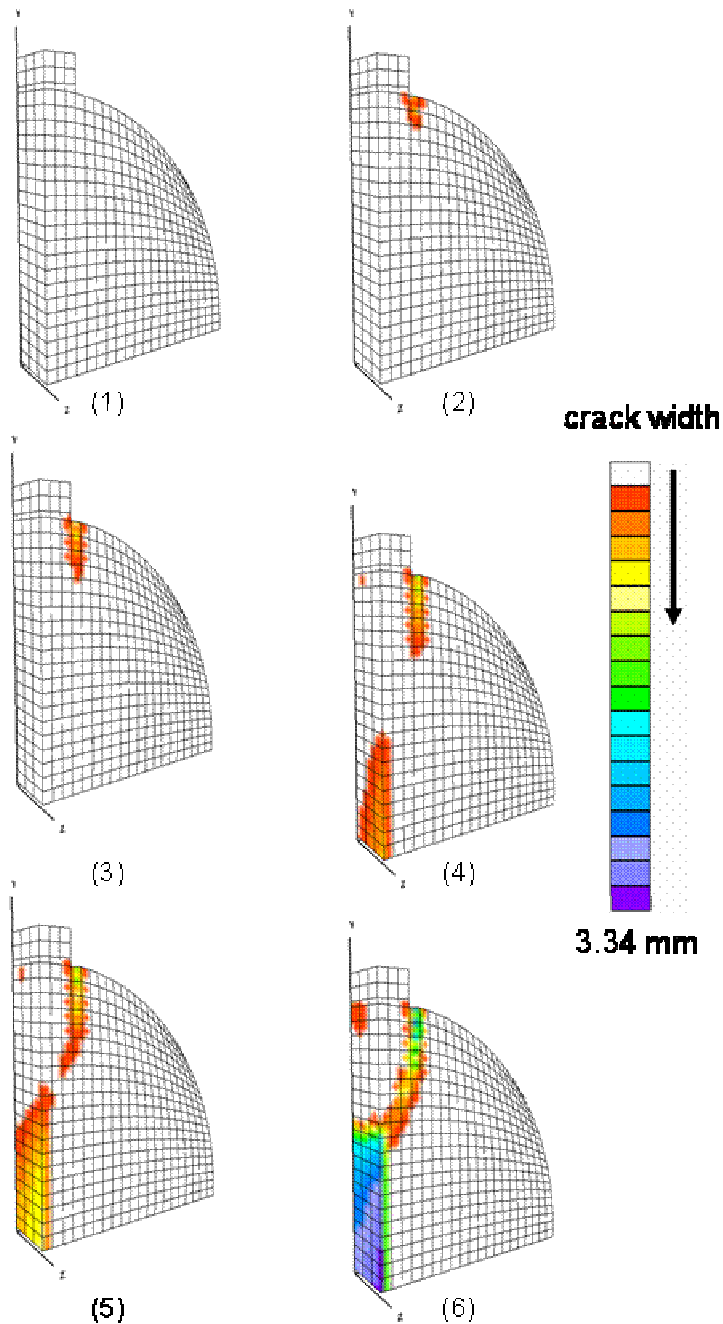


Figure 2.24 Evolution of Cracking in an ITT specimen (Medani 2006)

Given the fact that Desai's plasticity model seems to have remarkable prediction capabilities, it is used in this research to describe the behaviour of both the total asphalt mixture and the aggregate skeleton under monotonic loading. In addition, the Unified Model (Medani 2006) has been used to apply the principle of time-temperature super position to material properties. Both models will be briefly described hereafter.

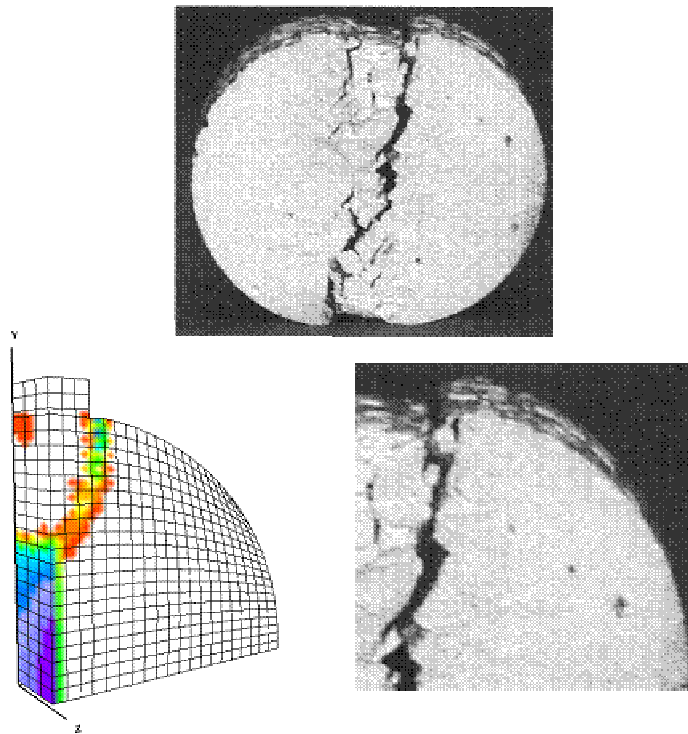


Figure 2.25 Crack evolution and experimental observation in an ITT specimen (Medani 2006)

2.7.1 Desai Model

In order to arrive at a better understanding of the damage mechanisms in asphalt concrete, it is necessary to establish more fundamental knowledge about the material properties and response. In studying the response, influence factors like temperature and strain rate must be considered. Furthermore, it must be realised that to truly investigate material behaviour, structural influences on the observed response should be prevented. For example, tests should be designed in such a way that uniform internal states of stress are obtained (Molenaar et al 2002).

A pre-requisite for the use of the Finite Element Method is the availability of material models that can describe the triaxial behaviour in both the linear and non-linear range. During the development and implementation of the finite element package CAPA-3D, a flow surface proposed by Desai (1986) was selected for purposes of describing the triaxial behaviour in both the linear and non-linear range (Scarpas et al 1997).

Briefly, the Desai flow surface can be schematised as shown in Figure 2.26. This figure compares the one- and two-dimensional situations. Originally, the behaviour is linearly elastic, represented by the straight line until point 1 in the left-hand diagram. From point 1, which corresponds to ellipse 1 in the 2D case, the response is non-linear but the load carrying capacity can still increase. This response is commonly known as hardening and in the 1D case it looks as a curve with diminishing slope (between points 1 and 3). In the 2D case, this phase of response corresponds to a series of successive, incremental ellipses (1 to 3). The strength (the maximum, point 3) in the 1D situation corresponds to the largest ellipse in the 2D case. After this point the strength decreases and softening is initiated. This is illustrated by the descending branch in the 1D diagram (between

point 3 and 4). In the 2D case, this again corresponds to a series of successive ellipses, this time diminishing in size (Molenaar et al 2002).

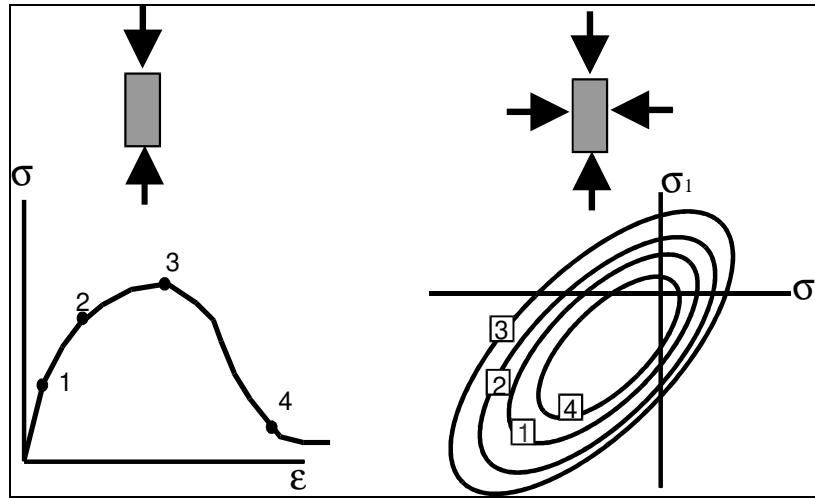


Figure 2.26 Schematisation of the Desai flow surface for the 1- and 2-dimensional case. The numbered points in the 1D diagram correspond to the ellipses in the 2D case (Molenaar et al 2002)

In the three dimensional case, the representation of the stress conditions for a certain state of material response (e.g. failure, initiation of plasticity etc.) is a bit more complex. As evident in the ACR model (Erkens 2002), the Desai flow surface is also applicable to the three dimensional case. Figure 2.27 shows the Desai flow surface. The expression for this surface is given in Equation 2.5.

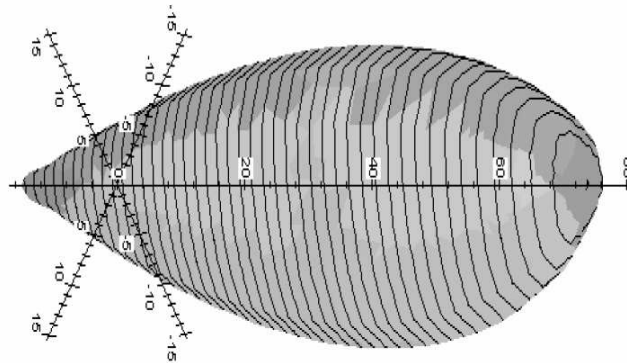


Figure 2.27 Desai surface [I_1 , $\sqrt{J_2}$, θ space, tension negative] (Ekens 2002)

$$f = \frac{J_2}{p_a^2} - \frac{\left[-\alpha \left(\frac{I_1 + R}{p_a} \right)^n + \gamma \left(\frac{I_1 + R}{p_a} \right)^2 \right]}{\sqrt{(1 - \beta \cos 3\theta)}} = 0 \quad 2.5$$

Where:

$$I_1 = \sigma_{xx} + \sigma_{yy} + \sigma_{zz}$$

$$J_2 = \frac{1}{2}(s_1^2 + s_2^2 + s_3^2)$$

$$= \frac{1}{6} \left[(\sigma_{xx} - \sigma_{yy})^2 + (\sigma_{yy} - \sigma_{zz})^2 + (\sigma_{zz} - \sigma_{xx})^2 \right] + \tau_{xy}^2 + \tau_{yz}^2 + \tau_{xz}^2$$

$$J_3 = (\sigma_{xx} - p)(\sigma_{yy} - p)(\sigma_{zz} - p) + 2\tau_{xy}\tau_{yz}\tau_{xz} - (\sigma_{xx} - p)\tau_{yz}^2 - (\sigma_{yy} - p)\tau_{xz}^2 - (\sigma_{zz} - p)\tau_{xy}^2$$

$$p = \frac{\sigma_{xx} + \sigma_{yy} + \sigma_{zz}}{3}$$

$$\cos 3\theta = \frac{3\sqrt{3}}{2} \frac{J_3}{(J_2)^{3/2}}$$

Where:

I_1	=	the first stress invariant,
J_2	=	the second deviatoric stress invariant,
J_3	=	the third deviatoric stress invariant,
p	=	isotropic stress,
s_i	=	i^{th} principal deviator stress,
p_a	=	0.1 [MPa],
α, γ, n and R	=	model parameters.

The model parameters α, γ, n and R govern specific aspects of the surface. These parameters are dependent on the test conditions such as temperature, strain rate, confinement or any other test variable. A description of the role played by each of the parameters with respect to the stress conditions represented by means of the I_1 -SQRT J_2 stress invariants can be found in Annex 2.

2.7.2 Unified Model

The application of time temperature super position principle is a common practice in developing master curves for the complex modulus of asphalt mixtures. However, until recently, this principle has not been used to quantify the strength and failure characteristics of asphalt mixtures. In this thesis, the Unified Model (Medani 2006) is mainly used as a tool to quantify the properties of the asphalt mixtures in relation to time temperature dependency. The main advantage of this model lies in the fact that it can be used to describe a wide range of properties such as stiffness, compressive strength and tensile strength in relation to temperature and time. The model also incorporates theoretical maximum and minimum limits of the property under consideration. The implications of this model are as follows:

1. The temperature susceptibility can be obtained from tests that are relatively easy to conduct.
2. Feasible estimation of minimum and maximum limits of desired material properties.
3. Construction of master curves for different material properties, for example stiffness, compressive strength and tensile strength.

The Unified Model is expressed as follows:

$$P = P_{high} + (P_{low} - P_{high})S \quad 2.6$$

Where:

$$S = e^{(-[u,\beta]^\lambda)} \quad 2.7$$

$$u_r = \frac{u}{u_0} \quad 2.8$$

$$\beta = e^{(-T_s[T-T_0])} \quad 2.9$$

P	=	property under consideration,
P_{high}	=	value of the property as the time derivative variable approaches infinity,
P_{low}	=	value of the property as the time derivative variable approaches zero,
u_0	=	a reference value of the time derivative,
u	=	time derivative,
T_s	=	temperature susceptibility factor,
T_0	=	a temperature reference,
T	=	temperature,
λ	=	model parameter.

A description of the influence of the parameters in this model can be found in Annex 2. The Unified Model was developed to capture the effect of strain rate and temperature on the properties of asphalt mixtures. Nevertheless, the parameters of this model can be modified to describe the effect of confinement on the aggregate skeleton. Apart from being applied on the total asphalt mixture, the Unified Model was also widely used to describe the effect of confinement on the aggregate skeleton. Application of the same model in the description of the mixture components, allowed a similar approach to be used in the characterization of the different components.

2.8 Test Program and Permanent Deformation Analyses

From the preceding sections it is clear that little or no quantitative information is available on how the various components of an asphalt mixture contribute towards the resistance to permanent deformation. This information is required in order to design rutting resistant mixtures. In this research it is postulated that knowledge on the deformation resistance, strength characteristics as well as tensile characteristics of the mastic/mortar is required for the design of rutting resistant mixtures especially for stone skeleton mixtures such as porous asphalt concrete and stone mastic asphalt. In addition it was shown that linear visco-elastic theory is incapable of predicting permanent deformation in practice. Consequently, it is hypothesized that the plasticity theory is better suited to model permanent deformation behaviour especially for the stone skeleton mixtures. Based on this, the test program was designed in such a way that the role played by the skeleton and the mortar/mastic components in both stone skeleton and mastic types asphalt mixtures could be determined and characterized by means of the same plasticity

model that was successfully used in earlier research programs (Medani 2006 and Erkens 2002).

2.8.1 Test Program

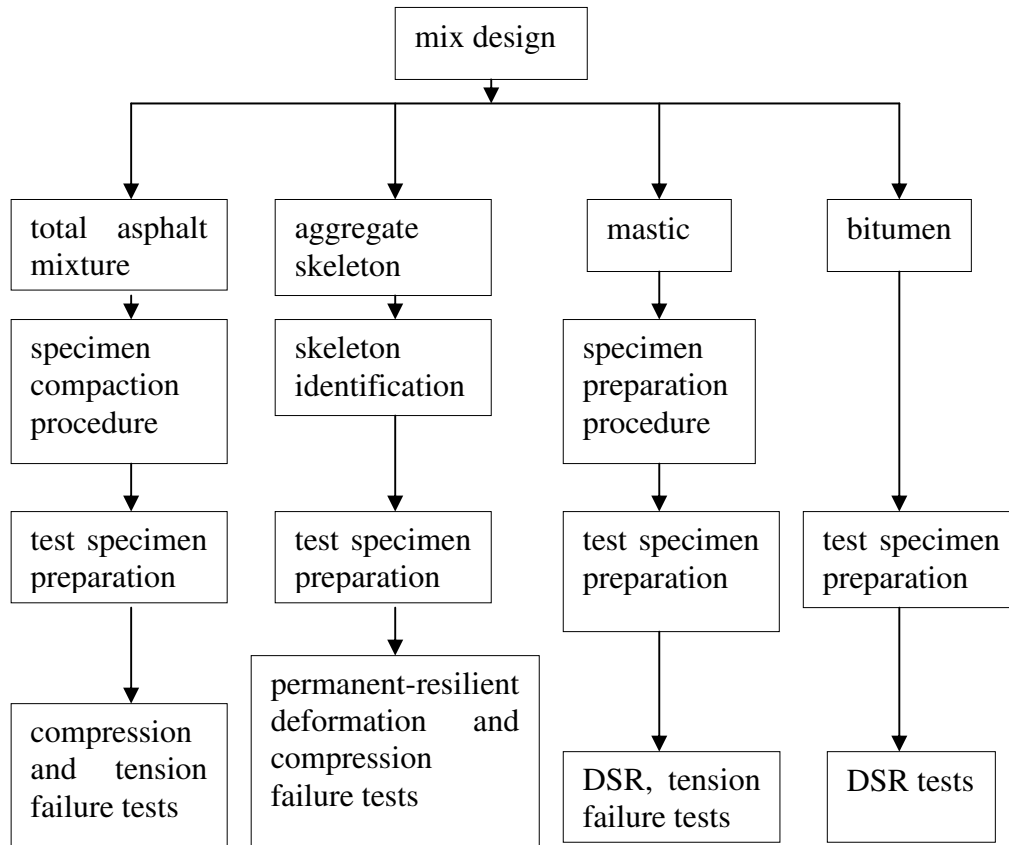


Figure 2.28 Overview of the test program

Figure 2.28 shows an overview of the test program in this research. The initial stage involved the design of the different asphalt mixtures considered in this research. The purpose of the mixture design was to determine the composition of the total asphalt mixture and to facilitate the determination of the composition of the aggregate skeleton and mastic/mortar components. Apart from enabling the composition of the different components, the mixture design also served in the provision of the target densities for the total asphalt mixture and aggregate skeleton test specimens.

The mixture design was followed by the development of test specimen preparation protocols. The specimen preparation protocols consisted of the development of specimen fabrication techniques for the total asphalt mixture, mastic and the aggregate skeleton. Prior to the development of the aggregate skeleton preparation protocols, the aggregate skeletons for the different asphalt mixtures were identified.

The total asphalt mixture was characterized by indirect tension tests, compression failure tests and tension failure tests. The aggregate skeleton was characterized by

compression failure tests and permanent-resilient deformation tests. During the permanent-resilient deformation tests, the permanent as well as the resilient deformation were measured. The mastic was characterized by DSR and tension failure tests while the bitumen was characterized by DSR tests. The purpose of the indirect tension tests performed on the asphalt mixtures and the DSR tests conducted on the mastic was to characterize the temperature susceptibility of the asphalt mixtures and the mastic.

2.8.2 Permanent Deformation Analyses

Figure 2.29 gives an overview of the permanent deformation analyses. Both the tests on the total mixture and the aggregate skeleton provided information on the visco-plasticity characteristics of the mixture and plasticity characteristics of the aggregate skeleton. Comparison between the dilation of the aggregate skeleton and the dilation of total mixture provided valuable information on the tensile stresses to which the mastic/mortar was subjected. The results of the tension tests on the mastic provide information on assessing the capability of the mastic in sustaining the tensile stresses. As it will be shown in the chapters to follow, this approach provides a fundamental understanding of the contributions of the various mixture components towards the resistance to permanent deformation of asphalt mixtures.

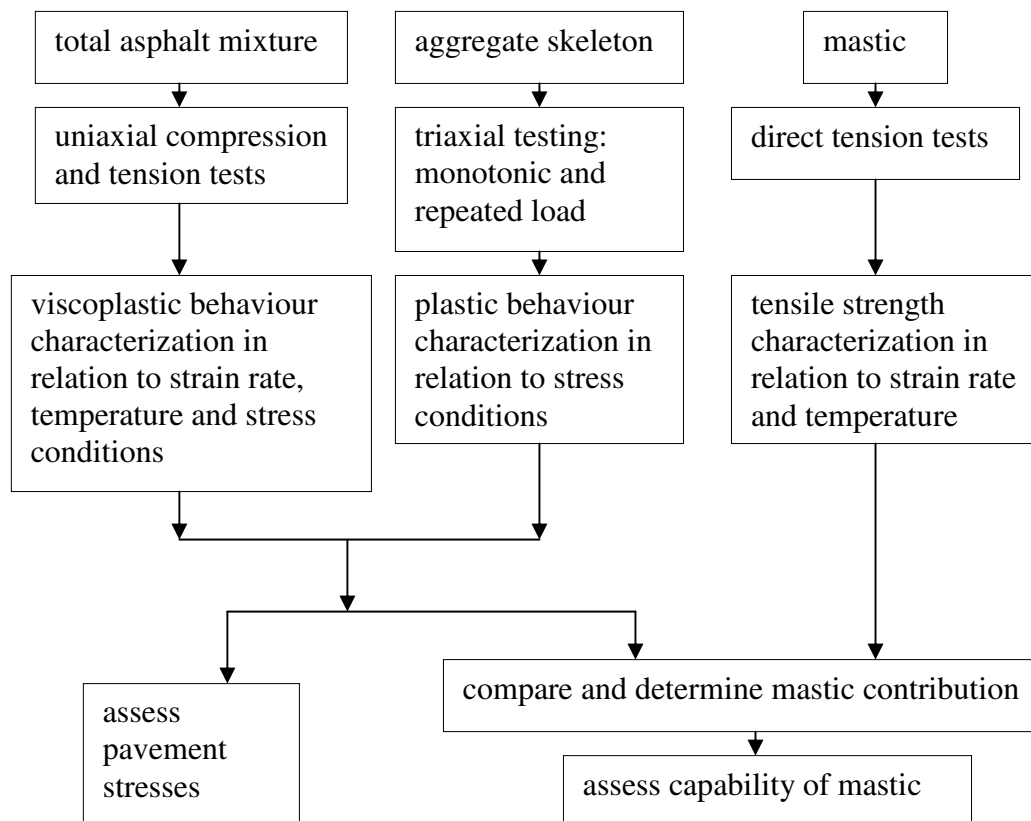


Figure 2.29 Overview of permanent deformation analyses

2.9 Conclusions

In this chapter several issues pertaining to the permanent deformation behaviour in asphalt mixtures were discussed. Based on these issues the following conclusions can be drawn:

- The skeleton and the mortar components play distinct roles in the resistance to permanent deformation. It is therefore important to understand and characterize the separate contribution of the components of an asphalt mixture.
- The contribution of the aggregate skeleton towards the resistance to permanent deformation becomes more important with increase in temperature. At high temperatures, the role of the aggregate skeleton in the resistance to permanent deformation is dominant over the role of the mortar.
- Mixture composition influences the permanent deformation behaviour in asphalt mixtures.
- Hybrid and visco-elastic models are not sufficient for purposes of describing the permanent deformation in asphalt mixtures. The pavement response calculated using the hybrid and visco-elastic models was much smaller than the measured pavement response. The magnitude of the calculated strains in the pavement as well as the calculated permanent deformation was also much smaller than the measured pavement deformation.
- Plasticity models can be used to describe the roles played by the components of an asphalt mixture towards resistance to permanent deformation.
- A testing and evaluation program could be developed to qualify and quantify the contribution of the various mixture components to resistance to permanent deformation of the total asphalt mixture.

2.10 References

- Anderson D.A., (1982), Tarris J.P. and Brock J.D., *Dust Collector Fines and Their Influence in Mixture Design*, Proceedings of the Association of Asphalt Paving Technologists Technical Sessions, vol. 51, pp. 363-397, Kansas City, Missouri, United States of America.
- Antes P.W., (2002), *Onderzoek naar Spanningsafhankelijk Gedrag van STAB en ZOAB*, Msc. Thesis, Delft University of Technology, Delft, the Netherlands.
- ASTM (C136-96a), Standard Test Method for Sieve Analysis of Fine and Coarse Aggregates, Designation.
- Ashton J.E. and Moavenzadeh F., (1967), *Analysis of Stresses and Displacements in a Three-Layered Viscoelastic System*, Proceedings of the Second International Conference Structural Design of Asphalt Pavements, pp. 209-224, University of Michigan Ann Arbor, United States of America.
- Awad I.S., (1972), *Characterisation of the Stress-Strain Relationships of Asphalt Treated Base Material*, Graduate Report, University of Washington.
- Brown E.R. and Cooley L.A., (1999), *Designing Stone Matrix Asphalt Mixtures for Rut-Resistant Pavements*, TRB, National Research Council, Washington D.C.

- Brown S.F. and Snaith M.S., (1974), *The Permanent Deformation of Dense Bitumen Macadam Subjected to Repeated Loading*. Proceedings of the Association of Asphalt Paving Technologists Technical Sessions, vol. 43, Virginia, United States of America.
- Brown S.F., 1992, *Bituminous Pavement Materials, Design and Evaluation*, Lecture Notes, University of Nottingham, United Kingdom.
- Bolk N.J.N.A., Heide J.P.J. van Der and Zantvliet M.C. van, (1982), *Basic Research into the Effect of Filler on the Mechanical Properties of Dense Asphaltic Concrete*, Proceedings of the Association of Asphalt Paving Technologists Technical Sessions, vol. 51, pp. 398-452, Kansas City, Missouri, United States of America.
- Célar B. (1977), *ESSO Road Design Technology, Fourth International Conference on Structural Design of Asphalt Pavements*, vol. 1, pp. 249-268, University of Michigan Ann Arbor, United States of America.
- Coree B. J. and Hislop W.P., (2001), *A Laboratory Investigation into the Effects of Aggregate-Related Factors on Critical VMA in Asphalt paving Mixtures*, Proceedings Association of the Asphalt Paving Technologists Technical Sessions, vol. 70, Clearwater, Florida, United States of America.
- Craus J., Ishai I. and Sides A., (1978), *Some Physico-Chemical Aspects of the Effect and the Role of the Filler in Bituminous Paving Mixtures*, Proceedings Association of the Asphalt Paving Technologists Technical Sessions, vol. 47, pp. 558-588, Lake Buena Vista, Florida, United States of America.
- CROW (2000), *Standaard RAW Bepalingen 2000*, C.R.O.W., Ede (In Dutch).
- De Beer M, Fisher C and Jooste F J, (1997), *Determination of Pneumatic/Pavement Interface Contact Stresses Under Moving Loads and Some Effects on Pavements with Thin Asphalt Surfacing layers*, Proceedings of the Eighth International Conference Structural Design of Asphalt Pavements, Vol. 1, pp. 179-223, Seattle, Washington, United States of America.
- Desai, C.S., Somasundaram, S. and Frantziskonis, G., (1986), *A Hierarchical Approach for Constitutive Modelling of Geologic Materials*, International Journal of Numerical and Analytical Methods in Geomechanics, vol. 10, No. 3 pp. 225-257.
- Dommelen A.E. van, (2000), *Twinwheels Manual*.
- Dommelen, A.E. van, Houben, L.J.M. and Miradi, A., (2001), *Analysis of triaxial test results at 40°C on asphalt samples from LINTRACK test section with DAC 80/100 wearing course* Report 7-01-200-36M, Road and Railroad Research Laboratory, Delft University of Technology, Delft, the Netherlands.
- Eckmann B., (1987), *Rut Depth Prediction: A Practical Verification*, Proceedings of the Sixth International Conference on Structural Design of Asphalt Pavements, vol.1, pp 209-219, University of Michigan Ann Arbor, United States of America.
- Erkens S.M.J.G., (2002), *Asphalt Concrete Response (ACRe) Determination, Modelling and Prediction*, Doctor of Philosophy Thesis, Delft University of Technology, the Netherlands.
- Galjaard P.J., (1996), *Soils and Unbound Granular Materials*, Lecture notes CT4850, Road and Rail Research Laboratory, Delft University of Technology, the Netherlands.

- Ghile D.B., (2006), *Effects of Nanoclay Modification on Rheology of Bitumen and on Performance of Asphalt Mixtures*, Msc. Thesis, Delft University of Technology, Delft, the Netherlands.
- Groenendijk J., Molenaar A.A.A., Dohmen L.J.M., and Maagdenberg A.M., (1997), *Pavement Performance Modelling using LINTRACK*, Proceedings of the Eighth International Conference on Asphalt Pavements, vol. 2, pp.1505-1526, Seattle, Washington, United States of America.
- Groenendijk J., (1998), *Accelerated Testing and Surface Cracking of Asphaltic Concrete Pavements*, Doctor of Philosophy Thesis, Delft University of Technology, the Netherlands.
- Harun H.M. and Jones C. R., (1992), *The performance of polymer modified asphaltic concrete on climbing lanes in Malaysia*, Proceedings of the 16th ARRB Conference, Melbourne, Australia.
- Heukelom W. and Wijga P.W.O., (1973), *Bitumen Testing*, Koninklijke/Shell – Laboratorium, Amsterdam.
- Himeno K., Kamijana T., Ikeda T., and Abe T., (1997), *Distribution of Tyre Contact Pressure of Vehicles and Its Influence on Pavement Distress*, Proceedings of the 8th International Conference of Asphalt Pavements, Vol. 1, pp. 129-139, Seattle, Washington, United States of America.
- Hopman P.C., (2000), *VEROAD User Manual Version 2000*, the Netherlands.
- Hopman P.C., Nilsson R.N., and Pronk A.C., (1997), *Theory, Validation and Application of the Visco-Elastic Multilayer Program VEROAD*, Proceedings of the 8th International Conference of Asphalt Pavements, Vol. 1, pp. 693-705, Seattle, Washington, United States of America.
- Houben L.J.M., Molenaar A.A.A., Miradi A. and Dommelen A.E. van, (2003), *Research into Rutting on Asphalt Motorway Pavements*, Proceedings of the Third International Symposium on Maintenance and Rehabilitation of Pavements and Technological Control, University of Minho, Guimarães, Portugal.
- FHWA, <http://www.nhi.fhwa.dot.gov/download/material/131053/RM/RML02.pdf>
- Huang, Y.H., (1993), *Pavement Analysis and Design*, Prentice Hall, New Jersey, United States of America.
- Huang Y.H., (1967), *Stresses and Displacements in Viscoelastic Layered Systems under Circular Loaded Areas*, Proceedings of the Second International Conference Structural Design of Asphalt Pavements, pp. 225-244, University of Michigan Ann Arbor, United States of America.
- Huurman M., (1997), *Permanent Deformation in Concrete Block Pavements*, Doctor of Philosophy Thesis, TU Delft, The Netherlands.
- Kalcheff I.V. and Tunnicliff D.G., (1982), *Effects of Crushed Stone Aggregate Size and Shape on Properties of Asphalt Concrete*, Proceedings of the Association of Asphalt Paving Technologists Technical Sessions, vol. 51, pp. 453-483, Kansas City, Missouri, United States of America.
- Kandhal P.S. and R.B. Mallick, (1999), *Effect of Aggregate Gradation on Permanent Deformation Potential of Dense Graded Hot Mix Asphalt*. Proceedings of the 7th Conference on Asphalt Pavements for Southern Africa, Victoria Falls, Zimbabwe.
- Kandhal P.S. and R.B. Mallick, (2001), *Effect of Mix Gradation on Rutting Potential of Dense-Graded Asphalt Mixtures*, Transportation Research Board, Transportation Research Record 1767, pp. 146-157.

- Kenis J.W., (1977), *Predictive Procedures, A Design Method for Flexible Pavements Using the VESYS Structural Subsystem*, Proceedings of the Fourth International Conference Structural Design of Asphalt Pavements, vol. 1, pp. 101-130, University of Michigan Ann Arbor, United States of America.
- Kenis W.J., Sherwood J.A., and McMahon T.F., (1982), *Verification and Application of the VESYS Structural Subsystem*, Proceedings of the Fifth International Conference on the Structural Design of Asphalt Pavements, vol. 1, pp. 333-346, Delft University of Technology, The Netherlands.
- Kett I. (1998), *Asphalt Materials and Design Mix*, Noyes Publications, New Jersey, United States Of America.
- Linden F. and Heide J van Der, (1987), *Some Aspects of the Compaction of Asphalt Mixes and its Influence on Mix Properties*, Proceedings of the Association of Asphalt Paving Technologists Technical Sessions, vol. 56 pp. 408-426, Reno, Nevada, United States of America.
- May R.W. and Witczak M.W., (1992), *An Automated Asphalt Concrete Mix Analysis System*, Proceedings of the Association of Asphalt Paving Technologists Technical Sessions, vol. 61. Charleston, South Carolina, United States of America.
- Medani T.O., (2006), *Design Principles of Surfacing on Orthotropic Steel Bridge Decks*, Doctor of Philosophy Thesis, Delft University of Technology, the Netherlands.
- Molenaar A.A.A., (1993), *Road materials Part III-Asphaltic Materials*, Lecture Notes, Delft University of Technology, The Netherlands.
- Molenaar A.A.A., (1998), *Structural Design of Pavements Part I: Stresses and Strains in Flexible Pavements*, Lecture Notes, Delft University of Technology, The Netherlands.
- Molenaar A.A.A., Erkens S.M.J.G., Huurman M., Medani T.O. and Visser A.F.H.M., (2002), *Characterisation and Modelling of Airfield Pavement Structures for Tomorrow's Extra Large Aircraft*, Federal Aviation Administration Technology Transfer Conference, United States of America, CD Version.
- Morris J., (1973), *The Prediction of Permanent Deformation in Asphalt Concrete Pavements*. Ph.D. Thesis, University of Waterloo, Ontario, Canada.
- Muraya, P.M., Houben, L.J.M and Dommelen, A.E. van, (2002), *LINTRACK research into Rutting of Asphalt Concrete Test Pavement*, Report 7-02-200-43M, Road and Rail Research Laboratory, Delft University of Technology, the Netherlands.
- Muraya P.M. & Molenaar A.A.A. & Dommelen A.E. van., (2003), *Visco-elastic Analyses of Test Pavements from LINTRACK ALT Rutting Research. Third International Symposium on Maintenance and Rehabilitation of Pavements and Technological Control*, University of Minho, Guimarães, Portugal.
- Muraya P.M. & Dommelen A.E. van., (2004). *APT Testing and Visco-elastic Analysis of Asphalt Motorway Pavements*, Proceedings of the 2nd International Conference on Accelerated Pavement Testing, Minnesota, United States of America.
- Nijboer L.W., (1955), *Dynamic Investigations of Road Constructions*, Shell Bitumen Monograph No. 2, London.

- Parajuli U., (2002), *Stress dependent Analysis of Asphalt Concrete*, Msc. Thesis, Delft University of Technology/IHE, Delft, the Netherlands.
- Pellinen T.K. and Witzczak M.W., (2002), *Stress Dependent Master Curve Construction for Dynamic (Complex) Modulus*. Proceedings of the Association of Asphalt Paving Technologists Technical Sessions, vol. 71, CD Version.
- Roberts F.L., Kandhal P.S., Brown E.R., Lee D. and Kennedy T.W., (1996), *Hot Mix Asphalt Materials, Mixture Design and Construction*, Lanham, Maryland, United States of America.
- Scarpas A., van Gurp C.A.P.M., Al-Khoury R.I.N., Erkens S.M.J.G., (1997), *Finite Element Simulation of Damage Development in Asphalt Concrete Pavements*, Proceedings of the Eighth International Conference on Asphalt Pavements, vol 1 pp. 673-692, Seattle, United States of America.
- Sousa J.B., Craus J. and Monismith C.L., (1991), *Summary Report on Permanent Deformation in Asphalt Concrete*, SHRP-A/IR-91-104, National Research Council, Washington D.C., United States of America (internet document).
- Su Z., (1996), *Mineral Aggregates: Their Classification and Properties*, ESHA Research Report, RT010-96-02, Department of Research and Technology, Smid & Hollander Service b.v.
- Sweere G.T.H., (1990), *Unbound Granular Bases for Roads*, Doctor of Philosophy Thesis, TU Delft, The Netherlands.
- Vavrik W.R., Pine W.J., Huber G., Carpenter S.H. and Bailey R., (2001), *The Bailey Method of Gradation Evaluation: The Influence of Aggregate Gradation and Packing Characteristics on Voids in the Mineral Aggregate*, Proceedings of the Association of Asphalt Paving Technologists Technical Sessions, vol. 70, Clearwater, Florida, United States of America.
- Ven M.F.C. van de, Smit André de F., Lorio R. and McGennis R., (1997), *Validation of Some Superpave Design Parameters by Wheel Testing with the Scale Model Mobile Load Simulator*, Proceedings of the Eighth International Conference of Asphalt Pavements, Vol. 1, pp. 1245-1256, Seattle, Washington, United States of America.
- Verstraeten J., (1967), *Stresses and Displacements in Elastic Layered Systems: General Theory-Numerical Stress Calculations in Four-Layered Systems with Continuous Interfaces*, Proceedings of the Second International Conference Structural Design of Asphalt Pavements, pp. 277-290, University of Michigan Ann Arbor, United States of America.
- Woodside A.R., Wilson J and Liu G.X., (1992), *The Distribution of Stresses at the Interface Between the Tyre and Their Effect on Surface Chippings*, Proceedings of the Seventh International Conference Structural Design of Asphalt Pavements, pp. 428-442, Nottingham, United Kingdom.
- Yoder E.J., (1959), *Principles of Pavement Design*, John Willey & sons inc, New York, United States of America.

3 Material Procurement and Mixture Design

It is not the quantity but quality that matters. On the other hand sufficient quantity is a prerequisite for acceptable quality.

3.1 Introduction

The objective of the mixture design was to compose different types of asphalt mixtures with similar mineralogical compositions that meet pavement mixture specifications. Mixtures with similar mineralogical composition would allow the comparison of the different mixtures without the influence of the aggregate mineralogical composition.

3.2 Material Procurement

Initially, it was envisaged that six different asphalt mixtures composed from sieved aggregate fractions would be considered in this research. Early procurement of sufficient material quantities was as such necessary for the preparation of these mixtures. A total of more than 20 tonnes of aggregates from the BAM NBM construction company and about 2 tonnes of bitumen from Q8 petroleum industry were procured. The breakdown of these material quantities is shown in Table 3.1. The aggregates consisted of crushed Norwegian aggregates, crushed sand, natural sand, Wigro filler and Wigro 60K filler. The procured bitumen consisted of two types of bitumen namely 70/100 and 40/60 bitumen. In addition drainage deterrent natural cellulose fibres were also procured.

Table 3.1 Breakdown of Material Quantities

Crushed aggregate fractions	16/22	11/16	8/11	4/8	2/6	Crushed sand	Natural coarse sand	Wigro filler	Wigro 60K filler	Total Aggregates
Weight [kg]	900	2600	4600	3200	2400	4900	600	1500	200	20900
Bitumen	70/100	40/60	Cellulose fibres							
Weight [kg]	500	1300	5							

The crushed aggregates fractions were delivered in huge bags by a self-loading truck. The bags were stored in a dry area prior to sieving. Figure 3.1 shows the delivery of the crushed aggregate fractions and the aggregate storage area.



Figure 3.1 Delivery of the aggregates and the aggregate storage area

3.3 Material Sieving

The sieving of such quantities of aggregates called for large scale sieving equipment. A large scale sieving equipment was used in earlier research projects (Sweere 1990 & Van Nierkerk 2002). The large scale sieving equipment consisted of two vibrating sieving units with inclined parallel sieves with sieve sizes that ranged from 45 mm to 2 mm. The sieves were arranged in order of decreasing sieve size with largest sieve being placed on top and the smallest sieve at the bottom. The aggregates were delivered to the sieving units by means of a dumper and conveyer belts. The large scale sieving equipment and the dumper are shown in Figure 3.2.



Figure 3.2 Large scale sieving equipment and the dumper (Van Nierkerk 2002)

However, despite varying the inclination of sieves and vibration frequencies, the large-scale sieving equipment could not sieve the crushed aggregates to acceptable standards. The sieved fractions contained considerable portions of finer aggregates. Figure 3.3 shows an example of the gradation the aggregates retained on the 8 mm sieve after sieving at the steepest inclination. The figure shows that the sieved material contains about 20% aggregates that are smaller than the 8 mm sieve.

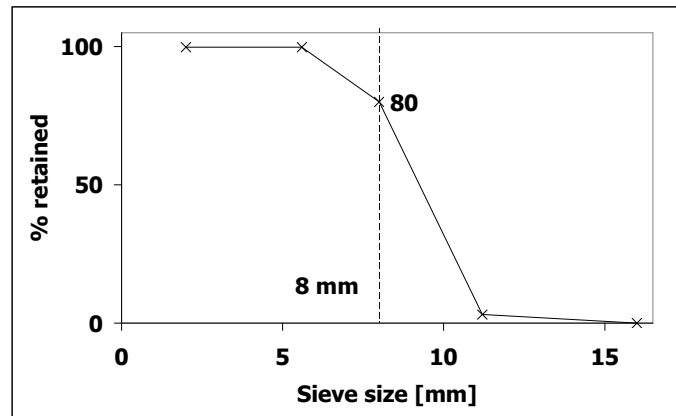


Figure 3.3 Gradation of aggregates retained on the 8 mm sieve after sieving

In order to retain homogenous fractions, an ordinary laboratory sieving machine in which 350 mm diameter sieves were mounted had to be used to sieve the aggregates. The consequence was that sufficient material for the envisaged six mixtures could not be sieved effectively and the asphalt mixtures were decreased from six to three. The three asphalt mixtures were selected in consultation with the Netherlands Road and Hydraulic Engineering Division, Ministry of Transport, Public Works and Water Management. The porous asphalt concrete (PAC), stone mastic asphalt (SMA) and dense asphalt concrete (DAC) mixtures were selected on the basis of their importance in pavement construction in the coming years in the Netherlands. These asphalt mixtures are typically used as surface layers and are exposed to the highest pavement temperature making them susceptible to rutting.

3.4 Mixture Design

In order to determine the material compositions for the three selected mixtures, a Marshall mixture design was carried out in accordance with the Dutch RAW specifications (CROW 2000) for the PAC (0/16), SMA (0/11) and DAC (0/16) asphalt mixtures. During the initial stages of the mixture design process, designs for PAC, SMA and DAC were obtained from BAM-NBM in which the materials were similar to the procured material. These designs were used as a guide for mixture design in this research.

A summary of the material properties that were used to compose the three mixtures is shown in Table 3.2 to Table 3.4. Table 3.2 shows the type of bitumen and filler that were used in the composition of the three asphalt mixtures and the corresponding bitumen properties. The term EVT (Equiviscous Temperature) refers to the temperature at which the bitumen attains a viscosity of 170 cSt.

Table 3.3 shows the filler properties. The specific densities of the sieved aggregate fractions determined by means of a pycnometer and dichloromethane are shown in Table 3.4. The purpose of the two types of sieved 5.6 – 2 mm fractions was to compose stone skeleton mixtures (PAC and SMA) and the DAC mixture from separate 5.6 – 2⁴ mm fractions. The RAW specifications stipulate that the PAC and SMA mixtures should be prepared from fractions without any aggregates from the 2/6 crushed aggregate fraction. The purpose of this stipulation is to minimize the content of 5.6 – 2 mm aggregate fraction in the PAC and SMA asphalt mixtures.

Table 3.2 Type of bitumen, filler and sand used in the composition of the mixtures and bitumen properties

Asphalt mixture	Bitumen	Filler	Sand	Bitumen Properties					
				Type	EVT [°C]	pen [0.1 mm]	softening point [°C]	Penetration index	Density [kg/m ³]
PAC	70/100	Wigro 60K	Crushed sand	70/100	158 ± 5	99	44.8	-0.8	1029
SMA		Wigro		40/60	160 ± 5	50	50	-1.2	1035
DAC	40/60								

EVT: temperature at which the viscosity of bitumen = 170 cSt

Table 3.3 Filler properties

Filler	Bitumen number [ml/100g]	Ca(OH) ₂ [%] by mass	Mass loss 150°C [%]	Analysis after drying at 110°C			
				Density [kg/m ³]	Voids [%]	Sovability [%] by mass	
						H ₂ O	HCL
Wigro 60K	61	26.7	1	2570	46	11.4	79.4
Wigro	48	-	0.5	2750	37	1.4	66.9
Cummulative retained [%] by mass							
sieve size [mm]	2	0.5	0.18	0.09	0.063		
Crushed sand	8.2	57.2	85.6	-	98.2		
Wigro 60K	0	-	-	6	13		
Wigro	0	-	-	12	19		

Table 3.4 Densities of aggregate fractions

Fraction	crushed sand	5.6 - 2	22.4 - 16	16 - 11.2	11.2 - 8	8 - 5.6
Specific Density	2.677	2.766 ^a , 2.781 ^b	2.796	2.774	2.762	2.765

a: density of the 5.6 - 2 mm aggregate fraction sieved from fractions excluding 2/6 crushed fraction

b: density of the 5.6 - 2 mm aggregate fraction sieved from fractions including 2/6 crushed fraction

The three mixtures were composed of crushed Norwegian aggregates and Scottish crushed sand. The PAC and SMA consisted of 70/100 pen bitumen and the DAC consisted of 40/60 pen bitumen. The design criteria for the PAC and the SMA were purely volumetric (air voids content) while the DAC was designed according to the complete Marshall mixture design. The air voids content was calculated from Equation 3.1 and the maximum density was determined by dissolving the loose and separated asphalt specimen aggregates in a bitumen solvent (methylene dichloride). The specimen density was obtained by means of the saturated surface dry technique for SMA and DAC or through direct measurement of specimen dimensions for PAC.

⁴ The reader should note that the fraction range of the aggregates produced by the crusher is not always exact. The 2/6 fraction is expected to contain a higher content and a smaller size of aggregates in the range of 5.6-2 mm in comparison to the 4/8 fraction.

$$\text{air void content [\%]} = \frac{\text{maximum density} - \text{specimen density}}{\text{maximum density}} \times 100 \quad 3.1$$

Prior to the composition of the asphalt mixtures, the sieved aggregate fractions were first washed in water to remove the dust. The purpose of removing the dust was to have a better control of the composition of the mixture. After washing, the aggregates were dried in the oven ready for specimen preparation. Although the procured aggregates were supposedly virgin, traces of recycled aggregates coated with bitumen were found in the procured aggregates. This led to the painstaking manual task of removing the bitumen-coated aggregates.

The aggregate fractions were then weighed and heated in the oven together with the moulds, base plate, mixing arm and the mixing pan for at least 8 hours. The aggregates for the PAC and the DAC mixtures were heated at a temperature of 10⁰C above the bitumen EVT temperature and the SMA aggregates at 20⁰C above the bitumen EVT temperature. The heated aggregates were then mixed together with bitumen heated at EVT temperature for PAC and DAC, and at 10⁰C above the EVT for the SMA. After mixing for 1.5 minutes using the Hobart mixer, the mixture was compacted by a pre-heated 4.54 kg Marshall hammer. During the compaction process 2 x 50 blows were applied on the specimen with each side receiving 50 blows.

3.4.1 Porous Asphalt Concrete (PAC 0/16) Mixture Design

The aim of the PAC mixture design was to obtain a PAC 0/16 composition containing an air voids content of more than 20%. At the time the mixture design for the PAC was executed, the sieving of the stipulated 5.6-2 mm aggregate fraction for the SMA and the PAC was still in progress. Consequently, this fraction was omitted from the trial compositions considered in the PAC mixture design.

Table 3.5 Mixture compositions considered for PAC 0/16 mixture design

Sieve size [mm]	Cumulative percentage retained by mass [%]					
	BAM-NBM	Trial composition		Specification		
		1	2	desired	min	max
16	3.0	0.0	0.0	-	0.0	7.0
11.2	22.5	23.8	26.0	-	15.0	30.0
8	56.0	57.8	63.0	-	50.0	65.0
5.6	77.5	82.8	83.5	-	70.0	85.0
2	85.0	83.9	84.5	85.0	-	-
0.063	95.5	96.4	96.1	95.5	-	-
<0.063	100.0	100.0	100.0			
70/100 Bitumen content ^c [%]	4.3	4.3	4.3	4.5	-	-
Average voids content [%]	20.2	19.8	20.6	-	20.0	-
Number of specimens	4	4	4			
Specimen density [kg/m ³]	2040.0	2057.4	2040.6			
Measured maximum density ^m [kg/m ³]	2556	2567	2570			

c: bitumen content on 100% aggregates by weight

m: density determined by dissolving the loose and separated asphalt specimen aggregates in methylene dichloride

In order to maximise the air voids content, lower filler quantities and coarser aggregate gradation than in the BAM-NBM mixture were used in the preparation trial compositions. Table 3.5 shows the BAM-NBM mixture design, trial compositions considered for the PAC 0/16 mixture design and the stipulated specifications. The table shows that trial composition 2 met the specifications and was as such used for further research.

3.4.2 Stone Mastic Asphalt Mixture (SMA 0/11) Design

The aim of the SMA mixture design was to obtain an SMA 0/11 Type 2 composition with an air voids content of 5%. In accordance with the Dutch specifications, the SMA mixture design is performed by progressively varying the aggregate fraction retained on the 2 mm sieve. During this process, the bitumen content and the ratio of the sand to filler content are kept constant. The appropriate aggregate composition is then interpolated at the required air voids content.

At the time the mixture design for the SMA was executed, the cellulose fibres required to prevent drainage were not yet available. Subsequently the fibres were omitted during the SMA mixture design but used in the preparation of the test specimens. Table 3.6 shows the BAM-NBM SMA mixture, trial compositions that were considered during the SMA 0/11 mixture design and the specifications. In the trial mixture compositions, the aggregates greater than 2 mm were progressively varied from 73 to 82.5%. During this process, the ratio of sand:filler by weight was held constant at 1.5:1 while the bitumen content remained at 6.7% on 100% of the aggregates by weight. The percentage of the required material retained on the 2 mm sieve to meet a 5% air void content was then interpolated as shown in Figure 3.4. The numbers in this figure refer to the trial composition number. The final composition in Table 3.6 and in Figure 3.4 represents the interpolated composition at 5% air voids.

Table 3.6 Mixture Compositions considered for SMA 0/11 mixture design

Sieve size [mm]	Cumulative percentage retained by mass [%]									
	BAM-NBM	Trial composition						Specification		
		1	2	3	4	5	final	desired	min	max
16	0.0	0.0	0.0	0.0	0.0	0.0	0.0	-	-	-
11.2	5.2	4.7	4.9	5.0	5.2	5.4	5.1	-	0.0	8.0
8	49.0	44.7	45.9	47.5	49.0	50.5	48.5	-	40.0	55.0
5.6	72.2	65.9	67.7	69.9	72.2	74.5	71.5	-	60.0	75.0
2	80.0	73.0	75.0	77.5	80.0	82.5	79.2	77.5	72.5	82.5
0.063	92.9	90.4	91.1	92.0	92.9	93.8	92.6	92.0	90.0	94.0
<0.063	100.0	100.0	100.0	100.0	100.0	100.0	100.0			
70/100 Bitumen content ^c [%]	6.7	6.7	6.7	6.7	6.7	6.7	6.7	7.0	-	-
Fibre content ^d [%]	0.3	-	-	-	-	-	-	0.0	-	-
Average voids content [%]	5.0	2.0	3.3	3.8	5.6	7.4	5.2	5.0		
Number of specimens	4	3	3	3	3	3	2			
Specimen density [kg/m ³]	2358.0	2444.7	2414.4	2402.6	2365.2	2325.7	2371.5			
Measured maximum density ^m [kg/m ³]	2481	2495	2497	2497	2504	2510	2501			

c: bitumen content on 100% aggregates by weight

d: fibre content on 100% aggregates by weight

m: density determined by dissolving the loose and separated asphalt specimen aggregates in methylene dichloride

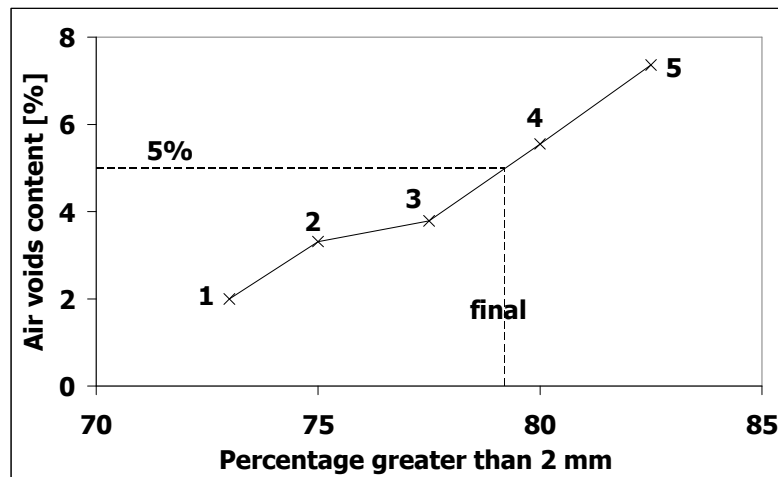


Figure 3.4 Interpolation for the 5% air voids content for SMA 0/11

3.4.3 Dense Asphalt Concrete (DAC) Mixture Design

The aim of the DAC mixture design was to obtain a DAC 0/16 that met the mixture specifications for Vehicle Class 4. Apart from attaining the mixture specifications, the other aim was to compose the DAC with aggregate of similar mineralogical composition as the PAC and SMA mixtures. Similar to the PAC and the SMA mixtures, the Wigro filler was used in the aggregate composition of the DAC 0/16. Table 3.7 shows the BAM-NBM mixture, trial compositions and the specifications for Vehicle Class 3 and 4. The guideline BAM-NBM mixture was composed of 70/100 bitumen and Vulcom 40K filler while the trial compositions were composed of 40/60 and Wigro filler. With the exception of the difference in the mineralogical composition of the filler, the BAM-NBM mixture was composed of a softer bitumen, a filler of higher Ridgen voids content and lower density. In order to obtain a mixture with properties similar to those of the BAM-NBM mixture, a general optimization approach was adopted. The approach involved optimization of the bitumen, sand and filler content on aggregate gradations close to the BAM-NBM gradation within the specification limits of the bitumen and the aggregates retained on the 0.063 mm sieve. However, despite of fabricating mixtures with the minimum bitumen content and different combinations of sand and filler contents, one specification for Vehicle Class 4 could not be met. The voids filled with bitumen in the trial mixtures were higher than the specified maximum value of 80. As a result trial composition 6 was selected on the basis of meeting the other specifications and having the lowest content of voids filled with bitumen. This mixture did not meet all the requirements for Vehicle Class 4 but it met the mixture design requirements for Vehicle Class 3.

Table 3.7 Mixture Compositions considered for DAC 0/16 mix design

Sieve size [mm]	Cumulative percentage retained by mass [%]											
	Trial composition							Specification for Vehicle Class ^f				
	BAM-NBM	1	2	3	4	5	6	3&4 desired	3 min max		4 min max	
16	1.7	0.0	1.7	1.7	1.6	0.0	0.0	-	0.0	6.0	0.0	6.0
11.2	12.0	12.0	12.0	12.0	11.5	12.0	11.5	-	5.0	25.0	5.0	25.0
8	23.0	23.0	23.0	23.0	22.0	23.0	22.0	-	-	-	-	-
5.6	35.0	35.0	35.0	35.0	33.5	35.0	33.5	-	30.0	55.0	30.0	55.0
2	60.0	60.0	60.0	60.0	57.5	60.0	57.5	60.0	57.0	63.0	57.0	63.0
0.063	93.2	92.9	92.7	93.9	93.9	93.9	93.9	92.9	92.4	93.9	92.4	93.9
<0.063	100	100	100	100	100	100	100					
Sand content [%]	32	35	34	36	39	36	39					
Filler content [%]	6.9 ^f	8.0	8.5	6.8	6.7	6.8	6.7					
40/100 Bitumen content ^c [%]	5.9 ^e	6.0	5.8	5.8	5.8	5.8	5.8	-	6.0	6.4	5.8	6.2
Average voids content [%]	4.0	2.7	2.2	2.7	2.8	2.7	2.8	-	-	4.0	-	6
Marshall Flow [mm]	2.6	3.9	4	3.55	3.75	3.3	3.2	-	2	4	2	4
Marshall stability [kN]	9.8	10.3	9.8	11.565	12.27	10.79	11.565	-	7	-	7.5	-
Marshall quotient [N/mm]	3820	2652.5	2450	3280	3265	3280	3610	-	2500	-	3000	-
Voids filled with bitumen [%]	76.0	83.4	85.4	82.5	82.2	82.6	82.0	-	-	83.0	-	80
Number of specimens	4	4	2	2	2	2	2					
Specimen density [kg/m ³]	2380.0	2437.2	2455.7	2440.6	2437.1	2434.0	2428.1					
Measured maximum density ^m [kg/m ³]	2478	-	-	-	-	2502.0	2498.9					

c: bitumen content on 100% aggregates by mass

■ air voids content determined based on calculated maximum density

e: 70/100 bitumen

f: Vulcom 40K filler

m: density determined by dissolving the loose and separated asphalt specimen aggregates in methylene dichloride

n: in the Dutch specifications vehicle class 3 and 4 represent a road with moderate and heavy traffic respectively

3.4.4 Composition Determination for PAC 0/16 and SMA 0/11

As part of the mixture design, the composition of two PAC specimens and two SMA specimens was determined. Table 3.8 shows the extraction results and the RAW tolerance limits for the PAC and the SMA mixtures. The table shows that the composition of these specimens was finer than the original mixture composition as a result of crushing during the Marshall compaction. The table also shows that the average difference between the original gradation and the extracted gradation was higher than the tolerance limits dictated by the Dutch standards (RAW). After ample consideration a decision was reached to ignore the differences and carry on with the selected compositions and mixtures as designed.

Table 3.8 PAC and SMA extraction results and the RAW tolerance limits.

Sieve size [mm]	PAC				SMA			
	cum. ret. by mass [%]		difference	RAW tolerance	cum. ret. by mass [%]		difference	RAW tolerance
	original	extracted			original	extracted		
16	0	0.0	0.0	1.5				
11.2	26	23.8	2.2	4	5.1	5.4	0.3	1.5
8	63	54.6	8.4	3.5	48.5	40.8	7.7	3.5
5.6	83.5	75.4	8.1	3	71.5	63.8	7.7	3.5
2	84.5	83.0	1.5	2	79.2	77.1	2.1	2
0.063	96.1	94.1	1.9	0.75	92.6	89.9	2.8	0.75
<0.063	100	100.0			100	100		
Bit ^c [%]	4.3	4.0	0.3	0.25	6.7	6.2	0.5	0.25

Bit^c = bitumen content on 100% aggregates by mass

3.5 Summary

The composition of the asphalt mixtures was based on a Marshall Mixture design that was performed in accordance with the Dutch specifications. The composition

of the asphalt mixtures and the Marshall densities of the mixtures, equiviscous temperature of the bitumen (EVT), mixing temperatures and the bitumen penetration index are shown in Table 3.9. Figure 3.5 shows the aggregate mixture gradation for the three asphalt mixtures.

Table 3.9 Final summary of the Marshall mixture design for PAC, SMA and DAC

Cumulative percentage passing by mass[%]			
Sieve size [mm]	PAC	SMA	DAC
16	100.0	100.0	100.0
11.2	74.0	94.9	88.5
8	37.0	51.5	78.0
5.6	16.5	28.5	66.5
2	15.5	20.8	42.5
0.063	3.9	7.4	6.1
Bitumen content ^c [%]	4.3	6.7	5.8
Air voids content [%]	20.6	5.2	2.8
Density [kg/m ³]	2040.6	2371.5	2428.1
Marshall Flow [mm]	3.2		
Marshall stability [kN/mm]	11.6		
Marshall quotient [N/mm]	3610		
Voids filled with bitumen [%]	82.0		
EVT [°C]	158 ± 5	158 ± 5	160 ± 5
Mixing temperature [°C]	160	160	170
Bitumen Penetration Index	-0.8	-0.8	-1.2

c: bitumen content on 100% aggregates by mass

EVT: temperature at which the viscosity of bitumen = 170 cSt

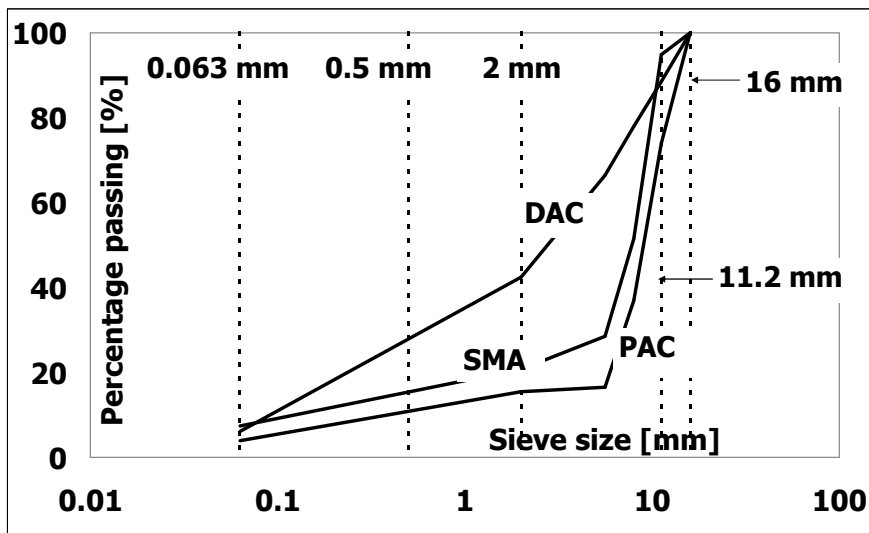


Figure 3.5 Aggregate Mixture gradation for the three asphalt mixtures

3.6 Conclusions

The design for the three mixtures was performed in accordance with the Dutch specifications. The following conclusions were reached with regard to the material procurement and the mixture design:

- The aggregate fraction sieved by the large-scale sieving machine contained considerable amounts of finer aggregates.
- The virgin ex-crusher aggregates contained some re-cycled aggregates.
- The selected PAC 0/16 and the SMA 0/11 mixture compositions met the volumetric requirements but the extent of crushing was above the tolerance limits in the Dutch specifications. However, after ample consideration a decision was reached to ignore the differences and carry on with the selected compositions and mixtures as designed.
- The selected DAC 0/16 mixture composition met all the specifications for Vehicle Class 4 except the requirement on the voids filled with bitumen. The DAC 0/16 met the mixture design requirements for Vehicle Class 3.

3.7 References

- CROW (2000), *Standaard RAW Bepalingen 2000*, C.R.O.W., Ede (In Dutch).
- Sweere G.T.H., (1990), *Unbound Granular Bases for Roads*, PhD Dissertation, Delft University of Technology, Delft, The Netherlands.
- Van Niekerk A.A., (2002), *Mechanical Behavior and Performance of Granular Bases and Sub-bases in Pavements*, PhD Dissertation, Delft University of Technology, Delft, The Netherlands.

4 Aggregate Skeleton

A body without a skeleton is incomplete.

4.1 Introduction

The objective of the tests performed on the aggregate skeleton was to characterize its influence on the permanent deformation of asphalt mixtures. The characterization of the aggregate skeleton was performed by means of triaxial testing. The triaxial testing involved displacement controlled monotonic constant confinement (DCMCC) failure tests and permanent deformation (PD) tests conducted under cyclic and constant confinement. Prior to laboratory testing, the skeleton components were identified for the purposes of fabricating the specimens.

4.2 Triaxial Testing

Triaxial testing offers a possible means of testing the aggregate skeleton at different confinement levels. Other laboratory based methods such as the wheel tracking test offer more complex alternatives with limited ability of testing the aggregate skeleton component. However, direct duplication of the stresses occurring in the pavement is presently unfeasible in the triaxial test but stress invariants provide a possible means of linking pavement stresses to stress conditions that can be generated in the laboratory under triaxial test conditions (Brown 1975, Brown and Bell 1977).

4.2.1 Test Set-Up

The test set-up for the aggregate skeletons as used in this research consisted of the UTM 25 triaxial cell shown in Figure 4.1 and a data acquisition system that was developed during a previous research on granular materials (van Niekerk 2002). The cell comprised a vertical hydraulic actuator and a pneumatic silicon oil confinement generation system capable of delivering a maximum of about 15 kN and 800 kPa respectively. The cell pressure was applied by means of an air bellow that pressurised the oil to the required confinement level. The triaxial cell was capable of performing different types of tests including DCMCC tests and repeated permanent deformation (PD) tests that were conducted under a constant and cyclic cell pressure.

The specimen deformation during the DCMCC and PD tests was measured by means of three axial and three radial LVDTs with a maximum range of ± 5 mm. The data acquisition system had a capacity of sampling the data at a frequency of 50 Hz. In order to determine the resilient behaviour from the PD tests, the data at all load repetitions was sampled during the first 100 load repetitions. After which the data was sampled at 200...1000, 2000...10000 and 20000 load repetitions.



Figure 4.1 UTM 25 triaxial cell

4.3 Identification of Aggregate Skeleton

4.3.1 Introduction

The composition of the aggregate skeleton specimens was based on the composition of the designed asphalt mixtures discussed in Chapter 3. Prior to the specimen preparation, a mixing procedure was developed and the aggregate skeleton in each of the three asphalt mixtures identified. The aggregate skeleton for each asphalt mixture was identified on the basis of the aggregate grid interlock between the different aggregate fractions. Aggregate fractions that fell through the aggregate grid interlock were omitted from the composition of the aggregate skeleton. In order to identify this grid interlock, aggregate fractions were mixed together without bitumen and visually observed during mixing and compaction process. Figure 4.2 shows the approach that was used to establish the mixing procedure and to identify the aggregate skeleton. The identification process involved step-wise elimination of fractions that fell through the aggregate grid interlock either during mixing or compaction. The smaller aggregate fractions were continuously eliminated with the process being terminated and the aggregate skeleton identified if little or no segregation was observed during compaction using the Kango hammer.

The specimens were compacted in three equal layers to target densities determined based on the density of the designed mixtures presented in Chapter 3 and the aggregate content. The aggregate content was obtained from the cumulative percentage of the aggregate fraction in the total mixture. The expression used to calculate the density of the aggregate skeleton is shown in Equation 4.1. The specimens were compacted in a split mould. Prior to extraction from the mould, a vacuum of about 80 kPa was applied on the specimen to hold the aggregate specimen together. Further details on the preparation of the aggregate skeleton specimens will be provided in section 4.4.

$$\rho_{agg} = \frac{C}{100} \rho_m \quad 4.1$$

Where:

- ρ_{agg} = target density of the aggregate skeleton,
- C_{agg} = cumulative percentage of the aggregate fraction in the total mixture by weight,
- ρ_m = Marshall mixture design density of the asphalt mixture.

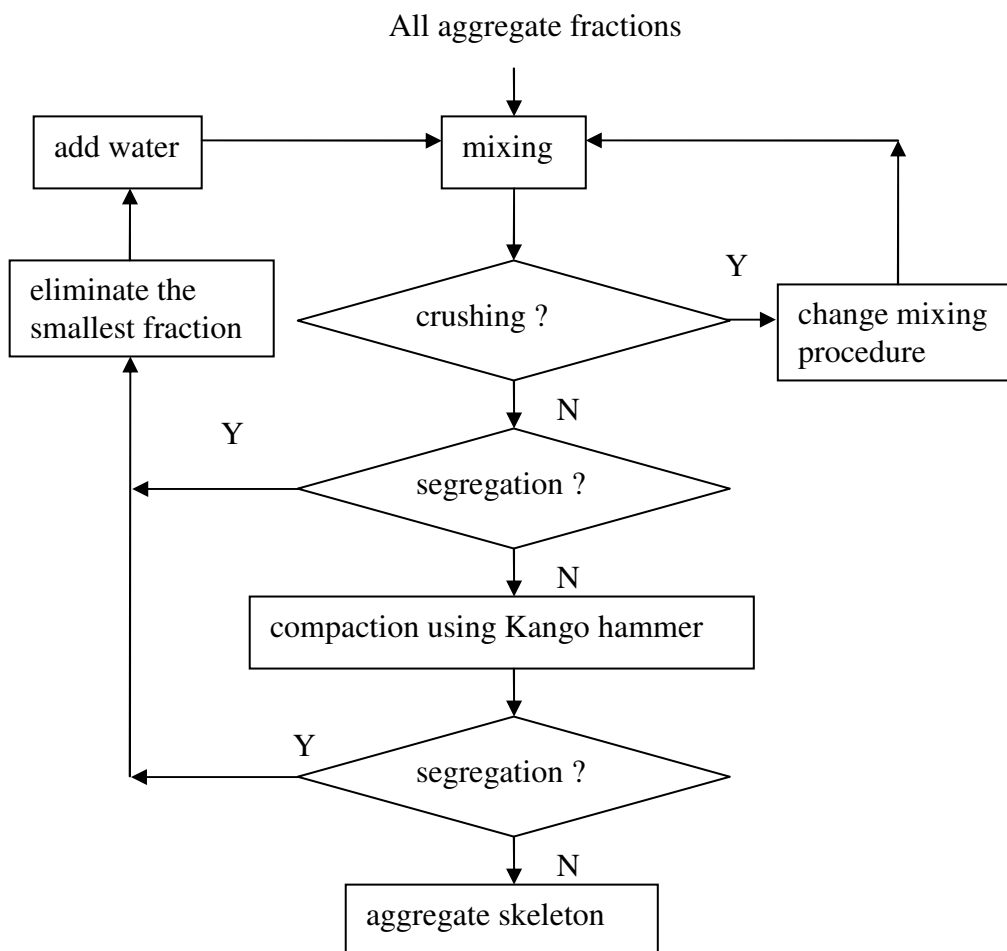


Figure 4.2 Approach used in the establishment of mixing procedure and identification of the aggregate skeletons

Initially, the PAC aggregate skeleton was identified after which the aggregate skeletons for SMA and DAC were identified based on experience gained from the identification of the PAC aggregate skeleton. Apart from the identification process, an X-ray tomography analysis was also performed to inspect the compaction homogeneity of the compacted specimens.

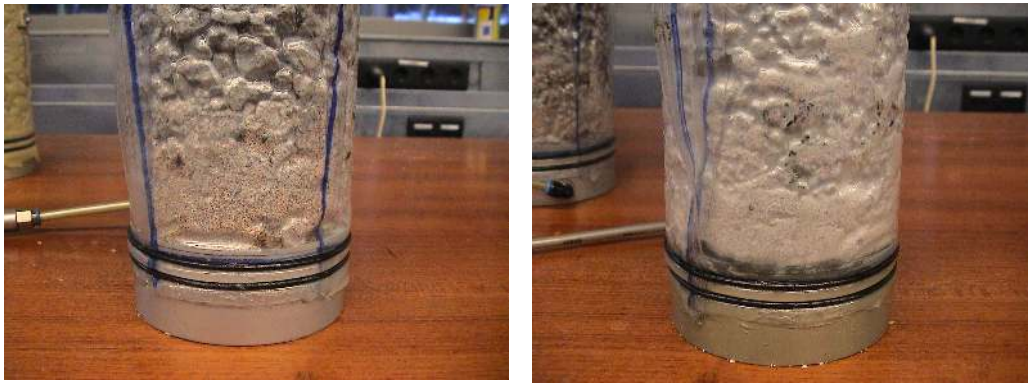
4.3.2 PAC aggregate skeleton

During the preparation of the PAC aggregate skeleton the following observations were made:

1. Transparent plastic membranes were suitable for the visual observation of the compacted aggregate skeletons. However, due to concerns that the plastic membrane was quite stiff and could interfere with the displacement of aggregates at high confinement during testing, latex membranes were used in the preparation of the test specimens.
2. A manual aggregate mixing procedure was adopted to decrease the crushing of aggregates that was observed when the Hobart mixer was used.
3. The filler was omitted from the aggregate fraction since it segregated during mixing and compaction. Apart from segregating, the filler was also observed to clog the vacuum pipes during removal of the specimens from the mould.
4. Addition of a small amount of water (0.7% by weight) during mixing facilitated the mixing process. The water caused the small aggregate fractions (< 2 mm) to adhere to the larger aggregates.
5. The PAC aggregate skeleton was composed of aggregates in the PAC asphalt mixture larger than 0.5 mm. The aggregates smaller than 0.5 mm were observed to segregate during mixing and were therefore omitted from the composition of test specimens for PAC aggregate skeleton.

4.3.3 SMA Aggregate Skeleton

During the identification process of the SMA aggregate skeleton, two types of aggregate skeleton mixtures A and B were prepared using transparent plastic membrane. Mixture A was composed of aggregates in the SMA asphalt mixture retained on the 0.5 mm sieve while Mixture B was composed of aggregates retained on the 0.063 mm sieve. The filler was omitted since it was found to segregate during mixing. Similar to the preparation of the PAC aggregate skeleton, the SMA aggregate skeleton mixtures were mixed by hand with a small amount of water (0.7% water by weight) being added. Since addition of water during the mixing process may have led to undesired capillarity effects, the sand fraction less than 0.063 mm was omitted in Mixture B. During the mixing stage, no segregation was observed in the two mixtures. The mixtures were then compacted using the Kango hammer and observed. Figure 4.3 shows the two types of aggregate mixtures after compaction. In both mixtures, the aggregate fraction smaller than 2 mm fell through the aggregate interlock grid to the bottom. This segregation meant that aggregates smaller than 2 mm were not part of the skeleton and were excluded from the composition of the test specimens for SMA aggregate skeleton. Since the aggregates in SMA skeleton were larger than 2 mm, water was omitted during the preparation of test specimens.



Mixture A: aggregates > 0.5 mm

Mixture B: aggregates > 0.063 mm

Figure 4.3 SMA aggregate skeleton mixtures

4.3.4 DAC Aggregate Skeleton

Table 4.1 shows four mixtures that were prepared in order to identify the DAC aggregate skeleton. These mixtures were prepared without the filler since the filler was observed to segregate during mixing.

Table 4.1 DAC skeleton mixtures

fraction [mm]	large aggregates					Sand					filler
	22.4 - 16	16 - 11.2	11.2 - 8	8 - 5.6	5.6 - 2	5.6 - 2	2 - 0.5	0.5 - 0.18	0.18 - 0.063	<0.063	
Mixture A											
Mixture B											
Mixture C											
Mixture D											

Mixture A was composed of all aggregates larger than 0.5 mm. However, Mixture A was observed to compact to the target density without compaction effort. Consequently, this mixture was not considered further. Mixture B was composed of all the aggregates. Mixture C consisted of aggregate fractions larger than 0.18 mm and Mixture D aggregate fractions larger than 0.063 mm.

Mixture B was mixed in two stages without water since it contained aggregate fractions that were less than 0.063 mm and addition of water may have led to undesired capillary effects. In the first stage the large aggregate fractions were mixed without water and in the second the sand was added in the Kango mould prior to compaction. Mixtures C and D were mixed with water to facilitate better distribution of the sand fractions in the mixture.

After compaction, the segregation in Mixtures B and C was observed to be much higher than the segregation in Mixture D. The sand particles smaller than 0.063 mm in Mixture B were observed to settle at bottom of the specimen. This observation suggested that sand particles smaller than 0.063 mm were not part of the DAC skeleton. The sand particles smaller than 0.5 mm in Mixture C were observed to segregate. This observation implied that the omission of the sand fraction between 0.063 and 0.18 mm in Mixture C also caused segregation. However, the inclusion of the fraction between 0.063 and 0.18 mm in Mixture D resulted in less segregation. These observations suggested that the DAC aggregate skeleton was composed of aggregate fractions larger than 0.063 mm excluding the filler.

4.3.5 X-Ray Tomography

Apart from visual observation, an X-ray tomography analysis was also performed on the PAC and the SMA aggregate skeleton mixtures. The purpose of the X-ray tomography was to inspect the compaction homogeneity in the compacted aggregate skeletons. The X-ray tomography involved determination of the air void distribution in the aggregate skeleton specimens. The analysis was performed on five PAC specimens and five SMA specimens. However, the results of one PAC specimen were omitted due to incomplete scanned data.

The images for the X-ray tomography were scanned by means of a Siemens SOMATON plus 4 volume zoom scanner. The resolution for each pixel in the scanned images was 0.294 mm by 0.294 mm. The X-ray tomography analysis was performed using MATLAB image analysis tool by fitting the air/aggregate boundary based on the actual volumetric composition of the aggregate skeleton specimens. Two different algorithms available in MATLAB were considered in the analysis, namely regionprops-Area command and bwarea command. The difference between these two commands is that the regionprops-Area command obtains the area by counting the number of pixels, while the bwarea command compensates for the distortion that is inherent in representing a continuous image with discrete pixels. In this case both algorithms gave the same results. Since bwarea algorithm is slightly easier to use, it was used to process the data. The X-ray tomography analysis process for aggregate skeleton was similar to the X-ray tomography conducted on total asphalt mixtures which is presented later in section 5.2.4. Further details regarding the X-ray tomography analysis procedure can be found in section 5.2.4 and in Annex 3.

Figure 4.4 shows the results of one PAC specimen and one SMA specimen that were obtained from the regionprops-Area and bwarea commands. The results show that the air void distributions determined using the two types of commands were similar in both types of aggregate skeletons. Figure 4.5 shows the air void distribution of four PAC and the five SMA aggregate specimens. The figures show that the air void distribution in the four PAC specimens was similar and the air void distribution in the five SMA specimens was also similar. Figure 4.6 shows the average air void distribution in four PAC and the five SMA aggregate skeleton specimens. The figures show that the air voids were evenly distributed over the height of the PAC and SMA aggregate skeleton specimens. This suggests that the aggregate skeleton specimens were evenly compacted. The figures also show a decrease in the air void content at the bottom of the specimens. This can be attributed to crushing that may have occurred during the compaction process.

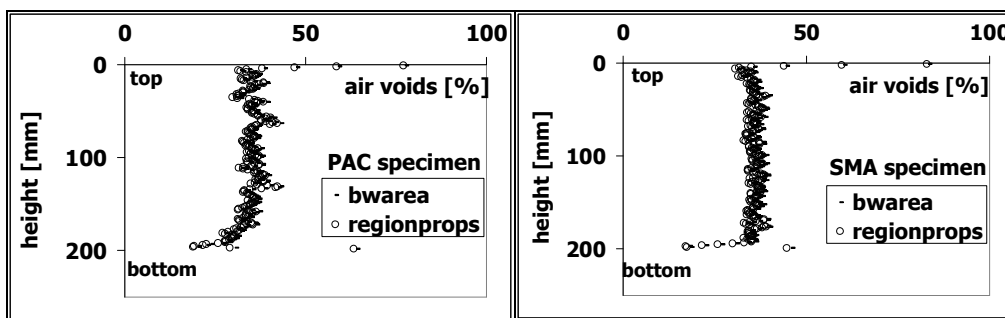


Figure 4.4 Bwarea and regionprops-Area commands

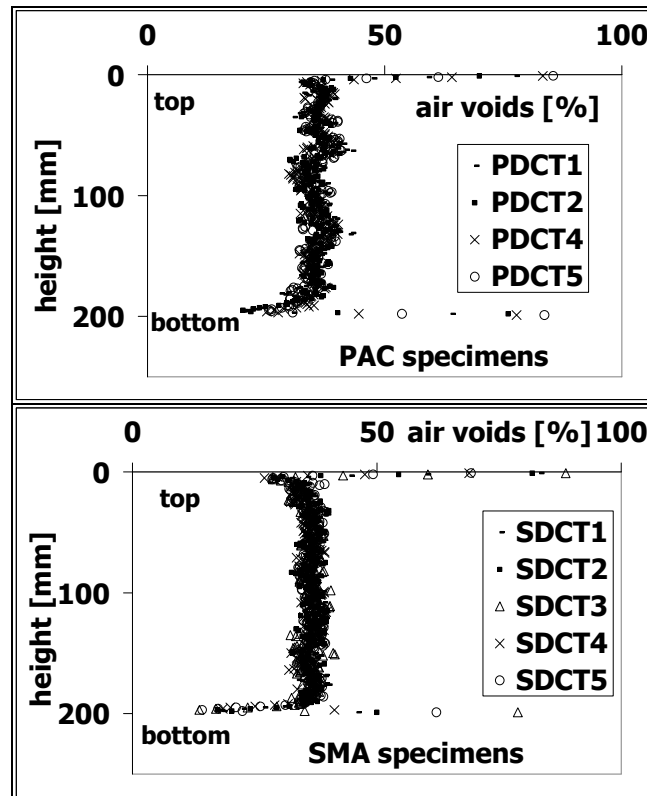


Figure 4.5 Air void distribution of the four PAC and the five SMA aggregate skeleton specimens

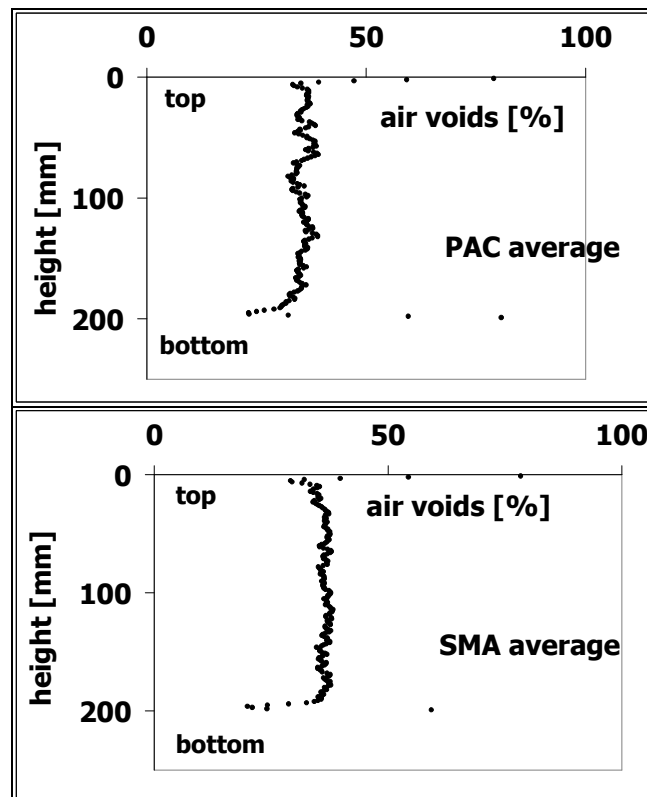


Figure 4.6 Average air void distribution of four PAC and five SMA aggregate skeletons

4.3.6 Aggregate Skeleton Summary

The PAC, SMA and DAC aggregate skeleton specimens were composed of aggregates larger than the 0.5 mm, 2 mm and 0.063 mm respectively. The aggregates less than 0.5 and 2 mm for the PAC and SMA specimens respectively were observed to segregate during mixing. Based on the segregation, it was concluded that particles smaller than 0.5 mm and 2 mm for PAC and SMA respectively were not part of the aggregate skeleton. The DAC aggregate skeleton was found to consist of all aggregate fractions larger than 0.063 mm excluding the filler.

Table 4.2 shows the aggregate skeleton gradation, target densities, cumulative percentage of aggregate content in the total asphalt mixture and the Marshall mixture density for the asphalt mixtures. From this table it is evident that the DAC aggregate skeleton had the highest density followed by the PAC and then the SMA. However, SMA was quite difficult to compact, PAC was moderate and DAC was the easiest to compact.

Table 4.2 Aggregate skeleton gradation, target densities, cumulative percentage of aggregate content in the total asphalt mixture by weight and the Marshall density

Sieve [mm]	11.2	8	5.6	2	0.5	0.18	0.063	ρ_{agg} [kg/m ³]	C_{agg} [%]	ρ_m [kg/m ³]
Cumulative retained [%]	PAC	28.7	69.6	92.3	93.4	100	-	1770	86.8	2041
	SMA	6.5	61.3	90.3	100	-	-	1760	74.2	2371
	DAC	12.4	23.8	36.2	62.1	82.7	94.7	2125	87.5	2428

Figure 4.7 shows the mixture composition in relation to content of the aggregate skeleton, aggregates smaller than the minimum size of the aggregate skeleton, bitumen and air. The label d in this figure indicates the minimum size of the aggregate skeleton. The first part of the figure shows the composition by weight. The second part of the figure and Table 4.3 show the content by volume. The volumetric composition was determined at 20% air voids content for PAC and at 5% air voids content for the SMA and DAC asphalt mixtures. The volumetric composition was calculated assuming that no absorption of the bitumen took place. The expression used in the calculation of the volumetric composition is shown in Equation 4.3.

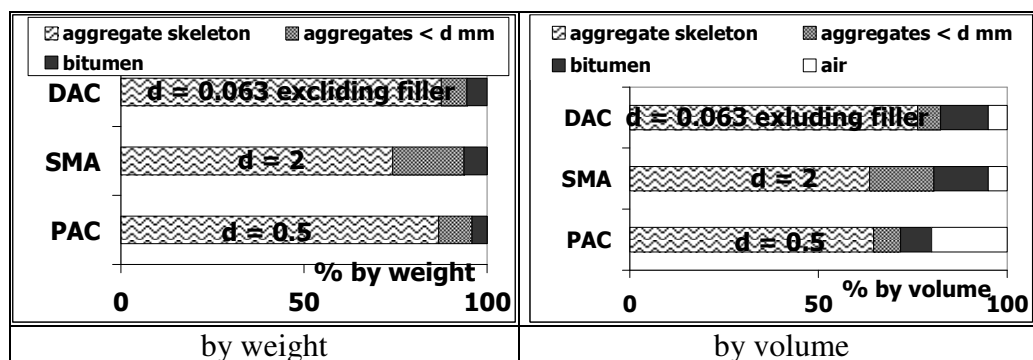


Figure 4.7 Mixture composition by weight and volume in relation to the content of aggregate skeleton, aggregates smaller than the minimum size of the aggregate skeleton, bitumen and air

Table 4.3 Mixture volumetric composition and the densities used to determine the volumetric composition

Mix	aggregate skeleton [%]	aggregates < d mm [%]	bitumen [%]	air [%]	total [%]	$\rho_{bitumen}$ [kg/m ³]	$\rho_{skeleton}$ [kg/m ³]	$\rho_{other\ aggregates}$ [kg/m ³]	ρ_{mb} [kg/m ³]	ρ_{max} [kg/m ³]
PAC	64.6	7.1	8.2	20.0	100	1029	2759	2628	2056	2569
SMA	63.5	17.0	14.4	5.0	100	1029	2763	2708	2365	2489
DAC	76.3	6.1	12.7	5.0	100	1035	2732	2743	2381	2507

Assuming that no absorption of bitumen takes place, then:

$$V_{total} = V_{air} + V_{bitumen} + V_{aggregates\ in\ skeleton} + V_{other\ aggregates\ smaller\ than\ the\ minimum\ aggregate\ in\ the\ skeleton}$$

The volumetric composition at a given air void content can be obtained as:

$$V_x = 100 \frac{\text{volume of component } x}{V_T} = 100 \frac{M_x / \rho_x}{V_T} \quad 4.2$$

$$= 100 \frac{\frac{M_T P_x}{100} / \rho_x}{V_T} = \frac{M_T P_x}{V_T \rho_x} = \frac{\rho_{mb} P_x}{\rho_x}$$

$$\rho_{mb} = \rho_{max} \left(1 - \frac{VTM}{100} \right) \Rightarrow V_x = \rho_{max} \left(1 - \frac{VTM}{100} \right) \frac{P_x}{\rho_x} \quad 4.3$$

Where:

- x = bitumen, aggregates in the skeleton and aggregates smaller than the minimum size of the aggregate skeleton,
- V_x = volumetric composition of component x [%],
- M_x = weight of component x [%],
- ρ_x = density of component x [kg/m³],
- P_x = percentage by weight of component x in the total asphalt mixture [%],
- ρ_{mb} = calculated density of the compacted mixture [kg/m³],
- ρ_{max} = calculated maximum density of the compacted mixture [kg/m³],
- V_T = total volume,
- M_T = total weight,
- VTM = air voids in the total asphalt mixture [%].

4.4 Preparation of Aggregate Skeleton Specimens

The aggregate skeleton compositions were mixed manually with a small percentage of water (0.7% by weight) being added to both the PAC and DAC compositions. Since the aggregate fractions in the SMA skeleton were larger than 2 mm, water was not required for the SMA aggregate skeleton.

The aggregates were then compacted using the Kango hammer (impact rate 1300 – 2600/min) to a size of 100 mm diameter by 200 mm height as shown in Figure 4.8. The compaction was performed in three equal layers for the DCMCC test specimens and in five equal layers for the PD test specimens to the target density calculated from Equation 4.1.



Figure 4.8 Kango hammer and an aggregate skeleton specimen

The difference in the number of compaction layers was as a result of application of different instrumentation procedures in the DCMCC and the PD tests as shown in Figure 4.9. The instrumentation of the DCMCC test specimens involved gluing of the LVDT holders on the specimen using a fast setting adhesive (Cyanolit) and a two component glue. The permanent deformation specimens were compacted in five layers to facilitate the placement of studs in the specimens. The studs were placed in the specimen to avoid undesired membrane effects during the measurement of resilient deformation.

The aggregates were compacted in a split mould fitted with a thin latex membrane (ELE part number 0716A0011) fastened to a bottom and top aluminium plate by means of two o-rings and vacuum grease as illustrated in Figure 4.9. The purpose of these top and bottom plates was to transmit the load to the specimen. A perforated disc and a permeable membrane were placed between the plates and the compacted material. The permeable membrane prevented the sucking of fines during vacuum application while the perforated disc protected the aluminium plate from being damaged by the aggregates.

Upon the removal of the specimen from the split mould, two additional thin latex membranes and an optional geo-textile were added on the specimen. The purpose of these extra latex membranes was to seal the leaks in the first membrane and to prevent leakage of oil into the specimen during testing. The optional geo-textile was added to prevent puncturing of the latex membranes that was observed during permanent deformation tests carried out at confining stresses of 150 and 250 kPa. A diameter of 108 mm was used for the geo-textile since there were concerns that a tight-fitting geo-textile would affect radial deformation.

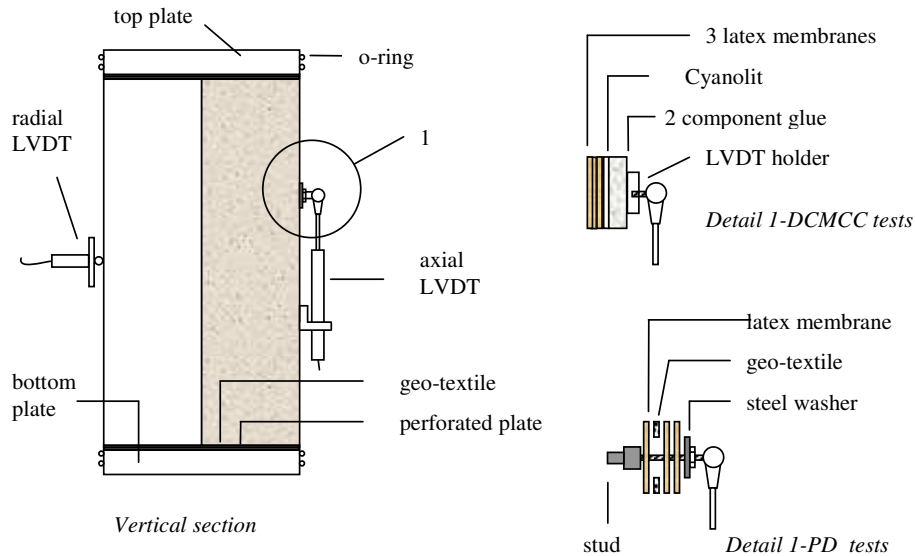


Figure 4.9 Instrumentation of aggregate specimens for DCMCC and PD test

4.5 Test Conditions

4.5.1 Displacement Controlled Monotonic Constant Confinement Failure Tests (DCMCC)

In order to investigate the effect of strain rate on aggregate skeletons some initial tests were performed on the PAC aggregate skeleton at 0.2 and 0.02%/s strain rates and confinement stress levels of 0.031 and 0.063 MPa as shown in Table 4.4. The findings from these initial tests suggested that change in strain rate resulted in only a slight change in the maximum vertical stress at failure. In other words, the effect of strain rate on the failure behaviour could be neglected. Consequently other tests were conducted at a strain rate of 0.02% (Muraya et al. 2004). Table 4.4 shows the test conditions for these initial tests and other tests conducted on the PAC, SMA and DAC aggregate skeleton. For each of these test conditions, three test repetitions were performed. Due to the capacity of the UTM 25 vertical actuator the tests conducted on PAC, SMA and DAC were limited to a maximum confinement of 0.313, 0.25 and 0.125 MPa respectively. The vertical stresses required at higher confinement levels were beyond the capacity of the UTM 25.

Table 4.4 DCMCC test conditions for the aggregate skeleton

skeleton	axial strain rate [%/s]	confining stress σ_3 [MPa]
PAC	0.2	0.031; 0.063
	0.02	0.031; 0.063; 0.188; 0.313
SMA		0.031; 0.188; 0.25
DAC		0.031, 0.063; 0.125

4.5.2 Permanent Deformation (PD) Tests

Stress invariants can be used to link the stresses occurring in the pavement to triaxial test conditions. The triaxial stress conditions can be determined from stress invariants calculated from stresses occurring in the pavement. In order to obtain some indication of the nature of suitable repeated permanent deformation test stress signals, profiles of triaxial vertical stress and triaxial confining stresses were determined based on visco-elastic stress analyses performed earlier as part of this research (Muraya et al. 2003). The description of the test pavement layers, Burger's parameters, Poisson's ratios and the wheel load characteristics are shown in Table 4.5. An illustration of the notation of the Burger's parameters is provided in Figure 4.10. The triaxial vertical stress and triaxial confining stress at the mid-depth of each layer were calculated from expressions given in Equation 4.4 to Equation 4.7 in relation to the I_1 and J_2 stress invariants determined from the stresses in the pavement. The pulse durations for the triaxial vertical stress and triaxial confining stress were determined using the expression shown in Equation 4.8. The pulse durations were calculated based on the distance in the direction of wheel movement in which both the triaxial vertical stress and triaxial confining stress fell to 6% of the maximum stress. A limiting percentage of 6% was chosen since it offered a good fit of the haversine function for both triaxial vertical stress and triaxial confining stress in the top and the second layers.

Table 4.5 Description and material properties for the test pavement layers

layer	material abbreviation	η_1 [MPa.s]	η_2 [MPa.s]	E_1 [MPa]	E_2 [MPa]	Poissons ratio [-]
top layer 40 mm thick	DAC	9557	38	868	384	0.35
Second layer 60 mm thick	OAC	1799	28	391	200	0.35
Third layer 80 mm thick	STAC	1953	48	616	145	0.35
fourth layer 90 mm thick		1683	55	764	131	0.35
fifth layer 250 mm thick	AGRAC	-	-	2200	-	0.45
subgrade	WCS	-	-	150	-	0.5
wheel load characteristics	std. wide based tyre 45 kN load, 0.9 MPa tyre pressure, 0.123 m contact radius, 20 km/h speed					
temperature	between 38 - 40 ⁰ C at the top of the pavement and 32 - 34 ⁰ C at the top of the base					
Material abbreviation	Material description					
DAC	Dense asphalt concrete					
OAC	Open asphalt concrete					
STAC	Stone asphalt concrete					
AGRAC	Cement bound asphalt aggregate base					
WCS	over 5 m well compacted sand					

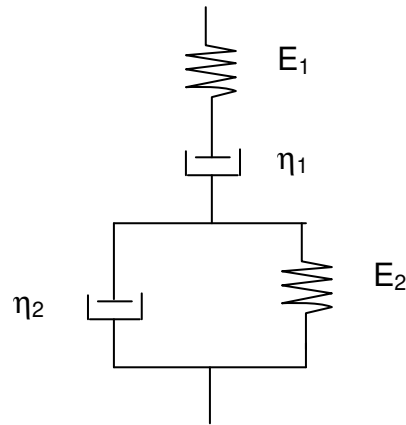


Figure 4.10 Burger's model

$$I_1 = \sigma_{xx} + \sigma_{yy} + \sigma_{zz} \quad 4.4$$

$$J_2 = \frac{1}{6} \left[(\sigma_{xx} - \sigma_{yy})^2 + (\sigma_{yy} - \sigma_{zz})^2 + (\sigma_{zz} - \sigma_{xx})^2 \right] + \tau_{xy}^2 + \tau_{yz}^2 + \tau_{xz}^2 \quad 4.5$$

$$\sigma_h = \frac{1}{3} (I_1 - \sqrt{3J_2}) \quad 4.6$$

$$\sigma_v = \frac{1}{3} (I_1 + 2\sqrt{3J_2}) \quad 4.7$$

$$\text{pulse duration} = \frac{D}{v} \quad 4.8$$

Where:

I_1, J_2	=	stress invariants,
σ_h	=	triaxial horizontal stress,
σ_v	=	triaxial vertical stress,
$\sigma_{xx}, \sigma_{yy}, \sigma_{zz}, \tau_{xy}, \tau_{yz}, \tau_{xz}$	=	stresses in the test pavement,
D	=	distance in the direction of wheel movement in which both the triaxial vertical and horizontal stresses fall to 6% of the maximum stress occurring at the mid-depth of a given layer,
v	=	wheel velocity = 5.56 m/s.

Figure 4.11 shows the shape and the pulse duration of the triaxial vertical and confining stresses and the haversine function. The figure shows that both the vertical triaxial stress and the triaxial horizontal stresses vary with time. Figure 4.11 also shows that the vertical and horizontal pulse durations differ. The implication of this figure is that triaxial vertical and horizontal cyclic stress signals of unequal pulse durations may provide a better stress simulation for the upper pavement layers than other test methods that involve a cyclic vertical stress and a constant confining stress. However, the stress rotation that is also known to

occur under pavement loading conditions cannot be simulated under triaxial test conditions.

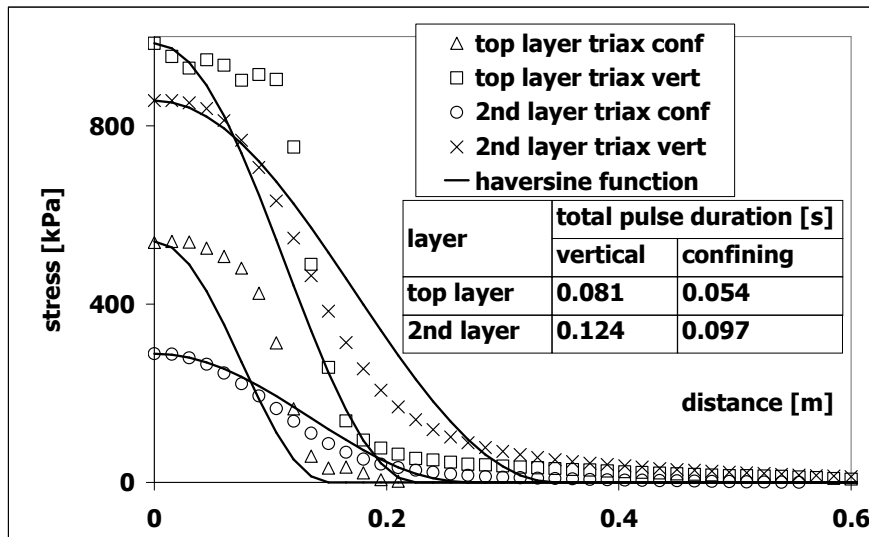


Figure 4.11 Shape and pulse duration for the triaxial vertical and horizontal stresses

Table 4.6 shows the test conditions for the PD tests performed on the PAC, SMA and DAC aggregate skeletons at a confining stress of 0.05 to 0.25 MPa and at various stress ratios. The stress ratios were determined as a ratio of the vertical stress to the maximum vertical stress determined from the DCMCC tests as shown in Equation 4.9. The test conditions were selected in such a way to obtain permanent deformation curves at low, medium and high vertical stresses for a maximum of 20,000 load repetitions.

For purposes of investigating the influence of the nature of the confinement signal on the permanent deformation behaviour of aggregate skeleton, pilot permanent deformation tests were conducted at cyclic and constant confining stresses of 0.05, 0.15 and 0.25 MPa on both the PAC and DAC aggregate skeletons as shown by the shaded regions in Table 4.6.

Table 4.6 Permanent deformation test conditions

Nature of confining stress	skeleton	magnitude of confining stress [MPa]											
		0.05				0.15				0.25			
cyclic confinement	PAC	0.620	0.823	1.063		0.600	0.971	1.034		0.63	0.828	1.008	
	DAC	0.4245	0.682	0.808		0.432	0.469	0.504	0.584	0.190	0.391	0.640	
	SMA	0.549	0.922	1.027	1.159	0.818	0.979	1.029		0.517	0.911	0.947	1.027
constant confinement	PAC	0.586		1.034			0.960			0.622	0.981	0.996	
	DAC	0.392	0.670				0.581	0.734		0.363	0.586	0.635	
pilot permanent deformation tests													

Note: the numbers in the table refer to the ratio of vertical stress to maximum vertical stress, f_{ca} , determined from the monotonic strain controlled failure tests

$$\text{stress ratio} = \sigma_1 / f_{ca} = \sigma_1 / a \left(\frac{\sigma_3}{\sigma_{3,0}} \right)^b \quad 4.9$$

Where:

f_{ca}	=	maximum stress at failure in the DCMCC tests,
$\sigma_{3,0}$	=	reference stress = 1,
σ_1	=	vertical stress,
σ_3	=	confining stress.

Despite the difference in the pulse durations for the triaxial vertical and horizontal stresses, a single pulse duration of 0.2 seconds for both pulse durations was adopted for the PD tests. This was done because different vertical and horizontal pulse times could not be accommodated in the UTM 25. Figure 4.12 shows the nature of the cyclic and constant confining stress signals. At any given level of confining stress, the magnitude of the vertical stress was maintained at similar levels in both the cyclic and constant confining tests. In order to hold the specimen together during the cyclic confinement tests, a static confinement of 12 kPa was maintained during the 1.7 seconds rest duration between any two consecutive load pulses. The purpose of this rest duration was to perform the aggregate skeleton tests at similar stress conditions to anticipated tests for the total asphalt mixture. Analysis of the triaxial test data on PAC and DAC asphalt mixtures from studies conducted by Antes (2002) and Parajuli (2002) indicated that a 1.7 seconds rest duration was sufficient to dissipate most of the visco-elastic strain at a load pulse duration of about 0.2 seconds and below. However, permanent deformation tests on the total asphalt mixtures in which the dissipation of the visco-elastic strain was required were not conducted.

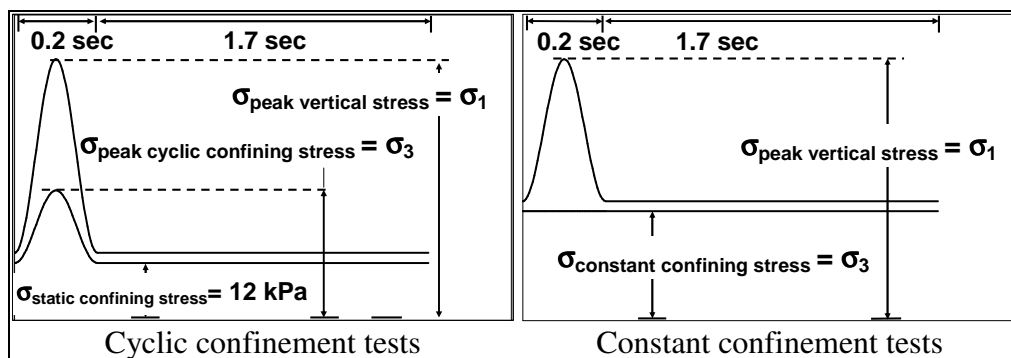


Figure 4.12: Cyclic and constant confining signals for cyclic and constant confinement tests

4.6 Test results

4.6.1 Displacement Controlled Monotonic Constant Confinement Failure Test (DCMCC)

Figure 4.13 to Figure 4.16 show the vertical stress versus radial/ axial strain plots for all the DCMCC tests performed on the three aggregate skeletons. Three test repetitions were performed at each confinement. The numbers in these figures indicate the confinement level at which the three test repetitions were performed. From these figures it is evident that the rate of decrease of the vertical stress after the maximum stress is much lower in the PAC and SMA aggregate skeletons than in the DAC skeleton. This observation suggests that in the presence of confinement the PAC and SMA aggregate skeletons retain considerable post-peak

stability even at such high axial strains as 5%. Figure 4.17 shows an example of the volumetric strain⁵ in the DCMCC tests for the three aggregate skeletons. The volumetric strain indicates that the aggregate skeletons exhibit only a slight amount of compaction (<0.2%) and that dilation is the main mode of deformation.

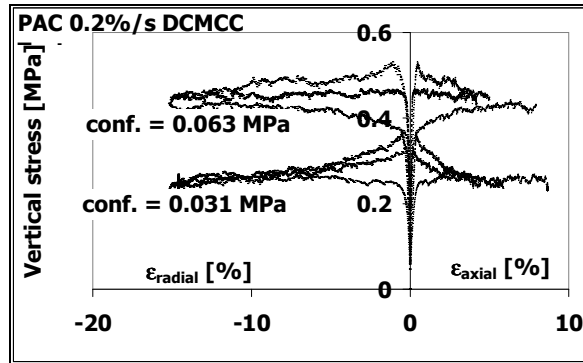


Figure 4.13 Vertical stress versus axial/radial plots for DCMCC test results of PAC aggregate skeleton at 0.031 and 0.063 MPa confining stress and at a strain rate of 0.2%/s

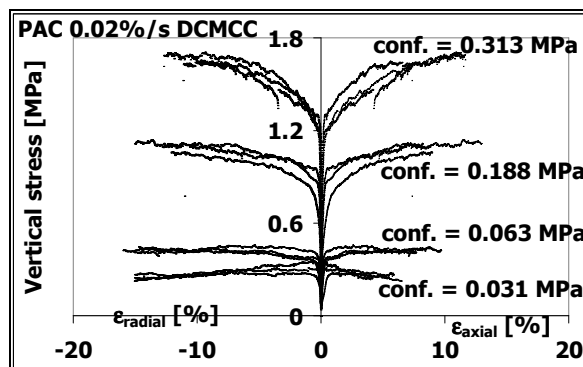


Figure 4.14 Vertical stress versus axial/radial plots for DCMCC test results of PAC aggregate skeleton at 0.031, 0.063, 0.188 and 0.313 MPa confining stress and at a strain rate of 0.02%/s

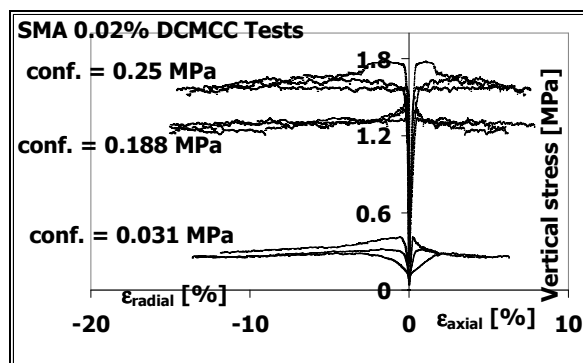


Figure 4.15 Vertical stress versus axial/radial strain plots of DCMCC test results for SMA aggregate skeleton at 0.031, 0.188 and 0.25 MPa confining stress and at a strain rate of 0.02%/s

⁵ Volumetric strain = 2(radial strain) + axial strain

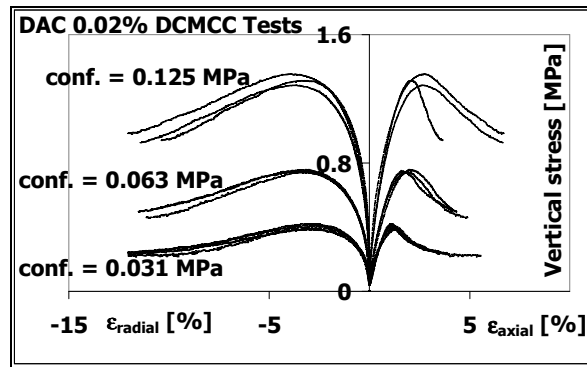


Figure 4.16 Vertical stress versus axial/radial strain plots of DCMCC test results for aggregate skeleton at 0.031, 0.063 and 0.125 MPa confining stress and at a strain rate of 0.02%/s

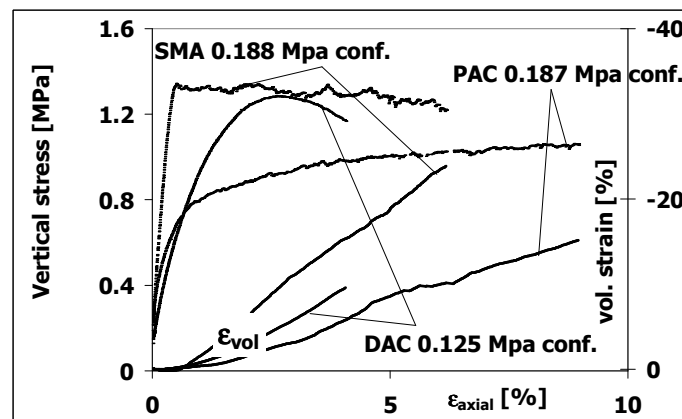


Figure 4.17 An example of the test results for PAC, SMA and DAC aggregate skeletons at a strain rate of 0.02%/s

4.6.1.1 Determination of Properties from the DCMCC tests

The properties derived from the DCMCC tests results included maximum stress, tangent stiffness, stress at initiation of plasticity, Poisson's ratio and stress at initiation of dilation. Traditionally, the initiation of plasticity is defined by the termination of linear part of the vertical stress versus axial strain plot which occurs before the onset of dilation. However, since the mode of deformation in the aggregate skeletons was mainly dilation, the termination of the linear part often occurred beyond the point of initiation of dilation. Consequently, a different definition for the initiation of plasticity was adopted for the aggregate skeleton tests. The initiation of plasticity for the aggregate DCMCC tests was defined by the point of termination of the linear part of the radial strain versus axial strain plot. The determination of initiation of plasticity, tangent stiffness, Poisson's ratio and initiation of dilation from the test results is illustrated in Figure 4.18. The figure shows a plot of the vertical stress, radial strain and volumetric strain against the axial strain in one of the PAC tests. A more detailed explanation on the determination of the tangent modulus and the Poisson's ratio can be found in Annex 4.

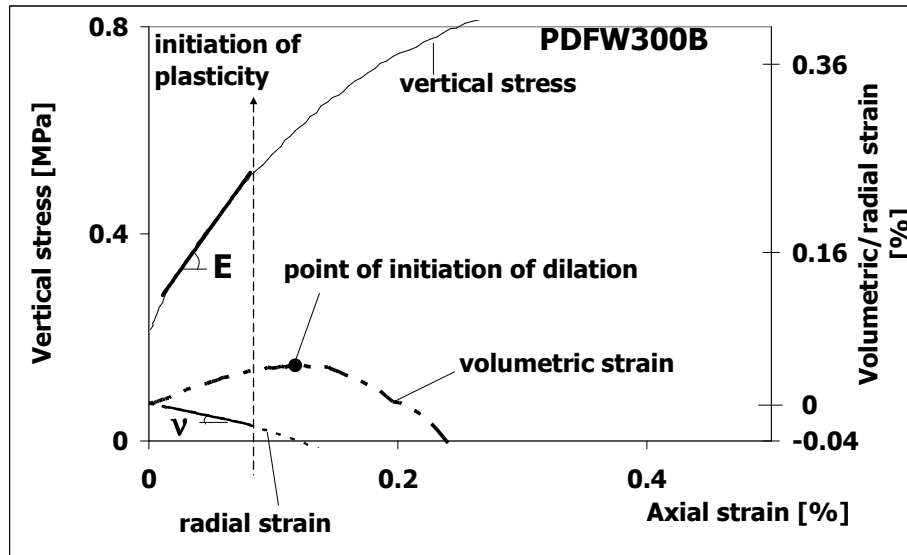


Figure 4.18 An illustration of the determination of tangent stiffness, Poisson's ratio and point of initiation of plasticity and dilation from a DCMCC test

Table 4.7 Properties determined from the DCMCC tests (PAC)

skeleton	Test	Compaction	*axial strain rate	confining stress	Maximum stress	Tangential stiffness	Plasticity	Poisson's ratio	Dilation
		[%]	[%/s]	σ_3 [MPa]	f_{ca} [MPa]	E_{ac} [MPa]	σ_{pa} [MPa]	ν_a [-]	σ_{da} [MPa]
PAC	PDFX50A	100.8	0.21	0.031	0.36	155	0.09	0.60	0.108
	PDFX50B	100.0	0.21	0.031	0.32	-	-	-	0.059
	PDFX50C	100.0	0.20	0.031	0.26	-	-	-	0.059
	PDFX100A	100.1	0.20	0.062	0.52	199	0.14	0.48	0.149
	PDFX100B	100.1	0.21	0.062	0.45	-	-	-	0.096
	PDFX100C	99.7	0.20	0.062	0.43	133	0.21	0.19	0.206
	PDFW50A	100.5	0.02	0.031	0.30	191	0.12	0.47	0.198
	PDFW50B	100.8	0.02	0.031	0.27	68	0.08	0.37	0.161
	PDFW50C	100.5	0.02	0.031	0.34	-	-	-	0.045
	PDFW100A	**	0.02	0.062	0.43	-	-	-	0.076
	PDFW100B	99.8	0.02	0.062	0.45	220	0.14	0.48	0.142
	PDFW100C	99.8	0.02	0.063	0.43	268	0.14	0.44	0.142
	PDFW300A	99.7	0.02	0.187	1.04	369	0.31	0.16	0.505
	PDFW300B	99.6	0.02	0.187	1.11	336	0.51	0.28	0.599
	PDFW300C	99.9	0.02	0.187	1.09	347	0.56	0.30	0.686
	PDFW500A	99.9	0.02	0.313	1.67	400	0.69	0.16	0.868
	PDFW500B	99.6	0.02	0.312	1.66	468	0.94	0.40	1.214
PDFW500C	99.9	0.02	0.312	1.62	694	0.91	0.25	1.021	

* strain rate over the total height of the specimen

** not measured

pure dilation mode

Table 4.7 and Table 4.8 give a summary of the properties derived from the DCMCC tests. The shaded cells indicate tests in which the mode of deformation was purely dilation. These tests included 3 initial PAC tests at 0.2%/s strain rate, 2 PAC at 0.02%/s strain rate and 2 SMA tests. In these tests, the tangent stiffness, initiation of plasticity and Poisson's ratios were not determined. The initiation of dilation in these tests was assumed to occur at the beginning of the test.

Table 4.8 Properties determined from DCMCC tests (SMA and DAC)

skeleton	Test	Compaction	*axial strain rate	confining stress	Maximum stress	Tangential stiffness	Plasticity	Poisson's ratio	Dilation
		[%]	[%/s]	σ_3 [MPa]	f_{ca} [MPa]	E_{ac} [MPa]	σ_{pa} [MPa]	ν_a [-]	σ_{da} [MPa]
SMA	SDFW50A	99.2	0.02	0.031	0.40	-	-	-	0.054
	SDFW50B	99.2	0.02	0.031	0.31	97	0.12	0.37	0.112
	SDFW50C	98.4	0.02	0.031	0.28	-	-	-	0.053
	SDFW300A	100.2	0.02	0.188	1.31	298	0.93	0.21	1.236
	SDFW300B	100.1	0.02	0.188	1.37	518	1.23	0.31	1.372
	SDFW300C	99.9	0.02	0.187	1.47	638	0.90	0.36	1.073
	SDFW400A	100.3	0.02	0.250	1.57	504	1.20	0.10	1.446
	SDFW400B	100.2	0.02	0.250	1.61	369	0.70	0.42	0.936
	SDFW400C	100.4	0.02	0.250	1.75	458	1.07	0.31	1.097
DAC	DDFW50A	99.3	0.02	0.031	0.40	52	0.05	0.37	0.059
	DDFW50B	99.5	0.02	0.031	0.38	69	0.05	0.29	0.054
	DDFW50C	99.8	0.02	0.031	0.41	38	0.06	0.41	0.070
	DDFW100A	99.5	0.02	0.063	0.74	73	0.16	0.37	0.183
	DDFW100B	100.0	0.02	0.063	0.73	89	0.14	0.42	0.157
	DDFW100C	99.6	0.02	0.062	0.73	87	0.12	0.39	0.122
	DDFW200A	100.0	0.02	0.125	1.26	134	0.27	0.40	0.285
	DDFW200B	99.9	0.02	0.125	1.29	129	0.34	0.32	0.494
	DDFW200C	100.0	0.02	0.125	1.33	192	0.22	0.42	0.224

* strain rate over the total height of the specimen

pure dilation mode

4.6.1.2 Modelling of Properties Determined from the DCMCC Tests

As already mentioned in section 2.7.2, the Unified Model was used to model some of the properties derived from the aggregate skeleton tests. The Unified Model was used to provide a similar approach for the aggregate skeleton, total mixture, mastic and the bitumen. The model captures the effect of strain rate and temperature on the total asphalt mixture, mastic and bitumen and the effect of confinement on the aggregate skeleton.

In the modelling of the properties determined from the DCMCC tests, a power model and a modified Unified Model were used to describe the results derived from the DCMCC tests. A power model was used to describe the maximum stress and the modified Unified Model to describe the tangent stiffness, stress at initiation of dilation and plasticity. The Unified Model was also applied in the modelling of the Poisson's ratios for PAC and SMA. A constant value was used to represent the Poisson's ratios for DAC.

The power model shown in Equation 4.10 was used to describe the relationship between the maximum stress and the confining stress since it resulted in a realistic data fit. Figure 4.19 shows the data fit of the maximum stress based on a power model and the well known Mohr-Coulomb failure criterion for the three types of aggregate skeletons. Figure 4.19 shows that both the power model and the Mohr-Coulomb failure criterion can be used to describe the measured maximum stresses, f_{ca} . The power model gives a more realistic data fit in comparison to the Mohr-Coulomb failure criterion. The reason for this is the fact that all the material fractions that could result in cohesion were omitted during the preparation of aggregate skeleton specimens, and, as a result, no cohesive strength was expected in the aggregate skeleton specimens.

Figure 4.19 also shows that the vertical stress required to fail the DAC aggregate skeleton is higher in comparison to the SMA and the PAC aggregate skeletons and that the three aggregate skeletons can be ranked in order of decreasing ultimate vertical stress as DAC, SMA followed by PAC.

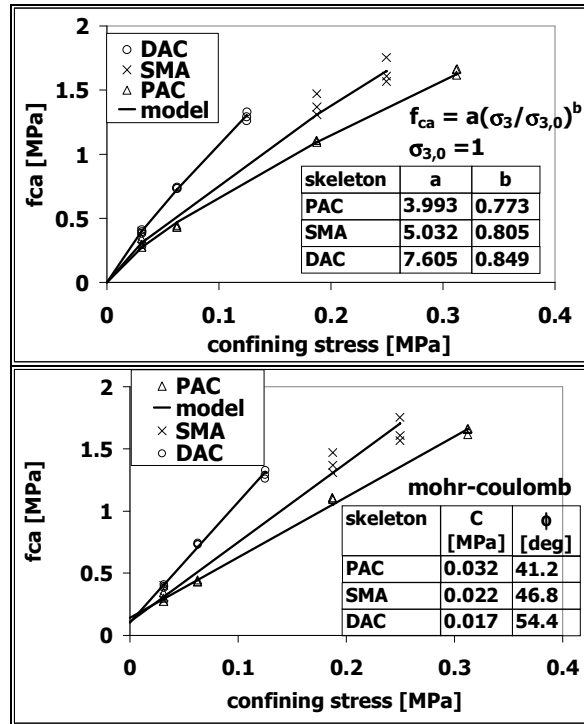


Figure 4.19 Measured and modelled maximum vertical stress, f_{ca} for PAC, SMA and DAC aggregate skeleton

A modified version of the Unified Model (Medani et al 2004) shown in Equation 4.11 was applied to describe the tangent stiffness, stress at initiation of dilation, stress at initiation of plasticity and the Poisson's ratios for PAC and SMA. The Unified Model was used to define these properties because the test results dictated the need of a model that incorporates a sigmoidal function. Initially, parameter β in the Unified Model was expressed as shown in Equation 4.13 to model the stress at initiation of dilation. However, in order to decrease the number of model parameters, this was later changed to the format shown in Equation 4.14. The β format in Equation 4.14 was also used to model the tangent modulus and the stress at initiation of plasticity. Since all the material fractions that could result in cohesion were omitted during the preparation of the aggregate skeleton, the value of the minimum theoretical limit, P_{low} was set to zero for the tangent modulus and the stress at initiation of plasticity. The β format in Equation 4.15 was also used to define the Poisson's ratios for PAC and SMA aggregate skeleton. A constant value model was used to describe the Poisson's ratios for DAC since the confinement did not appear to influence the Poisson's ratios for the DAC aggregate skeleton. Table 4.9 shows the Unified Model parameters determined from DCMCC tests conducted on PAC, SMA and DAC aggregate skeletons and the constant value for DAC Poisson's ratio.

$$f_{ca} = a\sigma_3^b \quad 4.10$$

$$P = P_{high} + (P_{low} - P_{high})S \quad 4.11$$

Where:

$$S = e^{(-[\beta]^\lambda)} \quad 4.12$$

$$\beta = \frac{a\sigma_3}{(1+a\sigma_3)^b} \quad 4.13$$

$$\beta = \frac{\sigma_3}{\sigma_{3,0}} \quad 4.14$$

$$\beta = \frac{\sigma_{3,0}}{\sigma_3} \quad 4.15$$

Where:

P	=	Value of property P ,
P_{high}	=	maximum theoretical limit for property P ,
P_{low}	=	minimum theoretical limit for property P ,
f_{ca}	=	maximum stress determined from the DCMCC tests,
σ_3	=	confinement [MPa],
$\sigma_{3,0}$	=	model parameter [MPa],
λ	=	model parameter [-],
a, b, c	=	model coefficients [-].

Table 4.9 Unified Model parameters for PAC, SMA and DAC aggregate skeletons and the constant value for DAC Poisson's ratio

skeleton	property	symbol	Unified model parameter				Constant value
			$\sigma_{3,0}$	λ	P_{low}	P_{high}	
PAC	tangent stiffness [MPa]	E_{ca}	0.377	0.810	0.0	800	-
	stress at initiation of dilation [MPa]	σ_{da}	2.024	1.254	0.0	11.2	-
	stress at initiation of plasticity [MPa]	σ_{pa}	2.056	1.230	0.0	10.006	-
	Poisson's ratio [-]	ν_a	0.125	2.499	0.23	0.45	-
SMA	tangent stiffness [MPa]	E_{ca}	0.076	1.733	0.0	500	-
	stress at initiation of dilation [MPa]	σ_{da}	0.157	1.769	0.0	1.44	-
	stress at initiation of plasticity [MPa]	σ_{pa}	0.150	1.765	0.0	1.304	-
	Poisson's ratio [-]	ν_a	0.091	1.500	0.19	0.37	-
DAC	tangent stiffness [MPa]	E_{ca}	0.904	0.904	0.0	1000	-
	stress at initiation of dilation [MPa]	σ_{da}	4.196	1.152	0.0	16.5	-
	stress at initiation of plasticity [MPa]	σ_{pa}	0.773	1.148	0.0	2.281	-
	Poisson's ratio [-]	ν_a	-	-	-	-	0.39

4.6.1.3 Tangent Stiffness and Poisson's ratios

Figure 4.20 shows an illustration of the model fit on the tangent stiffness and Poisson's ratio for the three aggregate skeletons. The figure shows that the properties derived from the PAC and SMA aggregate skeletons had a higher degree of scatter in comparison to the properties derived from the DAC aggregate skeleton. The figure also shows that the model provided a reasonable description of the measured data.

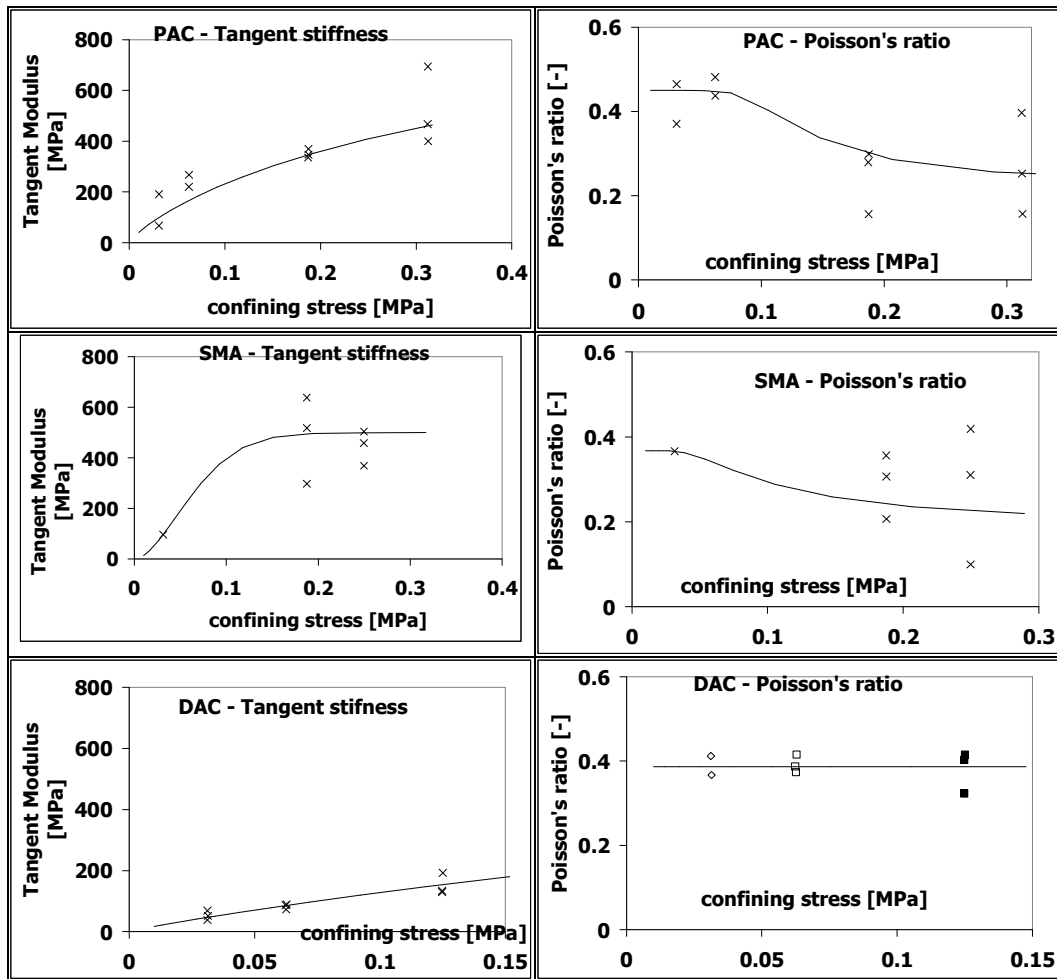


Figure 4.20 An illustration of the model fit on the tangent modulus and Poisson's ratios for the three aggregate skeletons

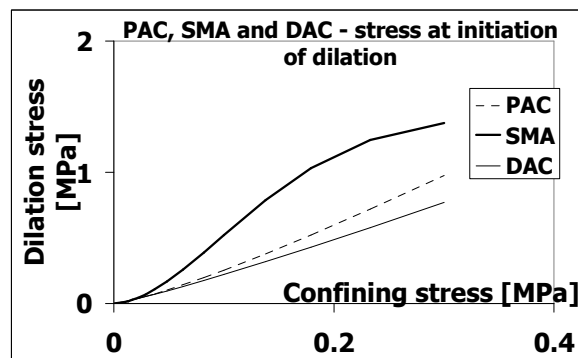


Figure 4.21 A comparison of the modelled stress at initiation of dilation for the three aggregate skeletons

4.6.1.4 Stress at initiation of Dilation

Figure 4.21 shows the predicted stress at initiation of dilation for the three aggregate skeletons in relation to the confinement level. The figure shows that the effect of confinement on the stress at initiation of dilation is different for the SMA in comparison with the PAC and DAC aggregate skeletons. The stress at initiation of dilation for the three aggregate skeletons increases with increase in confinement. However, the SMA aggregate skeleton seems to approach the

limiting stress at relatively lower levels of confinement. The effect of confinement on stress at initiation of dilation for SMA is only evident up to about 0.2 MPa. Above 0.2 MPa, the effect of the level of confinement is clearly reduced. This is probably caused by the reduction in the influence of the confinement on the density of the SMA skeleton. Figure 4.22 and Figure 4.23 show the densities of the PAC, SMA and DAC aggregate skeletons at initiation of dilation. The figures show that the density at initiation of dilation generally increases with increase in confinement for the PAC and DAC aggregate skeletons. The density of the SMA aggregate skeleton increases with increase in confinement in the interval between 0.05 and 0.188 MPa. However, change in confinement in the interval between 0.188 and 0.25 MPa has little or no influence on the density at initiation of dilation. The initiation of dilation occurs when the aggregates are arranged in such a manner to occupy the minimum volume. This minimum volume decreases with increase in the confinement level leading to increase in density as evident in Figure 4.22 and Figure 4.23. However, the minimum volume cannot be expected to decrease indefinitely with increase in confinement. At a certain confinement, the aggregates will occupy the minimum possible volume and beyond this point no further increase in density can be expected.

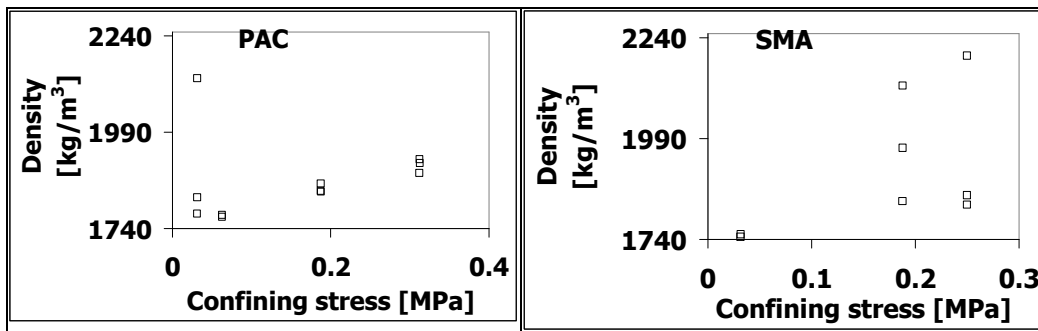


Figure 4.22 Density at initiation of dilation for the PAC and SMA aggregate skeletons

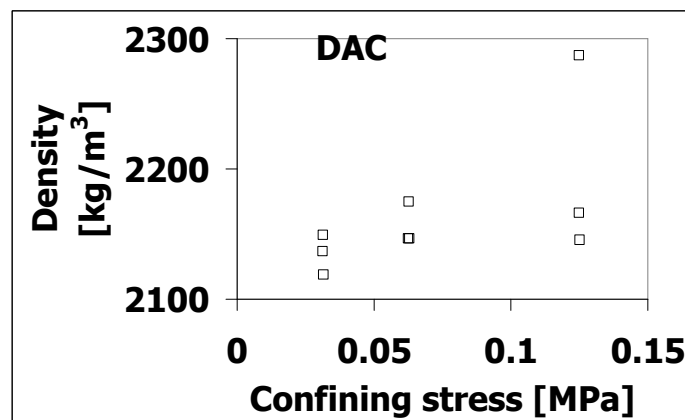


Figure 4.23 Density at initiation of dilation for the DAC aggregate skeleton

4.7 Flow Surface

The flow surfaces for the three aggregate skeletons were developed based on the response surface shown in Equation 4.16 that was developed by Desai (Desai et al 1986). The flow surface for the aggregate skeletons was derived with the sign notation being positive for compression with σ_1 and σ_3 symbolizing the vertical and confining stress respectively.

$$f = \frac{J_2}{p_a^2} - \frac{\left[-\alpha \left(\frac{I_1 + R}{p_a} \right)^n + \gamma \left(\frac{I_1 + R}{p_a} \right)^2 \right]}{\sqrt{(1 - \beta \cos 3\theta)}} = 0 \quad 4.16$$

Table 4.10 Desai surface model and stress invariants for the aggregate skeleton

Term	Expression
f	$f = \frac{J_2}{p_a^2} - \left[-\alpha \left(\frac{I_1}{p_a} \right)^n + \gamma \left(\frac{I_1}{p_a} \right)^2 \right] = 0$
I_1, J_2, J_3, p_a	$I_1 = \sigma_1 + 2\sigma_3; J_2 = \frac{(\sigma_1 - \sigma_3)^2}{3}; J_3 = \frac{2}{27}(\sigma_1 - \sigma_3)^3; p_a = 0.1 \text{ [MPa]}$

Table 4.11 Desai surface parameters for the aggregate skeleton

Model parameter	Expression
γ, R	$\gamma = \frac{(f_{ca} - \sigma_3)^2}{3(f_{ca} + 2\sigma_3)^2}; R = 0; f_{ca} \text{ as defined in Equation 4.10}$
n, α	$n = \frac{2}{1 - \frac{1}{3\gamma} \left(\frac{\sigma_{da} - \sigma_3}{\sigma_{da} + 2\sigma_3} \right)^2}; \alpha = \frac{-\frac{J_2}{p_a^2} + \gamma \left(\frac{I_1}{p_a} \right)^2}{\left(\frac{I_1}{p_a} \right)^n}$ $\sigma_{da} \text{ as defined in Equation 4.11}$

The model parameters were determined by imposing the following conditions on the Desai surface to obtain the expressions shown in Table 4.10 and Table 4.11:

- β assumed to be equal to zero since $\cos 3\theta = (1.5(3)^{0.5}J_3)/(J_2)^{1.5} = 1$ for the DCMCC tests.
- At ultimate surface, $\alpha = 0$, and parameter γ and R can be determined using this condition.
- Parameter n can be determined by considering the fact that, in the I_1 -SQRT J_2 space, the point at which dilation is initiated corresponds to the apex of the flow surface and the partial derivative, $\partial f/\partial I_1 = 0$ (Scarpas 2005).

4.7.1 Model Parameters

Figure 4.24 shows the effect of confinement on the model parameters γ and n . The figure shows that the γ parameter decreases with increasing confinement level and tends to a limiting value at high confinement levels. The figure also shows that the effect of confinement on parameter n is dependent on the aggregate skeleton. Parameter n for the SMA aggregate reaches a maximum value at around 0.2 MPa after which it decreases. This is caused by the increase and decrease of the effect of the level of confinement on the stress at initiation of dilation as explained in paragraph 4.6.1.4. The value of the denominator in the Equation for determination of n decreases as a result of decrease of the σ_{dil}/σ_3 ratio. The higher n values for PAC in comparison to the DAC are also caused by the effect of the confinement level on stress at initiation of dilation. This effect is relatively higher on the PAC aggregate skeleton than on the DAC aggregate skeleton as was evident from Figure 4.21.

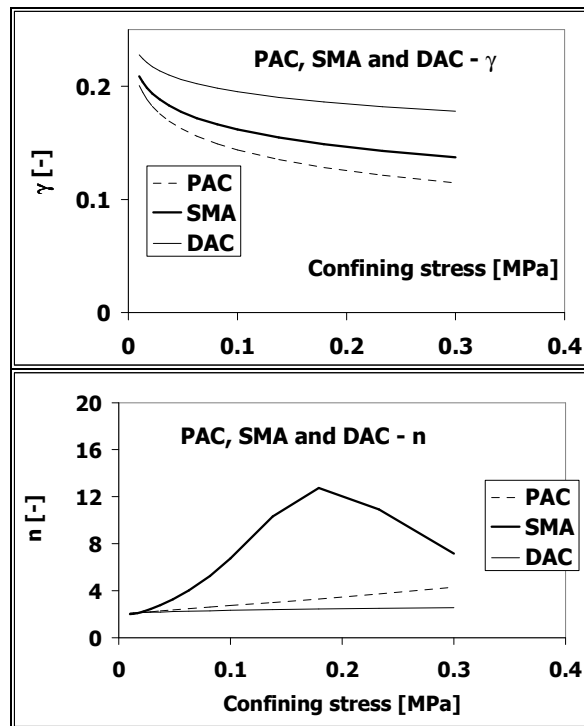


Figure 4.24 Model parameter γ and n for PAC, SMA and DAC aggregate skeletons

4.7.2 Flow Surfaces

The flow surfaces were derived for the three aggregate skeletons at confinement levels of 0.05, 0.1 and 0.3 MPa. These confinement levels represent low, moderate and high confinements within the test conditions.

Figure 4.25 shows the flow surfaces for the three aggregate skeletons at initiation of dilation. The figure shows that the size of the flow surface at initiation of dilation depends on the effect of the level of confinement. At the three confinement levels, the size of the surfaces can be ranked in order of decreasing size as SMA, PAC and DAC. This ranking order is the same as the ranking order of the stress at initiation of dilation shown in Figure 4.21.

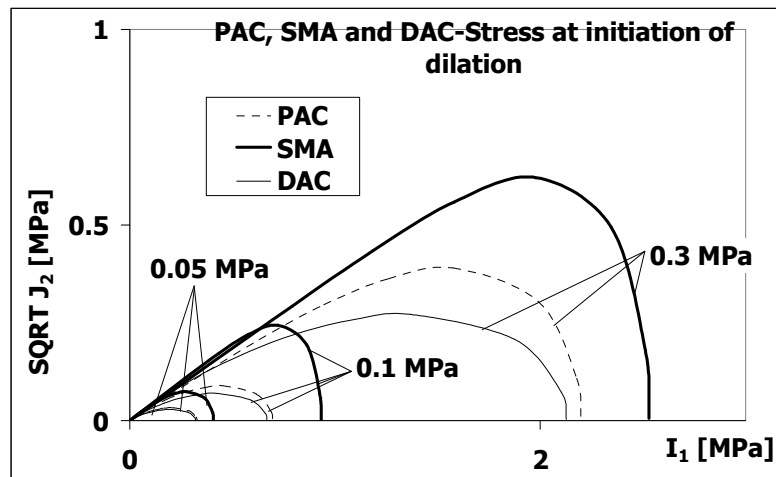


Figure 4.25 Flow surfaces at initiation of dilation for the three aggregate skeletons

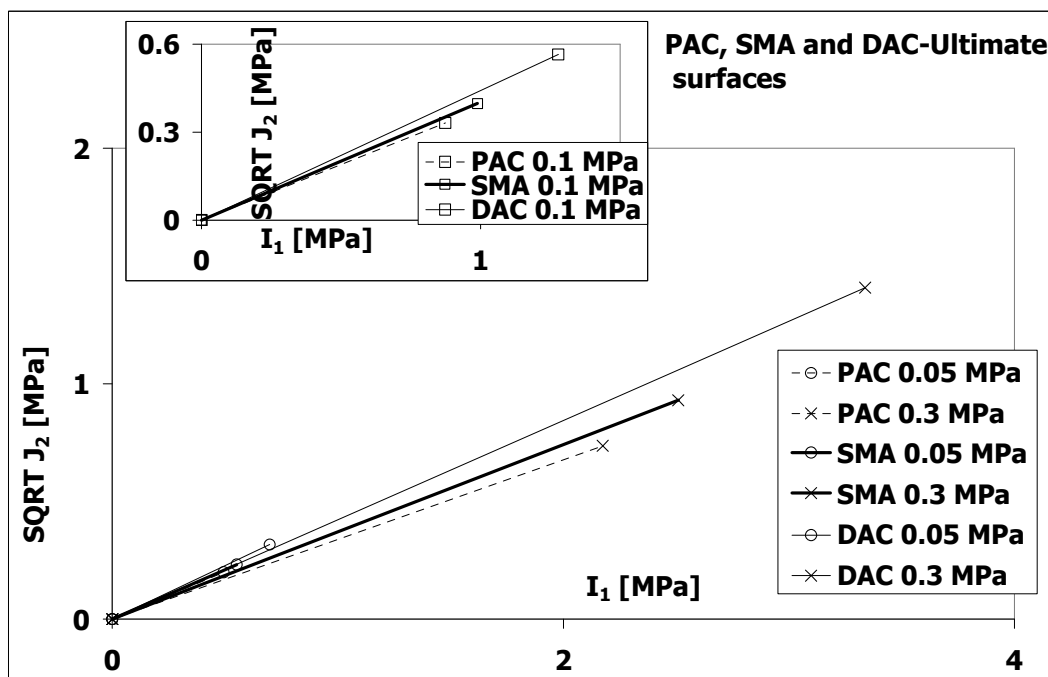


Figure 4.26 Ultimate surfaces for PAC, SMA and DAC aggregate skeletons

Figure 4.26 shows the ultimate flow surfaces for PAC, SMA and DAC aggregate skeletons. The figure shows that regardless of the level of confinement, the three aggregate skeletons can be ranked in order of decreasing size of the ultimate surface as DAC, SMA and PAC. This order of ranking is a direct consequence of order of ranking that was observed for the maximum stress at failure (see paragraph 4.6.1.2).

4.7.3 Permanent Deformation

The results obtained from the PAC and DAC aggregate skeleton pilot permanent deformation tests are shown in Figure 4.27 to Figure 4.30. The numbers expressed to 3 decimal points in the figures refer to the stress ratio (see Equation 4.9) while the numbers in the brackets refer to the level of confinement in MPa. These figures show that 8 out of the 10 tests conducted at cyclic confinement resulted in

higher permanent deformation in comparison to the tests conducted at constant confinement and at similar vertical to maximum stress ratios. The other 2 cyclic confinement tests conducted on the DAC aggregate skeleton at 0.05 MPa confinement at stress ratios of 0.682 and 0.424 resulted in a lower permanent deformation than the constant confinement tests at stress ratios of 0.670 and 0.392. This discrepancy from the other test results is probably due to scatter in test results and the 0.050 MPa DAC tests results may be treated as outliers. As a result of this observation and the fact that the triaxial horizontal pavement stresses in the upper pavement layers were shown to be cyclic, the other permanent deformation tests shown in the unmarked part of Table 4.6 were only conducted under cyclic confinement.

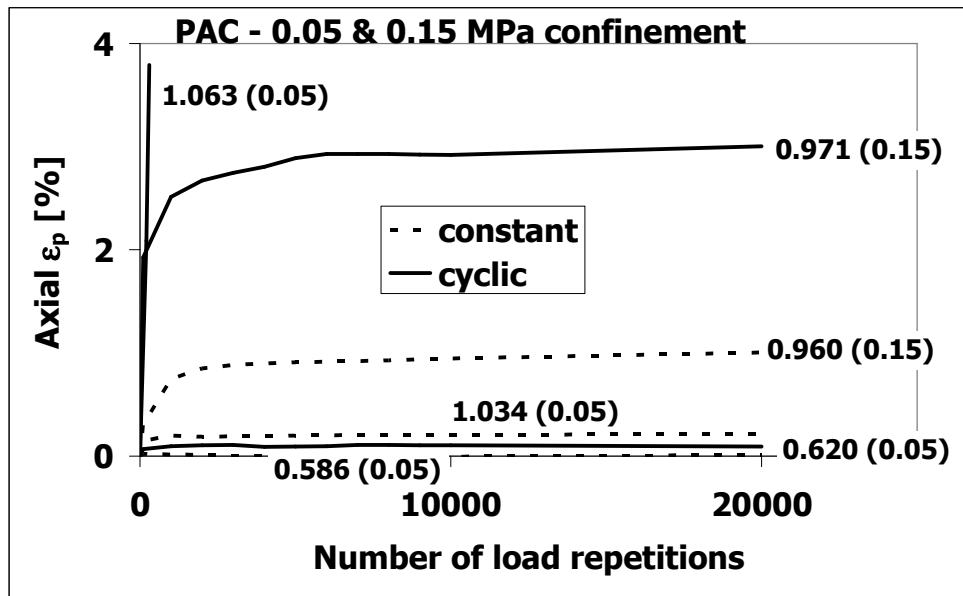


Figure 4.27 PAC aggregate skeleton pilot cyclic and constant tests at 0.05 and 0.15 MPa

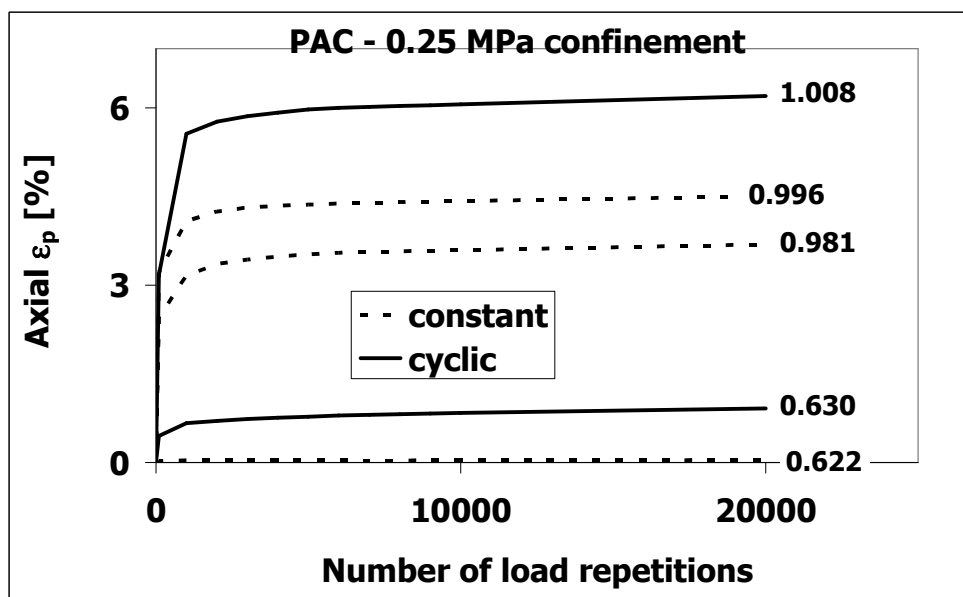


Figure 4.28 PAC aggregate skeleton pilot cyclic and constant tests at 0.25 MPa

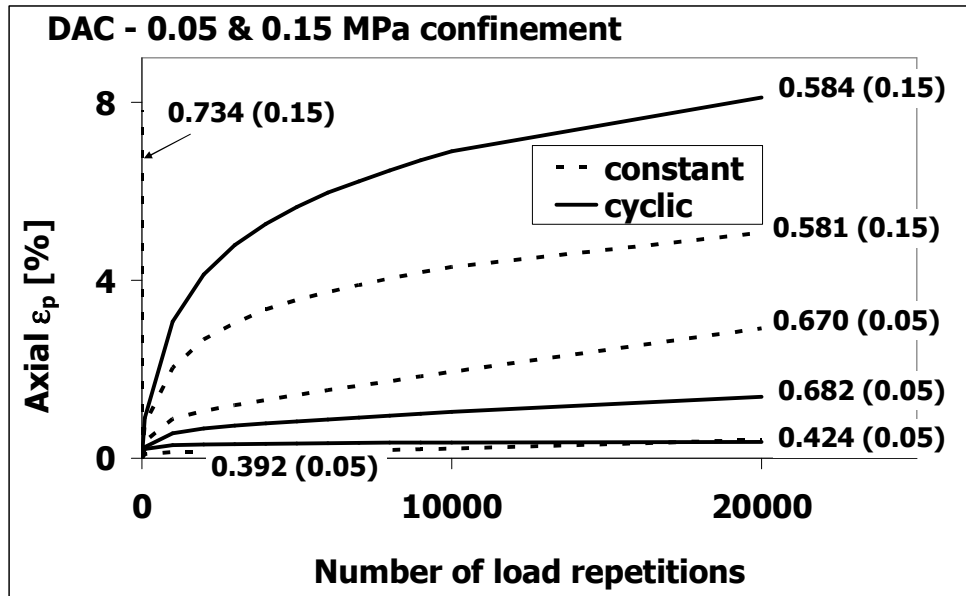


Figure 4.29 DAC aggregate skeleton pilot cyclic and constant tests at 0.05 and 0.15 MPa

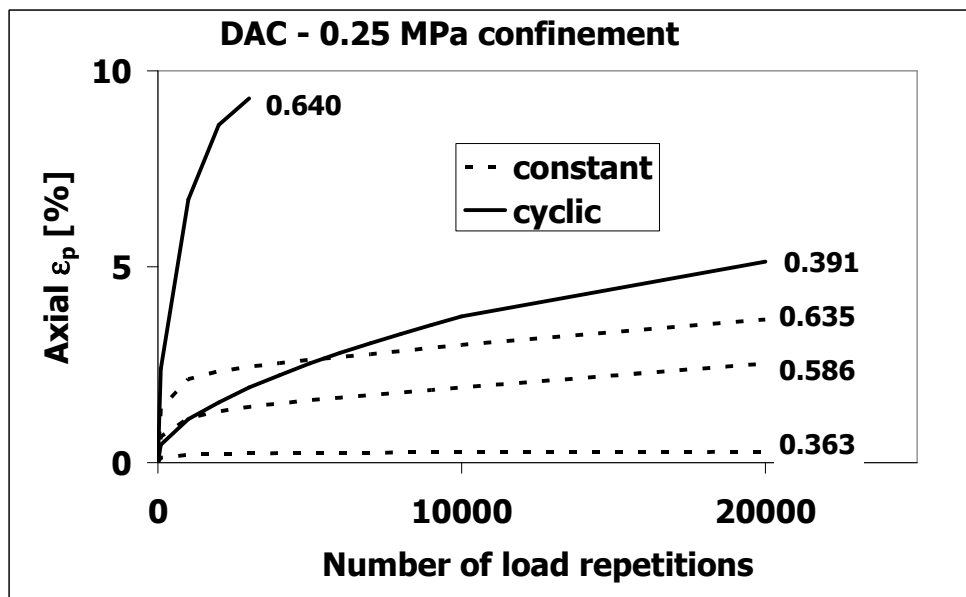


Figure 4.30 DAC aggregate skeleton pilot cyclic and constant tests at 0.25 MPa

4.7.3.1 Determination of Resilient Modulus and Poisson's Ratio

The resilient modulus and Poisson's ratio were determined using the following relationships:

$$\epsilon_{ax,res} = \frac{(\Delta\sigma_1 - 2\nu\Delta\sigma_3)}{M_R} \quad 4.17$$

$$\varepsilon_{rad,res} = \frac{(\Delta\sigma_3(1-\nu) - \nu\Delta\sigma_1)}{M_R} \quad 4.18$$

Re-writing Equation 4.17 and 4.18:

$$M_r = \frac{(\Delta\sigma_1 - \Delta\sigma_3)(\Delta\sigma_1 + 2\Delta\sigma_3)}{\varepsilon_{ax,res}(\Delta\sigma_1 + \Delta\sigma_3) - 2\varepsilon_{rad,res}\Delta\sigma_3} \quad 4.19$$

$$\nu = \frac{\Delta\sigma_1 \cdot \varepsilon_{rad,res} - \Delta\sigma_3 \cdot \varepsilon_{ax,res}}{2\Delta\sigma_3 \cdot \varepsilon_{rad,res} - \varepsilon_{ax,res}(\Delta\sigma_1 + \Delta\sigma_3)} \quad 4.20$$

Where:

- M_r = resilient modulus,
- ν = Poisson's ratio,
- $\Delta\sigma_1$ = change in the vertical stress,
- $\Delta\sigma_3$ = change in the confining stress,
- $\varepsilon_{ax,res}$ = axial resilient deformation,
- $\varepsilon_{rad,res}$ = radial resilient deformation.

The symbols used in Equation 4.20 are illustrated in Figure 4.31.

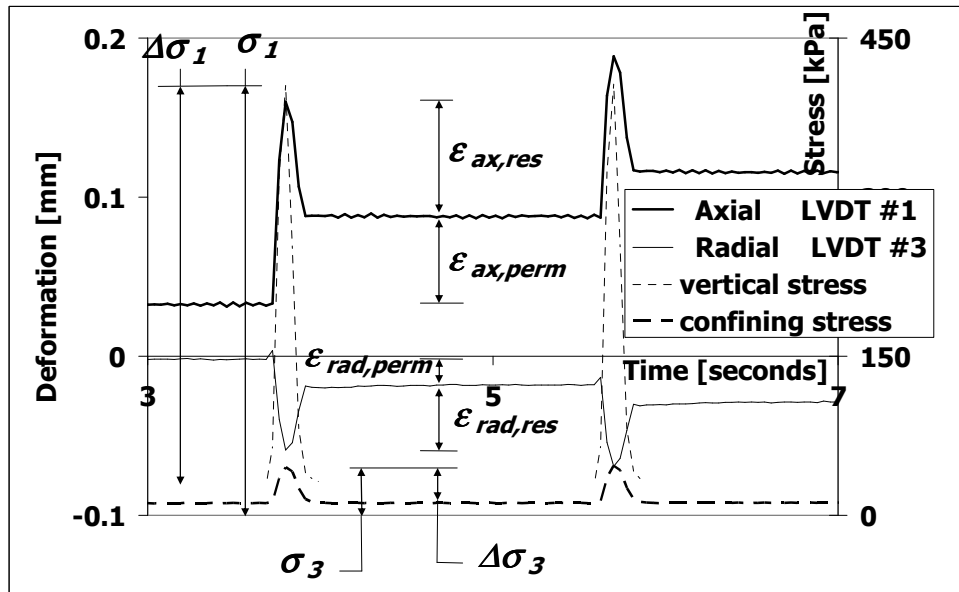


Figure 4.31 An illustration of the resilient deformation and stresses extracted from a cyclic confinement permanent deformation test for a PAC aggregate skeleton

Figure 4.32 to Figure 4.37 show the resilient modulus values and the Poisson's ratios for the three aggregate skeletons. The first part of the labels in these figures denotes the confinement in MPa and the second part in brackets denotes the stress ratio determined from Equation 4.9. The figures show that the resilient modulus values and the Poisson's ratios for the DAC aggregate skeleton exhibit more stability than the resilient modulus values and Poisson's ratios for the PAC and SMA aggregate skeleton. A comparison of the resilient modulus and Poisson's

ratios for the PAC aggregate skeleton with those of the SMA aggregate skeleton also shows that the PAC has a more stable resilient deformation behaviour. The relative stability of the aggregate skeletons resilient deformation behaviour can be ranked in order of decreasing stability as DAC, PAC and SMA. This can be attributed to the increase in order of the relative coarseness in the three aggregate skeletons. The aggregate skeleton in the three asphalt mixtures was identified to consist of the aggregates above 2 mm for the SMA, 0.5 mm for the PAC and 0.063 mm for the DAC.

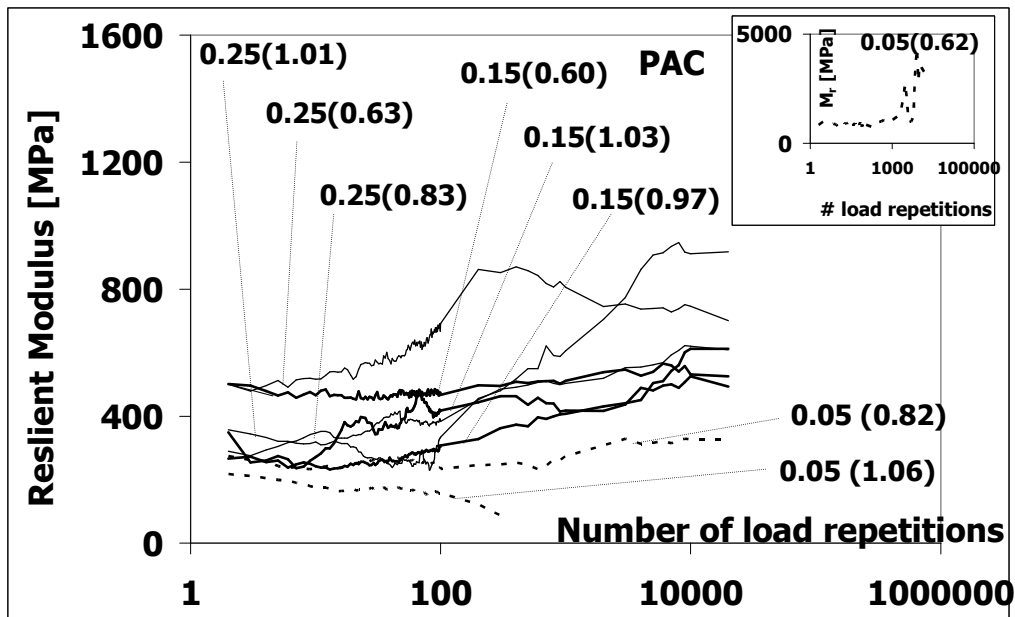


Figure 4.32 Resilient modulus values for PAC aggregate skeleton

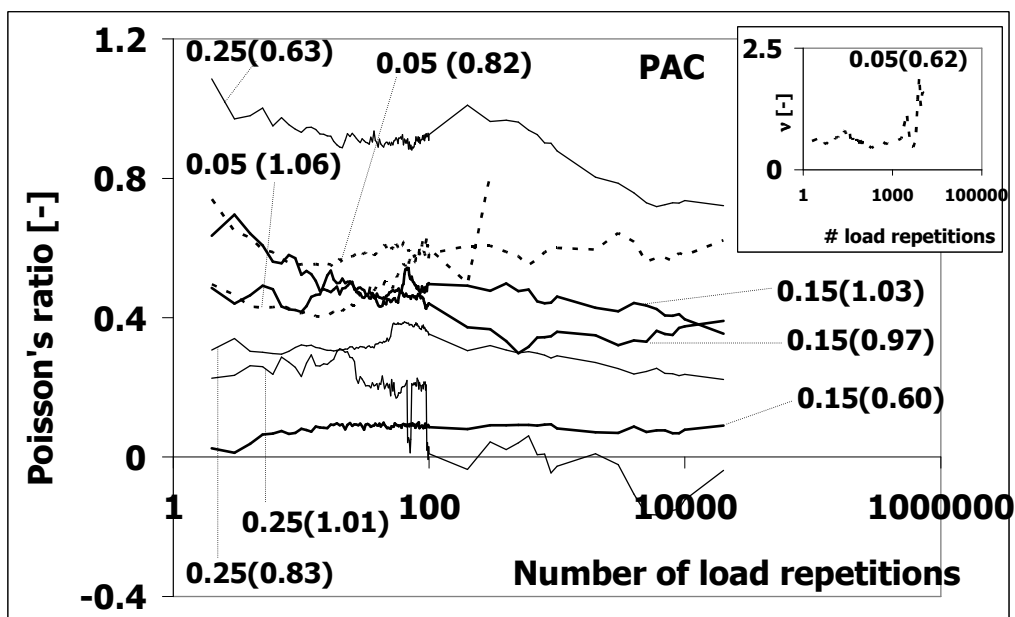


Figure 4.33 Poisson's ratios for PAC aggregate skeleton

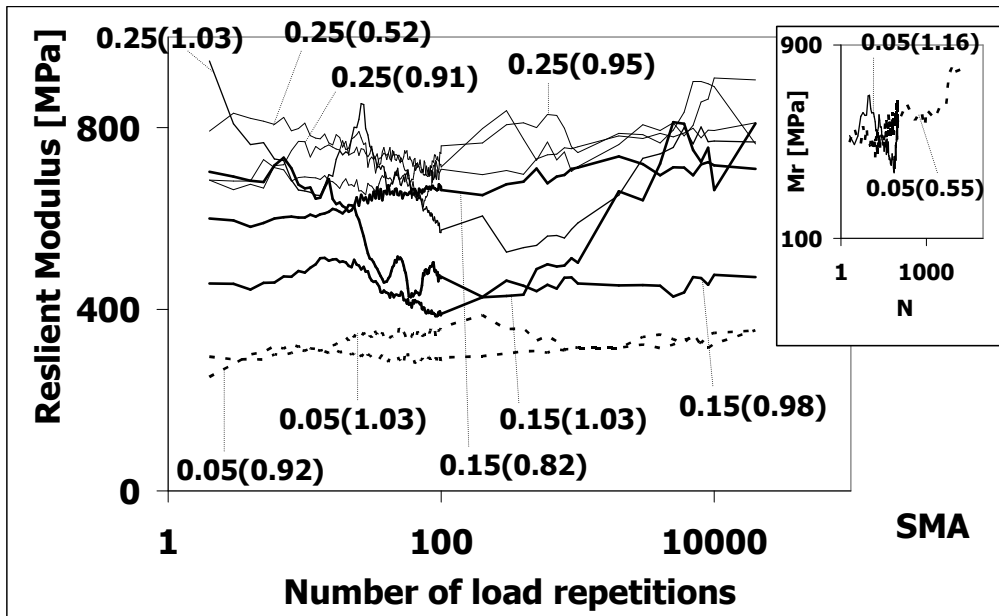


Figure 4.34 Resilient modulus values for SMA aggregate skeleton

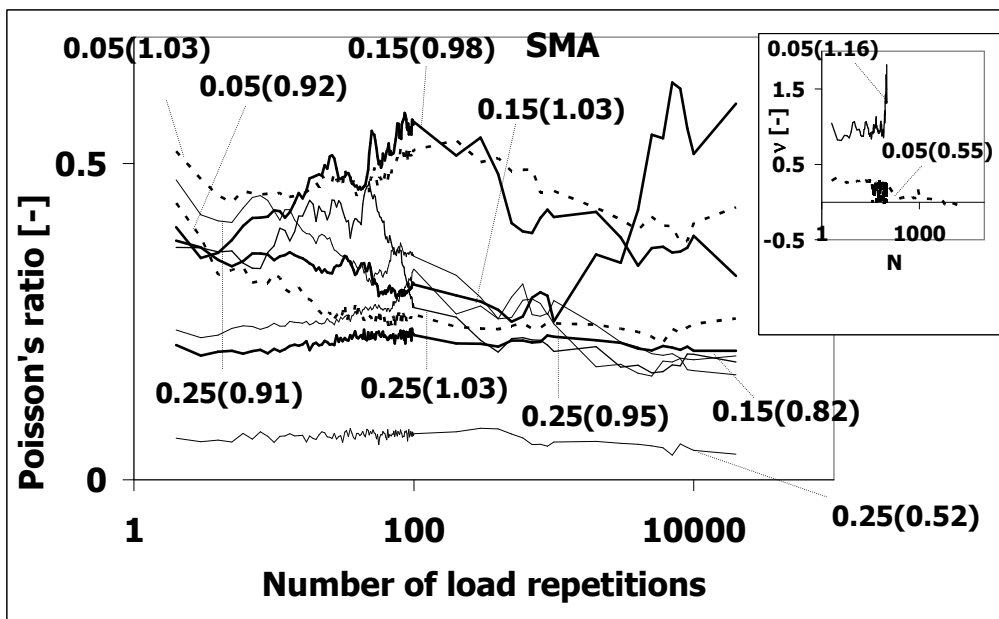


Figure 4.35 Poisson's ratios for SMA aggregate skeleton

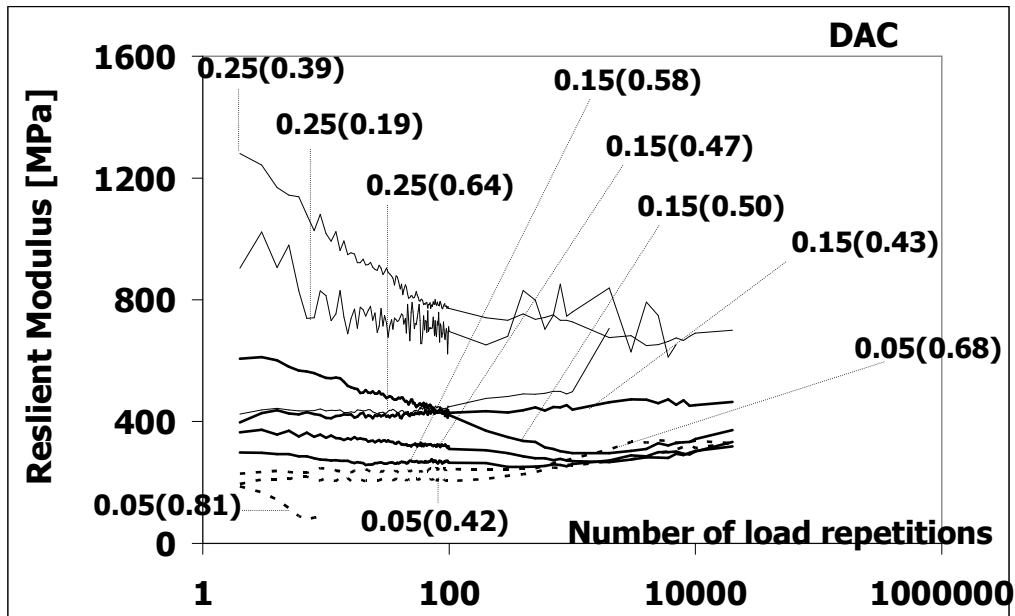


Figure 4.36 Resilient modulus values for DAC aggregate skeleton

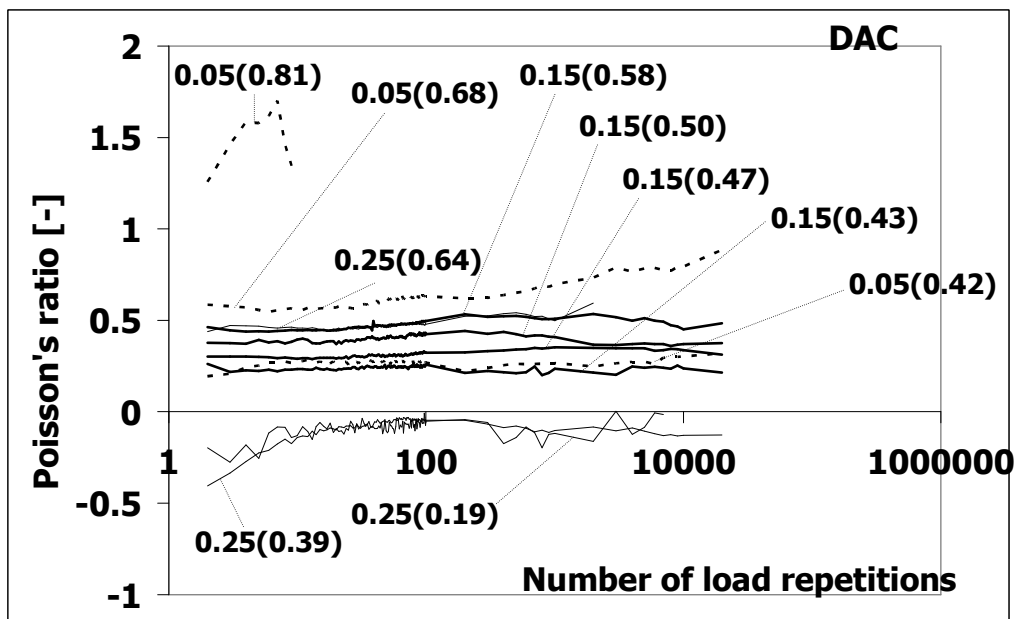


Figure 4.37 Poisson's ratios for DAC aggregate skeleton

Table 4.12 shows a summary of the cyclic confinement PD tests. The table also shows the final axial and radial permanent strain, maximum number of load repetitions and stress ratio. The table also shows the average resilient modulus and average Poisson's ratio that were determined from the 50th to 100th load repetitions in the PD test results. Due to some anomalies, the determination of the resilient modulus and Poisson's ratio was not possible in some tests. The tests in which the anomalies were detected are shown in a different shade in the table. The anomalies detected in the test data are also outlined in Table 4.13.

Table 4.12 Summary of the cyclic confinement PD tests

skeleton	test	confinement level, σ_3 [MPa]	Final $\epsilon_{ax, perm}$ [%]	Final $\epsilon_{rad, perm}$ [%]	N_{max}	σ_1/f_{ca}	Average M_r [MPa]	Average ν
PAC	PDV50A	0.049	0.1	-0.03	20000	0.620	874	0.59
	PDV50A1	0.049	0.6	-0.5	20000	0.823	254	0.59
	PDV50B	0.048	3.8	-4.1	300	1.063	162	0.57
	PDV150A	0.148	0.4	0.0	20000	0.600	473	0.09
	PDV150B	0.149	3.0	-2.8	20000	0.971	288	0.46
	PDV150D	0.149	5.8	-3.7	20000	1.034	426	0.49
	PDV250A1	0.247	0.9	-0.01	20000	0.630	641	0.91
	PDV250B	0.247	2.3	-1.6	20000	0.828	382	0.38
	PDV250D	0.247	6.2	-4.3	20000	1.008	258	0.20
SMA	SDV50A	0.049	0.1	0.001	20000	0.549	581	-
	SDV50B	0.049	0.1	0.1	20000	0.922	289	0.26
	SDV50D	0.049	0.4	-0.7	20000	1.027	348	0.50
	SDV50D1	0.048	7.6	-10.8	200	1.159	-	-
	SDV150B	0.149	0.3	-0.1	20000	0.818	662	0.23
	SDV150D	0.148	3.3	-4.0	20000	0.979	469	0.54
	SDV150D1	0.148	7.0	-6.9	20000	1.029	404	0.30
	SDV250A	0.246	0.1	0.01	20000	0.517	713	0.07
	SDV250C	0.247	3.7	-3.3	20000	0.911	711	0.35
	SDV250D	0.247	2.4	-2.4	20000	0.947	680	0.29
	SDV250D1	0.247	6.6	-4.7	20000	1.027	631	0.36
DAC	DDV50A	0.049	0.4	-0.1	20000	0.424	209	0.27
	DDV50C	0.049	1.4	-1.1	20000	0.682	243	0.62
	DDV50C1	0.050	10.4	-8.9	10	0.808	-	-
	DDV150A1	0.148	0.6	-0.1	20000	0.432	430	0.25
	DDV150AB	0.149	7.4	-2.9	20000	0.469	322	0.31
	DDV150A2	0.148	9.5	-4.9	20000	0.504	441	0.42
	DDV150B	0.149	8.1	-3.3	20000	0.584	268	0.48
	DDV250A0	0.246	0.2	0.0	10000	0.190	709	-
	DDV250A	0.246	5.1	-2.5	20000	0.391	789	-
	DDV250D	0.247	9.3	-5.2	3000	0.640	443	0.48

Table 4.13 Test Anomalies

Skeleton	Label	Test code	Property excluded	Observation	Cause
SMA	0.05(0.55)	SDV50A	Poisson's ratio	High fluctuation Poisson's ratio in the first 100 load repetitions	Low resilient deformation. Radial resilient fluctuates from in the direction of radial permanent deformation and in the opposite direction
	0.05(1.16)	SDV50D1	Poisson's ratio and Resilient modulus	High fluctuations in both resilient modulus and high Poisson's ratios	Rapid permanent deformation accompanied by high resilient deformation
DAC	0.05(0.81)	DDV50C1	Poisson's ratio and Resilient modulus	High fluctuations in both resilient modulus and high Poisson's ratios	Rapid permanent deformation accompanied by high resilient deformation
	0.25(0.19)	DDV250A0	Poisson's ratio	Negative Poisson's ratios	Low resilient deformation. Specimen contracted in the radial direction leading to negative Poisson's ratios.
	0.25(0.39)	DDV250A	Poisson's ratio	Negative Poisson's ratios	Permanent radial deformation expands but direction of radial resilient deformation opposite to radial permanent deformation.

4.7.3.2 Modelling of Permanent Deformation

The permanent deformation behaviour measured in the cyclic confinement tests was characterized by means of the permanent deformation model shown in Equation 4.21. This equation was first proposed by the Belgian Road Research Centre (Verstraeten et al. 1977) for asphalt mixtures. The Belgian model consists of one part that describes low and moderate deformation and another part that describes severe permanent deformation. In the first part of the model, the low and moderate permanent deformation is described by parameters A and B . In the second part of the model, C activates parameter D to describe severe deformation. In this research, parameter C was considered to take a value of 1 if the ratio of the vertical stress to the maximum stress determined from the monotonic failure tests exceeded a certain limiting ratio. In asphalt mixtures, the model parameters A , B and D are thought to be dictated by test conditions such as stresses and material properties such as elastic modulus and Poisson's ratios.

$$\varepsilon_p = AN^B + C \left(e^{\frac{DN}{1000}} - 1 \right) \quad \& \quad C = \begin{cases} 1 & \text{for } \frac{\sigma_l}{f_{ca}} \geq \text{limiting } \frac{\sigma_l}{f_{ca}} \\ 0 & \text{for } \frac{\sigma_l}{f_{ca}} < \text{limiting } \frac{\sigma_l}{f_{ca}} \end{cases} \quad 4.21$$

Where:

ε	=	axial or radial permanent deformation [%],
N	=	number of load repetitions [-],
σ_l	=	vertical stress in the permanent deformation test,
f_{ca}	=	maximum stress determined from the DCMCC tests.

The determination of the relationship between the model parameters and the test conditions or material properties was done in two phases. In the first phase, the values of parameters A and B were fitted on the axial deformation test results after which the trends with respect to test condition or material property were observed. The second phase involved the modelling of the parameters in relation to the observed trends.

Phase 1

In the first phase, parameter A and B were fitted on the tests exhibiting low to moderate axial permanent deformation. During this phase, the excel solver was allowed to obtain the parameters A and B in a logical sequence such that the parameters increased or remained constant with increase in the vertical stress. Parameters A and B were determined by minimizing the absolute error calculated from Equation 4.22. The trends in these parameters were then observed in relation to test condition and material property. The test conditions included vertical stress, confinement and the maximum stress determined from the DCMCC tests. The material properties consisted of the average Poisson's ratio and the average resilient modulus determined from the permanent deformation tests.

$$\text{total absolute error} = \sum \left(100 \left[\frac{|data - model|}{data} \right] \right) \quad 4.22$$

Parameter A was observed to follow logical trends with respect to two parameters. The two parameters consisted of the ratio of applied vertical stress to the vertical

stress at failure determined from the DCMCC tests and the ratio of the deviator stress to the resilient modulus. Logical trends for parameter A were observed in relation to stress ratio and the confinement for the three mixtures. However, only SMA exhibited logical trend between parameter A and the ratio of the deviator stress to the average resilient modulus. No logical trends were observed for parameter B in connection with either the test conditions or the material properties.

Figure 4.38, Figure 4.39 and Figure 4.40 show the trends for parameter A with respect to the two ratios for the PAC, SMA and DAC aggregate skeletons respectively. The term σ_3 in these tables denotes the confinement in MPa.

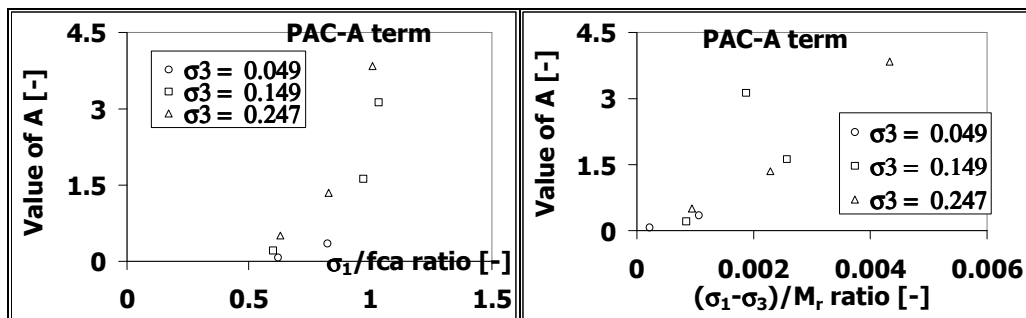


Figure 4.38 Parameter A trends with respect to the stress ratio and the ratio of the deviator stress to resilient modulus for PAC aggregate skeleton tests exhibiting low to moderate axial permanent deformation strain

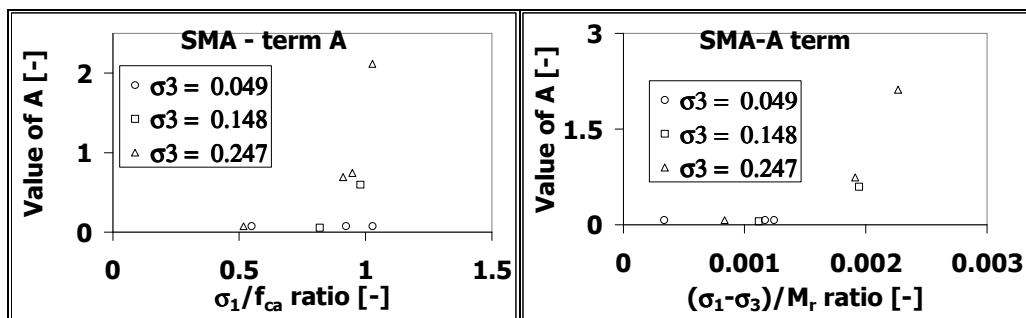


Figure 4.39 Parameter A trends with respect to the stress ratio and the ratio of the deviator stress to resilient modulus for SMA aggregate skeleton tests exhibiting low to moderate axial permanent deformation strain

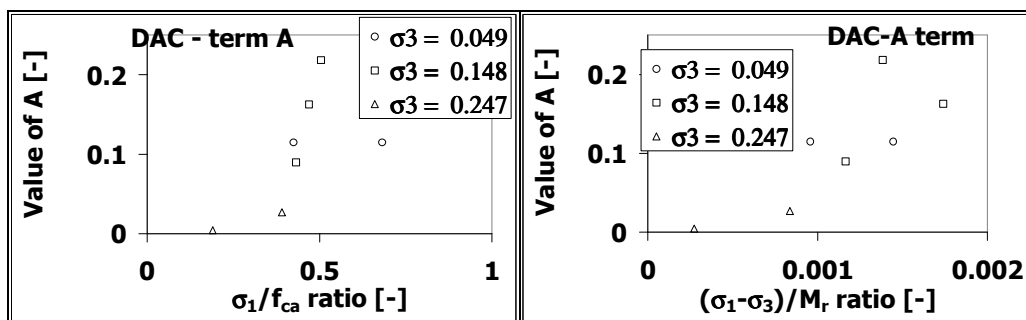


Figure 4.40 Parameter A trends with respect to the stress ratio and the ratio of the deviator stress to resilient modulus for DAC aggregate skeleton tests exhibiting low to moderate axial permanent deformation strain

A closer examination of these figures reveals that parameter A tends to some minimum value at low stress ratios and especially so for the SMA (Figure 4.39). The figures also show that the trend exhibited by term A can be described by an exponential function. Although term A can be described by an exponential function, the first part of the permanent deformation model cannot describe severe deformation that may occur after some load repetitions or at initiation of the test. This suggests the need for a certain limit for A prior to the activation of the second part of the model. At this limit, the permanent deformation is a function of both parts of the model for tests in which severe deformation occurs after a certain number of load repetitions. Beyond this limit, most of the permanent deformation may be described using the second exponential part of the model.

Phase 2

Owing to the observed dependency on the stress ratio and the level of confinement, parameter A was modelled in relation to these parameters. Apart from the stress level and confinement, a theoretical lower and an upper limit were incorporated to describe the minimum and maximum values of parameter A. In order to combine the effect of the stress ratio and confinement in an exponential function with a minimum and a maximum, parameter A was modelled by the Unified Model (Medani et al 2004) shown in Equation 4.23. Although no logical trends were observed for parameter B in relation to either the stress conditions or the material properties, the same format of the Unified Model was applied in its modelling.

$$P = P_{high} + (P_{low} - P_{high})S \quad 4.23$$

Where:

P = parameter A or B in the permanent deformation model

$$S = e^{(-[u\beta]^{k_5})} \quad 4.24$$

$$u = \left(\frac{k_1 \sigma_3}{1 + k_1 \sigma_3} \right)^{k_2} \quad 4.25$$

$$\beta = \left(k_3 \left(\frac{\sigma_1}{f_{ca}} \right) \right)^{k_4} \quad 4.26$$

Table 4.14 shows the regressions coefficients determined for the permanent deformation model. Figure 4.41 to Figure 4.43 show an illustration of model fit on the measured axial and radial permanent deformation for the PAC, SMA and DAC aggregate skeletons at different confinement levels and at various stress ratios. The figures show that the model fitted reasonably well on the measured data.

Table 4.14 Permanent deformation regression coefficients

skeleton	coefficients	axial			radial		
		A	B	D	A	B	D
PAC	k_1	6.697	1.420	1	0.001	1	1
	k_2	0.514	21.846	0	21.257	0	0
	k_3	0.842	8.304	1	2.323	10	1
	k_4	1.973	18.278	0	174.872	10	0
	k_5	3.084	33.781	0	0.039	0.743	0
	P_{max}	13.544	0.112	5.764	11.866	0.030	6.524
	P_{min}	0.143	0.065	0	0	0	0.390
	limiting σ_1/f_{ca}	1.063					
SMA	k_1	9430.458	1	1	85521.282	1	1
	k_2	100.080	0	0	43446.290	0	0
	k_3	1.051	10	0.966	1.078	10	0.965
	k_4	0.797	10	400	76.611	10	400.051
	k_5	22.656	1	2	0.734	1	1.836
	P_{max}	2.507	0.125	6.993	1.980	0.092	11.000
	P_{min}	0.037	0	0.007	0	0	0.001
	limiting σ_1/f_{ca}	1.02914					
DAC	k_1	3.252	1	1.579	1.155	1	1.579
	k_2	76.253	0	22.466	56.663	0	22.466
	k_3	3.777	10	1.673	4.590	10	1.673
	k_4	150.287	10	289.839	140.987	10	289.839
	k_5	0.233	1	0.693	0.272	1	0.693
	P_{max}	0.162	0.433	232.533	0.214	0.327	232.533
	P_{min}	0.004	0	0	0	0	0
	limiting σ_1/f_{ca}	0.640					

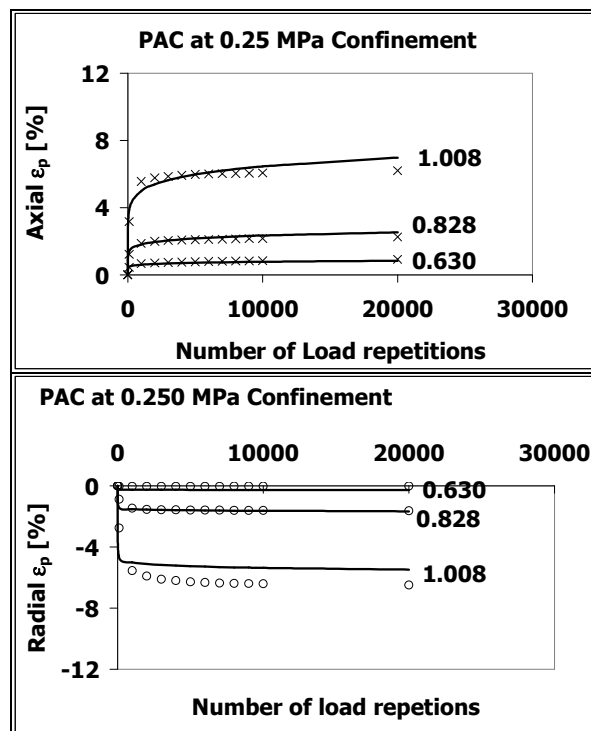


Figure 4.41 Model fit of the measured axial and radial permanent deformation for PAC aggregate skeleton at confinement levels of 0.25MPa

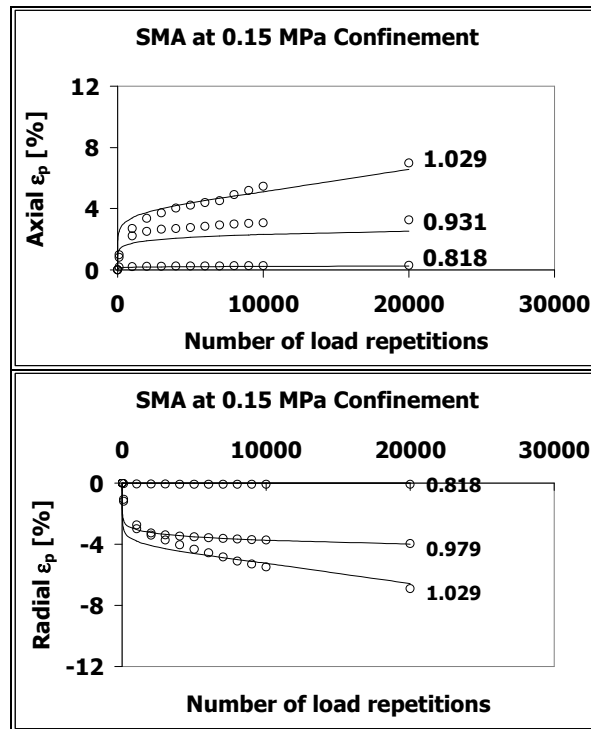


Figure 4.42 Model fit on the measured axial and radial permanent deformation for SMA aggregate skeleton at confinement levels 0.15 MPa

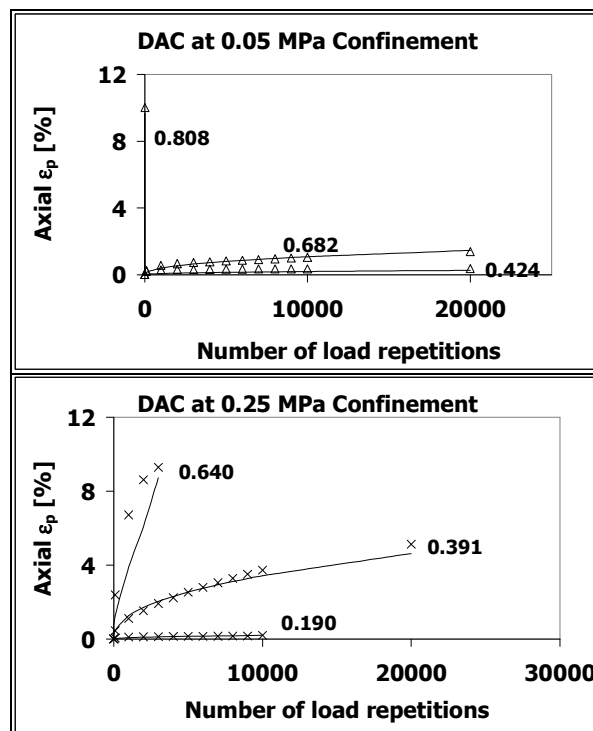


Figure 4.43 Model fit on the measured axial permanent deformation for DAC aggregate skeleton at confinement levels 0.05 and 0.25 MPa

Apart from demonstrating the reasonable data fit, Figure 4.43 also shows that the permanent deformation is higher at high confinement in comparison to the permanent deformation at similar stress ratios at lower confinement. This can be

explained by defining a relationship between the confinement and the vertical stress in such a way that the permanent deformation remains constant irrespective of the confinement. For example consider the following hypothesis:

1. The relationship between the confinement and the maximum stress at failure from the PAC DCMCC tests is given by Equation 4.27.

$$f_{ca} = a\sigma_3^b \quad 4.27$$

2. Assume a relationship 1 that relates the vertical stress to the confinement using the same format as f_{ca} and results in the same magnitude of permanent deformation for all confinement stresses as shown in Table 4.15.
3. Assume another relationship 2 that relates the vertical stress to the confinement using the same format as f_{ca} and also results in the same magnitude of permanent deformation for all the confinement stresses as shown in Table 4.15.

Table 4.15 PAC DCMCC failure stress and hypothetical relationships 1 and 2

relationship	a_f	b_f
f_{ca}	3.99307	0.77285
1	3.99307	1.1
2	2	0.6

Figure 4.44 shows a comparison of the stress ratios of the vertical stress to confining stress (σ_1/σ_3) and the vertical stress to the failure stress (σ_1/f_{ca}). The figure demonstrates that the permanent deformation can be higher or lower at high confinement in comparison to the permanent deformation at similar stress ratios depending on the nature of the relationship defining points of the same permanent deformation.

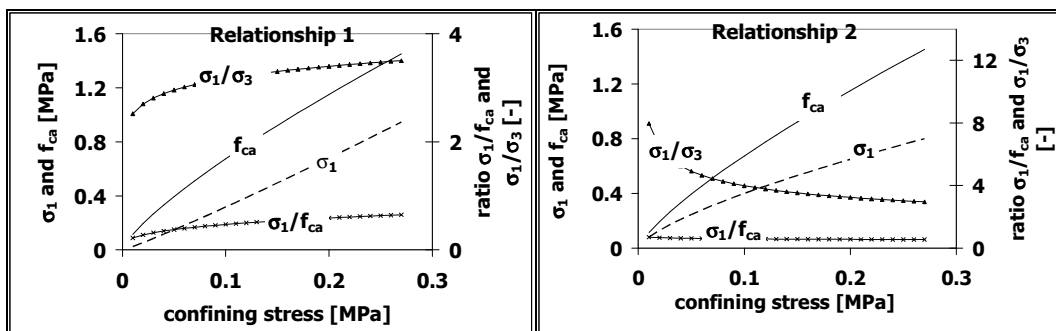


Figure 4.44 Stress ratios based on the two hypothetical relationships

4.7.3.3 Modelling of the Average Resilient Modulus and Poisson's Ratios

Logical trends were observed for the average resilient moduli of all the mixtures and the average Poisson's ratios of DAC with respect to the vertical to confinement stress ratio. Because the observed trends suggested the need for a sigmoidal function, the Unified Model format shown in Equation 4.28 and Equation 4.29 was used to model the moduli and the DAC Poisson's ratios respectively. The format of maximum limiting value shown in Equation 4.28 and 4.33 was introduced to cater for the dependency of the maximum resilient modulus of the DAC aggregate skeleton on the level of confinement. This

dependency is activated by the k_2 coefficient in Equation 4.33. In case of no dependency this coefficient takes a value of 0. No logical trends could be observed for the average Poisson's ratios of the PAC and SMA aggregate skeletons. Consequently a constant value was used to model the average Poisson's ratios of the PAC and SMA aggregate skeletons.

$$P = P_{high,\sigma_3} + (P_{low} - P_{high,\sigma_3})S \text{ for } M_r \quad 4.28$$

$$P = P_{high} + (P_{low} - P_{high})S \text{ for DAC } \nu \quad 4.29$$

Where:

$$S = e^{(-[\beta]^\lambda)} \quad 4.30$$

$$\beta = k_1 \left(\frac{\sigma_3}{\sigma_1} \right) \text{ for } M_r \quad 4.31$$

$$\beta = k_1 \left(\frac{\sigma_1}{\sigma_3} \right) \text{ for DAC } \nu \quad 4.32$$

$$P_{high,\sigma_3} = P_{high} \left(\frac{\sigma_3}{1 + \sigma_3} \right)^{k_2} \text{ for } M_r \quad 4.33$$

P	=	Value of property P ,
P_{high}	=	maximum theoretical limit for property P ,
P_{high,σ_3}	=	confinement dependent maximum theoretical limit for property P ,
P_{low}	=	minimum theoretical limit for property P ,
M_r	=	average resilient modulus,
ν	=	average Poisson's ratio,
σ_3	=	confinement [MPa],
σ_1	=	vertical stress [MPa],
λ	=	model parameter [-],
P_{high}	=	maximum theoretical limit for property P ,
k_1, k_2	=	model parameter.

Table 4.16 Regression coefficients for the Unified Model parameters and constant value

skeleton	property	symbol	Unified model parameter					Constant value
			λ	k_1	k_2	P_{low}	P_{high}	
PAC	Resilient modulus [MPa]	M_r	1.373	1.000	0	0	3246	-
	Poisson's ratio [-]	ν	-	-	-	-	-	0.49
SMA	Resilient modulus [MPa]	M_r	15.766	6.795	0	346	689	-
	Poisson's ratio [-]	ν	-	-	-	-	-	0.30
DAC	Resilient modulus [MPa]	M_r	2.697	4.831	0.575	99	1801	-
	Poisson's ratio [-]	ν	3.342	0.186	-	0	0.63	-

Table 4.16 shows the regression coefficients for the Unified Model parameters and the constant value. Figure 4.45⁶ shows the model fit on the average resilient modulus and Poisson's ratios for the three aggregate skeletons. The figure shows that the models fitted the data reasonably well.

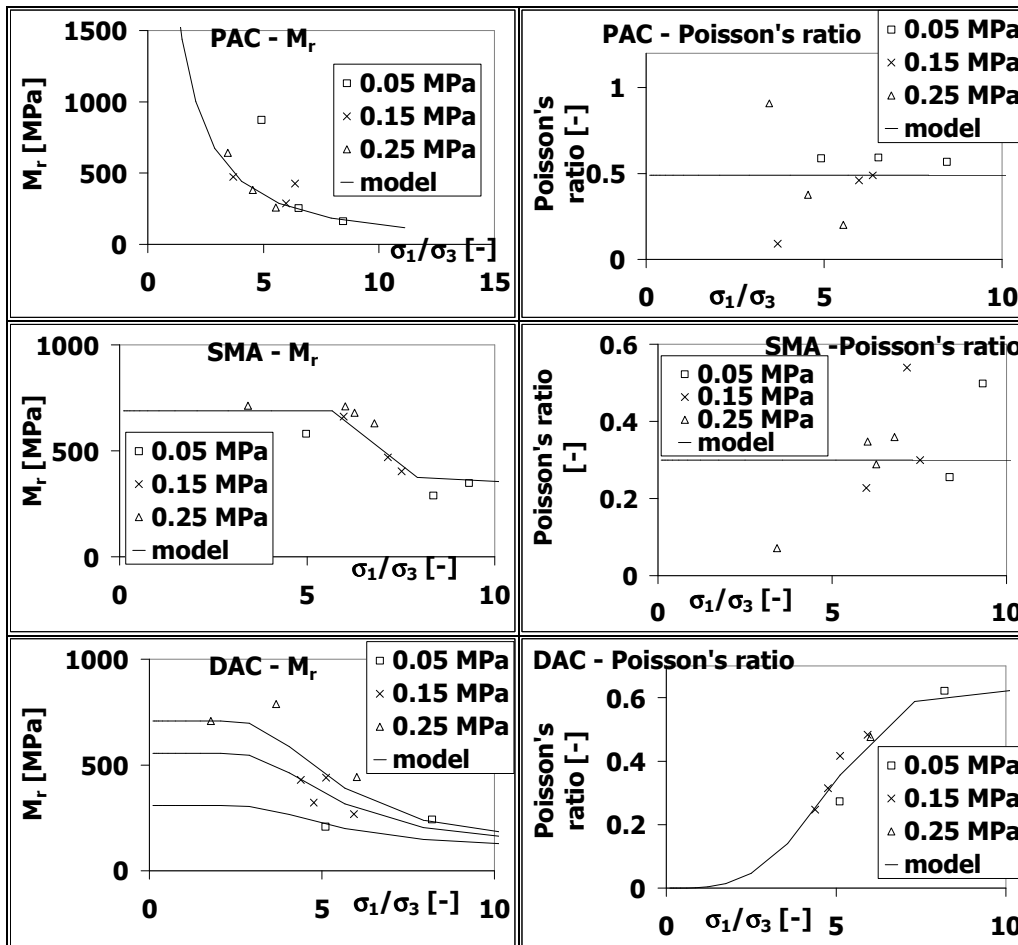


Figure 4.45 Model fit on the average resilient modulus and average Poisson's ratios for the three aggregate skeletons (numbers in the labels denote the confinement)

For purposes of comparing the permanent deformation behaviour of the three aggregate skeletons, the stress combinations leading to about 10 and 1% axial permanent deformation after 20,000 load repetitions were determined using the permanent deformation model. Figure 4.46 shows these stress combinations presented in the SQRT J_2 - I_1 space. The figure shows that the stone skeleton mixtures i.e. SMA and PAC are more resistant to permanent deformation in comparison to the DAC skeleton and that the skeletons can be ranked in order of decreasing resistance to permanent deformation as SMA, PAC followed by DAC. The figure also shows that the permanent deformation behaviour of the SMA and DAC skeletons is much more sensitive to stress conditions in comparison to the PAC skeleton. The permanent deformation in SMA and DAC skeletons occur

⁶ The reader should note that the upper part of the sigmoidal curve of the PAC M_r (3246 MPa) is beyond the plot shown in the figure. The reader should also note that the sigmoidal curves are plotted using a series of straight lines. Thus the plot for SMA M_r does not appear as a smooth sigmoidal curve.

within a narrow stress band in comparison to the stress band in PAC. This implies that special attention is required in the design of SMA and DAC mixtures.

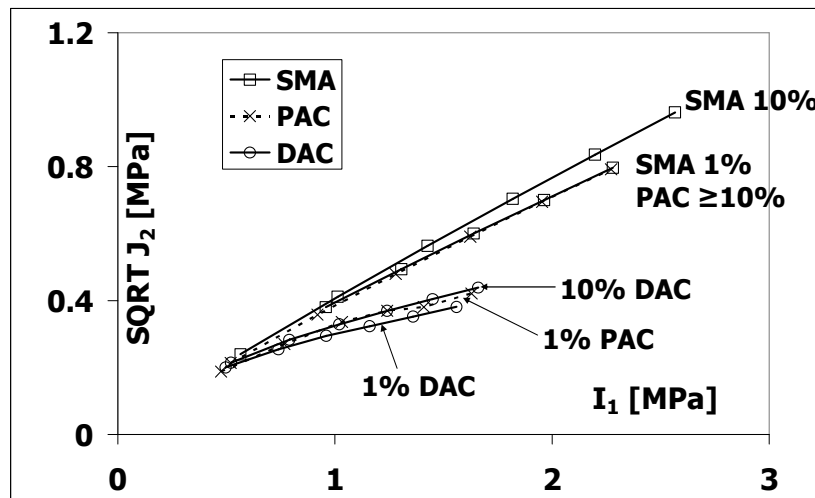


Figure 4.46 Stress combinations leading to ≥ 10 and 1% axial permanent deformation in PAC, SMA and DAC aggregate skeletons

Figure 4.47 shows a comparison of the maximum stress at failure in the DCMCC tests and the stress combinations leading to 10% axial permanent deformation in PAC, SMA and DAC aggregate skeletons. The figure shows that severe permanent deformation in the PAC and SMA stone skeletons takes place at stress conditions close to the maximum stress and that severe permanent deformation in the fine DAC skeleton occurs at lower stress combinations in comparison to the maximum stresses. This difference can be attributed to the better post-peak stability exhibited by the PAC and SMA stone skeletons (see paragraph 4.6.1) in comparison to the DAC aggregate skeleton. The figure also shows that the maximum stress in DCMCC tests is a good indicator of stress conditions leading to severe permanent deformation in PAC and the SMA stone skeletons but a poor indicator for severe stress conditions in the DAC aggregate skeleton.

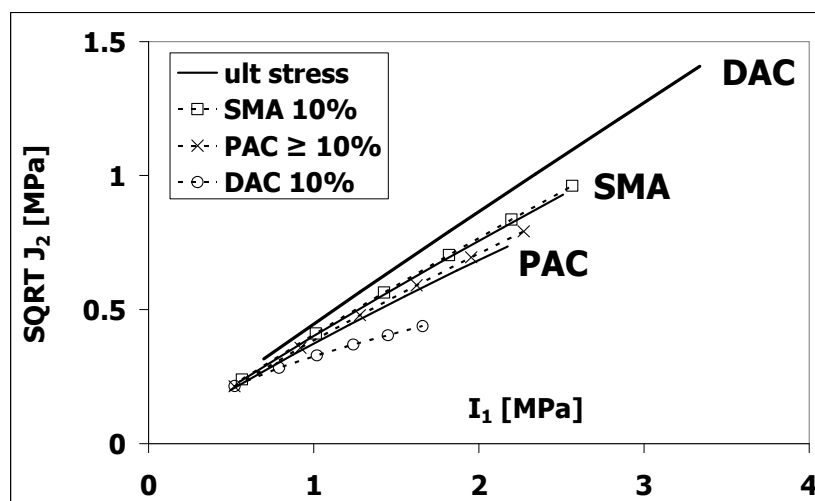


Figure 4.47: Ultimate stress at failure in DCMCC tests and stress combinations leading to $\geq 10\%$ axial permanent deformation in PAC, SMA and DAC aggregate skeletons

4.8 Conclusions

The Desai plasticity model was applied to the three aggregate skeletons based on the DCMCC tests and the Unified Model. In addition, the permanent deformation behaviour was described using the Belgian and Unified Model. The following conclusions were reached based on this characterisation of the failure and permanent deformation behaviour:

- In the presence of confinement the PAC and SMA aggregate skeletons retain considerable post-peak stability even at such high axial strains as 5%.
- The aggregate skeletons exhibit only a slight amount of compaction and dilation is the main mode of deformation.
- The vertical stress at failure in the DCMCC tests performed on the DAC aggregate skeleton is higher in comparison to the SMA and the PAC aggregate skeletons. The three aggregate skeletons can be ranked in order of decreasing ultimate vertical stress as DAC, SMA followed by PAC.
- In the triaxial test, the permanent deformation of the aggregate skeleton under cyclic confinement is higher than the permanent deformation under constant confinement of similar magnitude.
- The permanent deformation behaviour of SMA and DAC aggregate skeletons is much more sensitive to stress conditions in comparison to the permanent deformation behaviour of PAC aggregate skeleton.
- SMA and PAC stone aggregate skeletons are more resistant to permanent deformation in comparison to the DAC aggregate skeleton and the three skeletons can be ranked in order of decreasing resistance to permanent deformation as SMA, PAC followed by DAC.
- Severe permanent deformation in the PAC and SMA stone skeletons takes place at stress conditions close to the DCMCC maximum stress while severe permanent deformation in the DAC skeleton occurs at much lower stress combinations in comparison to the DCMCC maximum stress at failure. This difference can be attributed to the better post-peak stability exhibited by the aggregate stone skeletons.
- The ultimate surface based on the constant confinement monotonic failure tests is a good indicator of stress conditions leading to severe permanent deformation for the stone skeleton mixtures such as PAC and SMA but a poor indicator for severe stress conditions for DAC aggregate skeleton.

4.9 References

- Antes P.W., (2002), *Research into Stress Dependent Behavior of STAC and PAC (in Dutch)*, Master of Science Thesis, TU Delft, the Netherlands.
- Awad I.S., (1972), *Characterisation of the Stress-Strain Relationships of Asphalt Treated Base Material*, Graduate Report, University of Washington.
- Brown S.F., (1975), *Improved Framework for Predicting Permanent Deformation in Asphalt Layers*. Transportation Research Record No. 537, Washington DC, United States of America.
- Brown, S.F. and Bell, C.A., (1977), *The Validity of Design Procedures for the Permanent Deformation of Asphalt Mixes*, Proceedings of the fourth International Conference on Structural Design of Asphalt Pavements, vol. 1, Michigan, United States of America.

- Brown S.F. and Snaith M.S., (1974), *The Permanent Deformation of Dense Bitumen Macadam Subjected to Repeated Loading*, Proceedings of the Association of Asphalt Paving Technologists Technical Sessions, pp. 224-252, vol. 43, Virginia, United States of America.
- Medani, T.O., Molenaar, A.A.A. and Hurman, M., (2004), *A single Model to Describe Several Properties of Bituminous Mixes*, 5th International PhD Symposium in Civil Engineering, pp.1411-1418, vol 2, Delft, The Netherlands.
- Morris J., (1973), *The Prediction of Permanent Deformation in Asphalt Concrete Pavements*. Ph.D. Thesis, University of Waterloo, Ontario, Canada.
- Muraya, P.M., Molenaar, A.A.A. and Dommelen, A.E. van., (2003), *Visco-elastic Analyses of Test Pavements from LINTRACK ALT Rutting Research*. Proceedings of 3rd International Symposium on Maintenance and Rehabilitation of Pavements and Technological Control, Guimarães, Portugal.
- Muraya P.M., Molenaar A.A.A. and van de Ven M.F.C., (2004), *Permanent deformation behavior in asphalt mixes*, 5th International PhD Symposium in Civil Engineering, pp. 765-772, vol 2, Delft, The Netherlands.
- Parajuli U., (2002), *Stress Dependent Analysis of Asphalt Concrete*. Master of Science Thesis, TU Delft/IHE Delft, the Netherlands.
- Pellinen T.K. and Witczak M.W., (2002), *Stress Dependent Master Curve Construction for Dynamic (Complex) Modulus*, Proceedings of the Association of Asphalt Paving Technologists Technical Sessions, vol. 71, CD-ROM.
- Scarpas, A., (2005), *International Course on Application of FE and Constitutive Models in Geotechnical Engineering*, Torino, Italy.
- Van Nierkerk A.A., (2002), *Mechanical Behavior and Performance of Granular Bases and Sub-bases in Pavements*, PhD Dissertation, Delft University of Technology, Delft, The Netherlands.
- Verstraeten J., Romain J.E. and Veverka V., (1977). *The Belgian Road Research Center's Overall Approach to Asphalt Pavements Structural Design*, Proceedings of the fourth International Conference Structural Design of Asphalt Pavements, Michigan, United States of America.

5 Total Asphalt Mixture

It is incredible what organised team work can accomplish within time constraints.

5.1 Introduction

This chapter presents the characterization of the total asphalt mixture. The characterization involved extensive laboratory tests performed in relation to the failure behaviour of the asphalt mixtures. Prior to laboratory testing, a specimen preparation procedure was developed for the purposes of fabricating specimens with reasonable compaction homogeneity over both the height and the width. Apart from compaction homogeneity, the other aim of the specimen preparation procedure was to compact the test specimen to a similar density level as determined in the Marshall mixture design. The Marshall density was taken as a reference density. It should be noted that the reference Marshall density is determined from cold specimens. As it will be shown later, the density of the specimens when hot is different from the density of the specimens when cold. The term hot density will be used to indicate the density of the specimen when hot.

The properties of asphalt mixtures are strongly influenced by temperature, loading time and stress conditions. However, it is not practical to perform tests over the entire range of stresses, temperature and loading time in order to determine the dependency on these factors. Mixture properties covering an entire temperature and loading time domain can be obtained using the equivalency principle between loading time and temperature (Molenaar 1993).

The equivalency principle employs shift factors to relate the loading time at a reference temperature to the loading times at other temperatures. The shift factor is described as a function of a temperature susceptibility factor and temperature. In relationships such as the Arrhenius formula, temperature susceptibility is expressed in terms of a temperature susceptibility factor and temperature as shown in Equation 5.1 (Verstraeten 1972). In other relationships such as the Unified Model (Medani 2006), temperature susceptibility is also expressed in terms of a temperature susceptibility factor and temperature but in a different format as shown in Equation 5.2. In literature (Verstraeten 1972), it has been suggested that the temperature susceptibility factor is approximately the same for different types of asphalt mixtures. However, later research has shown that this is not the case. The temperature susceptibility factor is mixture dependent. In his literature review, Groenendijk (1998) found different values of temperature susceptibility factor in studies conducted by other researchers. He found that Francken and Clauwaert (1987) reported a value of 10920 while the study conducted by Lytton et al (1993) resulted in a value of 13060 and the study performed by Jacobs (1995) resulted in a value of 7680. If the temperature susceptibility factor is assumed to be constant irrespective of the type of tests, then the temperature susceptibility determined from tests that are relatively easier to perform can be used in the characterization of properties determined from other tests that are more difficult to conduct.

$$\beta = e^{\left(C \left[\frac{1}{T} - \frac{1}{T_0} \right] \right)} \quad 5.1$$

$$\beta = e^{(-\tau_s [T - T_0])} \quad 5.2$$

Where:

β	=	shift factor,
C, T_s	=	temperature susceptibility factor,
T_0	=	a reference temperature,
T	=	temperature.

A large amount of testing is needed in order to characterize the tensile and the compressive strength of all three mixtures as a function of temperature and loading rate. The amount of tests was significantly reduced by the application of an experimental design in combination with the Unified Model. The approach consisted of two steps. In the first step, the resilient modulus indirect tension test (RMIT), which is relatively easy to conduct, was used to determine the temperature susceptibility of the three asphalt mixtures with regard to stiffness. In the second step, an experimental design technique on the displacement controlled monotonic compression (DCMC) and displacement controlled monotonic tension tests (DCMT) was implemented for the asphalt mixtures. This approach is fully described by Medani (Medani 2006).

The experimental design technique was based on the two-factor central composite design (Robinson 2000) shown in Figure 5.1. The advantage of such an experimental design lies in the fact that the properties and the data scatter in an entire temperature and loading time domain can be described with 13 tests. Such a dramatic reduction in the number of tests cannot be envisaged under traditional test practices that require at least 3 temperatures, 3 loading times with 3 test repetitions being conducted at each test condition making a total of at least 27 tests. This experimental design is presented in detail in section 5.4.1.

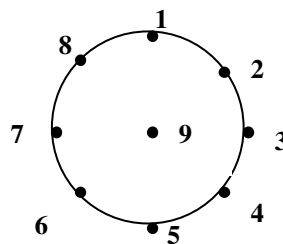


Figure 5.1 Central composite design

5.2 Specimen Preparation Procedure

5.2.1 Introduction

The purpose of the specimen preparation procedure was to set up a suitable laboratory specimen fabrication technique resulting in test specimens with reasonable compaction homogeneity over both the height and the width. Homogeneous specimens allow appropriate evaluation of the test results in order

to rank mixtures in relation to the test conditions without unwarranted effects that can occur as a result of non-homogeneous compaction. Unwarranted effects can occur if the influence of the compaction non-homogeneity on the test results is higher than the influence of the test conditions. Surface irregularities at the sides of the specimens may also lead to undesired effects during evaluation of test results. This is especially true if the evaluation involves different types of asphalt mixtures such as PAC, SMA and DAC. Because of the high content of coarse aggregates in PAC and SMA mixtures, the surface at the sides of the PAC and SMA specimens is more irregular than the surface of the DAC specimens. Effects of surface irregularities may be avoided by extracting test specimen from the inner part of the compacted specimen (Voskuilen and Ven van de, 2004).

Although several laboratory compaction procedures exist for asphalt mixtures, the use of these procedures in the production of specimens with homogeneous compaction densities is still debatable. Jönsson et al (2002) investigated different compaction methods using X-ray tomography. The compaction methods included Marshall, gyratory and rolling wheel compaction. Part of the study involved the investigation of the air-void distribution in specimens compacted to different compaction levels. The findings in this study suggested that none of the three compaction methods was able to produce homogeneously compacted asphalt specimens. However, the Marshall compaction method produced a more even air void distribution over the height and the width in comparison to the other methods.

The gyratory compactor was selected for specimen compaction on the basis of better automated compaction control relative to the Marshall and rolling wheel compaction methods, and reasonable specimen size for extraction of test specimens. Non-homogeneous compaction in gyratory compacted specimens has been reported in several studies. Studies performed by some researchers on air void distribution in gyratory compacted specimens indicate that the air void content is generally minimum at the middle of the specimen and maximum at the extremes of the vertical and lateral directions (Jönsson et al 2002, Masad et al 2002, Tashman et al 2001). However, high air void content in the middle part of the specimen and low air void content close to the top and bottom parts of the specimen has also been reported in literature (Tashman et al 2004). Because of this variation, extraction of test specimens from the inner part of gyratory compacted specimens is considered desirable for purposes of obtaining a uniformly compacted test specimen.

The compaction homogeneity within the gyratory compacted specimens in this study was investigated using coring methods and X-ray tomography analysis. The use of X-ray tomography analysis is currently being regarded as a viable non-destructive material characterisation technique and has been used extensively in the evaluation of air void distribution in asphalt mixtures (Jönsson et al 2002, Masad et al 2002, Tashman et al 2001).

In order to prepare homogeneous specimens with a reference density that met pavement specifications, the Marshall densities presented in Chapter 3 were used as reference densities for the gyratory compacted specimens.

5.2.2 Specimen Preparation

The composition of the asphalt mixtures was based on the Marshall Mix design presented in Chapter 3. The specimens were compacted using an IPC Servopac gyratory compactor. In this gyratory compactor, the vertical force is applied from the top of the specimen using a digital controlled actuator. A load cell is used to measure the vertical force and accurately set and maintain the vertical stress during compaction (Sinadinos, 1999).

The specimen preparation procedure was slightly different in comparison to other gyratory specimen preparation procedures. Prior to compaction, the top gyratory compacting disc was heated together with the aggregates. The aim of this deviation was to explore the possibility of decreasing the compaction variation due to temperature differences especially in the upper part of the specimens. After mixing, the mixed components were re-heated for half an hour at the mixing temperature to compensate for the fall in temperature during the mixing process. In accordance with the Dutch pavement specifications (CROW 2000), the mixing temperature for the PAC and DAC mixtures is equal to the bitumen EVT temperature and mixing temperature for the SMA mixture is 10⁰C higher than the bitumen EVT temperature. Ageing was not expected during the re-heating process. Ageing tests performed on pure bitumen prior to the preparation of mastic mixtures exhibited insignificant ageing (see section 6.2). After compaction, the PAC specimens were cooled for 2 hours in a cooling room at 14⁰C and the SMA and DAC specimens for 1.5 hours at the same temperature. These cooling times were sufficient to prevent distortion of the specimens during extraction from the mould and to ease the extraction process. Longer cooling times made extraction of the specimens from the mould extremely difficult. This observation is in contrast to the Dutch specifications (CROW 2000) for extraction of gyratory compacted specimens cooled at room temperature. The Dutch specifications stipulate that gyratory compacted specimens should be left to cool for at least 5 hours at room temperature prior to extraction or should be protected against water and cooled under running water for a period of 40-60 minutes before extraction.

The diameter of the compacted specimens was 150 mm with a height of 165 to 182 mm. The PAC and the DAC specimens were compacted at a constant vertical stress of 600 kPa and an external gyratory angle of 1⁰ while the SMA was compacted at a vertical stress of 600 kPa and an external gyratory angle of 1.25⁰. The gyratory angles were selected based on initial observations of some pilot specimens that were compacted to different number of gyrations using external gyratory angles of 1 and 1.25⁰ for the three asphalt mixtures (Table 5.1). Figure 5.2 shows a comparison between the reference Marshall density (cold) and the hot gyratory compaction densities of the pilot specimens. The hot density refers to the density of the specimen based on the dimensions of the hot specimen. This density was determined from the height of the hot specimen that was recorded during compaction and the weight of the specimen. As opposed to the PAC and DAC mixtures, that were relatively easier to compact implying that the Marshall densities would be achieved after a reasonable number of gyrations at an external gyratory angle of 1⁰, the SMA was more difficult to compact even at a gyratory angle of 1.25 degrees.

Table 5.1 Pilot specimens

Mixture	PAC			SMA			DAC					
Number of gyrations	30	50	70	30	30	50	70	30	30	50	70	
gyratory angle (degrees)	1			1.25			1.25			1		

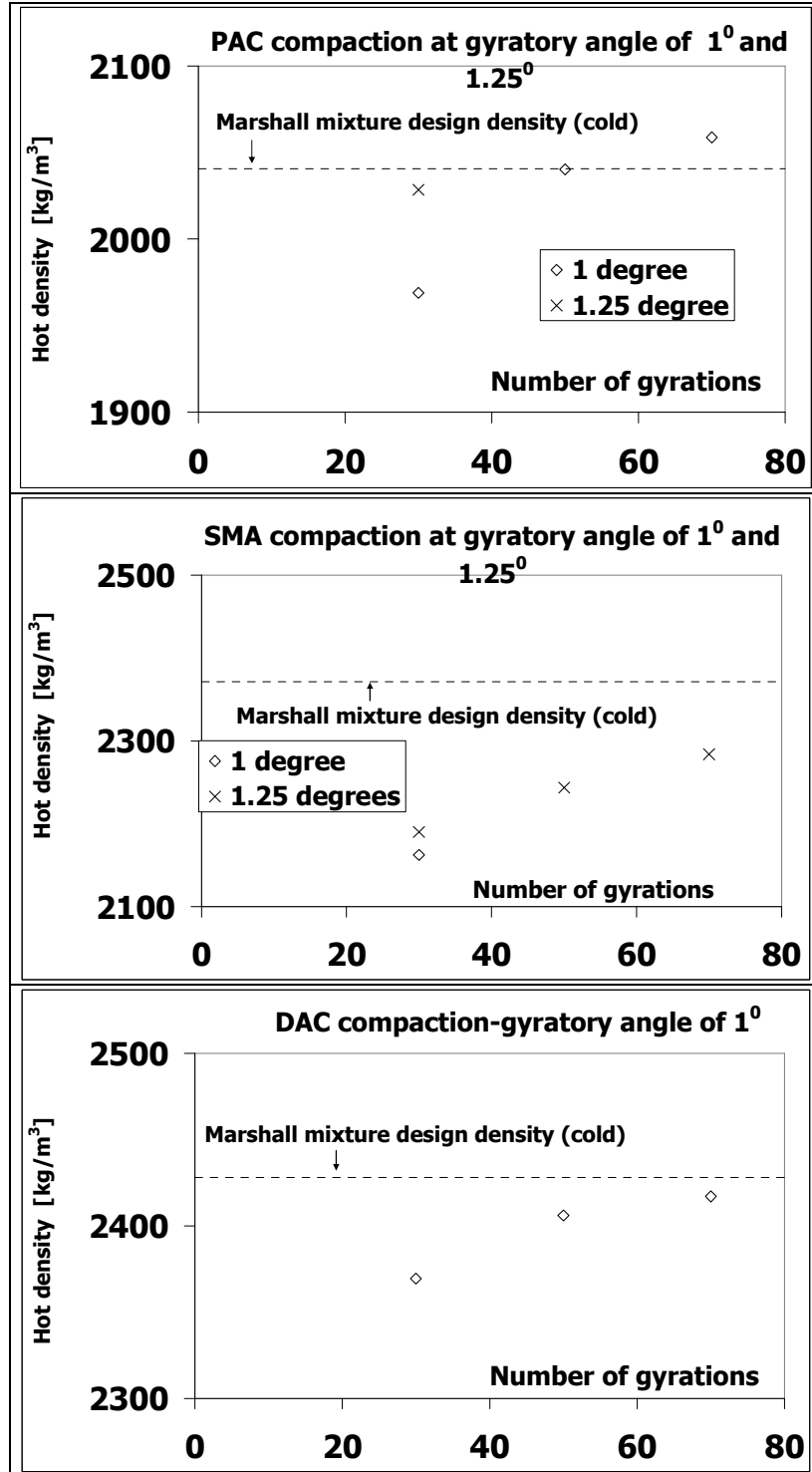


Figure 5.2 Comparison of hot density of gyration compacted specimens with Marshall density (cold)

5.2.3 Air-void Distribution

The air void distribution was determined using X-ray tomography and standard laboratory procedures. For each type of mixture three specimens were scanned. The X-ray tomography was performed on the pilot PAC and DAC specimens compacted at a gyratory angle of 1° and the pilot SMA specimens compacted at a gyratory angle of 1.25° . The standard laboratory procedures were performed on one specimen from each type of mixture. These included the PAC and DAC specimens compacted to 30 gyrations at a gyratory angle of 1° and the SMA specimen was compacted to 70 gyrations at a gyratory angle of 1.25° . The specimens were cored as shown in Figure 5.8.

The specimens considered for the standard laboratory procedures were selected based on the proximity of the hot gyratory compaction density to the reference Marshall density. PAC and DAC specimens compacted to 50 and 70 gyrations at a gyratory angle of 1° (refer to Figure 5.2) were not considered since their hot densities were too close to the reference Marshall density. The densities of specimens extracted from specimens with such densities that are too close to the reference Marshall density when hot may be higher than the reference Marshall density. A comparison of hot and cold densities presented later in this chapter showed that the specimen density increases on cooling. The SMA specimen compacted to 70 gyrations at a gyratory angle of 1.25° (refer to Figure 5.2) was considered to have the density closest to the reference Marshall density in comparison with the other SMA specimens.

5.2.4 X-ray Tomography Analysis

The x-ray tomography analysis was performed using the image-processing tool in the MATLAB computer package. Although MATLAB is not as user friendly as other image analysis packages such as AMIRA, MATLAB was chosen for this analysis because it offered better means of electronically “coring” and analysing the scanned specimens. The MATLAB code for this analysis can be found in Annex 3.

The resolution of the scanning equipment was 0.332 mm by 0.332 mm in the cross-section direction otherwise known as the pixel size, and 1 mm in the vertical (height) direction. The resolution in the vertical direction implied that the cross-section images for a given specimen were captured and stored at 1 mm intervals. The data stored for each vertical interval consists of one square slide written in the so-called DICOM format. Among other contents, the DICOM file consists of image intensity values for each pixel in a given square cross-section area.

In the initial step of the image processing, the slides were sorted out in order using the instance number field. This was followed by the removal of empty slides at the top and the bottom of the specimen after which the position of the centre of area of the specimen in a slide close to the top and in another slide close to the bottom was located. The purpose of locating these two positions was to enable the interpolation of the location of centre of area of the specimen in the other slides. As shown in Figure 5.3, the centre of area of the specimen in different slides was not the same.

The next step involved the determination of the intensity values for the aggregate/bitumen, (aggregate/cellulose, cellulose/bitumen for SMA specimen) and bitumen/air boundaries for each specimen. These boundaries were based on the actual volumetric composition of the specimens. The boundaries were located by means of trial and error in such a way that the aggregate, cellulose and bitumen volume determined in the analysis was similar to that in the actual specimens. Before the analysis of the air void content, the air in the square cross-section surrounding the circular specimen cross-section was segregated by setting these surrounding pixels to intensity values that were much higher than those in the specimen. The surrounding air was identified based on the specimen radius and the centre of area of the specimen in a given slide. Figure 5.3 and Figure 5.4 show an example of two slides in a porous asphalt specimen before and after the elimination of the air surrounding the specimen.

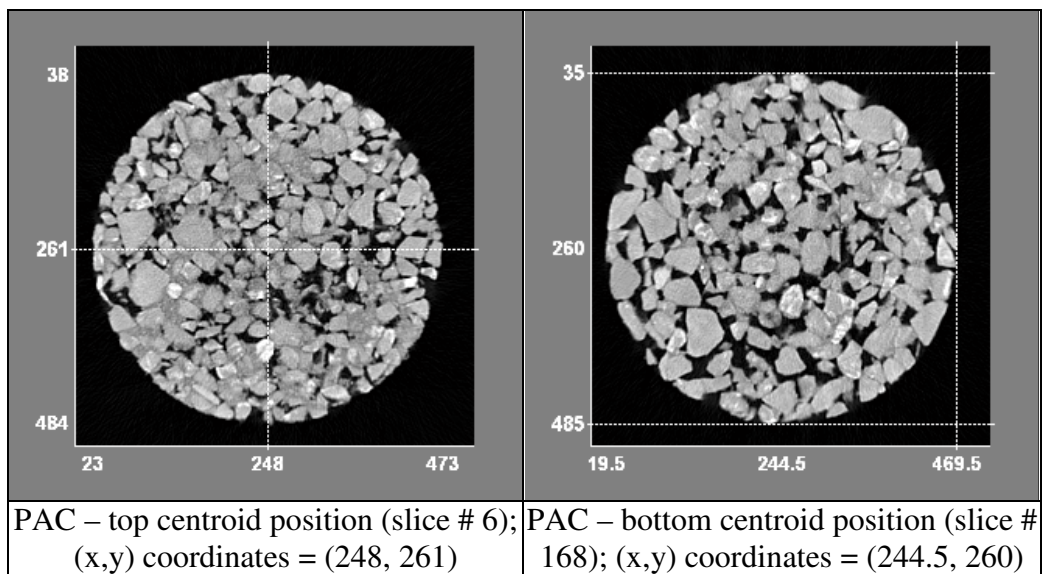


Figure 5.3 An illustration of two PAC slides before elimination of the air surrounding the specimen

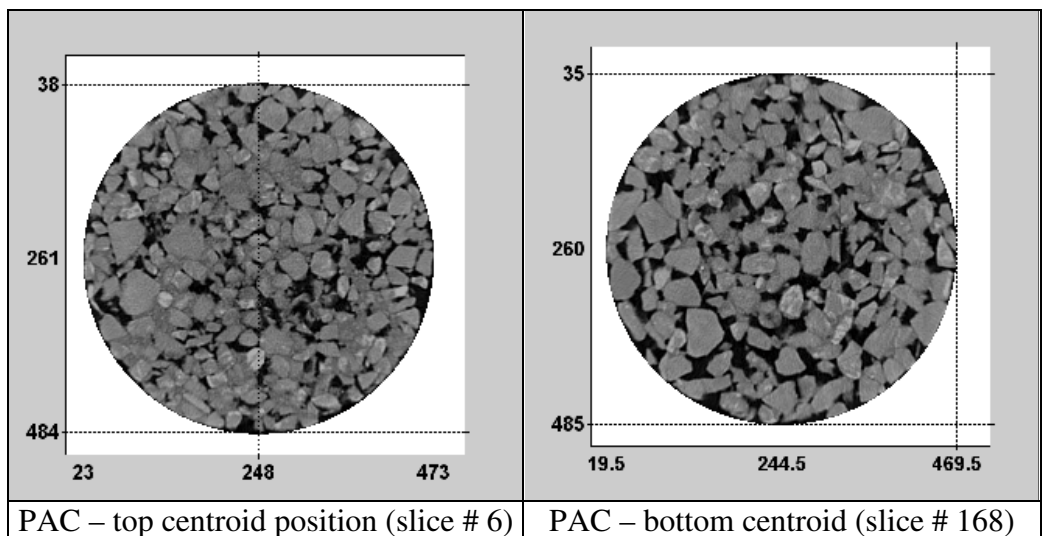


Figure 5.4 An illustration of two PAC slides after elimination of the air surrounding the specimen

The air void content was then obtained as a ratio between the areas of the pixels less than a certain intensity threshold for each slice and the x-section area of the specimen. Two different algorithms were considered in the analysis namely; regionprops-Area command and bwarea command. The difference between these two commands is that the regionprops-Area command obtains the area by counting the number of pixels, while the bwarea command supposedly compensates for the distortion that is inherent in representing a continuous image with discrete pixels. The air void content in the PAC was based on bwarea command while that of SMA and DAC was based on the regionprops-Area command. The reason behind this decision was that bwarea command resulted in an air void content that was closer to the laboratory determined air void content for PAC while the regionprops-Area command resulted in air void contents that were closer to the laboratory determined air void contents for SMA and DAC. This is illustrated in Figure 5.5 and Figure 5.6.

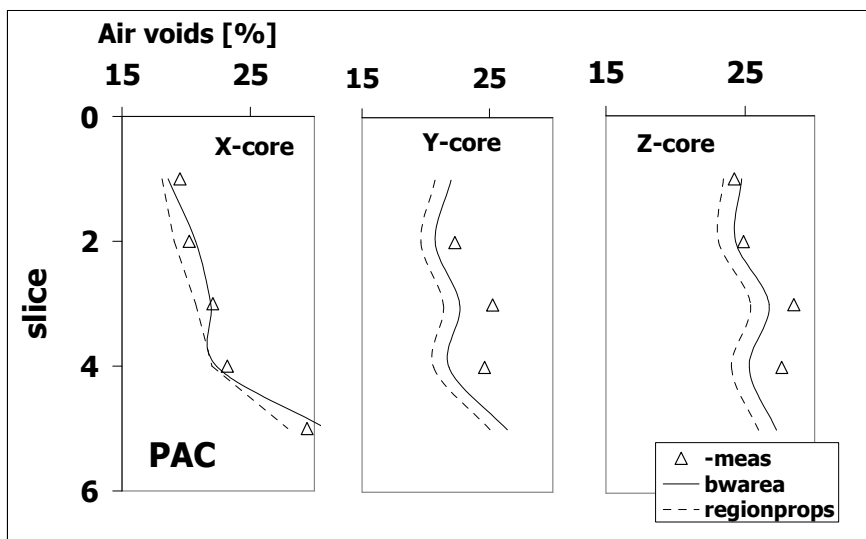


Figure 5.5 Air voids determined using bwarea, regionprops command and from laboratory procedure for the PAC specimen

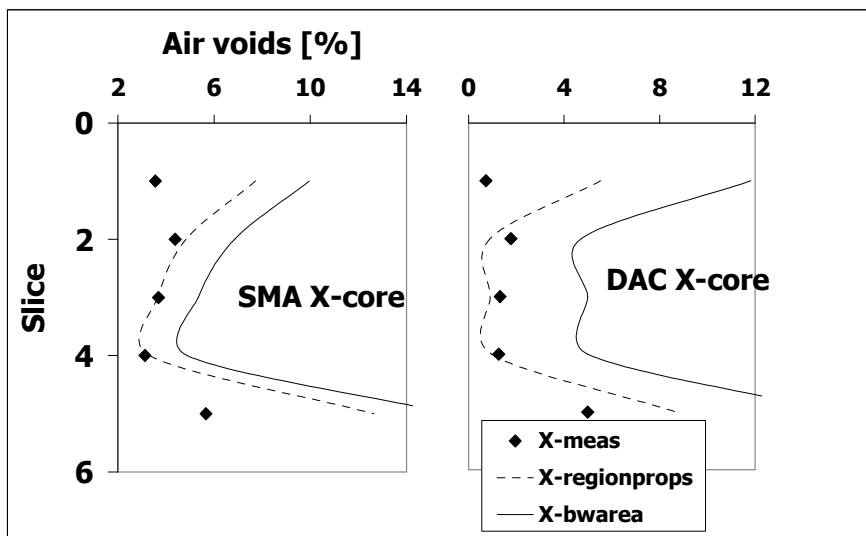


Figure 5.6 Air voids determined using bwarea, regionprops command and from laboratory procedure for the SMA and DAC specimens

Figure 5.7 shows the results of the X-ray tomography for the pilot specimens. The figure shows that the air void distribution in all the specimens varied considerably and the air void content was highest at the top and bottom parts of the specimens.

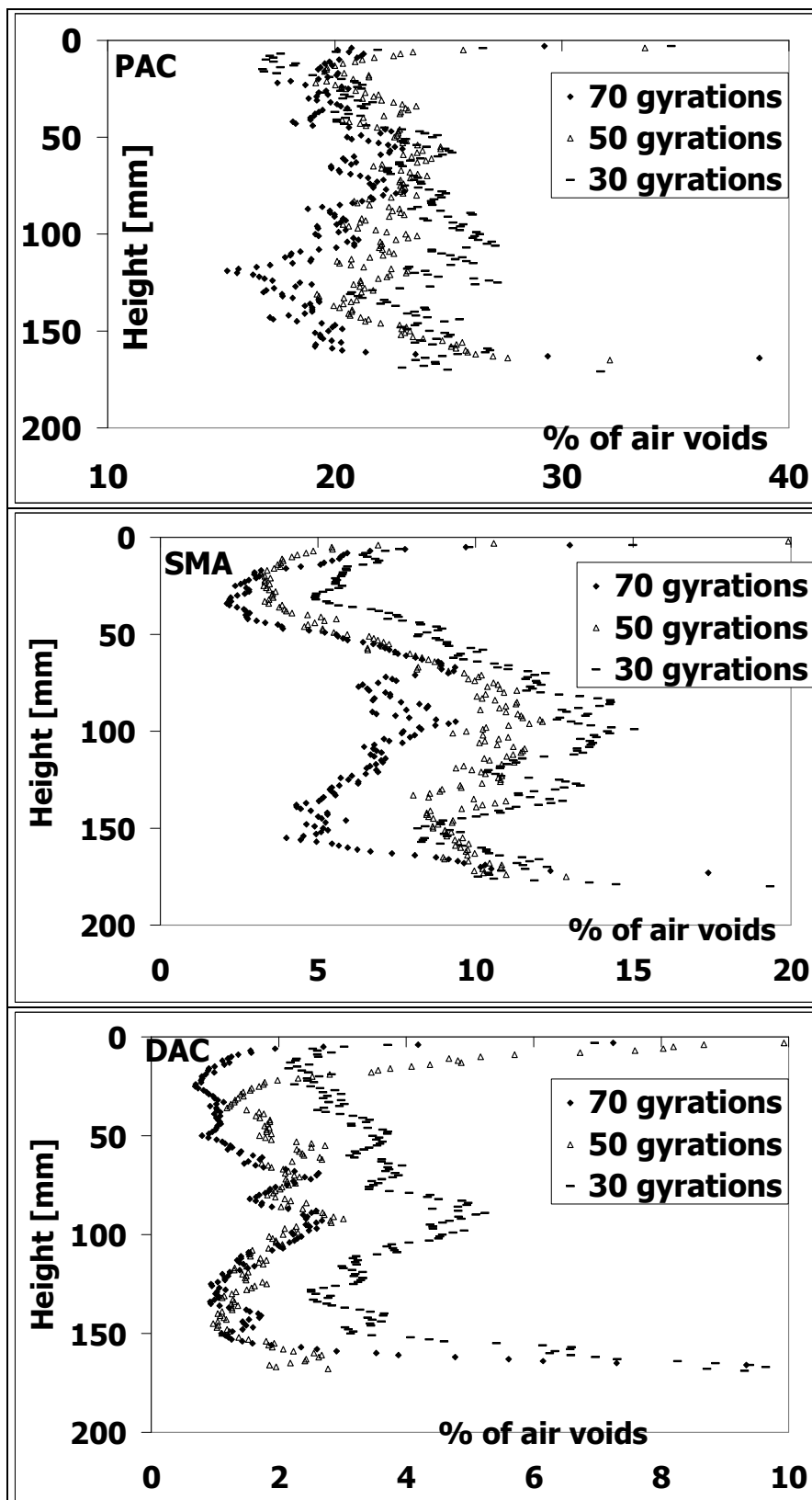


Figure 5.7 X-ray tomography analysis for the pilot specimens

5.2.5 Standard Laboratory Procedures

In order to compare the air void distribution obtained from the X-ray tomography analysis with the air void distribution determined according to the standard Dutch laboratory procedures (CROW 2000), the three specimens were cored into 3 cores of 50 mm, 100 mm and 150 mm diameter then sawed into 5 slices of 26 to 32 mm height as shown in Figure 5.8. This resulted in 15 specimen samples from each specimen. The main purpose of dividing the specimens into three cores was to measure the air void content in as many points as possible without damaging the cores. The sensitivity of the core sizes to damage was evident during the coring of the porous asphalt specimen. The Z-core sample at the bottom and the Y-core samples at the top and bottom were damaged during the coring and sawing of the PAC specimen. The air voids content in the 15 specimen samples was then determined by means of Equation 5.3 in accordance with the Dutch pavement specifications (CROW 2000). The densities of the PAC samples were determined based on specimen dimension measurements while those of SMA and DAC samples were determined using the saturated surface dry technique.

$$\text{air void content [\%]} = \frac{\text{maximum theoretical density} - \text{specimen density}}{\text{maximum theoretical density}} \times 100 \quad 5.3$$

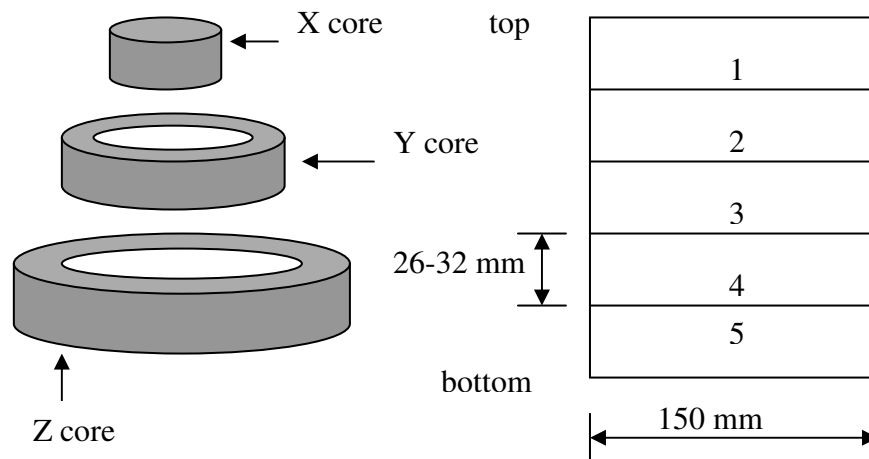


Figure 5.8 Specimen coring

5.2.6 Results

Figure 5.9 shows the results obtained from both the x-ray tomography air void analysis and the air void contents determined from standard laboratory methods for the cored PAC, SMA and DAC specimens respectively. The missing data points at the top and the bottom of part of the PAC specimen was due to damaged Y and Z-cores. The figures illustrate that the air void content varies with both the height and the diameter. The air void content in the PAC and DAC mixtures is lowest in the inner part of the specimen (X core) and increases progressively towards the outer parts of the specimen (Y and Z cores). However, such a trend is not clearly observed in the SMA mixture.

The figures also show that the similarity between the x-ray tomography analysis results and the measured air voids varied depending on the position and the type

of mixture. The air void distribution obtained from x-ray tomography analysis at positions 2-4 of the X core of the stone skeleton mixtures (PAC and SMA) and at positions 2-4 in the Z core of the DAC compare well to the measured air voids. However, the air void distribution obtained from x-ray tomography analysis in the rest of the cores differs from the measured values.

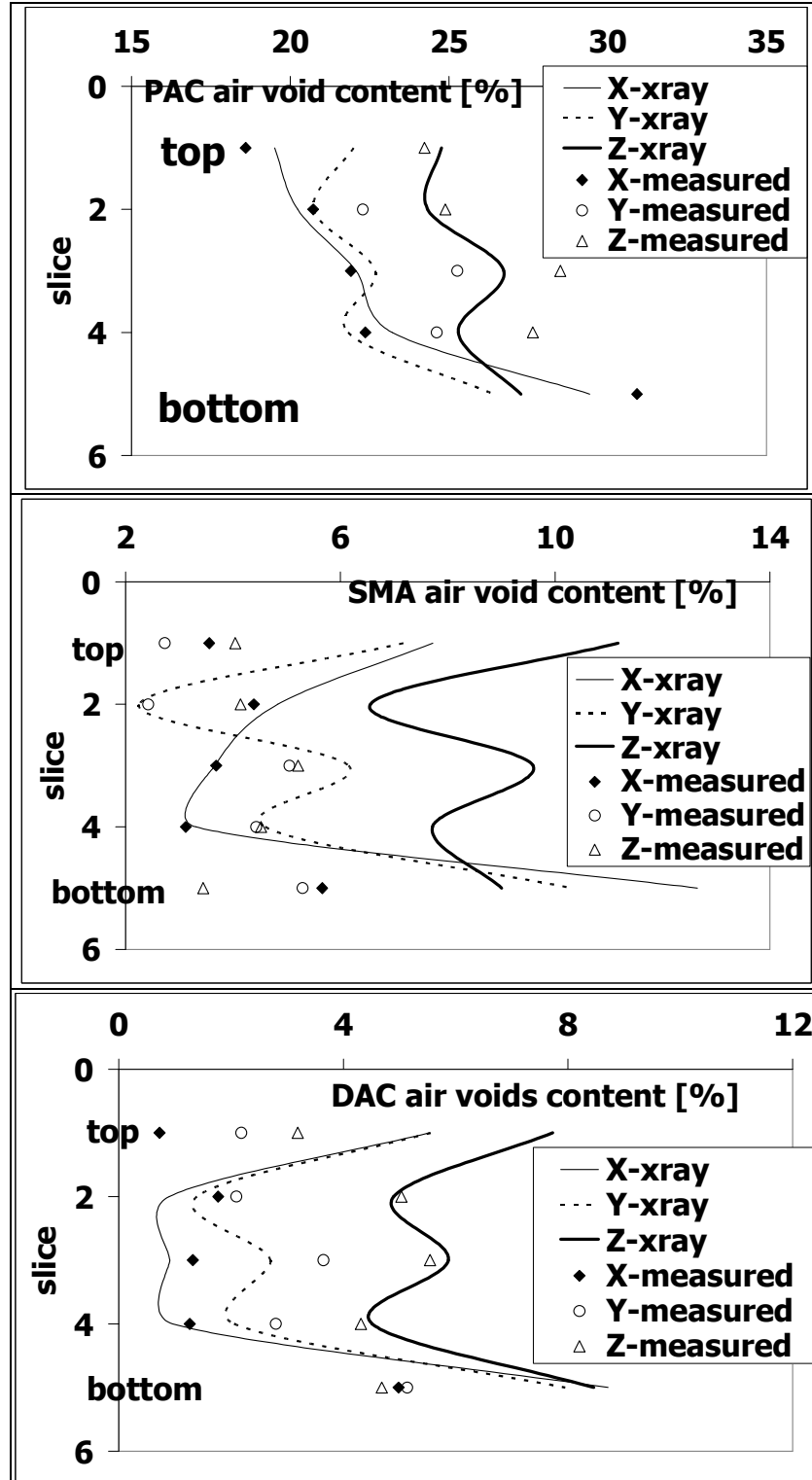


Figure 5.9 Laboratory measured air voids and x-ray tomography analysis air voids for the cored PAC, SMA and DAC specimens

5.2.7 Gyratory Specimen Compaction to Reference Marshall Density

Based on the preceding results it was considered necessary to remove the top, bottom and outside parts of the gyratory compacted specimens, in order to obtain test specimens with a homogeneous air void distribution. The diameter and the height of test specimens were set to 65 mm and 121 mm respectively to minimise this variation. A diameter of 65 mm offered a diameter that was slightly more than 4 times the maximum aggregate size of 16 mm and a height to diameter ratio of about 1.9.

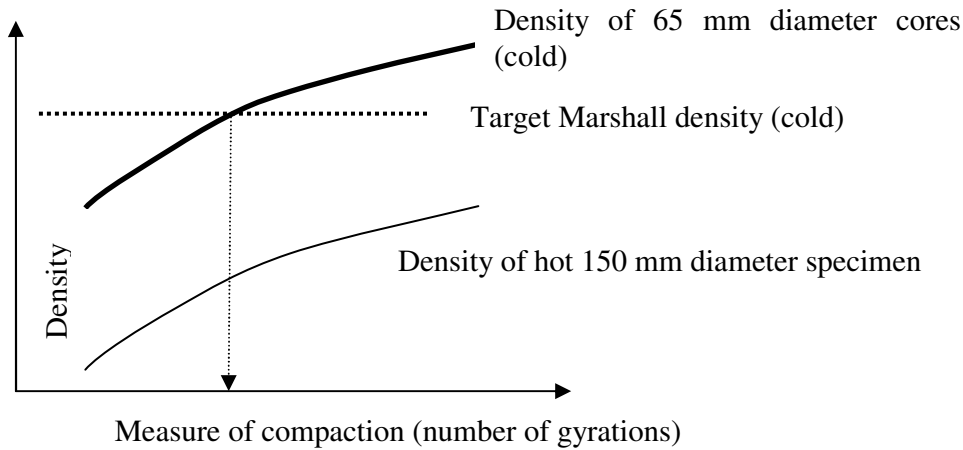


Figure 5.10 Approach of achieving desired Marshall density in 65 mm diameter cores

The approach used to achieve the reference Marshall density in the 65 mm diameter cores extracted from 150 mm diameter specimens is illustrated in Figure 5.10. The idea behind this approach was to predict the density of the cold 65 mm diameter cores based on the density of the hot 150 mm specimens. In this approach five 150 mm diameter specimens for each type of mixture were compacted to various hot densities. The 150 mm specimens were then cooled after which 65 mm cores were extracted. The hot density was used as compaction control parameter because it was anticipated that the hot density would provide a better means of obtaining consistent specimen densities in comparison to the number of gyrations. As shown later in this chapter the number of gyrations could not be used as a compaction control parameter.

For the purposes of obtaining the distribution of the compaction density within the 65 mm diameter cores, the 150 mm diameter specimens from each asphalt mixture were divided into five 65 mm diameter cores using two methods as shown in Figure 5.11. In the first method, one specimen for each type of mixture was sawed into five portions then each portion cored to obtain five 65 mm diameter slices. However, this method was discontinued due to difficulties in obtaining undamaged PAC samples. In the second method the specimens were first cored to extract 65 mm diameter cores after which the cores were sawed into five portions and their densities determined in accordance with the specifications (CROW 2000). The densities of the PAC portions were determined based on specimen dimension measurements while those of SMA and DAC portions were determined using the saturated surface dry technique.

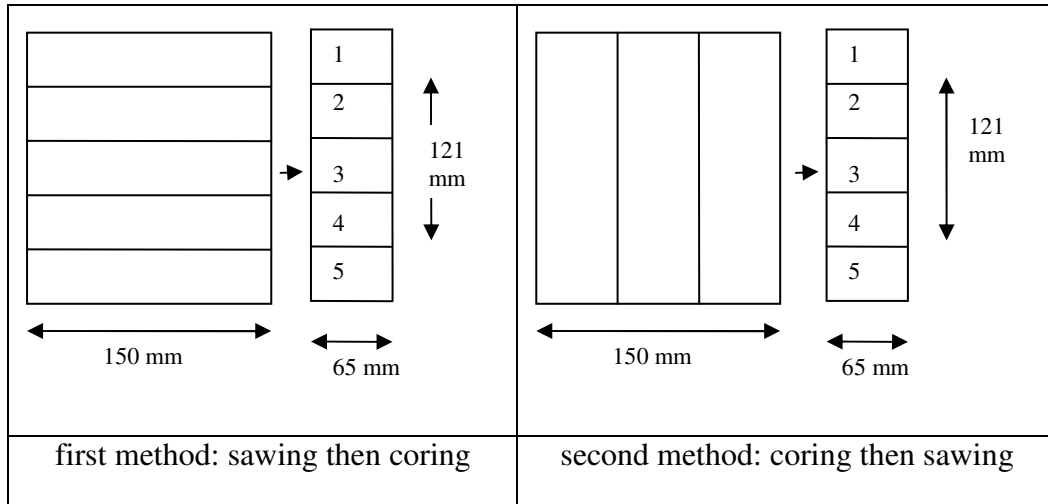


Figure 5.11 Division of the five 150 mm diameter specimens from each mixture

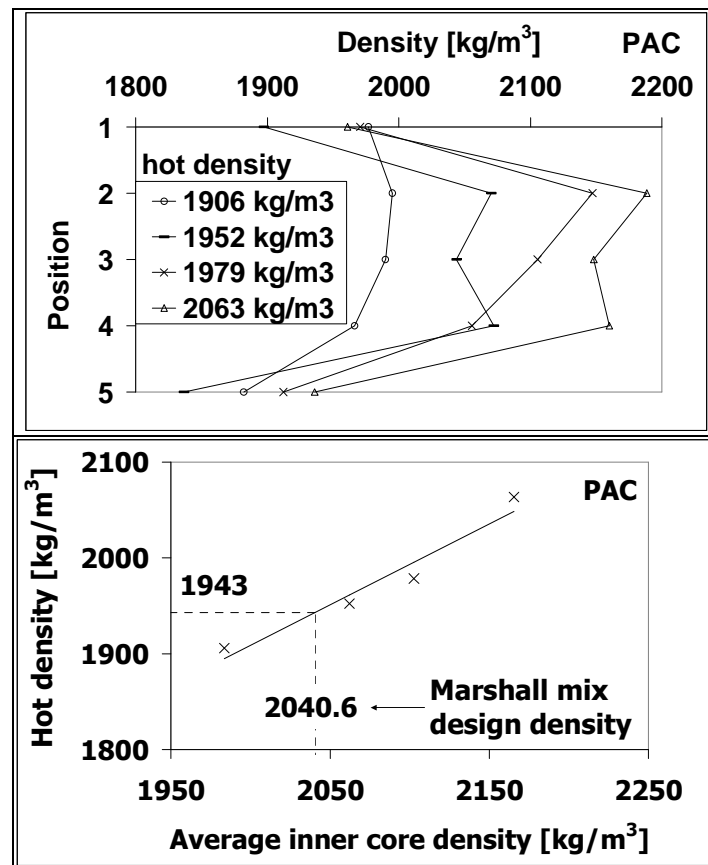


Figure 5.12 Determination of appropriate hot density for gyratory compaction of PAC specimens to the reference Marshall Mix design density

The hot density of 150 mm diameter specimens was then plotted against the average density of 65 mm portions at positions 2, 3, and 4 after which the appropriate hot density to obtain the reference Marshall density in the 65 mm diameter cores was interpolated. The densities of the 65 mm diameter portions and the interpolated hot densities for the three asphalt mixtures are shown in Figure 5.12, Figure 5.13 and Figure 5.14. The labels in the top part of each of the

figures refer to the hot density of the 150 mm diameter specimen while the horizontal axis in the bottom part of each figure refers to the average density of the 65 mm diameter portions. The first part of Figure 5.12, Figure 5.13 and Figure 5.14 show that the heating of the top gyratory compacting disc had little or no effect on the uniformity of density in the top part of the specimen (position 1) in comparison to the middle parts (position 2, 3 and 4). The density at the upper part (position 1) of the specimens was significantly lower than the density in the middle part of the specimen (positions 2, 3 and 4) but similar to the density at the bottom (position 5).

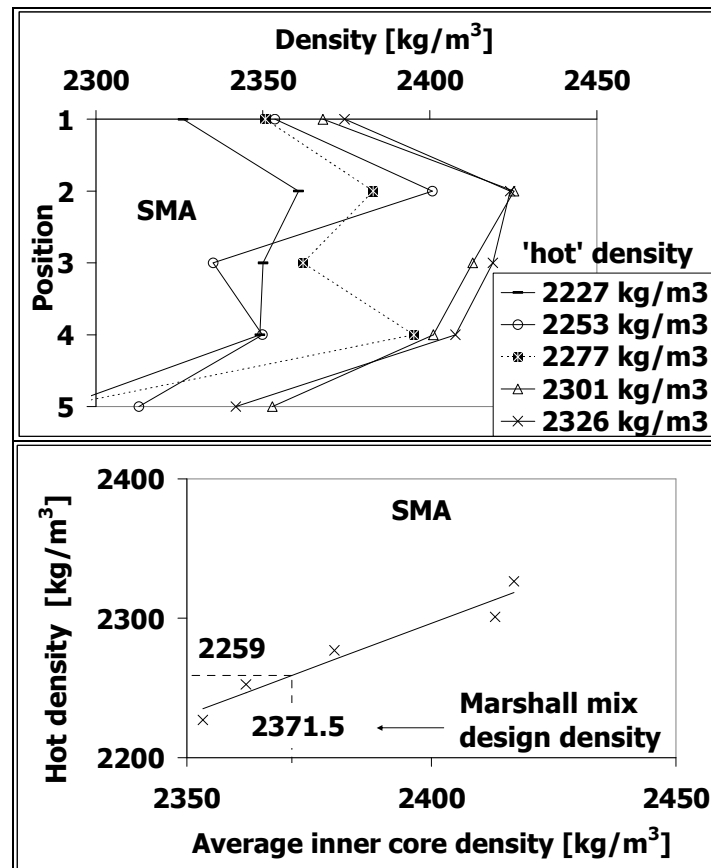


Figure 5.13 Determination of appropriate hot density for gyratory compaction of SMA specimens to the reference Marshall Mix design density

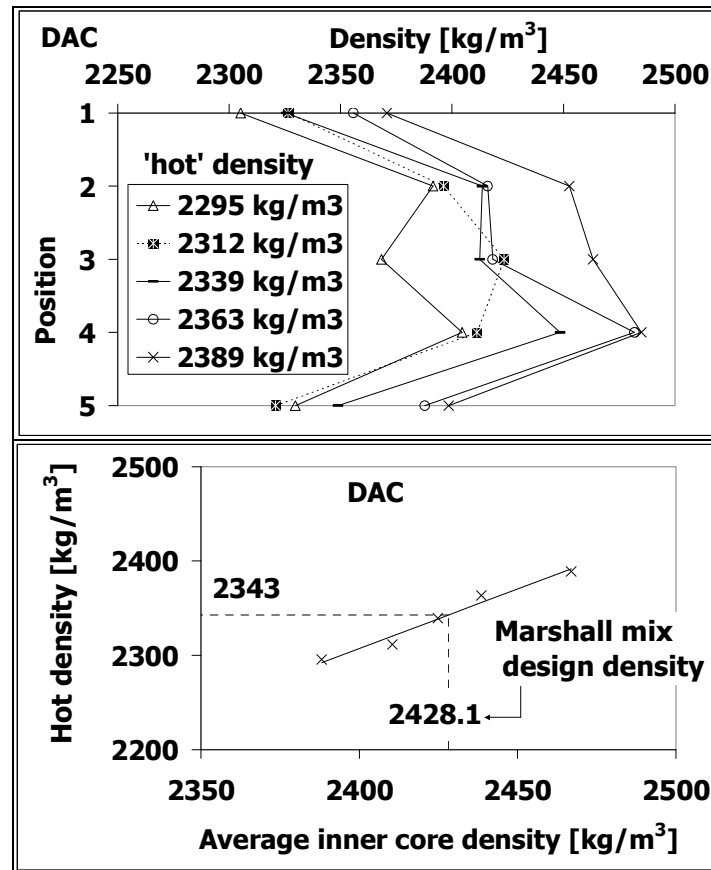


Figure 5.14 Determination of appropriate hot density for gyratory compaction of DAC specimens to the reference Marshall Mix design density

Prior to extraction of the 65 mm diameter cores, the densities of the cold 150 mm diameter specimens were determined. The densities of the cold 150 mm PAC specimens were determined based on specimen dimension measurements while the densities of the cold 150 mm diameter SMA and DAC specimens were determined using both specimen dimensions and the saturated surface dry technique.

The different densities determined for the asphalt mixtures are presented in Table 5.2, Figure 5.15, Figure 5.16 and Figure 5.17. The terms used to describe the various densities are also given in Table 5.2. The figures show that the specimens contracted on cooling and that the average density of the 65 mm cores was always higher than the density of the 150 mm specimens irrespective of the method of density determination. The figures also show that the hot density is lower than both the density based on the surface dry technique and the density based on specimen dimensions.

Table 5.2 Different densities for the asphalt mixtures

Mix	Gyratory angle [degrees]	number of gyrations	hot [kg/m ³]	150 D1 [kg/m ³]	150 D2 [kg/m ³]	65 D2 [kg/m ³]
PAC	1	13	1906	1910	-	1984
		23	1952	1974	-	2062
		29	1979	1999	-	2103
		47	2002	2003	-	-
		86	2063	2079	-	2166
SMA	1.25	52	2227	2243	2308	2353
		56	2253	2264	2324	2362
		60	2277	2292	-	2380
		108	2326	2347	2382	2417
		122	2301	2316	2375	2413
DAC	1	9	2295	2309	2341	2388
		16	2312	2327	-	2410
		16	2339	2358	2378	2425
		18	2363	2382	2399	2438
		30	2389	2396	2423	2467
definitions						
hot	density of 150 mm based on height of the hot specimen					
150 D1	density of 150 mm specimen after cooling based on specimen dimensions					
150 D2	density of 150 mm specimen after cooling based on saturated surface dry technique					
65 D2	average density of 65 mm cores at positions 2,3 &4 based on specimen dimension measurement technique for PAC and saturated surface dry technique for SMA and DAC					

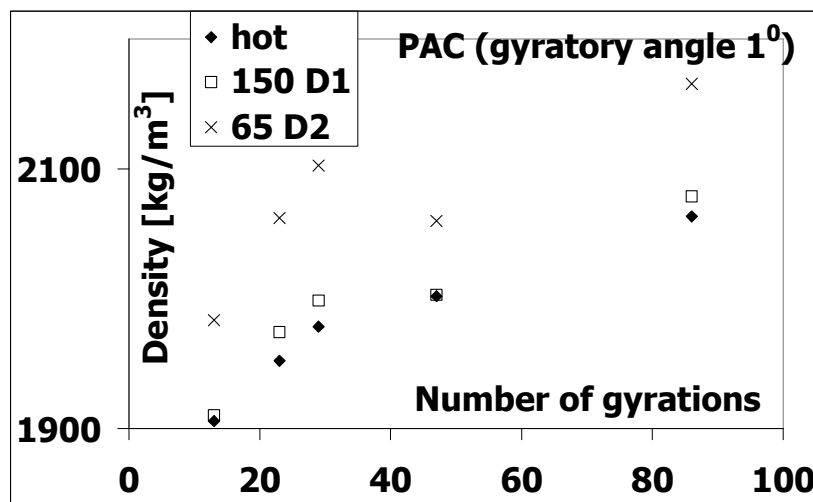


Figure 5.15 Different densities measured for the PAC asphalt mixture

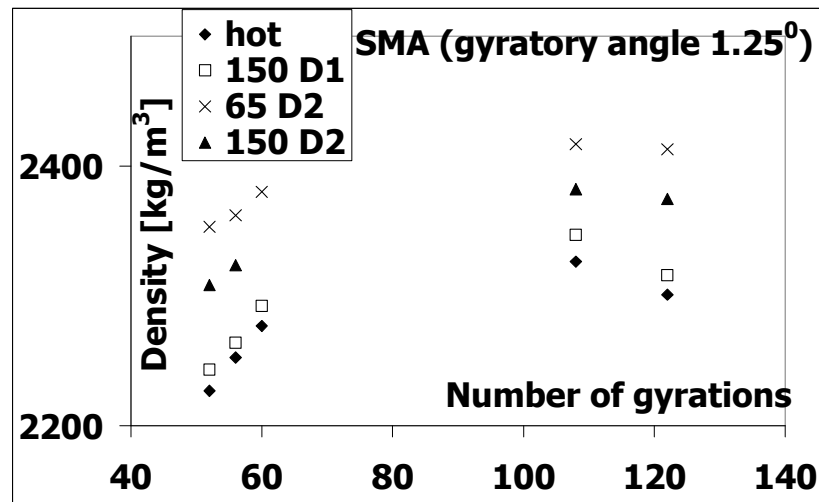


Figure 5.16 Different densities measured for the SMA asphalt mixture

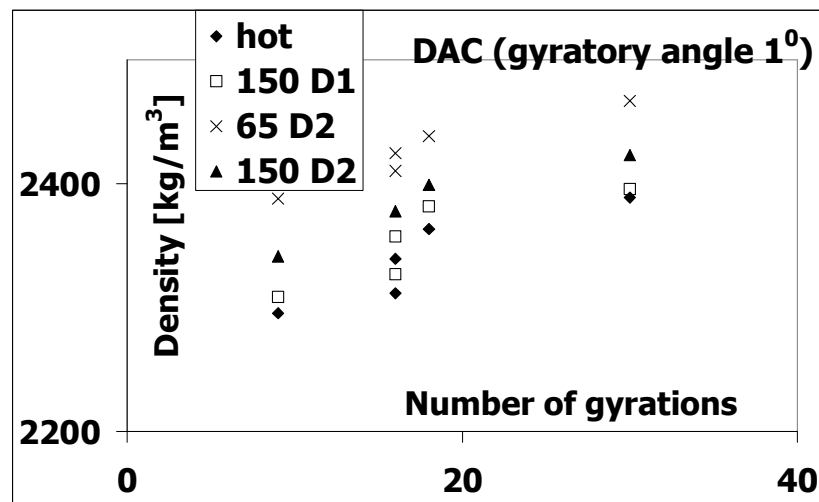


Figure 5.17 Different densities measured for the DAC asphalt mixture

5.2.7.1 Summary of the Gyratory Specimen Compaction to Reference Marshall Density

The procedure for gyratory compaction of homogeneous test specimens to reference Marshall density is summarized in Figure 5.18. In this procedure, the Marshall mixture design was performed to obtain the reference density, after which five 150 mm diameter specimens for each type of mixture were compacted using the gyratory compactor to various hot densities. The hot density was determined using the height of the hot specimen as recorded by the gyratory compactor. The specimens were then cooled and the densities determined. This was followed by the coring of 65 mm diameter specimens from the inner part of the 150 mm diameter specimens and removal of the top and bottom parts of the specimens prior to density determination. The hot densities of the 150 mm diameter specimens were subsequently plotted against the densities of 65 mm diameter cores. The appropriate hot density for the 150 mm diameter specimens required to obtain the reference Marshall density in the 65 mm diameter cores was

then interpolated. Consequently, 150 mm diameter specimens were compacted to the interpolated hot densities and 65 mm diameter specimens extracted.

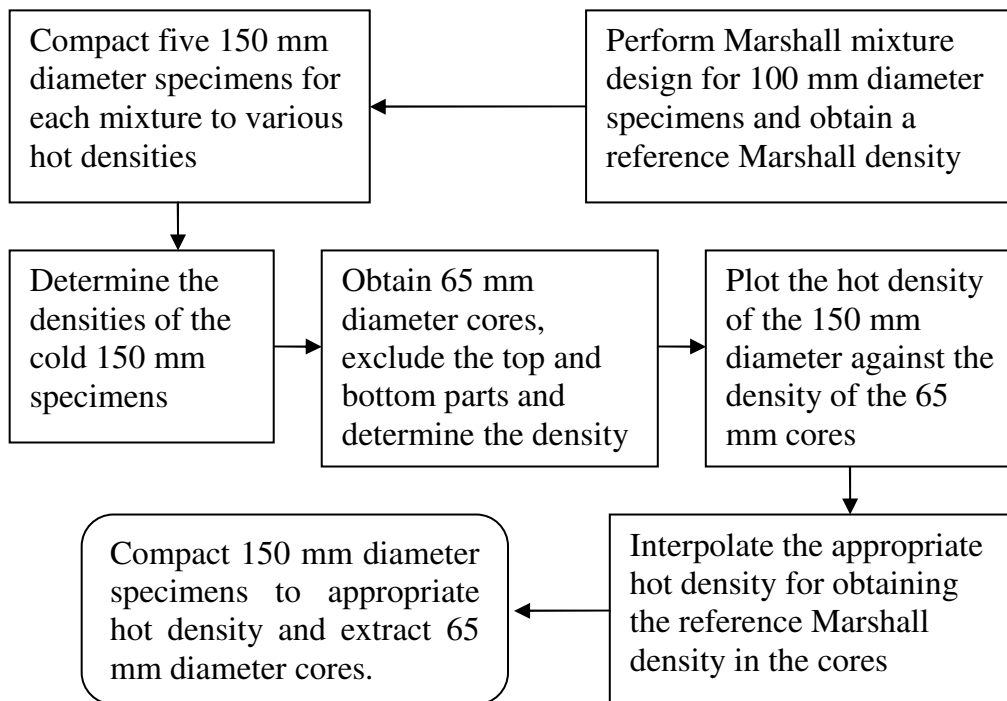


Figure 5.18 Summary of determination of appropriate density in hot 150 mm gyratory compacted specimens

5.2.8 Test Specimens

The RMIT, DCMC and DCMT test specimens were extracted from 150 mm diameter gyratory compacted specimens. The target size was 100 mm diameter by 30 mm thick and 65 mm diameter by 121 mm height for RMIT and the displacement controlled monotonic tests respectively. A 30 mm target thickness was chosen since the RMIT resilient modulus calculation is not valid for specimens over 30 mm thick (Lytton et al 1993).

5.2.8.1 Extracted 65 mm Diameter Specimens

Figure 5.19 shows the densities of the 65 mm diameter specimens with a height of 121 mm cored from 150 mm diameter gyratory specimens compacted to the interpolated hot density for the three mixtures. The figure shows a high inconsistency in the number of gyrations required to compact the asphalt mixture to the required density. This number differs from 10 to 21 gyrations in the PAC, 37 to 73 in SMA and 16 to 25 in DAC. This in effect implies that it was not possible to use the number of gyrations as a compaction control parameter. The figure also shows that the SMA mixture requires a higher number of gyrations at a gyratory angle of 1.25^0 in comparison with the PAC and the DAC mixtures which were easily compacted at 1^0 . This observation shows that SMA is more difficult to compact.

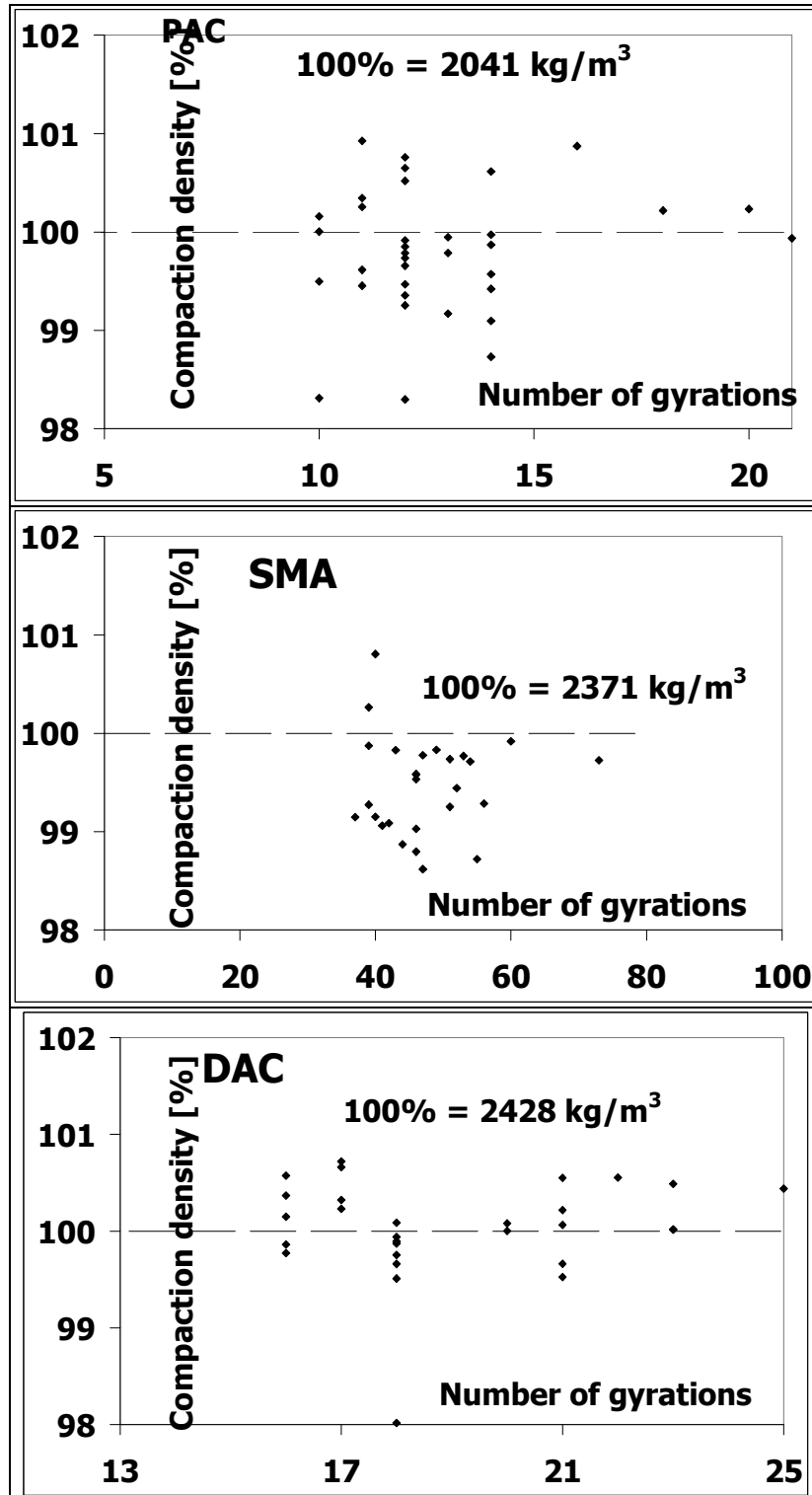


Figure 5.19 Densities of the 65 mm diameter test specimens extracted from 150 mm diameter gyratory compacted specimens for PAC, SMA and DAC (100% = Marshall density)

In order to evaluate the conformity of the relative density of 65 mm diameter specimens to the reference Marshall density, a statistical analysis was performed based on the normal distribution. The suitability of the normal distribution function in describing a set of data can be assessed by plotting the data on a normal probability paper. A linear plot implies that the data can be described

reasonably well by the normal distribution function (Nowak and Collins, 2000). Figure 5.20 shows the plot on a normal probability paper, the normal distribution, the standard deviation and the mean of the relative densities of the 65 mm diameter specimens. The figure also shows the air voids content (VTM) for the average relative density of the 65 mm diameter specimens. The straight plots on the normal probability paper indicate that the relative densities of the three asphalt mixtures can be described reasonably well by the normal distribution. The range of the mean (99.5 to 100%) and the low standard deviations (0.5 to 0.64 %) imply that there was a good agreement between the reference Marshall density and the densities of the 65 mm diameter specimens extracted from the 150 mm diameter gyratory compacted specimens. Literature suggests that a standard deviation of 1.02 % is considered to be a typical value for densities of hot mix asphalt (Roberts et al, 1996).

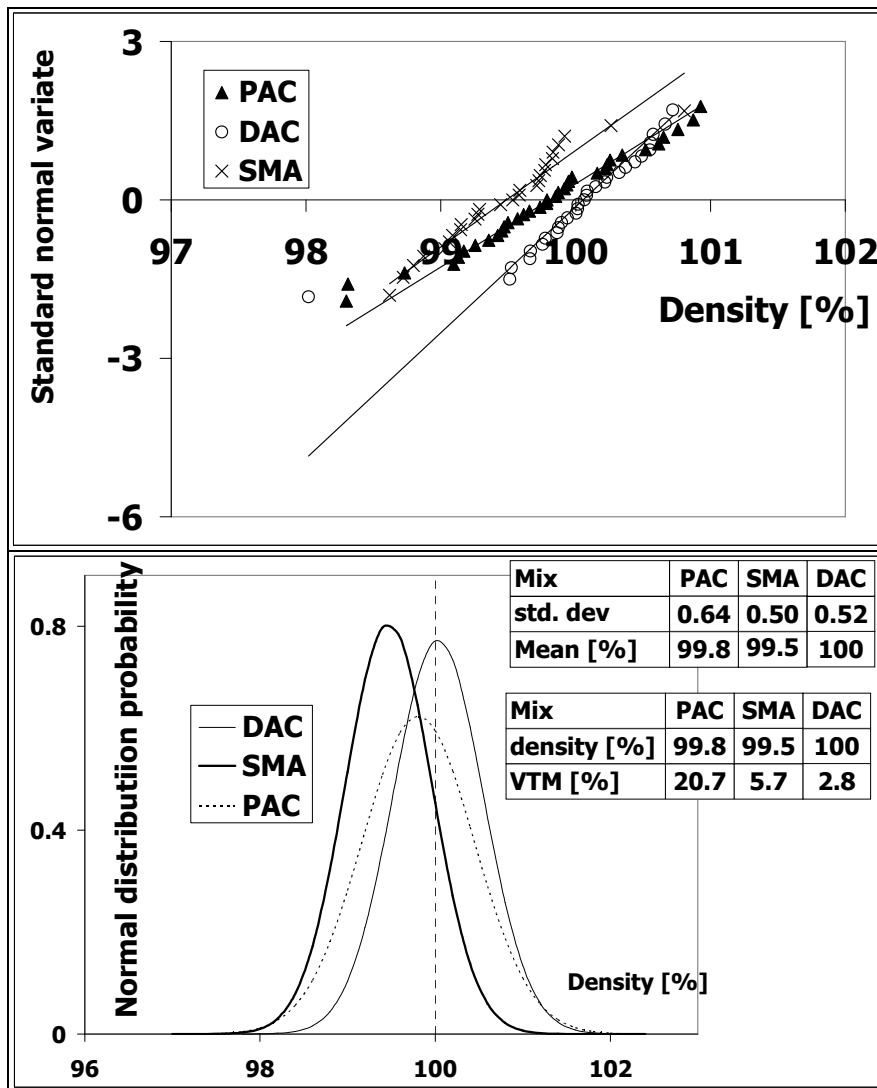


Figure 5.20 Plot on a normal probability paper and the normal distribution of the densities of the 65 mm diameter specimens

5.2.8.2 Extracted 100 mm Diameter Specimens

Apart from the 65 mm diameter specimens, 100 mm diameter RMIT specimens were also extracted from 150 mm diameter specimens compacted to the

appropriate densities discussed in section 5.2.7. The densities of the cored 100 mm diameter specimens are shown in Figure 5.21 and the air void contents for the average densities are shown in Table 5.3.

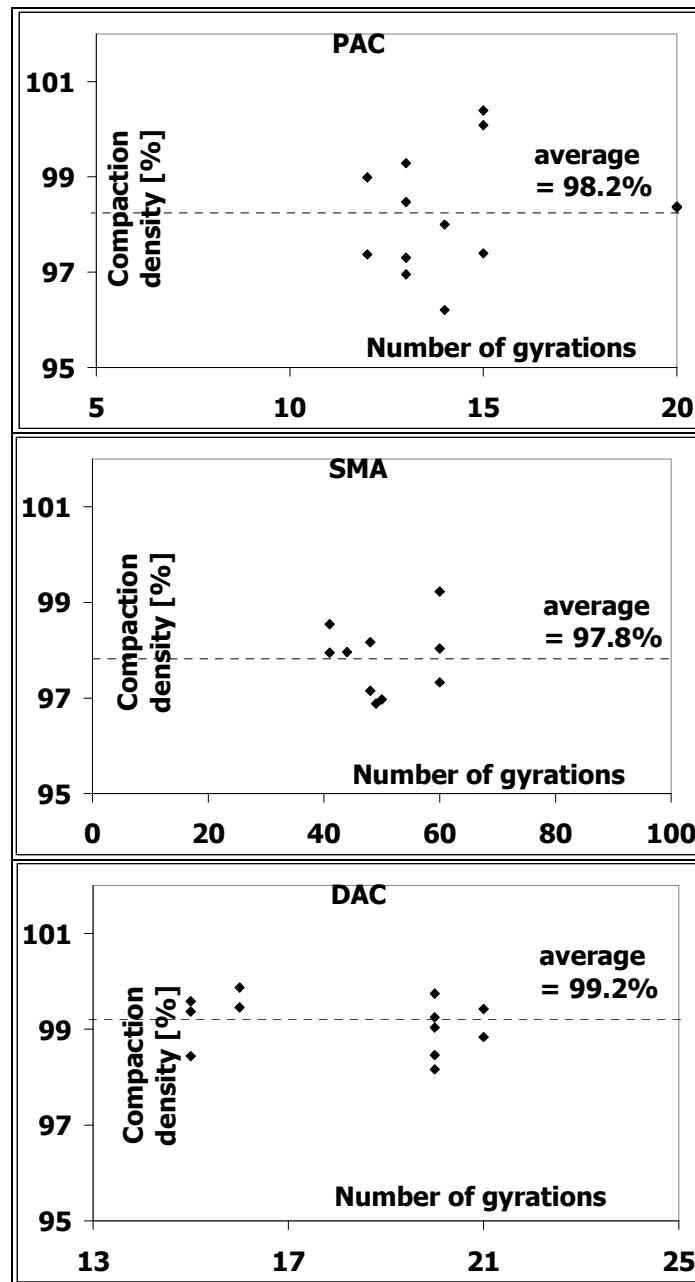


Figure 5.21 Extracted 100 mm diameter specimens for RMIT test

Table 5.3 Air void content for the RMIT 100 mm diameter specimens

Mix	average density [%]	air voids content [%]
PAC	98.2	22.0
SMA	97.8	7.2
DAC	99.2	3.6

5.3 Test Equipment

5.3.1 Resilient Modulus Indirect Tensile Test (RMIT)

Figure 5.22 shows the resilient modulus indirect tensile (RMIT) test set up. The RMIT test equipment consisted of a ± 0.6 kN actuator mounted on a small frame. The RMIT tests were performed in a temperature control cabinet capable of maintaining temperature within a range of 2.5 to 50°C. The horizontal deformation during the test was measured by two radial LVDTs that had a range of ± 62.5 μm . The measured data was collected by a data acquisition system at a sampling rate of 250 Hz.

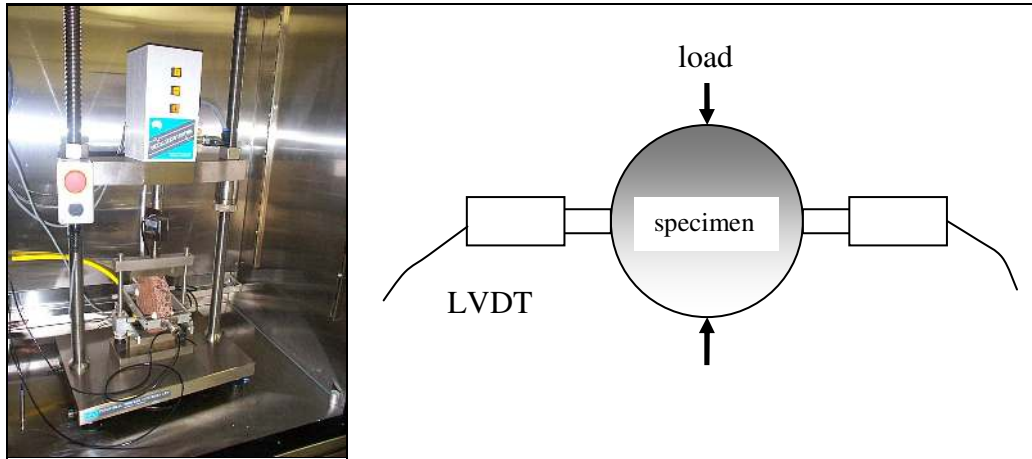


Figure 5.22 Resilient modulus indirect tensile test set up

5.3.2 Displacement Controlled Monotonic Compression Test (DCMC)

Figure 5.24 shows the displacement controlled monotonic compression (DCMC) test set up. The compression test equipment comprised of a 150 kN MTS hydraulic actuator mounted on a rigid support frame. The DCMC test cell was enclosed in a temperature control cabinet that was capable of maintaining temperatures within the range of -5 to 35°C. Similar to the ACRE project (Erkens 2002), the load was transmitted to the specimen through two thin steel plates that were placed at the top and bottom of the specimen in order to protect the top and the bottom part of the cell. For purposes of obtaining a uniform stress distribution, a friction reduction system was applied to the top and bottom ends of the specimen. The friction reduction system applied by means of a 50 μm thick Luflexen© foil and a soap that was spread on either side of the foil.

The deformation during the test was measured by one long range and two short range axial LVDTs, an extensometer and a string measuring system. The axial LVDTs took axial measurements over the total specimen height while the extensometer took the radial measurement at the middle of the specimen. The range of the axial LVDTs was ± 20 mm, ± 5 mm for the long range and the short range LVDTs respectively. The string and the extensometer had a range of ± 150 mm and ± 3.75 mm respectively. The purpose of the short range LVDTs and the extensometer was to enable accurate measurements in the initial stages of the test. The measured data was recorded by a data acquisition system at sampling rates ranging from 1 to 1000 Hz.

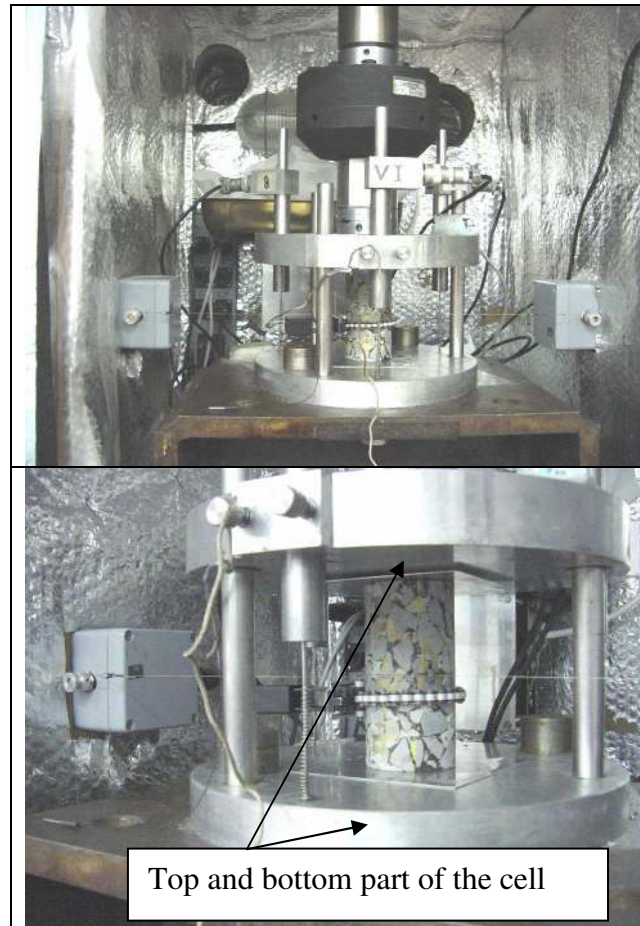


Figure 5.23 Direct compression test set up

5.3.3 Displacement Controlled Monotonic Tension Test (DCMT)

The displacement controlled monotonic tension (DCMT) test set up shown in Figure 5.24 consisted of a temperature controlled test system that was developed during the ACRE project (Erkens and Poot 2001). The test cell was composed of a rigid external frame with a 3 hinge loading system enclosed in a temperature cabinet capable of maintaining temperatures within -40 to 100°C . The purpose of the three hinge loading system was to minimize horizontal misalignment that would result in eccentric loading of the specimen during testing. The specimen was glued to the top and bottom end caps using a two component glue. In order to ensure adequate fastening, a stiff plastic ring was glued on both the specimen and the end caps at the top and bottom ends of the specimen.

The amount of deformation in the specimen during the test was measured using three axial LVDTs with a ± 10 mm range and a radial extensometer with a measuring range of ± 3.75 mm. The measured data was captured by a data acquisition system at sampling rates ranging from 3 to 1000 Hz.

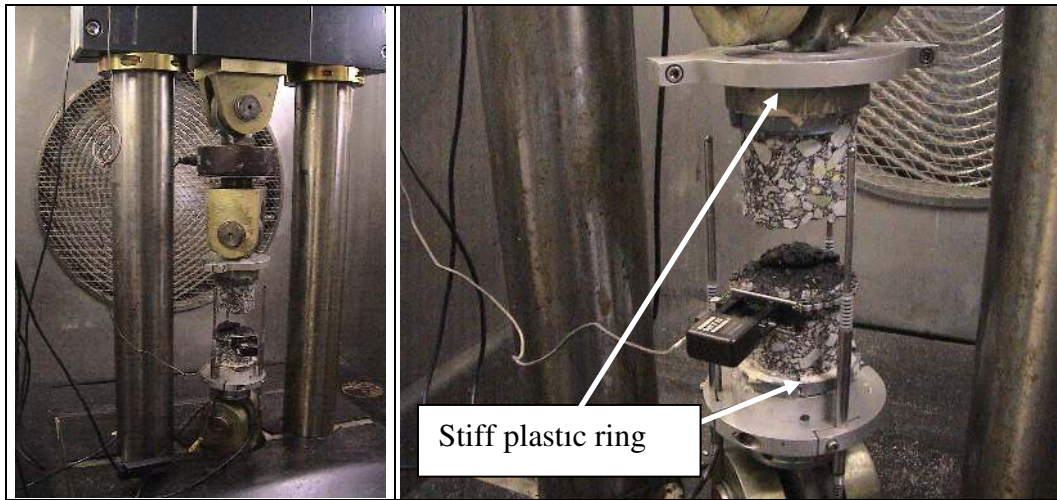


Figure 5.24 Tension test set up

5.4 Test Conditions

5.4.1 Experimental Design

Figure 5.25 shows an illustration of the central composite design in relation to temperature and rate of displacement. The test conditions in this experimental design consist of 9 test conditions as shown in Figure 5.25 with respect to displacement rate and temperature. The test conditions included one central test condition and 8 other test conditions located around the central test condition. One test repetition was performed at each of the 8 test conditions and five test repetitions at the central test condition. The purpose of the five test repetitions conducted at the central test conditions was to estimate the scatter in the data.

The central test conditions are determined as the average of the minimum and the maximum test conditions as shown in Equation 5.4. The test conditions at any of the points can be determined by considering their position with respect to central test conditions (point 9 in Figure 5.25). If T and d are used to denote the distance with respect to temperature and rate of displacement respectively then Equation 5.5 can be used to obtain any of the test conditions located around the central test condition (point 9). For example the test conditions at position 2 and 4 can be obtained as in Equation 5.6 and Equation 5.7 respectively.

$$T_{avg} = \frac{T_{max} + T_{min}}{2}, \quad d_{avg} = \frac{d_{max} + d_{min}}{2} \quad 5.4$$

$$(\text{test condition}) = \left(\left[T_{avg} + T \right], \left[d_{avg} + d \right] \right) \quad 5.5$$

$$(\text{test condition})_2 = \left(\left[T_{avg} + \left(\frac{T_{max} - T_{min}}{2} \right) \cos 45 \right], \left[d_{avg} + \left(\frac{d_{max} - d_{min}}{2} \right) \cos 45 \right] \right) \quad 5.6$$

$$(\text{test condition})_4 = \left(\left[T_{avg} + \left(\frac{T_{max} - T_{min}}{2} \right) \cos 45 \right], \left[d_{avg} - \left(\frac{d_{max} - d_{min}}{2} \right) \cos 45 \right] \right) \quad 5.7$$

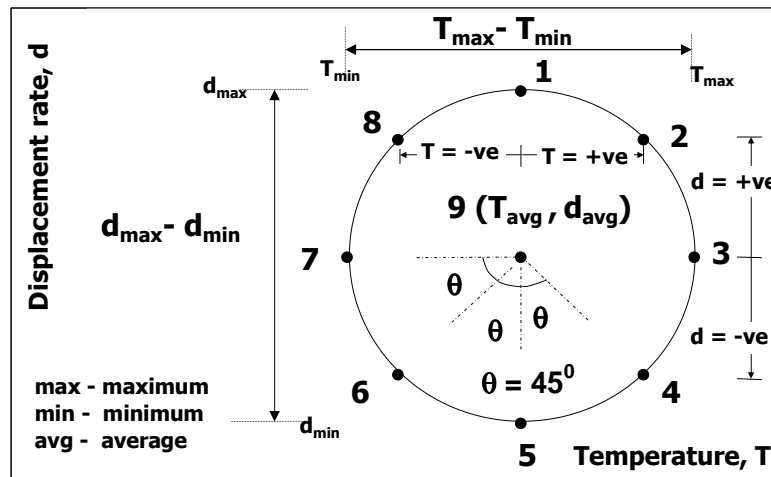


Figure 5.25 An illustration of the Central composite design with respect to temperature and displacement rate

Table 5.4 shows the test conditions for the RMIT tests. As explained in paragraph 5.1, the purpose of the RMIT was to determine the temperature susceptibility of the asphalt mixtures and as such the tests were conducted at numerous test conditions and also at the highest temperatures possible. The maximum test temperatures for PAC, SMA and DAC were 30, 35 and 35⁰C. These temperatures were adopted from some initial monotonic indirect tension tests that indicated that the specimens could be handled at these maximum temperatures. Although, successful RMIT tests carried out on PAC at 35⁰C have been reported for field-extracted cores (Withana 2001), the indirect tension tests that were conducted in this research, gave some unstable results at 30⁰C and 35⁰C for PAC and SMA mixtures respectively, while the DAC results were stable even at 35⁰C. The instability exhibited by the PAC and SMA mixtures in comparison to field-extracted cores may have been caused by the lower degree of ageing in the specimens investigated in this research. The RMIT tests were performed for 6 consecutive haver-sine pulse loading periods of 63, 125, 200, 500, 999 and 63 milliseconds per test repetition. Each loading period consisted of 5 load repetitions with each load repetition having a total pulse and rest duration of 6000 milliseconds. The load levels were based on the extensive experience of the operator.

The DCMC and DCMT tests were conducted at the target test conditions shown in Figure 5.26 and tabulated in Table 5.5 and Table 5.6. One extra test that was not part of the central composite design was added at 5⁰C to check the accuracy of the experimental design for failure test conditions outside the range of the experimental design.

Table 5.4 Resilient modulus indirect tensile target test conditions

Mix	PAC								SMA					DAC							
	10		15		20	25	30		15	20	25	30	35	15		20	25	30	35		
temp. [°C]	0.6	0.8	0.4	0.3	0.2	0.2	0.12	0.1	0.6	0.3	0.4	0.25	0.175	0.12	0.6	0.8	1	0.7	0.35	0.25	0.15
load [kN]	3	2	1	2	2	3			3	1	3			1	1	3	3				
test repetitions	114								96					102							
total tests	114								96					102							

haver-sine pulse duration of 63, 125, 200, 500, 999, 63 [ms]; pulse + rest duration = 6000 ms

Table 5.5 DCMC target test conditions for the three asphalt mixtures

PAC				SMA				DAC			
Label	Test code	Temp [°C]	Target strain rate [%/s]	Label	Test code	Temp [°C]	Target strain rate [%/s]	Label	Test code	Temp [°C]	Target strain rate [%/s]
1	P33_30_2.51	30	2.07	1	S18_32.1_0.74	32.1	0.61	1	d2_35_2.51	35	2.07
2	P30_27.1_0.74	27.1	0.61	2	S16_32.1_4.27	32.1	3.53	2	D16_32.1_4.27	32.1	3.53
3	P31_27.1_4.27	27.1	3.53	3	S32_25_0.01	25	0.01	3	D12_32.1_0.74	32.1	0.61
4	P18_20_0.01	20	0.01	4	S8_25_2.51	25	2.07	4	D18_25_2.51	25	2.07
5	P24_20_2.51	20	2.07	5	S23_25_2.51	25	2.07	5	D17_25_2.51	25	2.07
6	P21_20_2.51	20	2.07	6	S9_25_2.51	25	2.07	6	D22_25_0.01	25	0.01
7	P16_20_2.51	20	2.07	7	S24_25_2.51	25	2.07	7	D24_25_2.51	25	2.07
8	P15_20_2.51	20	2.07	8	S35_25_2.51	25	2.07	8	D3_25_2.51	25	2.07
9	P12_20_2.51	20	2.07	9	S39_25_2.51	25	2.07	9	D19_25_2.51	25	2.07
10	P19_20_5	20	4.13	10	S42_25_2.51	25	2.07	10	D20_25_5.0	25	4.13
11	P11_12.9_0.74	12.9	0.61	11	S17_25_5.0	25	4.13	11	D11_17.9_0.74	17.9	0.61
12	P29_12.9_4.27	12.9	3.53	12	S4_17.9_0.74	17.9	0.61	12	D21_17.9_4.27	17.9	3.53
13	P4_10_2.51	10	2.07	13	S5_17.9_4.27	17.9	3.53	13	d1_15_2.51	15	2.07
14	P20_5_5	5	4.13	14	s1_15_2.51	15	2.07	14	D15_5_5	5	4.13
				15	S13_5_5	5	4.13				

Table 5.6 DCMT target test conditions for the three asphalt mixtures

PAC				SMA				DAC			
Label	Test code	Temp [°C]	Target strain rate [%/s]	Label	Test code	Temp [°C]	Target strain rate [%/s]	Label	Test code	Temp [°C]	Target strain rate [%/s]
1	P27_30_2.51	30	2.07	1	S56_35_2.51	35	2.07	1	D6_35_2.51	35	2.07
2	P37_27.1_0.74	27.1	0.61	2	S26_32.1_0.74	32.1	0.61	2	D35_32.1_0.74	32.1	0.61
3	P22_27.1_4.27	27.1	3.53	3	S27_32.1_4.27	32.1	3.53	3	D28_32.1_4.27	32.1	3.53
4	P41_20_0.01	20	0.01	4	S14_25_0.01	25	0.01	4	D13_25_2.51	25	2.07
5	P10_20_2.51	20	2.07	5	S31_25_2.51	25	2.07	5	D31_25_5	25	2.07
6	P23_20_2.51	20	2.07	6	S38_25_2.51	25	2.07	6	D39_25_0.01	25	0.01
7	P28_20_2.51	20	2.07	7	S40_25_2.51	25	2.07	7	D29_25_2.51	25	2.07
8	P35_20_2.51	20	2.07	8	S41_25_2.51	25	2.07	8	D38_25_2.51	25	2.07
9	P38_20_2.51	20	2.07	9	S36_25_2.51	25	2.07	9	D30_25_2.51	25	2.07
10	P45_20_5	20	4.13	10	S15_25_5	25	4.13	10	D36_25_2.51	25	2.07
11	P13_12.9_0.74	12.9	0.61	11	S34_17.9_0.74	17.9	0.61	11	D32_17.9_4.27	17.9	3.53
12	P32_12.9_4.27	12.9	3.53	12	S19_17.9_4.27	17.9	3.53	12	D23_17.9_0.74	17.9	0.61
13	P34_10_2.51	10	2.07	13	S25_17.9_4.27	17.9	3.53	13	D33_17.9_4.27	17.9	3.53
14	P26_5_5	5	4.13	14	S7_15_2.51	15	2.07	14	D8_15_2.51	15	2.07
15	P17_30_2.51	30	2.07	15	S21_5_5	5	4.13	15	D34_5_5	5	4.13
								16	D57_17.9_4.27	17.9	3.53

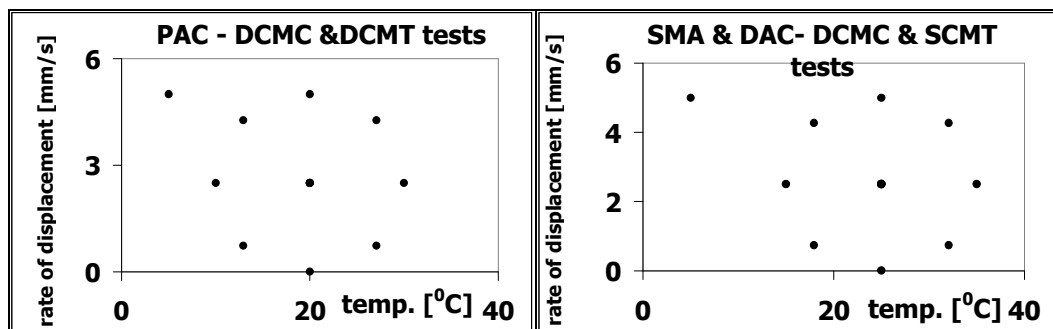


Figure 5.26 DCMC and DCMT target test conditions for PAC, SMA and DAC

5.5 Test Results

The test results from the RMIT, DCMC and DCMT tests were processed and modelled for the three asphalt mixtures. In the following sections the processed results, modelling and a comparison of the modelled results will be presented.

5.5.1 Resilient Modulus Indirect Tensile Test (RMIT)

5.5.1.1 Data processing and Test Results

The resilient modulus was calculated from the RMIT test results using Equation 5.8 (ASTDM 4123) with a Poisson's ratio of 0.35. A Poisson's ratio of 0.35 was chosen since it is not possible to determine Poisson's ratios from the RMIT test data in which the displacements are measured in the radial direction only. Due to asymmetric load signals in some of the tests, the loading time for all the tests was taken to be double the time it took for the load to rise from 0 to the peak value as illustrated in Figure 5.27. The processed RMIT test results for PAC, SMA and DAC are given in Table 5.7, Table 5.8 and Table 5.9. The tables also show the target and the actual pulse duration.

$$M_r = \frac{F(\nu + 0.27)}{LH} \quad 5.8$$

Where:

- M_r = resilient modulus [MPa],
- F = applied force [N],
- ν = Poisson's ratio [-] = 0.35,
- L = specimen thickness [mm],
- H = dynamic horizontal displacement = $\epsilon_r D$,
- ϵ_r = horizontal strain [-],
- D = specimen diameter [mm].

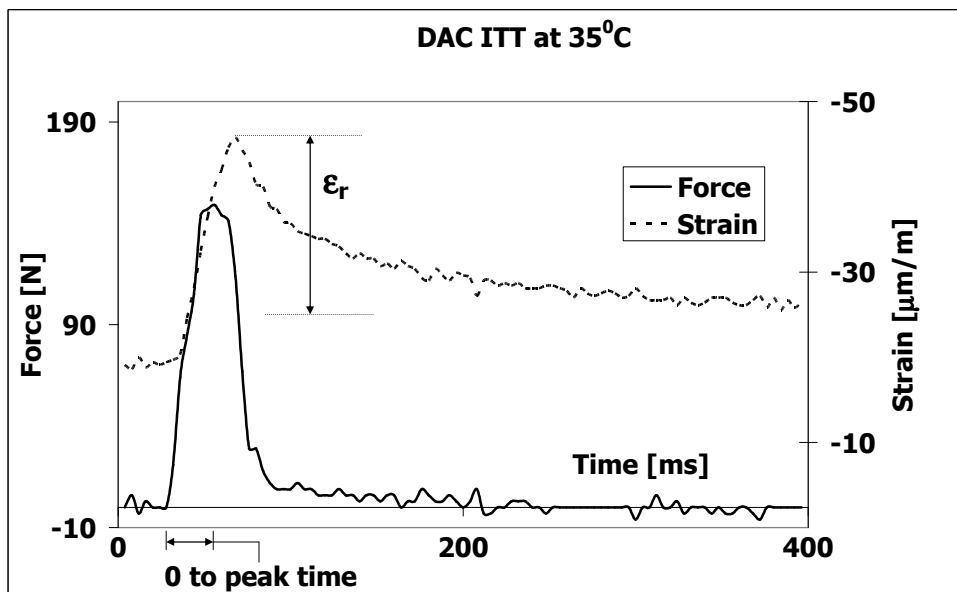


Figure 5.27 An illustration of determination of the loading time for the RMIT

Table 5.7 RMIT Test Results for PAC

Mix	temp [°C]	force [kN]	target pulse width [ms]	actual pulse width [ms]	M _r [MPa]	Mix	temp [°C]	force [kN]	target pulse width [ms]	actual pulse width [ms]	M _r [MPa]
PAC	10	0.6	63	52	5915	PAC	15	0.3	999	957	1808
		0.6	63	48	5961			0.3	999	973	1551
		0.6	63	52	4962			0.4	999	946	1811
		0.6	63	48	5167		20	0.2	63	57	8215
		0.6	63	52	6945			0.2	63	49	2756
		0.6	63	52	4761			0.2	63	54	2899
		0.8	63	53	5167			0.2	63	54	2198
		0.8	63	50	5412			0.2	63	50	2599
		0.8	63	48	4984			0.2	63	47	2279
		0.8	63	47	4637			0.2	125	117	3144
		0.6	125	117	5174			0.2	125	114	2064
		0.6	125	112	4449			0.2	125	109	2003
		0.6	125	114	5650			0.2	200	192	2462
		0.8	125	110	4784			0.2	200	190	1660
		0.8	125	108	5108			0.2	200	192	1625
		0.6	200	161	4738			0.2	500	484	1458
		0.6	200	179	4004			0.2	500	468	1116
		0.6	200	164	4716			0.2	500	485	1183
		0.8	200	166	4105			0.2	999	1022	1079
		0.8	200	182	4439			0.2	999	997	833
	0.6	500	451	3605	0.2	999	1005	902			
	0.6	500	442	2967	25	0.12	63	49	2559		
	0.6	500	446	3319		0.12	63	48	2042		
	0.8	500	443	3056		0.12	63	52	1533		
	0.8	500	462	3308		0.12	63	52	1510		
	0.6	999	886	2969		0.11	63	58	1913		
	0.6	999	901	2423		0.12	63	52	1179		
	0.6	999	904	2560		0.12	125	117	1234		
	0.8	999	883	2418		0.12	125	122	1241		
	0.8	999	880	2633		0.12	125	106	1896		
	0.2	63	55	4803		0.12	200	206	1027		
	0.2	63	54	4340		0.12	200	192	966		
	0.2	63	60	7538		0.12	200	200	1521		
	0.2	63	57	4916		0.12	500	534	707		
	0.3	63	56	5208	0.12	500	506	660			
	0.3	63	55	4314	0.12	500	546	1072			
	0.3	63	54	5533	0.12	999	974	579			
	0.3	63	54	4154	0.12	999	957	502			
	0.4	63	54	6352	0.12	999	1000	845			
	0.4	63	55	4611	30	0.1	63	37	700		
	0.2	125	118	3703		0.1	63	52	1507		
	0.2	125	128	3846		0.1	63	35	703		
	0.3	125	117	3859		0.1	63	30	1175		
	0.3	125	120	4131		0.1	63	33	1488		
	0.4	125	117	4462		0.1	63	30	1217		
	0.2	200	200	3411		0.1	125	119	1011		
	0.2	200	194	4295		0.1	125	72	2063		
	0.3	200	179	3319		0.1	125	68	1171		
	0.3	200	190	2997		0.1	200	202	780		
	0.4	200	182	3515		0.1	200	128	1730		
0.2	500	458	2539	0.1		200	122	997			
0.2	500	490	2703	0.1		500	548	417			
0.3	500	452	2052	0.1	500	318	742				
0.3	500	479	2325	0.1	500	319	591				
0.4	500	474	2424	0.1	999	941	288				
0.2	999	1011	2022	0.1	999	674	632				
0.2	999	997	2037	0.1	999	677	574				

Table 5.8 RMIT Test Results for SMA

Mix	temp [°C]	force [kN]	target pulse width [ms]	actual pulse width [ms]	M _r [MPa]	Mix	temp [°C]	force [kN]	target pulse width [ms]	actual pulse width [ms]	M _r [MPa]	
SMA	15	0.6	63	54	7397	SMA	25	0.25	125	110	1848	
		0.6	63	57	5781			0.25	125	111	1645	
		0.6	63	53	7331			0.25	125	117	1546	
		0.6	63	50	5689			0.25	200	181	1449	
		0.6	63	54	5606			0.25	200	190	1299	
		0.6	63	50	5439			0.25	200	185	1264	
		0.6	125	110	5406			0.25	500	462	989	
		0.6	125	98	5450			0.25	500	476	897	
		0.6	125	112	4560			0.25	500	470	895	
		0.6	200	187	4480			0.25	999	946	759	
		0.6	200	167	4371			0.25	999	970	659	
		0.6	200	176	3766			0.25	999	973	660	
		0.6	500	459	3109			30	0.17	63	51	1673
		0.6	500	458	2949				0.18	63	48	1246
		0.6	500	447	2671		0.17		63	46	1589	
		0.6	999	934	2418		0.17		63	43	1342	
		0.6	999	890	2223		0.18		63	46	1253	
		0.6	999	898	2068		0.17		63	48	1022	
		0.3	63	55	10591		0.17		125	108	1262	
		0.3	63	55	3648		0.17		125	106	1236	
	0.4	63	53	3702	0.18		125		104	970		
	0.4	63	55	3010	0.18		200		189	966		
	0.4	63	48	3608	0.18		200		182	962		
	0.4	63	53	2762	0.17		200		176	769		
	0.4	63	53	3779	0.17		500		456	709		
	0.4	63	55	3431	0.17		500		491	683		
	0.3	125	114	3748	0.17		500		473	560		
	0.4	125	114	2886	0.17		999		938	569		
	0.4	125	107	2539	0.17		999	920	580			
	0.4	125	112	2981	0.17		999	925	479			
	0.3	200	174	2827	35		0.12	63	53	1564		
	0.4	200	187	2204			0.12	63	54	1075		
	0.4	200	185	2028			0.12	63	46	988		
	0.4	200	190	2454			0.12	63	46	781		
	0.3	500	460	1838			0.12	63	50	908		
	0.4	500	483	1477			0.12	63	47	777		
	0.4	500	454	1325			0.12	125	118	1220		
	0.4	500	478	1710			0.12	125	113	724		
	0.3	999	946	1358			0.12	125	108	723		
	0.4	999	928	1090			0.12	200	187	1001		
	0.4	999	920	1024			0.12	200	178	628		
	0.4	999	930	1290			0.12	200	198	596		
	0.25	63	52	2520			0.12	500	486	770		
	0.25	63	55	2101			0.12	500	462	493		
	0.25	63	56	2297			0.12	500	447	485		
	0.25	63	56	1823			0.12	999	926	589		
	0.25	63	54	2131			0.11	999	894	405		
	0.25	63	56	1791			0.12	999	910	400		

Table 5.9 RMIT Test Results for DAC

Mix	temp [°C]	force [kN]	target pulse width [ms]	actual pulse width [ms]	M _r [MPa]		
DAC	15	0.6	63	51	10046		
		0.6	63	50	9934		
		0.8	63	51	10303		
		0.8	63	51	10936		
		1	63	47	9157		
		1	63	50	10201		
		1	63	52	11231		
		1	63	51	10871		
		1	63	50	10204		
		1	63	50	10073		
		0.6	125	114	8135		
		0.8	125	114	8803		
		1	125	113	9591		
		1	125	108	8570		
		1	125	118	9232		
		0.6	200	185	7152		
		0.8	200	178	7852		
		1	200	182	8574		
		1	200	187	7466		
		1	200	182	7749		
	0.6	500	477	5625			
	0.8	500	451	6239			
	1	500	451	6503			
	1	500	442	5667			
	1	500	442	5748			
	0.6	999	950	4642			
	0.8	999	904	5213			
	1	999	899	5363			
	1	999	885	4588			
	1	999	890	4589			
	20	7	0.7	63	54	7919	
			0.7	63	56	7425	
			0.7	63	53	8416	
			0.7	63	54	8312	
			0.7	63	54	7443	
			0.7	63	52	7501	
			0.7	125	105	6351	
			0.7	125	106	6983	
			0.7	125	108	5973	
			0.7	200	180	5378	
		7	0.7	200	176	5947	
			0.7	200	176	5374	
			0.7	500	469	3841	
			0.7	500	442	4382	
			0.7	500	447	3750	
			0.7	999	923	2992	
			0.7	999	912	3436	
			0.7	999	890	2996	
			25	0.35	63	57	5793
				0.35	63	55	5588
0.35	63	55		5171			
DAC	25	0.35	63	52	4640		
		0.35	63	61	4869		
		0.35	63	56	4775		
		0.35	125	114	4248		
		0.35	125	113	3629		
		0.35	125	114	3656		
		0.35	200	180	3586		
		0.35	200	184	3062		
		0.35	200	187	3026		
		0.35	500	468	2419		
		0.35	500	474	2074		
		0.35	500	494	2049		
		0.35	999	952	1786		
		0.35	999	910	1591		
		0.35	999	926	1489		
		30	0.25	63	52	2753	
			0.25	63	52	2523	
			0.25	63	48	2881	
			0.25	63	51	2618	
			0.25	63	55	3131	
	0.25		63	55	2889		
	0.25		125	109	2086		
	0.25		125	113	2048		
	0.25		125	105	2414		
	0.25		200	175	1713		
	35	0.25	200	170	1683		
		0.25	200	178	1955		
		0.25	500	493	1161		
		0.25	500	478	1173		
		0.25	500	488	1325		
		0.25	999	970	909		
		0.25	999	928	934		
		0.25	999	970	1018		
		0.15	63	56	1360		
		0.15	63	50	1247		
	0.15	63	47	1648			
	0.15	63	44	1391			
	0.15	63	45	1798			
	0.15	63	45	1680			
	0.15	125	109	1086			
	0.15	125	106	1325			
	0.15	125	113	1324			
	0.15	200	180	769			
	0.15	200	188	1076			
	0.15	200	173	1178			
	0.15	500	452	587			
	0.15	500	441	778			
	0.15	500	445	832			
	0.15	999	976	490			
	0.15	999	896	611			
0.15	999	928	671				

5.5.1.2 Determination of Unified Model Temperature Susceptibility Parameters

The RMIT test results were modelled using the Unified Model (Medani 2004) shown in Equation 5.9.

$$P = P_{high} + (P_{low} - P_{high})S \quad 5.9$$

Where:

$$S = e^{(-[u_r \beta]^\lambda)} \quad 5.10$$

$$u_r = \frac{1000}{u_0 t} \quad 5.11$$

$$\beta = e^{(-\tau_s [T - T_0])} \quad 5.12$$

u_0	=	a reference value [1/s] for RMIT tests,
t	=	loading time [ms]
$\dot{\epsilon}$	=	strain rate [% per sec],
T_s	=	temperature susceptibility factor [1/K],
T_0	=	a reference value [K],
T	=	temperature [K],
λ	=	model parameter [-].

The Unified Model is described with a range of different parameters and it is important to consider the effect of these parameters in order to obtain an appropriate data fit. Since the purpose of the RMIT was to determine the temperature susceptibility of the asphalt mixtures, the effect of the model parameters was considered based on the temperature susceptibility factors, T_0 and T_s . The theoretical minimum value, P_{low} of the resilient modulus was set to zero since little or no stiffness can be expected at high temperatures especially for compressive tests without confinement. In addition a Kelvin temperature scale was adopted in order to avoid negative temperatures.

The determination of the temperature susceptibility parameters was performed in two stages. In the first stage, the effect of parameter T_0 on other parameters was considered based on the actual data fit. During this stage, the parameter T_0 was fixed at values ranging from 243 K (-40°C) to 333K (60°C). The values of the other parameters were then determined using the excel solver to minimize the total absolute error calculated from Equation 5.13. The chosen temperature range represented temperatures within and without the range of the test temperatures. The second stage involved the optimisation of parameter T_s in such a way to obtain the least total absolute error.

$$total\ absolute\ error = \sum \left(100 \left[\frac{|data - model|}{data} \right] \right) \quad 5.13$$

Where:

total absolute error = sum of the percentage absolute error at all the data points [%],

data = data obtained from the test result,
model = value determined from the model.

Stage 1-Effect of Varying the Reference Temperature

Figure 5.28 shows an example of the data fit at a reference temperature of 273 K for the DAC and the total absolute error for all the data fits as a function of the different reference temperatures. Although the total absolute error may look enormous, it does not mean that the actual error is large. This is because the absolute error is a summation of all the percentage absolute errors at all data points. For example, the total absolute in Figure 5.28 represents a summation of the errors in 102 data points. The figure shows that the model provided a good data fit at all the reference temperatures that were considered for the three asphalt mixtures.

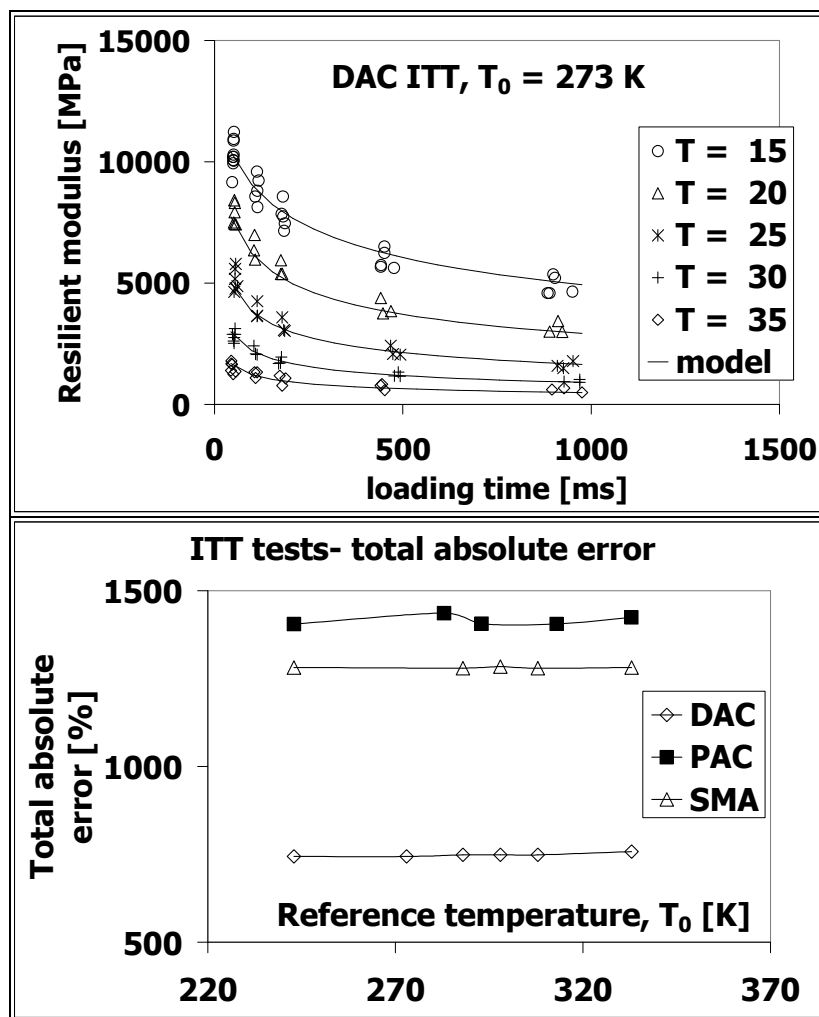


Figure 5.28 Example of the model data for DAC at a reference temperature of 273 K and total absolute error as a function of the reference temperature, T_0 , for DAC, PAC and SMA RMIT results

Figure 5.29 and Figure 5.30 show the variation of the model parameters with respect to all the reference temperatures that were considered for the three asphalt mixtures. Figure 5.29 shows the variation of T_s along with λ and Figure 5.30 shows variation of P_{high} and μ_0 . The two figures show that P_{high} , λ and T_s are

independent of the reference temperature and remain virtually constant irrespective of the reference temperature. The two figures also show that μ_0 is strongly dependent on the reference temperature. This finding indicates that a unique combination of λ , T_s , P_{high} can be confidently estimated irrespective of the reference temperature, T_0 .

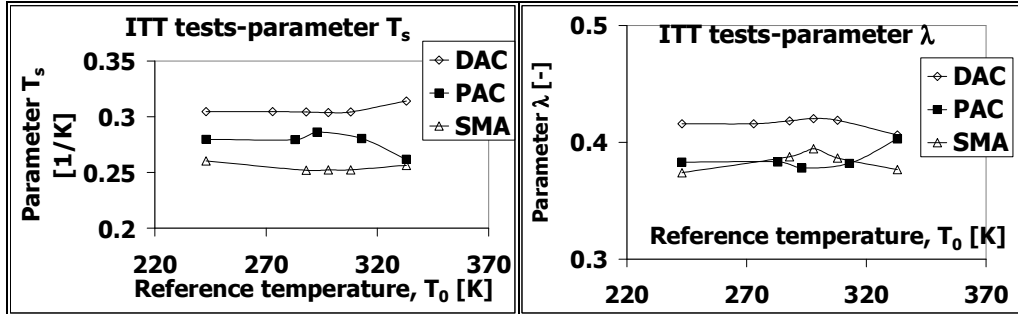


Figure 5.29 Parameter T_s and λ as a function of reference temperature, T_0 , for DAC, PAC and SMA the RMIT results

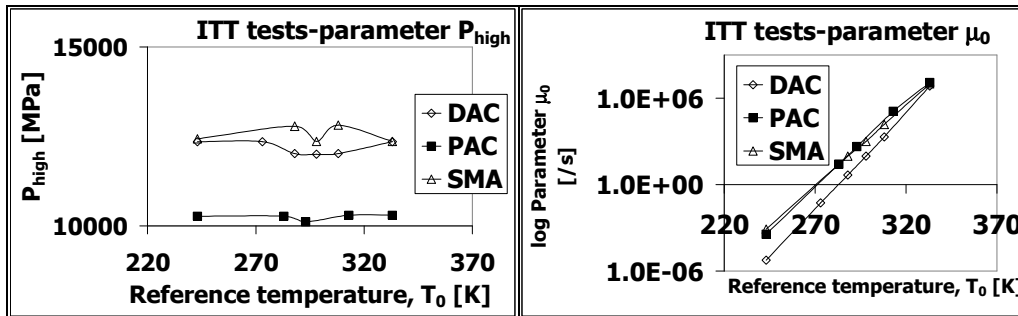


Figure 5.30 Parameter P_{high} and μ_0 as a function of reference temperature, T_0 , for DAC, PAC and SMA RMIT results

Stage 2 - Optimization of Parameter T_s

During the optimization stage, the reference temperature for each asphalt mixture was fixed at the average RMIT temperature and other model parameters were consequently determined. Since the objective of the RMIT tests was to determine the temperature susceptibility of the asphalt mixtures, the parameters P_{high} , λ and μ_0 were determined by optimizing parameter T_s in such a way that the total absolute error was minimum. The optimization process entailed the determination of other model parameters at fixed T_s to obtain a narrow range of T_s values at minimum error. The initial T_s value was then selected within the narrow range and initial values for parameters P_{high} , λ and μ_0 manually fitted to obtain the closest model fit. After which the excel solver was allowed to determine all the model parameters. Figure 5.31 shows the optimization along with the consequent λ values and Figure 5.32 shows the consequent μ_0 and P_{high} values. Figure 5.33, Figure 5.34 and Figure 5.35 show the final RMIT model fit for the PAC, SMA and DAC mixtures respectively while Table 5.10 shows the final model parameters for the three asphalt mixtures. Figure 5.33, Figure 5.34 and Figure 5.35 shows that the model parameters provided a reasonable fit for the measured data.

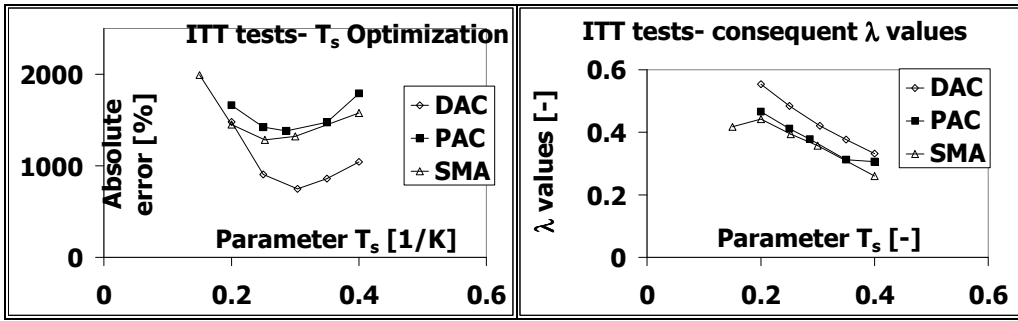


Figure 5.31 Optimization of parameter T_s and consequent λ values

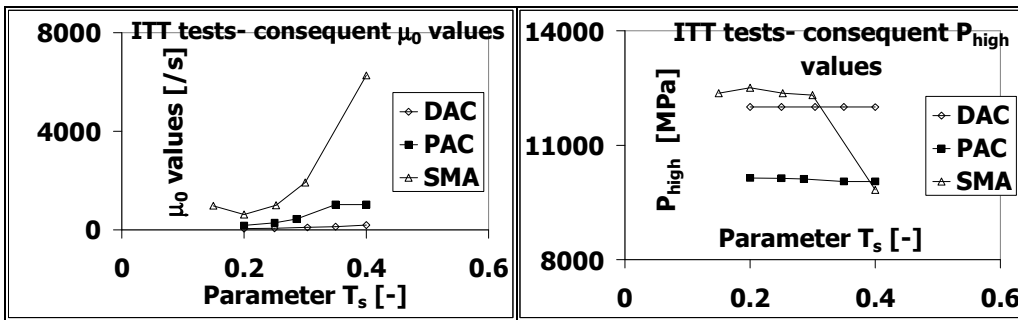


Figure 5.32 Consequent μ_0 and P_{high} values

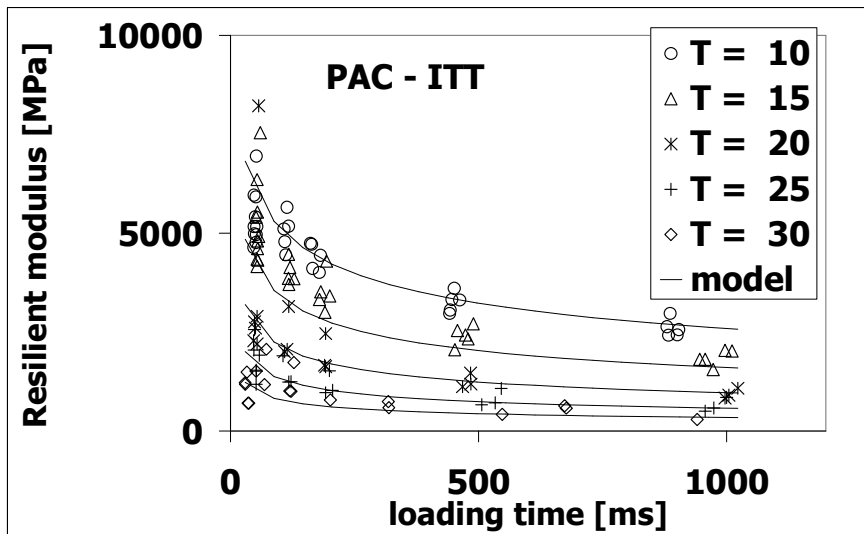


Figure 5.33 Final RMIT model fit for PAC

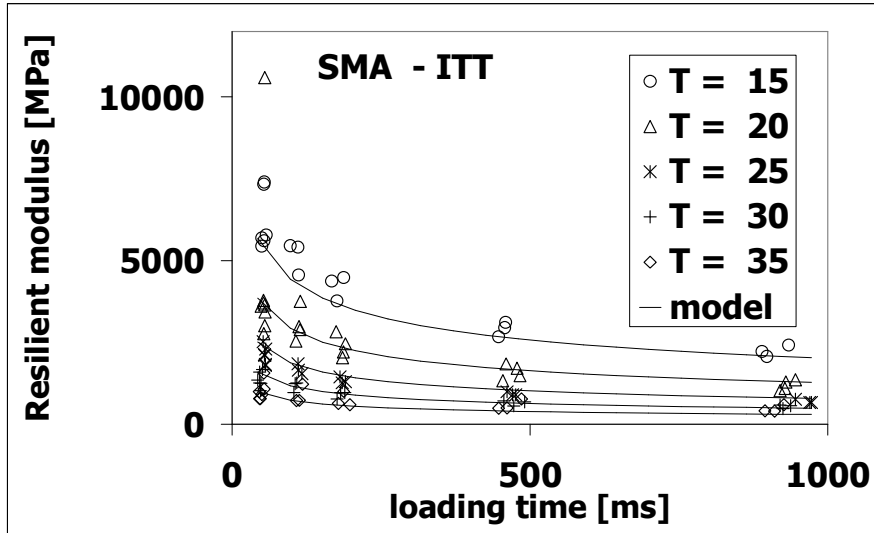


Figure 5.34 Final RMIT model fit for PAC

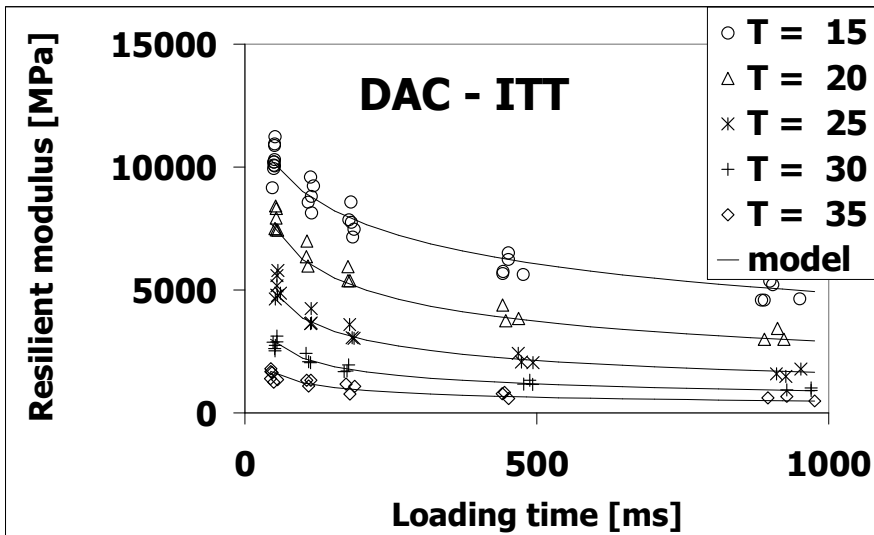


Figure 5.35 Final RMIT model fit for DAC

Table 5.10 Final RMIT Unified Model parameters for the three asphalt mixtures

Mix	Parameter					
	λ	T_s	T_0	u_0	P_{high}	P_{low}
PAC	0.378	0.286	293	438.1	10119	0
SMA	0.395	0.252	298	1001.1	12365	0
DAC	0.420	0.304	298	96.6	12005	0

5.5.1.3 A Comparison of the RMIT Results for PAC, SMA and DAC Asphalt Mixtures

Figure 5.36 shows a comparison of the RMIT results at loading times between 45 and 1000 ms and at a temperature of 15 and 35°C based on the final Unified Model parameters for the three asphalt mixtures. These loading times and temperatures represent the lowest and the highest temperatures at which RMIT tests were conducted. The figure shows that irrespective of the temperature and

loading time, the three asphalt mixtures can be ranked in order of decreasing stiffness as DAC, SMA and PAC.

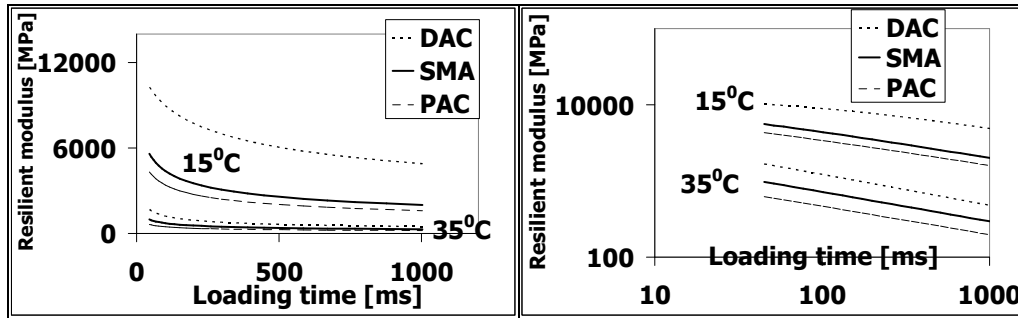


Figure 5.36 A comparison of the RMIT results at a low and a high temperature for the three asphalt mixtures

5.5.2 Displacement Controlled Monotonic Compression and Tension Tests (DCMC and DCMT)

5.5.2.1 Data Processing

The initial phase of DCMC and DCMT tests data processing involved the determination of the vertical stress, axial strain, radial strain and volumetric strains as in Equations 5.14, 5.15, 5.16 and 5.17.

$$\sigma_1 = \text{vertical stress} = (\text{load} + \text{self weight}) / \text{initial cross section area} \quad 5.14$$

$$\text{axial strain} = \varepsilon_a = \text{change in height} / \text{original height} = \Delta h / h_0 \quad 5.15$$

$$\text{radial strain} = \varepsilon_r = \text{change in radius} / \text{original radius} = \Delta r / r_0 \quad 5.16$$

$$\text{volumetric strain} = \varepsilon_v = 2\varepsilon_r + \varepsilon_a \quad 5.17$$

In the tension test and the initial part of the compression test, the radial deformation, Δr , was measured using the extensometer as shown in Figure 5.37 and calculated from Equation 5.18 (MTS manual).

$$\Delta r = \frac{l - l_i}{2 \left[\sin\left(\frac{\theta_i}{2}\right) + \left(\frac{2\pi - \theta_i}{2}\right) \cos\left(\frac{\theta_i}{2}\right) \right]} \quad 5.18$$

Where:

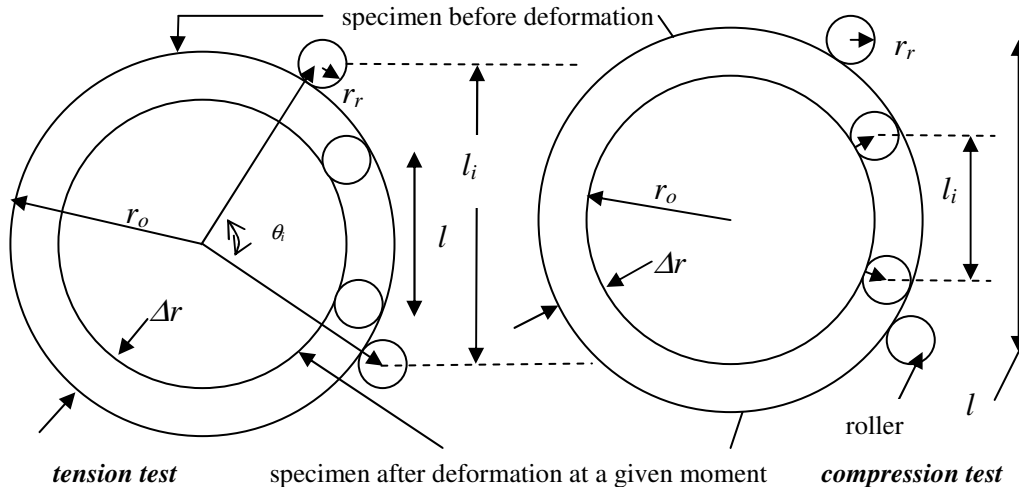
$$\theta_i = 2\pi - \frac{l_c}{(r_o + r_r)} \quad 5.19$$

Beyond the range of the extensometer, the radial deformation in the compression test was measured using two potentiometers and a string as illustrated in Figure 5.38 and calculated iteratively from Equation 5.20 (Erkens and Poot 2000).

5.20

$$\Delta r = \frac{P - \sqrt{\left(L_i^1\right)^2 + \left(\frac{\Delta h}{2}\right)^2 + \Delta r^2} + L_i^1 - \sqrt{\left(L_i^2\right)^2 + \left(\frac{\Delta h}{2}\right)^2 + \Delta r^2} + L_i^2}{2\pi}$$

where: P = change in the length of the string.



- $r_r = 3.048 \text{ mm}$
- $l_c = 206 \text{ mm (DCMC)}$
- $l_c = 199.7 \text{ mm (DCMT)}$
- $l =$ extensometer measurement at a given moment
- $l_i =$ initial extensometer measurement

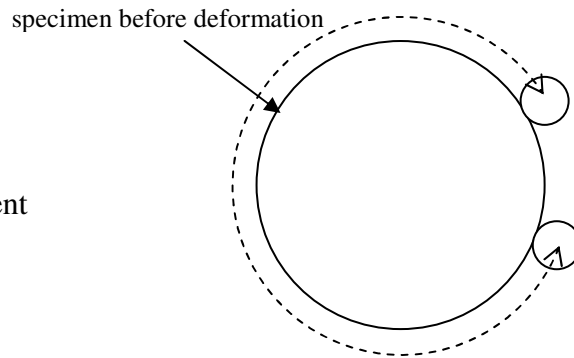


Figure 5.37 Measurement of radial deformation using an extensometer

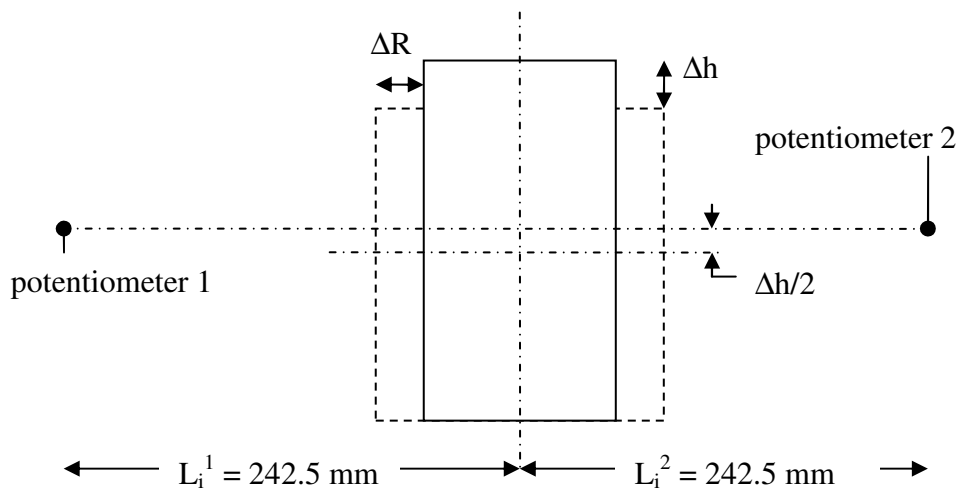


Figure 5.38 Determination of radial deformation in the compression test using two potentiometers and a string

The second phase of the processing concerned the determination of the strain rate, elastic modulus, Poisson's ratio, maximum stress and point of initiation of dilation. Figure 5.39 shows an illustration of the determination of these quantities from a DAC DCMC test conducted at 5⁰C and at a displacement rate of 5 mm/s.

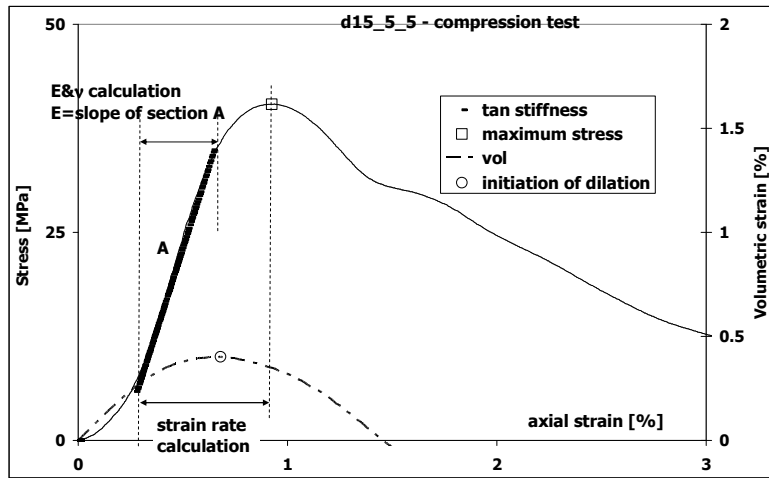


Figure 5.39 An illustration of the determination of strain rate, tangent stiffness, Poisson's ratio, maximum stress and point of initiation of dilation from a DCMC test

The strain rate for DCMC and DCMT tests was determined as the average strain rate up the point of maximum stress. The average strain rate up to the maximum stress was chosen due to inconsistent strain rates in the DCMT tests (see Figure 5.40 to Figure 5.44). This was in contrast to the DCMC tests in which the strain rates remained constant through out the duration of the tests (see Figure 5.46 to Figure 5.49).

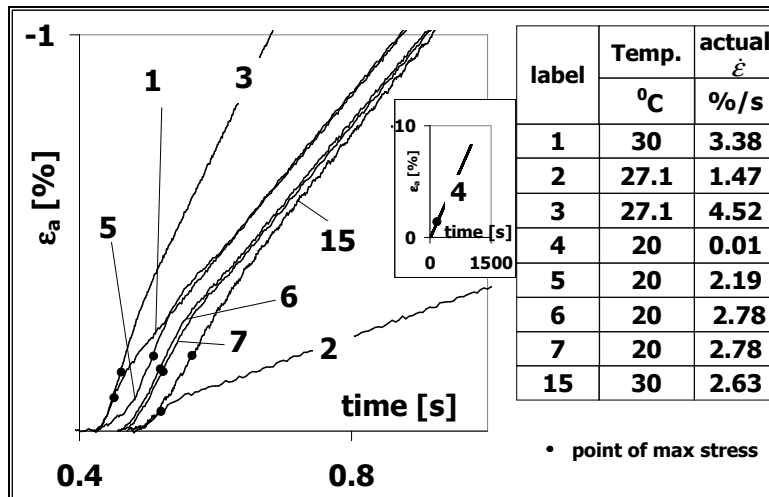


Figure 5.40 Strain versus time plots for the PAC DCMT tests-1

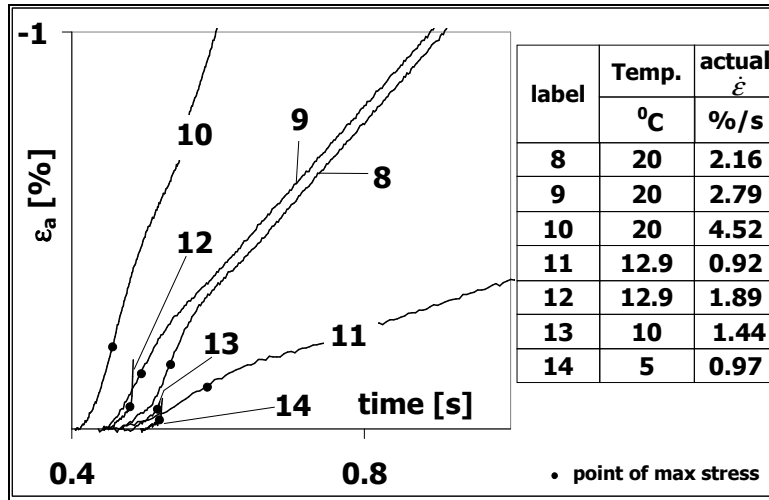


Figure 5.41 Strain versus time plots for the PAC DCMT tests-2

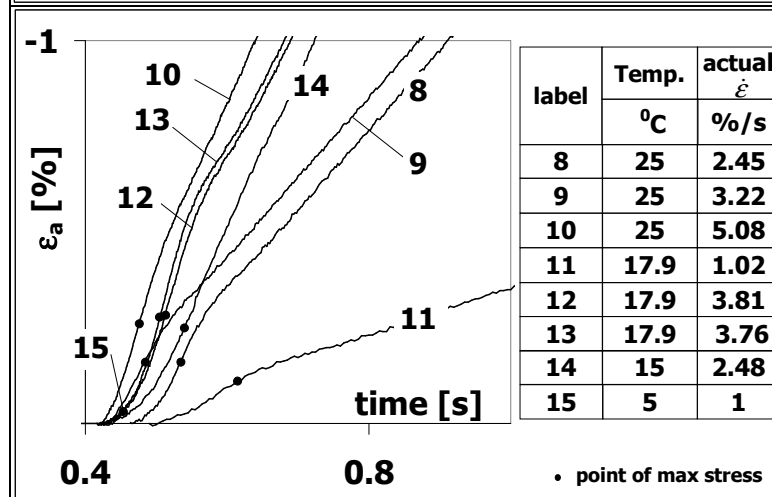
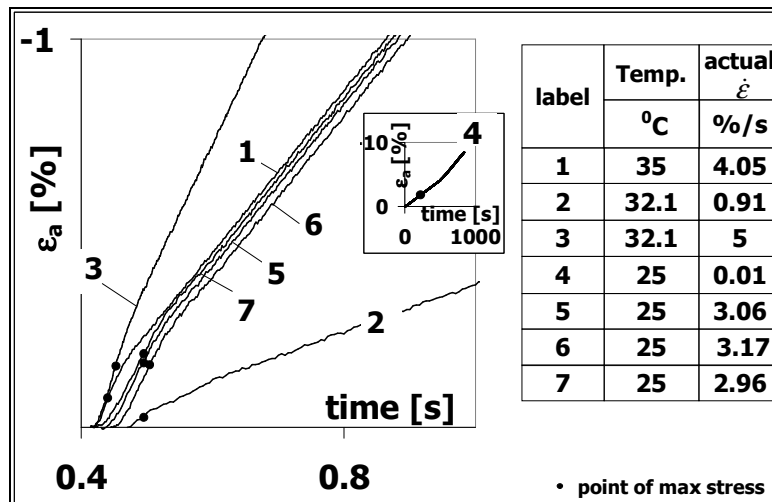


Figure 5.42 Strain versus time plots for the SMA DCMT tests

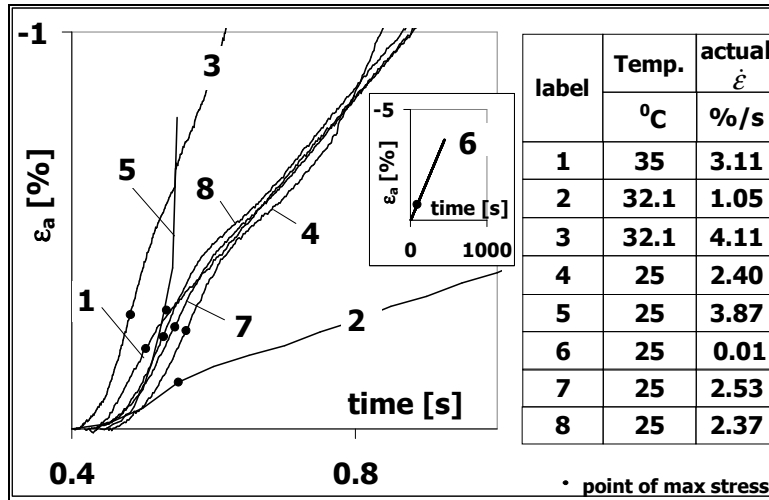


Figure 5.43 Strain versus time plots for DAC DCMT tests -1

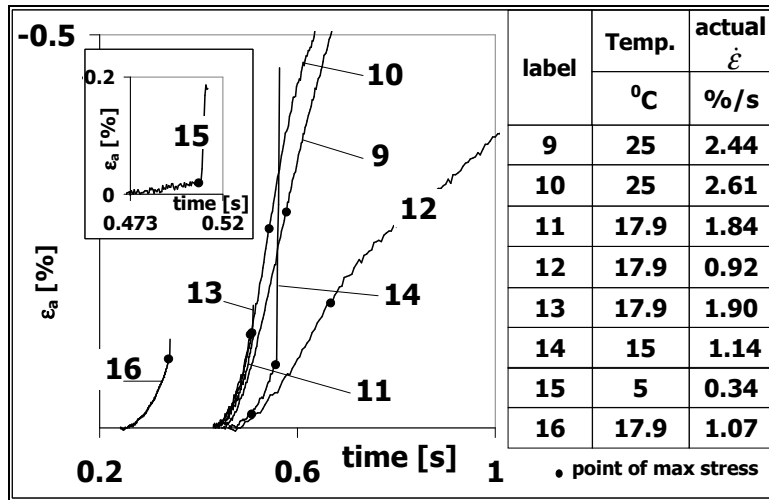


Figure 5.44 Strain versus time plots for the DAC DCMT tests-2

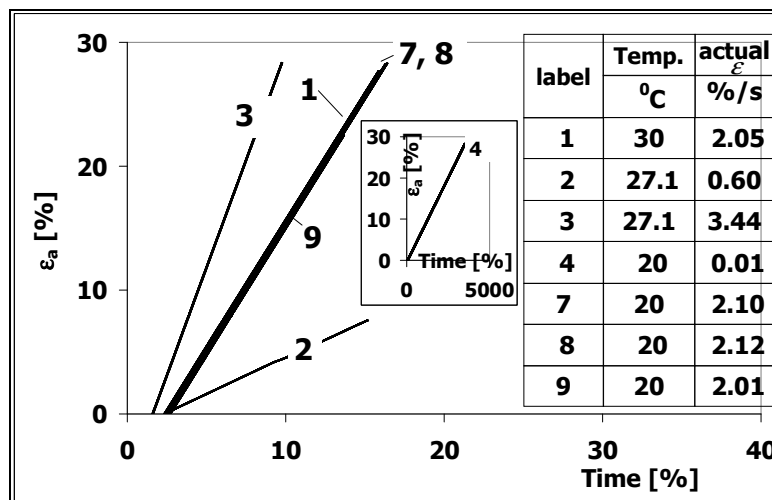


Figure 5.45 Strain versus time plots for the PAC DCMC tests-1

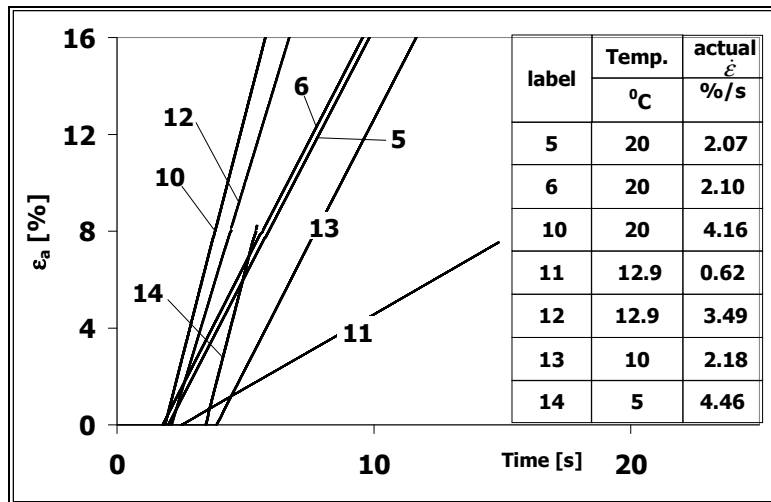


Figure 5.46 Strain versus time plots for the PAC DCMC tests-2

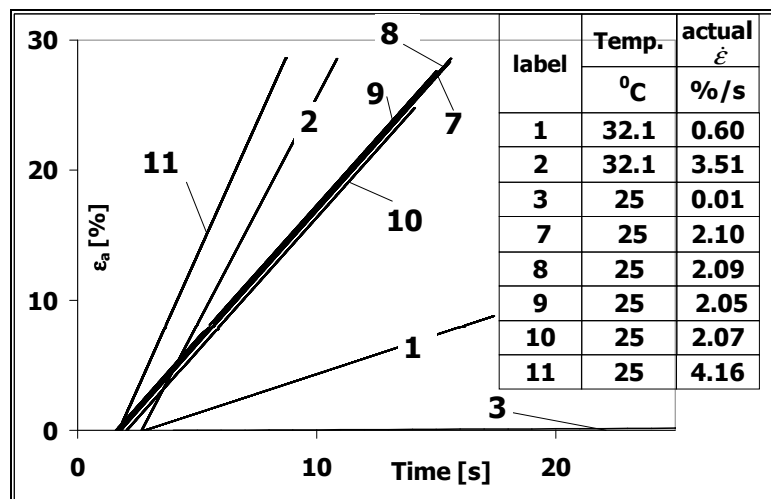


Figure 5.47 Strain versus time plots for SMA DCMC tests-1

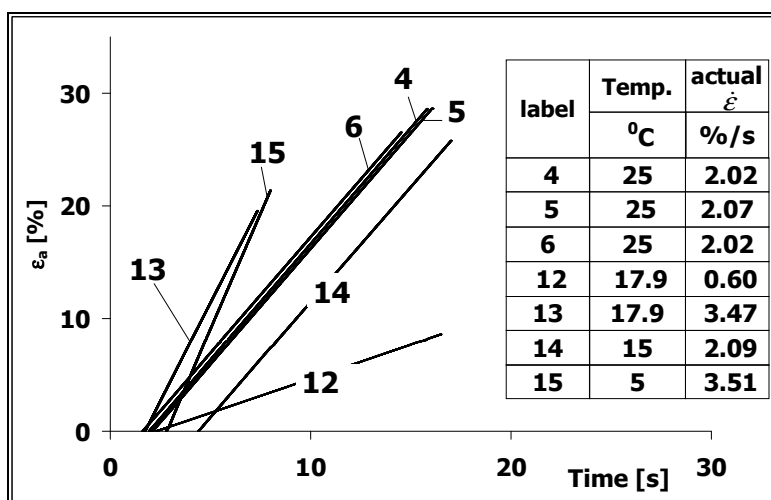


Figure 5.48 Strain versus time plots for the SMA DCMC tests -2

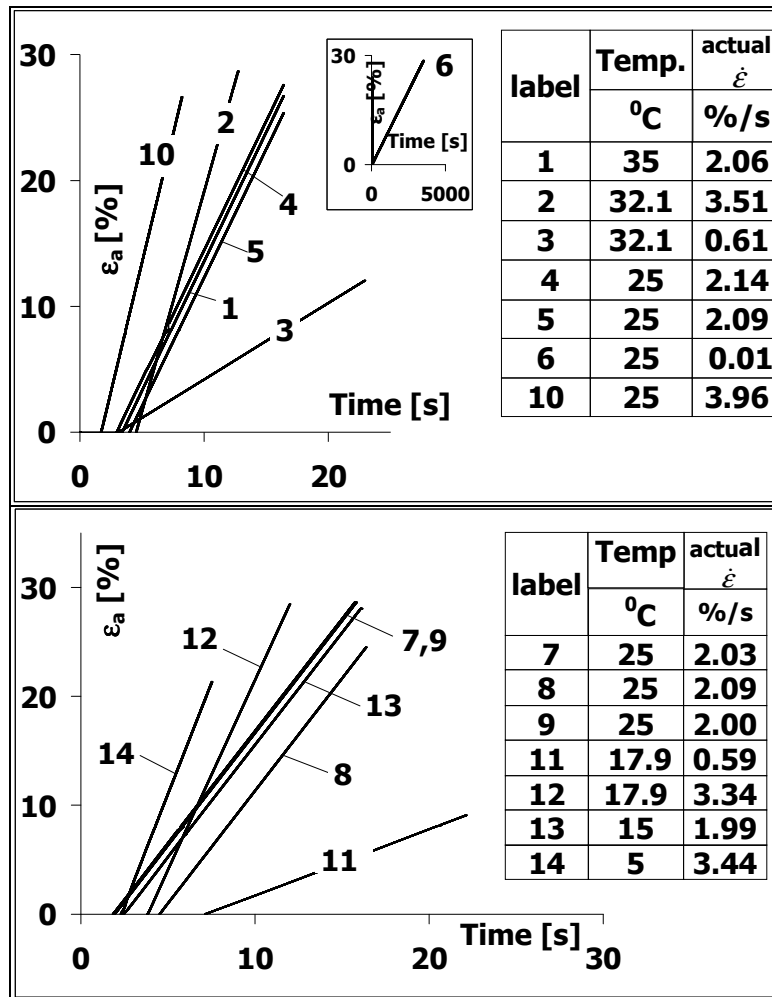


Figure 5.49 Strain versus time plots for the DAC DCMC tests

5.5.2.2 DCMC Test Results

The test results for the DCMC tests for the three asphalt mixtures are presented in Figure 5.50 to Figure 5.54. The strain rate in these figures represents the actual strain rate during the tests. The tabulated DCMC results are given in Table 5.11, Table 5.12 and Table 5.13.

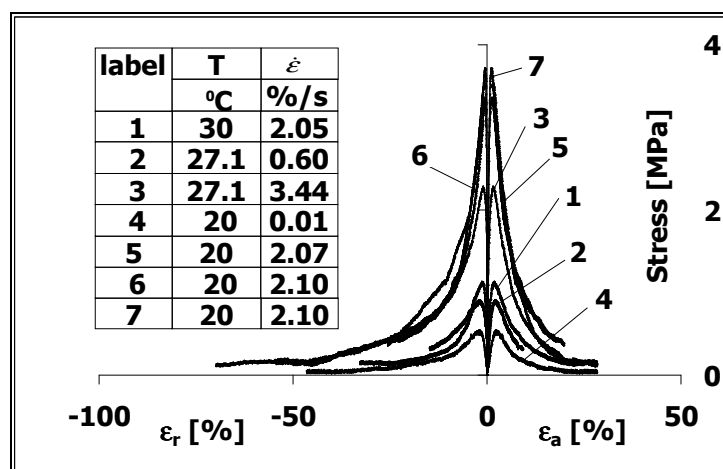


Figure 5.50 DCMC test results for PAC -1

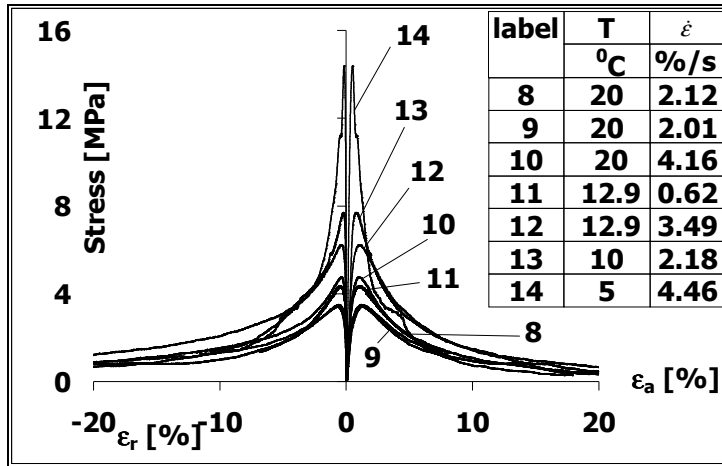


Figure 5.51 DCMC test results for PAC-2

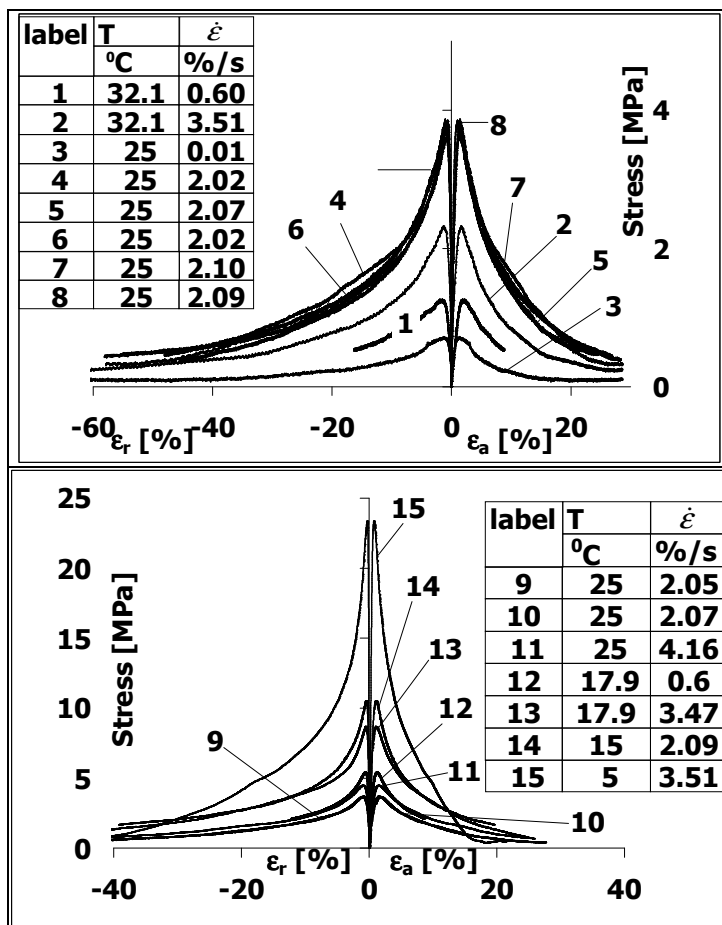


Figure 5.52 DCMC test Results for SMA at 5, 15, 17.9, 25 and 32.1°C

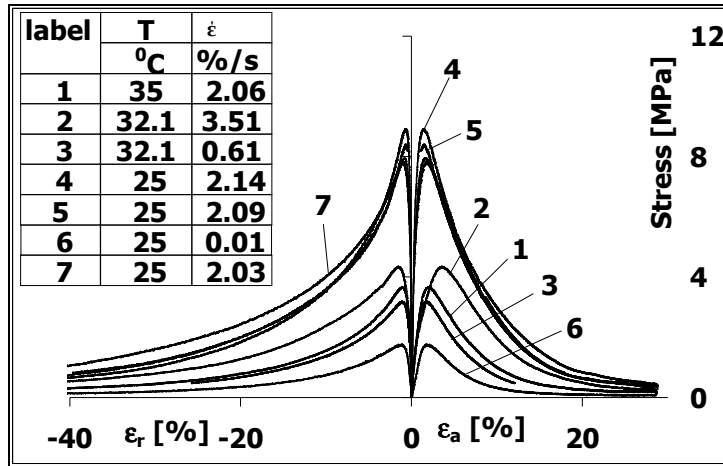


Figure 5.53 DCMC test results for DAC at 25, 32.1 and 35°C

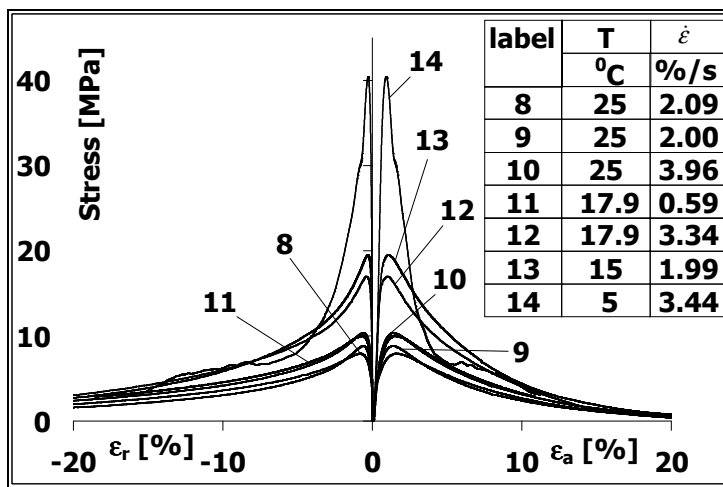


Figure 5.54 DCMC test results for DAC at 5, 15, 17.9, and 25°C

Table 5.11 DCMC test results for PAC

Label	Test code	Temp [°C]	Target strain rate [%/s]	Actual strain rate [%/s]	f_c [MPa]	Tangential E [MPa]
1	P33_30_2.51	30	2.07	2.05	1.1	195
2	P30_27.1_0.74	27.1	0.61	0.60	0.9	102
3	P31_27.1_4.27	27.1	3.53	3.44	2.2	376
4	P18_20_0.01	20	0.01	0.01	0.5	30
5	P24_20_2.51	20	2.07	2.07	3.5	641
6	P21_20_2.51	20	2.07	2.10	3.3	695
7	P16_20_2.51	20	2.07	2.10	3.6	875
8	P15_20_2.51	20	2.07	2.12	3.4	759
9	P12_20_2.51	20	2.07	2.01	3.4	633
10	P19_20_5	20	4.13	4.16	4.7	1124
11	P11_12.9_0.74	12.9	0.61	0.62	4.3	1128
12	P29_12.9_4.27	12.9	3.53	3.49	6.1	1348
13	P4_10_2.51	10	2.07	2.18	7.6	2064
14	P20_5_5	5	4.13	4.46	14.1	4581

Table 5.12 DCMC test results for SMA

Label	Test code	Temp [°C]	Target strain rate [%/s]	Actual strain rate [%/s]	f _c [MPa]	Tangential E [MPa]
1	S18_32.1_0.74	32.1	0.61	0.60	1.2	91
2	S16_32.1_4.27	32.1	3.53	3.51	2.3	462
3	S32_25_0.01	25	0.01	0.01	0.7	77
4	S8_25_2.51	25	2.07	2.02	3.5	939
5	S23_25_2.51	25	2.07	2.07	3.8	744
6	S9_25_2.51	25	2.07	2.02	3.7	701
7	S24_25_2.51	25	2.07	2.10	3.7	659
8	S35_25_2.51	25	2.07	2.09	3.8	561
9	S39_25_2.51	25	2.07	2.05	3.6	426
10	S42_25_2.51	25	2.07	2.07	3.6	524
11	S17_25_5.0	25	4.13	4.16	4.4	946
12	S4_17.9_0.74	17.9	0.61	0.60	5.3	1106
13	S5_17.9_4.27	17.9	3.53	3.47	8.5	1717
14	s1_15_2.51	15	2.07	2.09	10.3	2197
15	S13_5_5	5	4.13	3.51	22.9	5538

Table 5.13 DCMC test results for DAC

Label	Test code	Temp [°C]	Target strain rate [%/s]	Actual strain rate [%/s]	f _c [MPa]	Tangential E [MPa]
1	d2_35_2.51	35	2.07	2.06	3.6	369
2	D16_32.1_4.27	32.1	3.53	3.51	4.3	558
3	D12_32.1_0.74	32.1	0.61	0.61	3.1	474
4	D18_25_2.51	25	2.07	2.14	8.8	2000
5	D17_25_2.51	25	2.07	2.09	8.2	1872
6	D22_25_0.01	25	0.01	0.01	1.7	135
7	D24_25_2.51	25	2.07	2.03	7.7	1455
8	D3_25_2.51	25	2.07	2.09	7.8	1955
9	D19_25_2.51	25	2.07	2.00	8.7	2101
10	D20_25_5.0	25	4.13	3.96	10.2	2238
11	D11_17.9_0.74	17.9	0.61	0.59	9.9	1936
12	D21_17.9_4.27	17.9	3.53	3.34	16.7	3760
13	d1_15_2.51	15	2.07	1.99	19.4	4268
14	D15_5_5	5	4.13	3.44	39.7	7871

5.5.2.3 DCMT Test Results

The test results for the DCMT tests for the three asphalt mixtures are presented in Figure 5.55, Figure 5.56 and Figure 5.57. The tabulated DCMT results are given in Table 5.14, Table 5.15 and Table 5.16. The strain rates indicated in these figures represent the actual strain rate during the tests. In some of the DCMT tests, for example PAC test labels 3, 5, and 6, the radial strain was observed to decrease prior to the termination of the test. This decrease in radial strain can be explained by stress relaxation that occurs after the specimen is broken.

As it will be discussed later in section 5.5.3, some of the tension test results were observed to deviate from the modelled test results. The tests results in which a large deviation was observed are shown in a different shade in the tables for the tension test results.

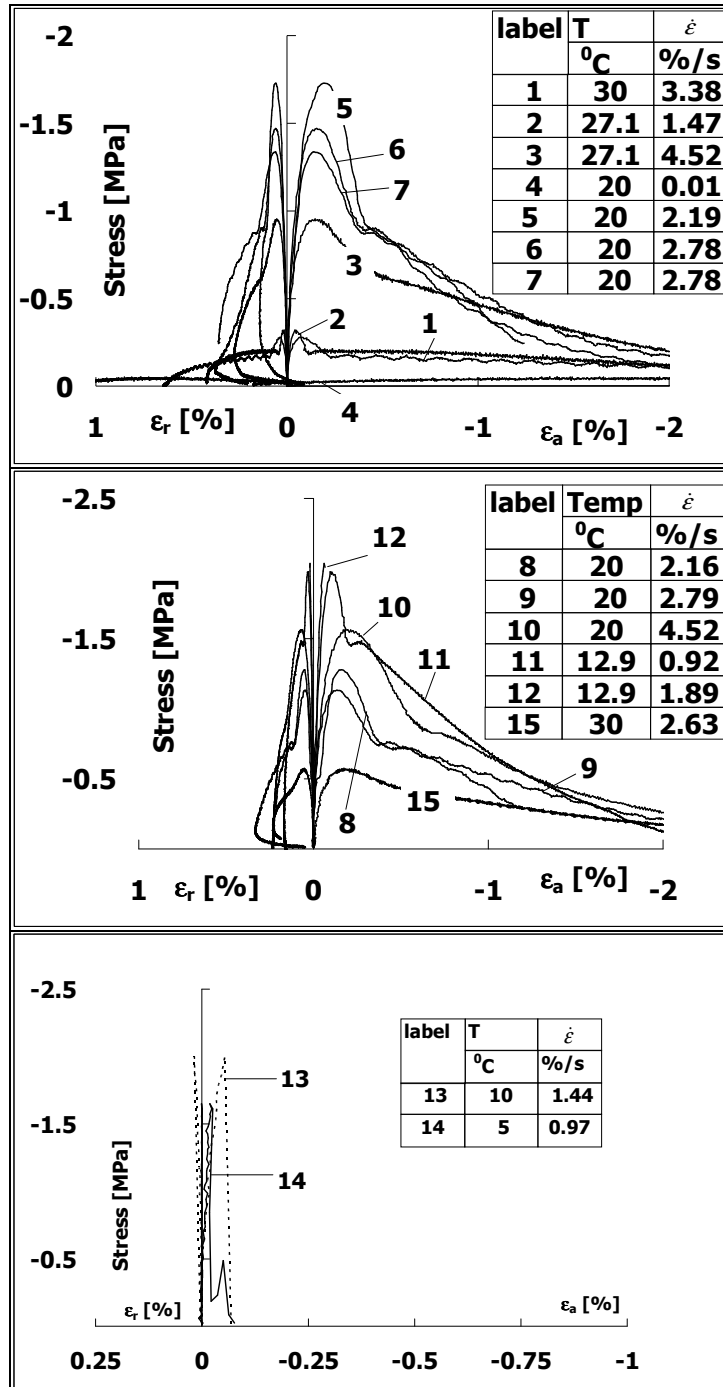


Figure 5.55 DCMT Test Results for PAC at 5, 10, 12.9, 20, 27.1 and 30°C

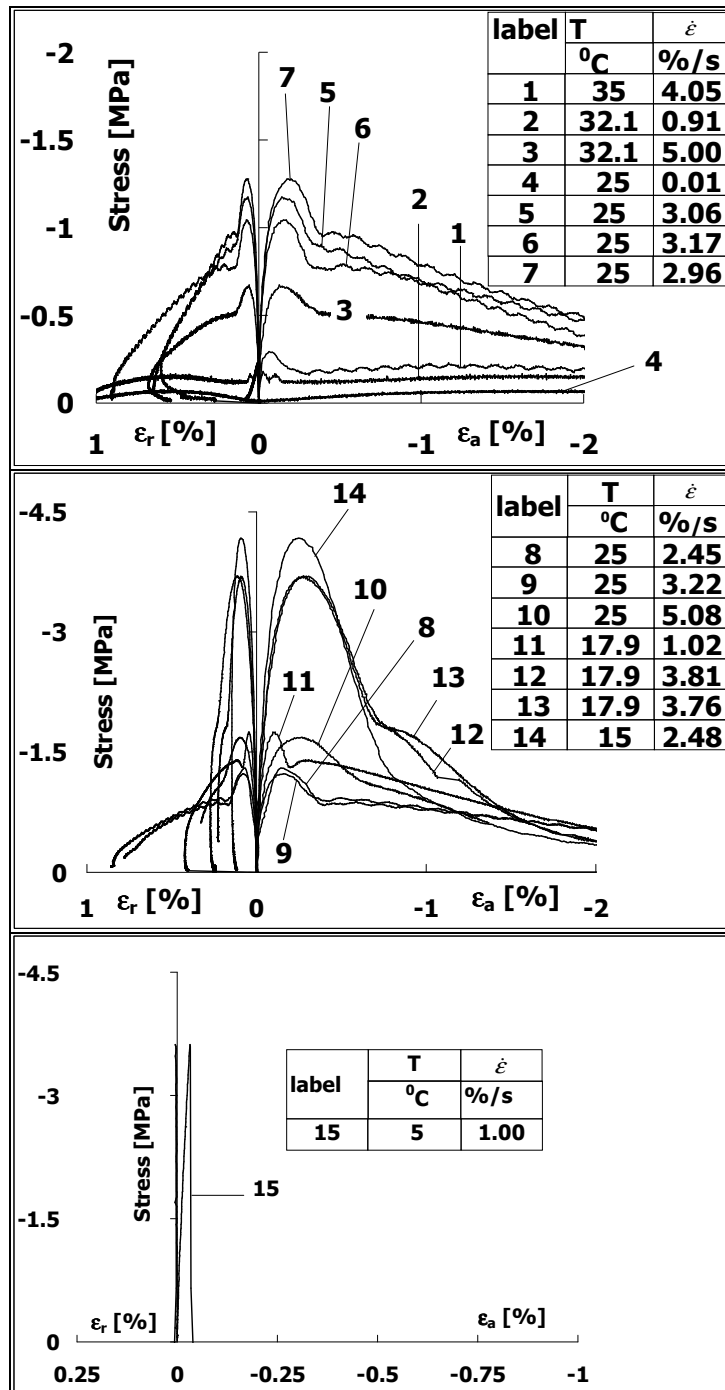


Figure 5.56 DCMT Test Results for SMA at 5, 15, 17.9, 25, 32.1 and 35°C

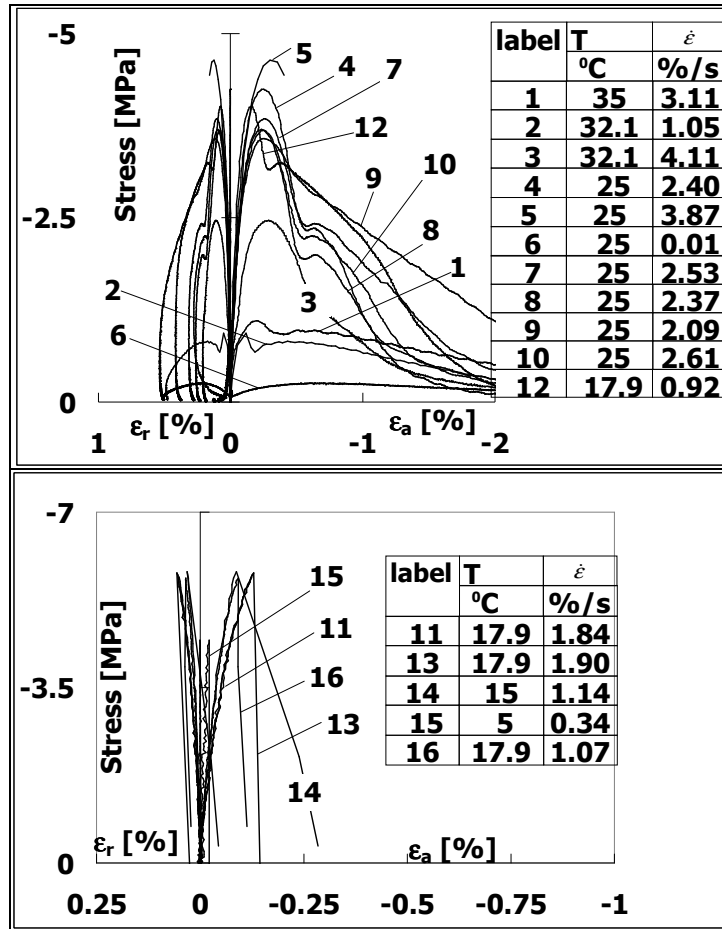


Figure 5.57 DCMT Test Results for DAC at 5, 15, 17.9, 25, 32.1 and 35^oC

Table 5.14 DCMT test results for PAC

Label	Test code	Temp [$^{\circ}\text{C}$]	Target strain rate [$\%/\text{s}$]	Actual strain rate [$\%/\text{s}$]	f_t [MPa]	Tangential E [MPa]
1	P27_30_2.51	30	2.07	3.38	0.27	824
2	P37_27.1_0.74	27.1	0.61	1.47	0.32	919
3	P22_27.1_4.27	27.1	3.53	4.52	0.94	1462
4	P41_20_0.01	20	0.01	0.01	0.05	2
5	P10_20_2.51	20	2.07	2.19	1.70	2139
6	P23_20_2.51	20	2.07	2.78	1.45	2329
7	P28_20_2.51	20	2.07	2.78	1.32	2241
8	P35_20_2.51	20	2.07	2.16	1.26	1974
9	P38_20_2.51	20	2.07	2.79	1.11	2392
10	P45_20_5	20	4.13	4.52	1.53	2026
11	P13_12.9_0.74	12.9	0.61	0.92	1.94	3449
12	P32_12.9_4.27	12.9	3.53	1.89	1.99	3638
13	P34_10_2.51	10	2.07	1.44	1.97	3332
14	P26_5_5	5	4.13	0.97	1.61	5664
15	P17_30_2.51	30	2.07	2.63	0.56	602

Table 5.15 DCMT test results for SMA

Label	Test code	Temp [°C]	Target strain rate [%/s]	Actual strain rate [%/s]	f_t [MPa]	Tangential E [MPa]
1	S56_35_2.51	35	2.07	4.05	0.29	630
2	S26_32.1_0.74	32.1	0.61	0.91	0.18	440
3	S27_32.1_4.27	32.1	3.53	5.00	0.66	976
4	S14_25_0.01	25	0.01	0.01	0.07	6
5	S31_25_2.51	25	2.07	3.06	1.15	1764
6	S38_25_2.51	25	2.07	3.17	1.02	1446
7	S40_25_2.51	25	2.07	2.96	1.25	1494
8	S41_25_2.51	25	2.07	2.45	1.27	1057
9	S36_25_2.51	25	2.07	3.22	1.21	1502
10	S15_25_5	25	4.13	5.08	1.65	1513
11	S34_17.9_0.74	17.9	0.61	1.02	1.71	2268
12	S19_17.9_4.27	17.9	3.53	3.81	3.63	2993
13	S25_17.9_4.27	17.9	3.53	3.76	3.62	2455
14	S7_15_2.51	15	2.07	2.48	4.10	4011
15	S21_5_5	5	4.13	1.00	3.56	16441

Table 5.16 DCMT test results for DAC

Label	Test code	Temp [°C]	Target strain rate [%/s]	Actual strain rate [%/s]	f_t [MPa]	Tangential E [MPa]
1	D6_35_2.51	35	2.07	3.11	1.08	934
2	D35_32.1_0.74	32.1	0.61	1.05	0.93	548
3	D28_32.1_4.27	32.1	3.53	4.11	2.42	1606
4	D13_25_2.51	25	2.07	2.40	4.17	3687
5	D31_25_5	25	2.07	3.87	4.56	3365
6	D39_25_0.01	25	0.01	0.01	0.25	71
7	D29_25_2.51	25	2.07	2.53	3.78	3572
8	D38_25_2.51	25	2.07	2.37	3.63	3684
9	D30_25_2.51	25	2.07	2.44	3.51	3310
10	D36_25_2.51	25	2.07	2.61	3.62	3069
11	D32_17.9_4.27	17.9	3.53	1.84	5.61	5518
12	D23_17.9_0.74	17.9	0.61	0.92	3.94	4119
13	D33_17.9_4.27	17.9	3.53	1.90	5.66	5696
14	D8_15_2.51	15	2.07	1.14	5.68	8172
15	D34_5_5	5	4.13	0.34	4.36	18810
16	D57_17.9_4.27	17.9	3.53	1.07	5.55	7999

5.5.3 DCMC and DCMT Tests

The test results derived from the DCMC and DCMT tests included maximum stress, Poisson's ratio, stress at initiation of plasticity and dilation for the DCMC tests, and tangent stiffness. Due to the considerable scatter, the results for the Poisson's ratio were modelled by a constant value closest to all the test values regardless of the temperature. Apart from the Poisson's ratio, the other tests results were modelled using the Unified Model and the temperature susceptibility factor, T_s , determined from the RMIT tests as shown in Equation 5.21. The theoretical minimum value, P_{low} of the properties derived from the DCMC and DCMT tests was set to zero since little or no strength and stiffness can be expected at high temperatures without confinement. Table 5.17 shows the Unified

Model parameters determined for the DCMC and DCMT tests and Figure 5.58, Figure 5.59, Figure 5.60 and Figure 5.61 show illustrations of the model fit on the data derived from the DCMC and DCMT tests. The figures show that the model provided a reasonable description of the test results. However, some of the tension test results were observed to deviate from the modelled test results. Figure 5.62 shows the data and modelled test results for tensile strength and tangent stiffness for the three asphalt mixtures. The figure shows that the tensile strength for SMA test label 4 exhibited a large deviation from the modelled test results. The figure also shows that the tangent stiffness for PAC (test label 4), SMA (test label 4, 15) and DAC (test label 6, 15) also exhibited large deviation from the modelled test results. The cause of this large deviation is not clear.

$$P = P_{high} + (P_{low} - P_{high})S \quad 5.21$$

Where:

$$S = e^{(-[u_r\beta]^\lambda)} \quad 5.22$$

$$u_r = \frac{\dot{\epsilon}}{u_0} \quad 5.23$$

$$\beta = e^{(-T_s[T-T_0])} \quad 5.24$$

- u_0 = a reference value [% per second],
 $\dot{\epsilon}$ = strain rate [% per sec],
 T_s = temperature susceptibility factor [1/K] determined from RMIT tests,
 T_0 = a reference value [K],
 T = temperature [K],
 λ = model parameter [-].

Table 5.17 Unified Model parameters for the DCMC and DCMT tests

Mix	Test	symbol	λ	T_s	T_0	u_0	P_{high}	P_{low}
PAC	maximum stress in compression	f_c	0.346	0.286	293	500.2	24	0
	tangent stiffness in compression	E_c	0.453	0.286	293	716.0	9102	0
	maximum stress in tension	f_t	0.628	0.286	293	2.6	2	0
	tangent stiffness in tension	E_t	0.382	0.286	293	113.3	9999	0
	stress at initiation of dilation	σ_{dm}	0.499	0.286	293	69.0	15	0
	stress at initiation of plasticity	σ_{pm}	0.597	0.286	293	30.8	10	0
SMA	maximum stress in compression	f_c	0.402	0.252	298	328.5	30	0
	tangent stiffness in compression	E_c	0.475	0.252	298	600.0	10000	0
	ultimate strength in tension	f_t	0.696	0.252	298	13.2	4	0
	tangent stiffness in tension	E_t	0.391	0.252	298	704.5	12988	0
	stress at initiation of dilation	σ_{dm}	0.650	0.252	298	83.2	20	0
	stress at initiation of plasticity	σ_{pm}	0.597	0.252	298	139.2	19	0
DAC	maximum stress in compression	f_c	0.316	0.304	298	805.6	57	0
	tangent stiffness in compression	E_c	0.446	0.304	298	76.3	8055	0
	ultimate strength in tension	f_t	0.551	0.304	298	2.6	6	0
	tangent stiffness in tension	E_t	0.480	0.304	298	13.2	8500	0
	stress at initiation of dilation	σ_{dm}	0.405	0.304	298	135.8	39	0
	stress at initiation of plasticity	σ_{pm}	0.479	0.304	298	168.8	36	0

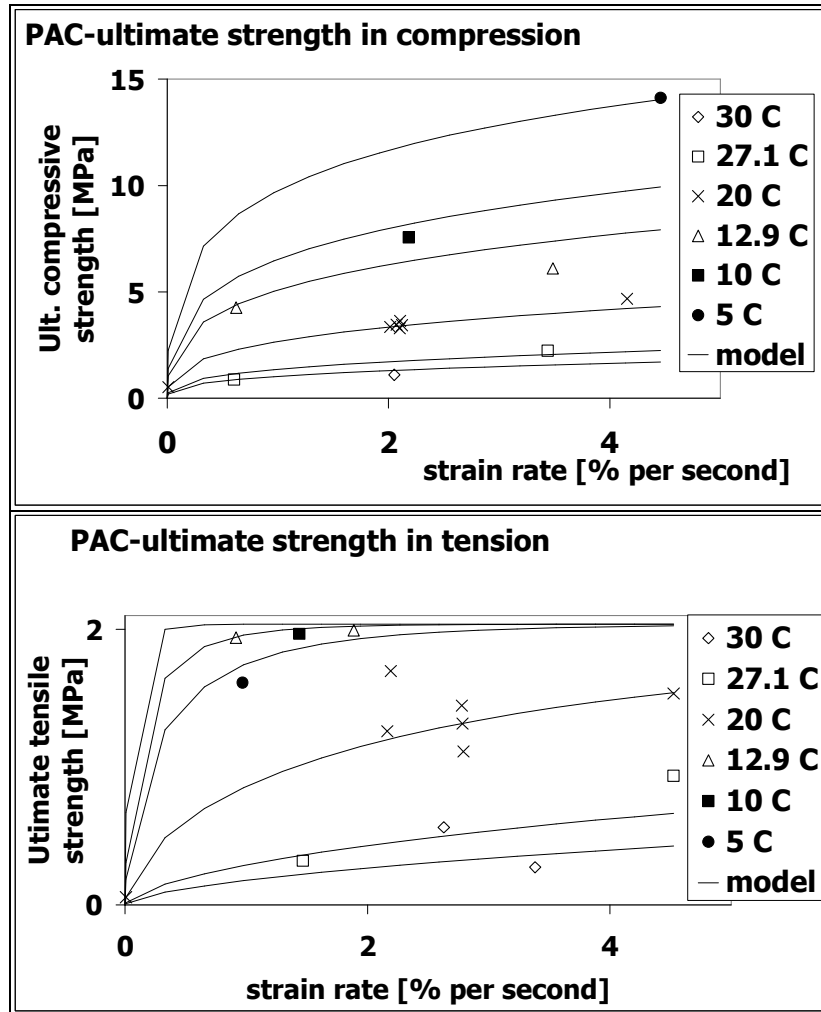


Figure 5.58 An illustration of the model fit on the results derived from the DCMC and DCMT tests for PAC

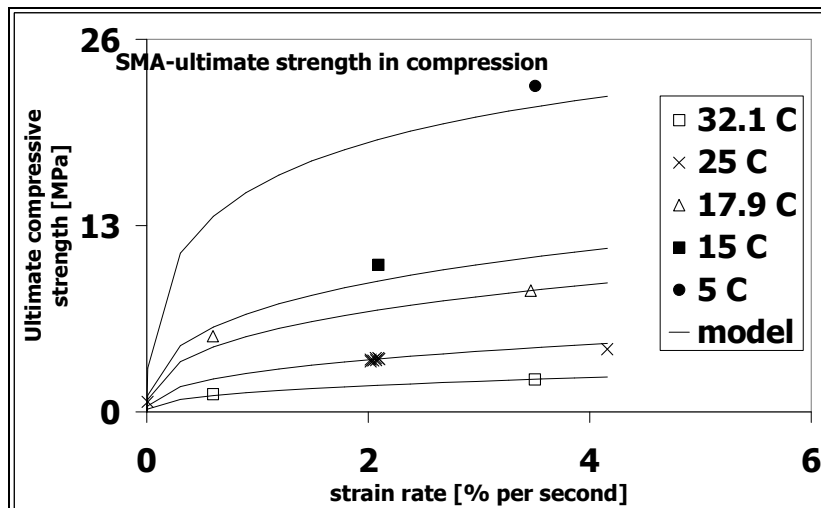


Figure 5.59 An illustration of the model fit on the results derived from the DCMC tests for SMA

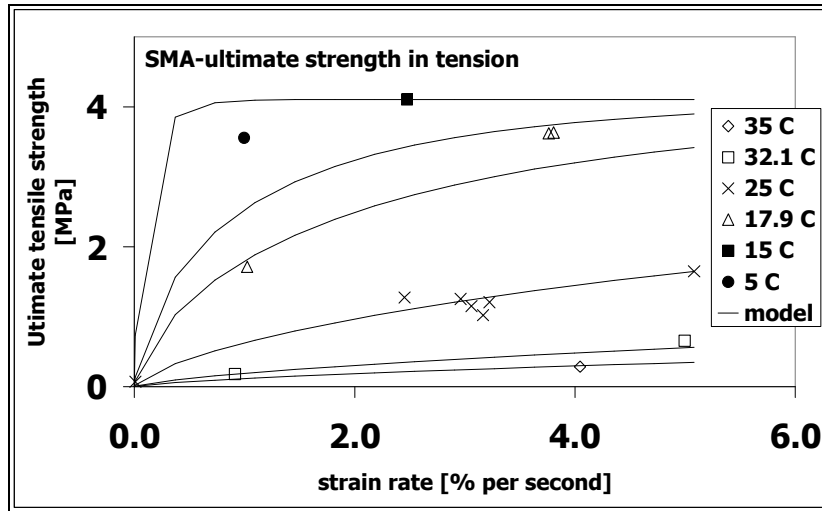


Figure 5.60 An illustration of the model fit on the results derived from the DCMT tests for SMA

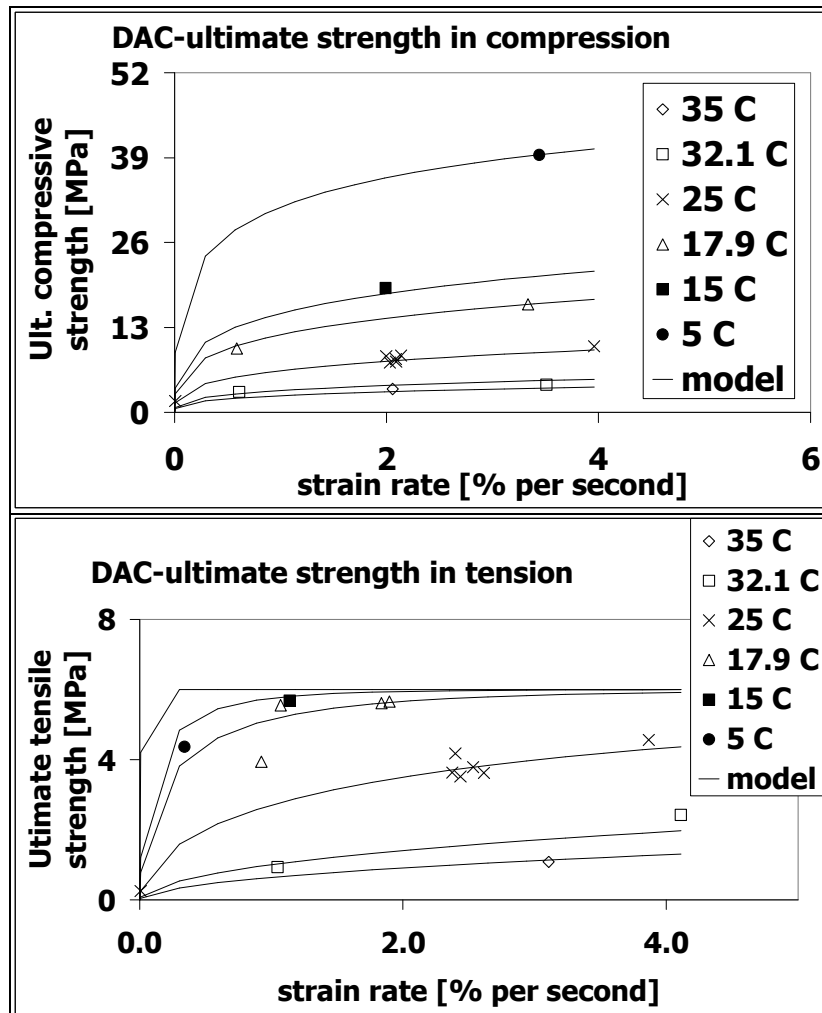


Figure 5.61 An illustration of the model fit on the results derived from the DCMC and DCMT tests for DAC

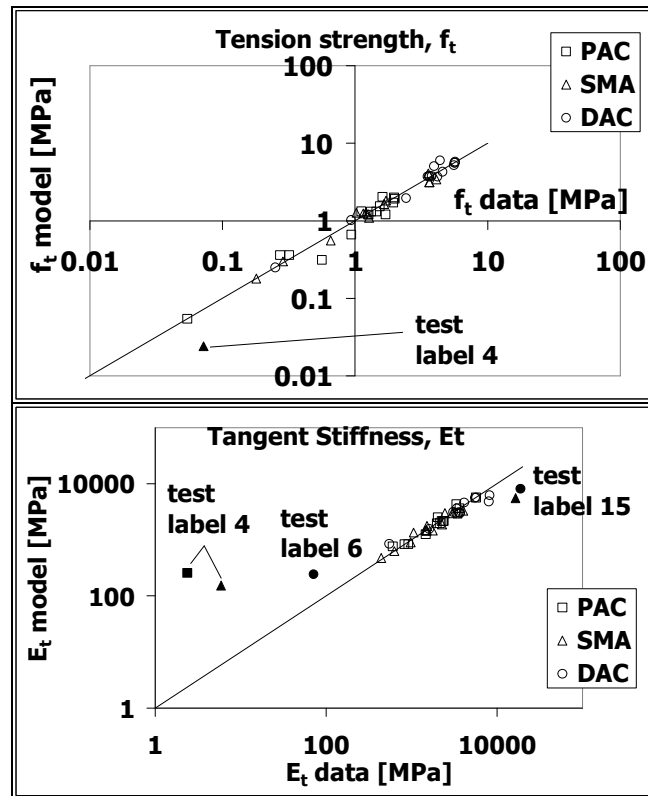


Figure 5.62 Data and Modelled test results for tensile strength and stiffness

Similar to the RMIT test results, the DCMC and DCMT tests results were compared at a temperature of 15 and 35°C. These temperatures were representative of the low and the high temperatures of the test conditions.

5.5.3.1 Maximum Stresses

Figure 5.63 and Figure 5.64 show a comparison of the modelled maximum compression and tension stresses for the three asphalt mixtures. The figures show that irrespective of the temperature and loading time, the maximum compressive stresses are higher than the maximum tensile stresses. The maximum stresses can be ranked in order of decreasing compression or tensile strength as DAC, SMA and PAC. The figure also show that at low temperatures the increase in tensile strength for PAC, SMA and DAC is higher and approaches the limiting maximum tensile strength at much lower strain rates in comparison to the strength in compression.

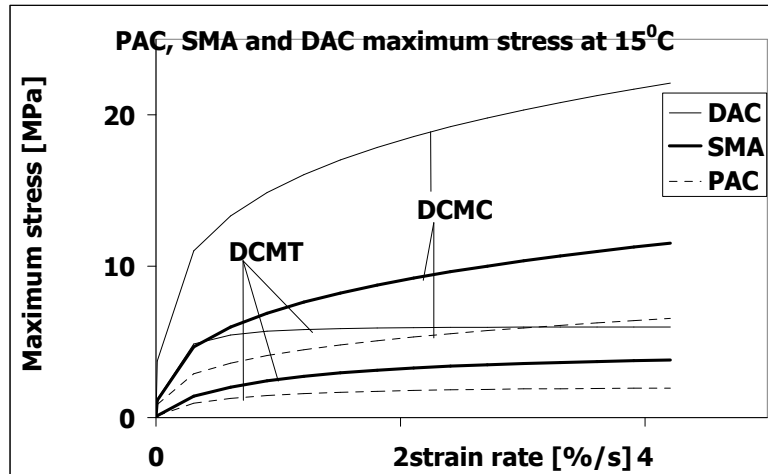


Figure 5.63 A comparison of the maximum stresses for the DCMC and the DCMT tests at 15°C

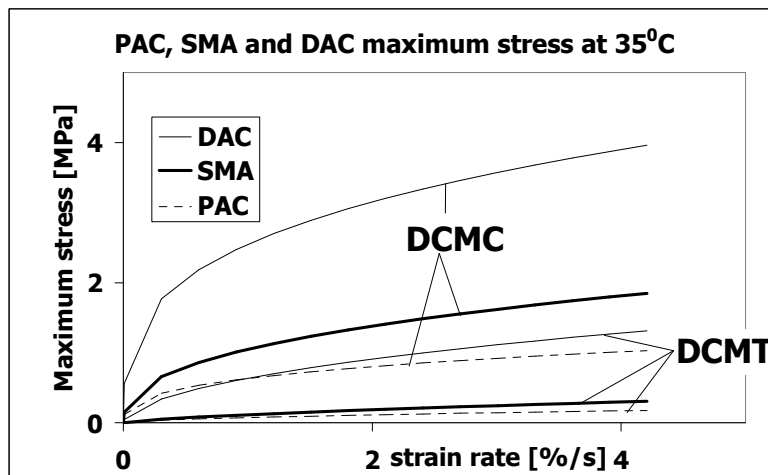


Figure 5.64 A comparison of the maximum stresses for the DCMC and the DCMT tests at 35°C

5.5.3.2 Tangent Stiffness

Figure 5.65 and Figure 5.66 show a comparison of the modelled tangent stiffness determined in the DCMC and DCMT tests for the three asphalt mixtures. The figures show that irrespective of the temperature and loading time, the tangent stiffness in the three asphalt mixtures can to a large extent be ranked in order of decreasing compression or tension tangent stiffness as DAC, SMA and PAC. The figures also show that the stiffness in tension is higher than the stiffness in compression.

The higher tangent stiffness in tension is thought to have been partly caused by the gluing of the end caps to the specimen in the DCMT tests. In literature (Erkens 2002), it has been shown that end restriction can lead to lower axial strains. In comparison to the DCMT tests, the end effects in the DCMC were considerably reduced by means of a soap and a thin foil. However, due to the fact that the specimen had to be firmly connected to the loading piston, a friction reduction system was not feasible in the DCMT tests.

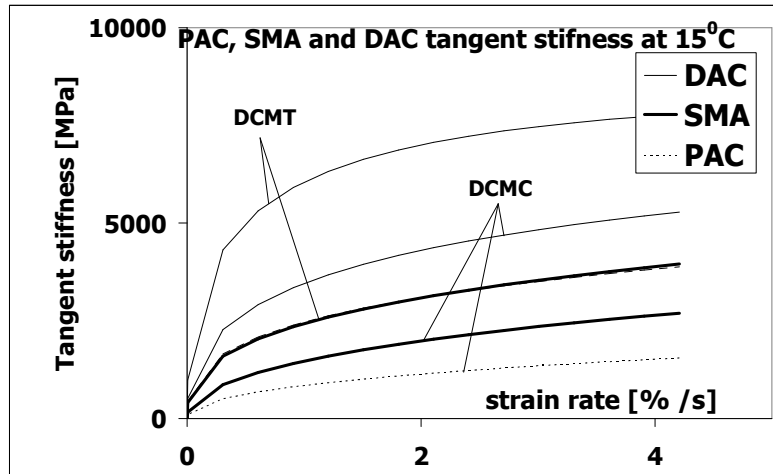


Figure 5.65 A comparison of the tangent stiffness for the DCMC and the DMCT tests at 15°C

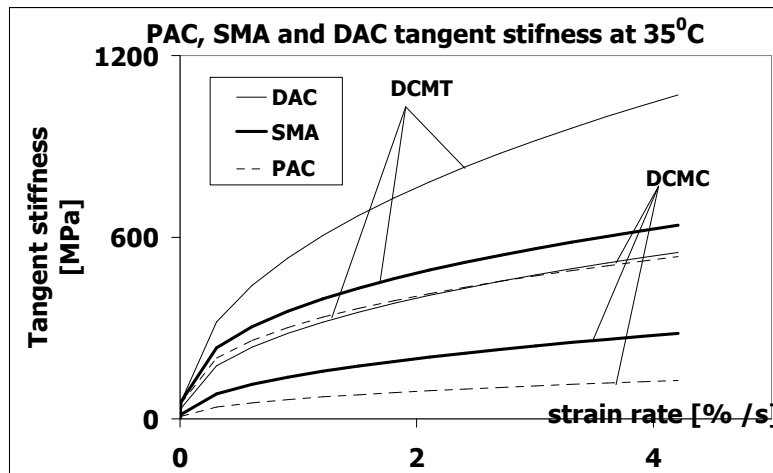


Figure 5.66 A comparison of the tangent stiffness for the DCMC and the DMCT tests at 35°C

5.5.3.3 Initiation of Plasticity and Initiation of Dilation

Figure 5.67 and Figure 5.68 show a comparison of the modelled stress at initiation of dilation with the modelled stress at initiation plasticity determined from the DCMC tests for the three asphalt mixtures. The figures show that the stress at initiation of dilation is higher than the stress at initiation of plasticity for the PAC and DAC at all temperatures and for SMA at low temperatures. At high temperatures, the stress at initiation of dilation for SMA is more or less similar to the stress at initiation of plasticity.

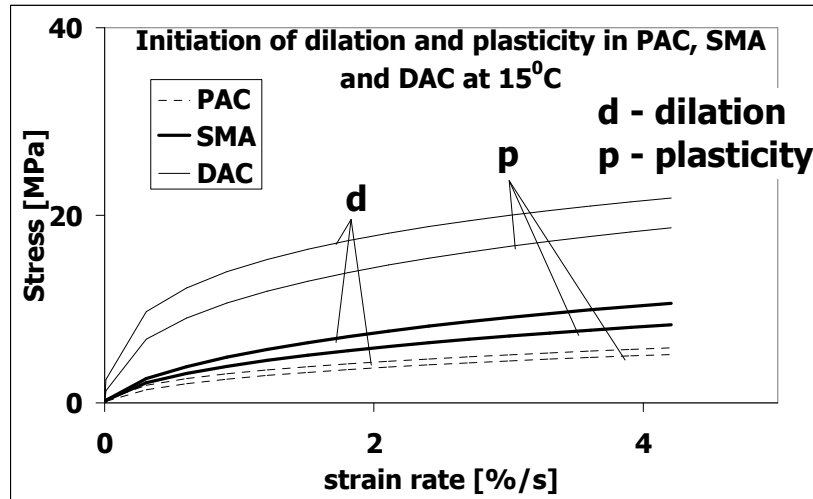


Figure 5.67 Stress at initiation of dilation and plasticity at 15°C

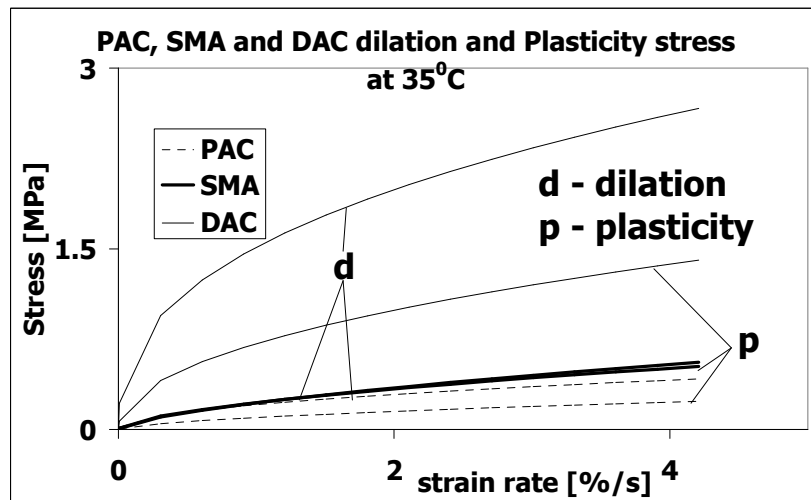


Figure 5.68 Stress at initiation of dilation and plasticity at 35°C

5.5.3.4 Poisson's Ratio

Due to the considerable scatter, the results for the Poisson's ratio were modelled by a constant value closest to all the test values irrespective of the temperature or the strain rate. Figure 5.69 and Figure 5.70 show the constant value and the Poisson's ratios determined in DCMC and DCMT tests. The figures show that the Poisson's ratios measured in the DCMT tests were higher than in the DCMC tests for the three asphalt mixtures. The higher Poisson's ratios determined from DCMT ratios may have been caused by the gluing of the end caps to specimen in the DCMT tests as explained in paragraph 5.5.3.2. The glue that connects the specimen to the end caps restrains radial deformation at the ends. Due to the contraction that results from the horizontal tensile stresses the axial strains near the caps are lower than without end restrictions. This does not affect the radial measurements taken at middle part of the specimen. However, the measurements taken by the axial LVDTs over the total height of the constrained specimen are lower than without end restrictions.

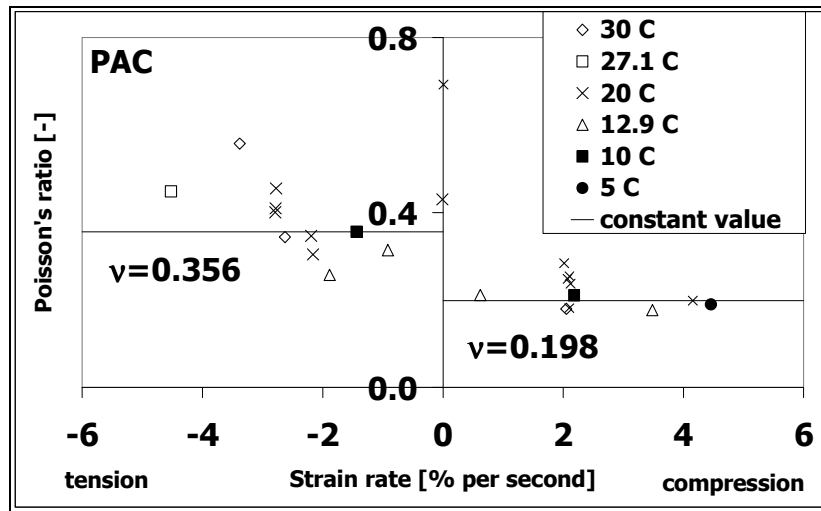


Figure 5.69 Poisson's ratios for the DCMC and DCMT tests (PAC)

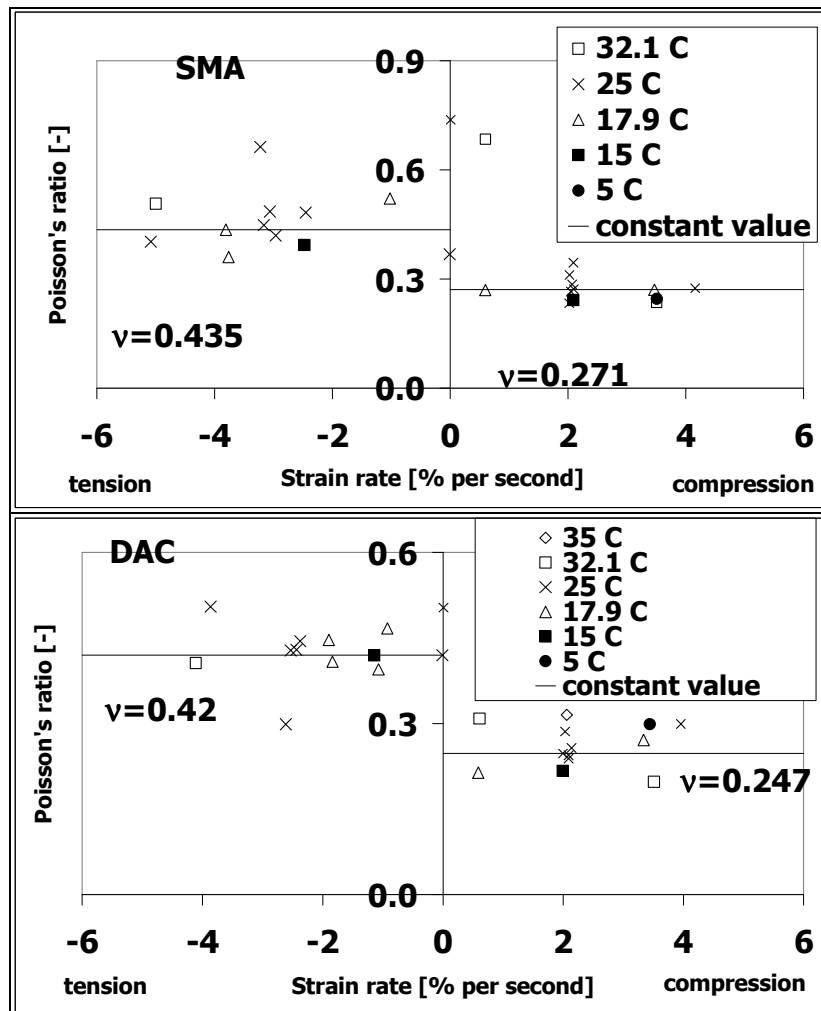


Figure 5.70 Poisson's ratios for the DCMC and DCMT tests (SMA and DAC)

5.6 Flow Surface

The flow surfaces for the three asphalt mixtures were developed using the Unified Model parameters given in Table 5.17. The flow surfaces were based on the response surface shown in Equation 5.25 that was developed by Desai (Desai et al 1986). The main advantage of the Desai surface model in comparison to other yield surface models is that it offers a closed surface that can describe the ultimate failure surface as well as the surface at initiation of dilation or plasticity. The flow surfaces for the asphalt mixtures were derived with the sign notation being positive for compression, negative for tension and the notation of the vertical stress being σ_1 .

$$f = \frac{J_2}{p_a^2} - \frac{\left[-\alpha \left(\frac{I_1 + R}{p_a} \right)^n + \gamma \left(\frac{I_1 + R}{p_a} \right)^2 \right]}{\sqrt{(1 - \beta \cos 3\theta)}} = 0 \quad 5.25$$

The model parameters were determined by imposing the following conditions on the Desai surface to obtain the expressions shown in Table 5.18:

- β assumed to be equal to zero since $\cos 3\theta = (1.5(3)^{0.5}J_3)/(J_2)^{1.5} = 1$ for the uniaxial tests.
- At ultimate surface, $\alpha = 0$, and parameter γ and R can be determined using this condition.
- Parameter n can be determined by considering the fact that, in the I_1 - $SQRTJ_2$ space, the point at which dilation is initiated corresponds to the apex of the flow surface and the partial derivative, $\partial f/\partial I_1 = 0$ (Scarpas 2005).

Table 5.18 Desai surface parameters for the asphalt mixtures

Term	Expression
f	$f = \frac{J_2}{p_a^2} - \left[-\alpha \left(\frac{I_1 + R}{p_a} \right)^n + \gamma \left(\frac{I_1 + R}{p_a} \right)^2 \right] = 0$
I_1, J_2, J_3, p_a	$I_1 = \sigma_1; J_2 = \frac{\sigma_1^2}{3}; J_3 = \frac{2}{27} \sigma_1^3; p_a = 0.1 \text{ [MPa]}$
Model parameter	Expression
γ, R	$\gamma = \frac{1}{3} \left(\frac{f_c - f_t }{f_c + f_t } \right)^2; R = \frac{2f_c f_t }{f_c - f_t }; f_c \text{ and } f_t \text{ as defined in Table 5.17}$
n, α	$n = \frac{2}{1 - \frac{1}{3\gamma} \left(\frac{\sigma_{dm}}{\sigma_{dm} + R} \right)^2}; \alpha = \frac{-\frac{J_2}{p_a^2} + \gamma \left(\frac{I_1 + R}{p_a} \right)^2}{\left(\frac{I_1 + R}{p_a} \right)^n} \sigma_{dm} \text{ as defined in Table 5.17}$

5.6.1 Model Parameter γ , R and n

Figure 5.72, Figure 5.72, Figure 5.75 and Figure 5.77 show the model parameters γ , R and n at 15, 30 and an extrapolation at 45°C for PAC, SMA and DAC. A temperature of 15°C represents a low temperature at which little or no permanent deformation is expected, 30°C represents a moderate temperature that is conducive to low magnitudes of permanent deformation and 45°C represents a high temperature that is conducive to a high magnitude of permanent deformation. The figures show that the general trend of all the model parameters for three asphalt mixtures is similar and that the trend for the three asphalt mixtures at low temperatures is different from the trend at higher temperatures.

5.6.1.1 Parameter γ

Figure 5.72 and Figure 5.72 show that the parameter γ decreases with increase in strain rate and temperature at 30 and 45°C but the trend at 15°C is different from the trend at 30 and 45°C. The difference in trend can be attributed to the effect relatively higher increase in tensile strength at low temperatures as mentioned in paragraph 5.5.3.1. The initial decrease and consequent increase in parameter γ at 15°C is caused by the by the decrease and consequent increase of the ratio of compressive strength to tensile strength at 15°C as illustrated in Figure 5.73. At 30 and 45°C this ratio decreases with increase in the strain rate as illustrated for the 45°C in Figure 5.73.

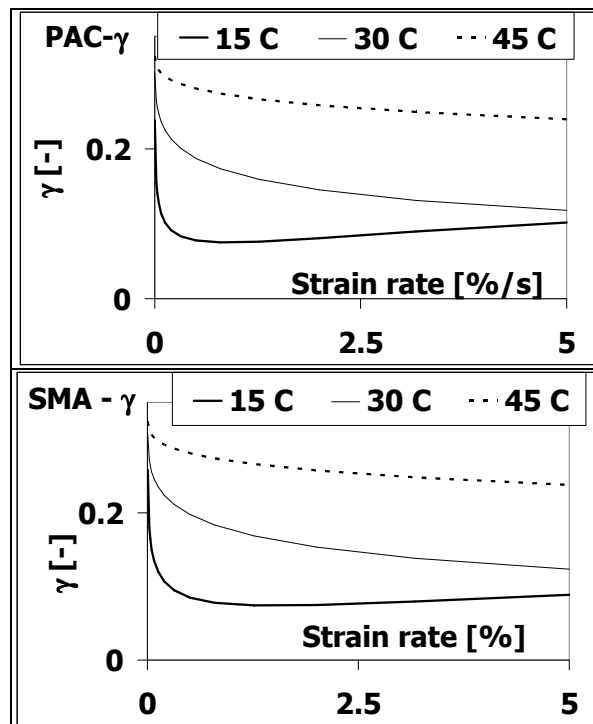


Figure 5.71 Model Parameter γ for PAC and SMA at 15, 30 and 45°C

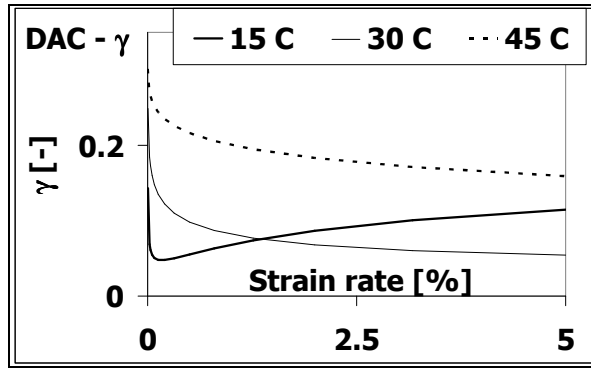


Figure 5.72 Model Parameter γ_{DAC} at 15, 30 and 45°C

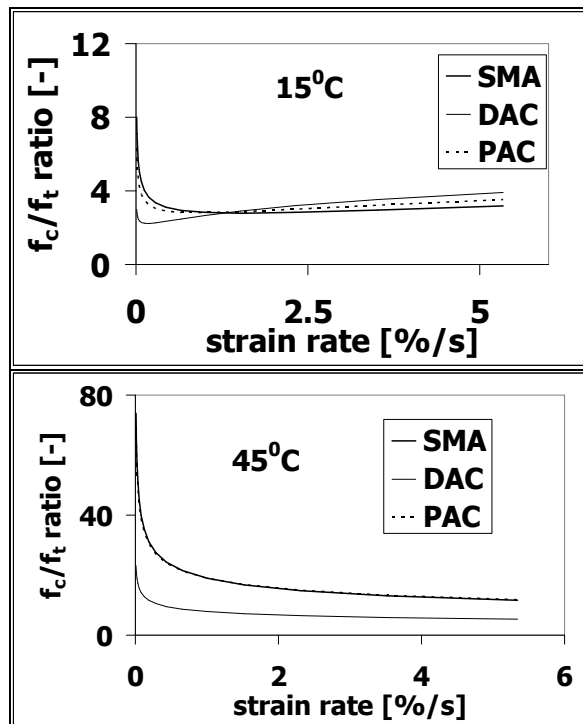


Figure 5.73 Ratio of compressive strength to tensile strength at 15°C and 45°C

5.6.1.2 Parameter R

Figure 5.74 and Figure 5.75 show that parameter R increases with decrease in temperature for the three asphalt mixtures but the trend in DAC at 15°C is different from the trend at 30 and 45°C. The R value for the DAC at 15°C peaks to a maximum and falls there after. This can be attributed to the decrease and consequent increase of compressive strength relative to the tension at 15°C as illustrated in Figure 5.73.

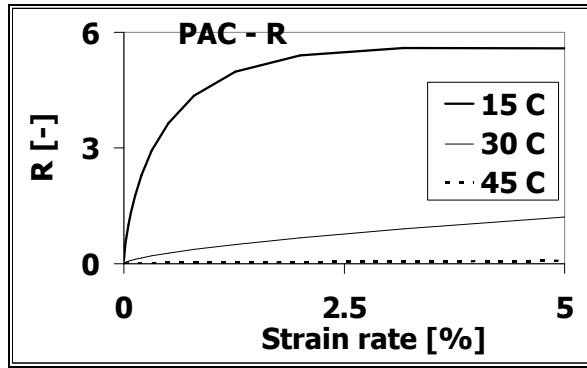


Figure 5.74 Model Parameter R for PAC at 15, 30 and 45°C

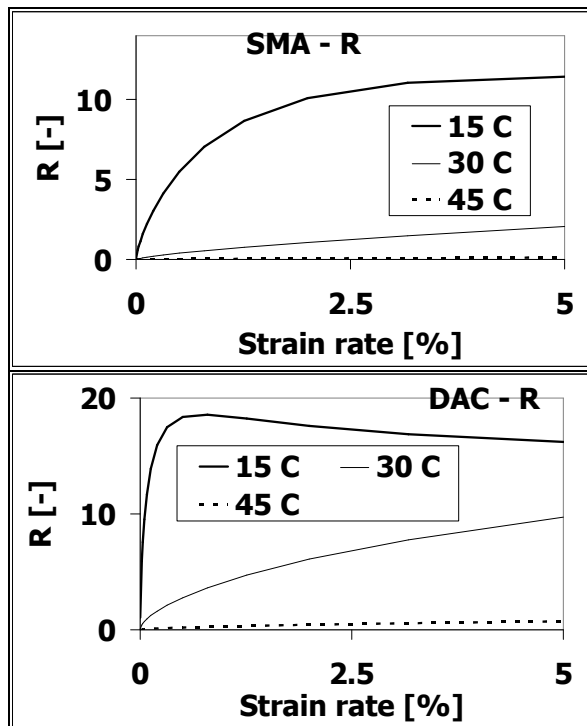


Figure 5.75 Model Parameter R for SMA and DAC at 15, 30 and 45°C

5.6.1.3 Parameter n

Similar to the parameter γ and n , the trend in parameter n is markedly different at 15°C in comparison to the trend at 30 and 45°C as shown in Figure 5.76 and Figure 5.77. Parameter n at 15°C increases rapidly with increase in strain rate. This is due to the combination of high R values, high stress at initiation of dilation and low γ values.

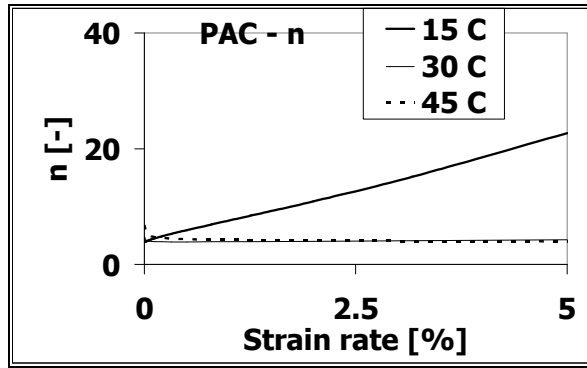


Figure 5.76 Model Parameter n for PAC at 15, 30 and 45°C

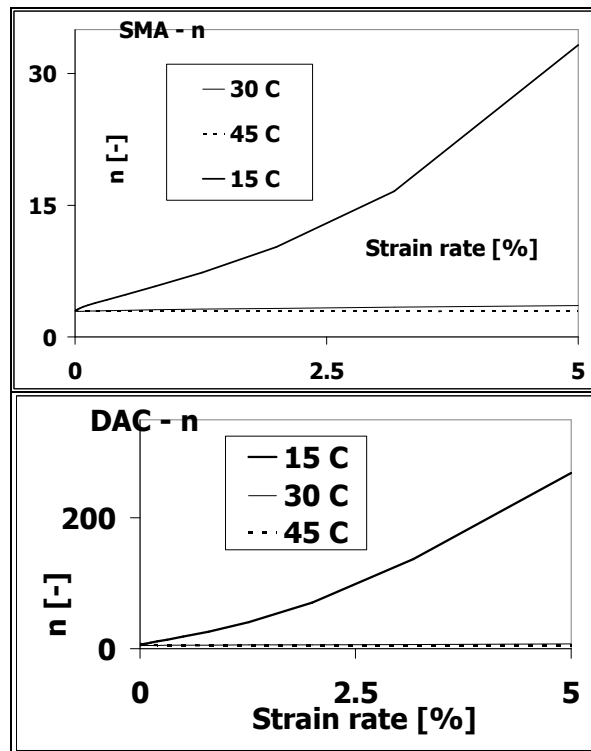


Figure 5.77 Model Parameter n for SMA and DAC at 15, 30 and 45°C

5.6.2 Flow Surfaces

The flow surfaces were derived at a 30°C and at an extrapolated temperature of 45°C for strain rates of 0.02 and 5%/s for the three asphalt mixtures. A temperature of 30°C represents a moderate temperature that is conducive to low magnitudes of permanent deformation and 45°C represents a high temperature that is conducive to a high magnitude of permanent deformation. A strain rate of 5% per second was chosen to represent a high strain rate while 0.02%/s represents low strain rates.

Figure 5.78 and Figure 5.79 show both the ultimate flow surface and the flow surface at initiation of dilation at 30 and 45°C for the three asphalt mixtures at a strain rate of 5%/s and 0.02%/s respectively. Figure 5.78 and Figure 5.79 show that the three asphalt mixtures can be ranked in order of decreasing ultimate surface as DAC, SMA and PAC. The figures also show that the surface at initiation of dilation for the DAC is bigger in size than that of either SMA or

PAC. However the relative order of the size of the flow surface at initiation of dilation for SMA and PAC depends on the magnitude of the strain rate. The flow surface for PAC is bigger in size at low strain rates but smaller at high strain rates in comparison to that of the SMA.

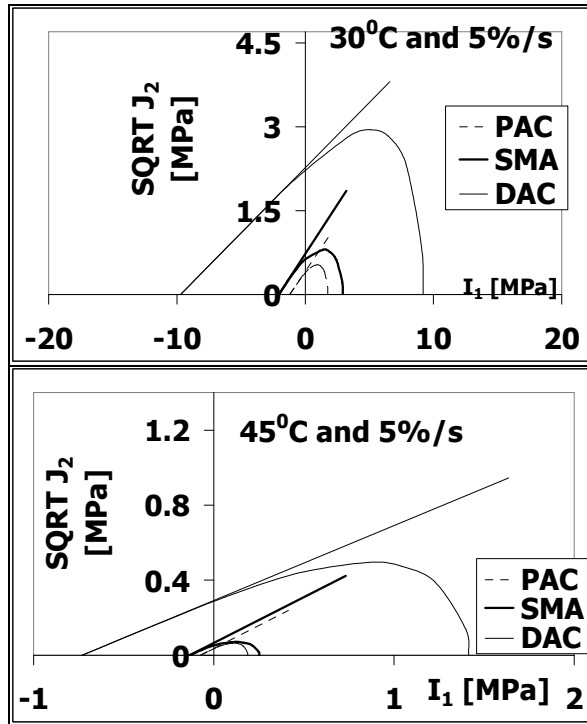


Figure 5.78 Ultimate and initiation of dilation surfaces at 5%/s strain rate at 30 and 45°C for PAC, SMA and DAC

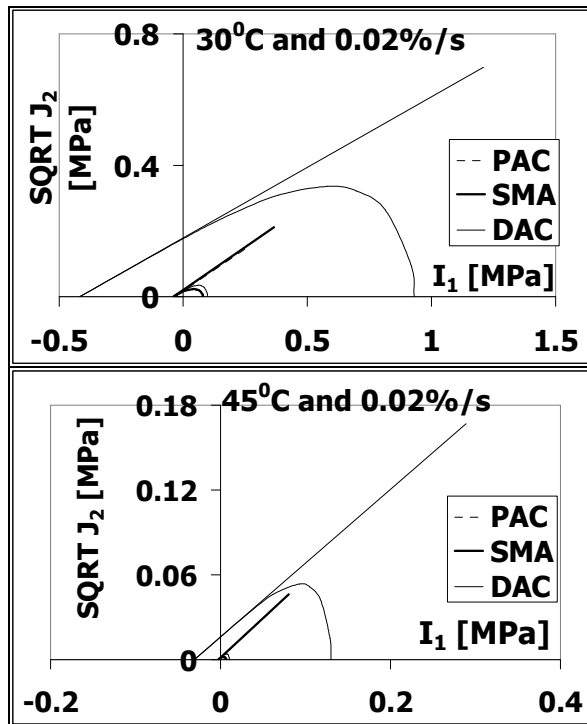


Figure 5.79 Ultimate and initiation of dilation surfaces at 0.02%/s strain rate at 30 and 45°C for PAC, SMA and DAC

5.7 Conclusions

5.7.1 Specimen Preparation Procedure

Apart from achieving compaction homogeneity in the test specimens, the specimen compaction procedure was also able to meet the target Marshall density for the three asphalt mixtures. This was attained by means of gyratory compaction control and extraction of the test specimens from the compacted specimens. With regard to the specimen preparation procedure the following conclusions were reached:

- The densities within gyratory compacted specimens vary considerably. In order to produce homogeneous test specimens, it is desirable to extract test specimens from the middle part and to remove the upper and lower parts of the gyratory compacted specimens.
- Heating of the top gyratory compaction disc did not alleviate compaction variation within the gyratory compacted specimens.
- The density of the hot specimens based on specimen dimensions is lower than both the cold density based on the surface dry technique and the cold density based on specimen dimensions. This suggests that the specimen density increases on cooling as a result of decrease in volume.
- The hot density of gyratory compacted specimens can be used as effective means of achieving desired density in extracted cores.
- The densities of the 65 mm diameter specimens extracted from the 150 mm diameter gyratory compacted specimens were similar to the reference Marshall mixture design densities.
- The SMA mixture is more difficult to compact in comparison to the PAC and the DAC mixtures even at a gyratory angle of 1.25° .
- In this research, it was not possible to use the number of gyrations as a compaction control parameter.

5.7.2 RMIT, DCMC and DCMT Tests

The parameters of the Desai plasticity model for the three asphalt mixtures were derived based on the temperature susceptibility derived from the RMIT tests and the failure behaviour determined from the DCMC and the DCMT tests. The Unified Model fitted the test data reasonably well. In addition to the plasticity parameters, the elastic behaviour of the three asphalt mixtures was also derived. The following conclusions were reached based on the elastic behaviour and the plasticity models developed in this research:

- The reference time or strain rate related parameter in the Unified Model is strongly dependent on the reference temperature. Apart from this parameter, all other Unified Model parameters can be confidently estimated irrespective of the reference temperature.
- The three asphalt mixtures can, to a large extent, be ranked in order of decreasing stiffness as DAC, SMA and PAC.
- The strength of the three asphalt mixtures is higher in compression than in tension and the three asphalt mixtures can be ranked in order of decreasing maximum compression or tensile strength as DAC, SMA and PAC.
- The stress at initiation of dilation is higher than the stress at initiation of plasticity for the PAC and DAC at all temperatures and for SMA at low

temperatures. At high temperatures, the stress at initiation of dilation for SMA is more or less similar to the stress at initiation of plasticity.

- Due to the considerable scatter, the Poisson's ratios were modelled by a constant value. No relationship was found between either the temperature or the strain rate and the Poisson's ratios.
- The three asphalt mixtures can be ranked in order of decreasing ultimate surface as DAC, SMA and PAC. The surface at initiation of dilation for the DAC is bigger in size than that of either SMA or PAC.

5.8 References

- CROW (2000), *Standaard RAW Bepalingen 2000*, C.R.O.W., Ede (In Dutch).
- Desai, C.S., Somasundaram, S. and Frantziskonis, G., (1986), *A Hierarchical Approach for Constitutive Modelling of Geologic Materials*, International Journal of Numerical and Analytical Methods in Geomechanics, vol. 10, No. 3 pp. 225-257.
- Erkens S.M.J.G., (2002), *Asphalt Concrete Response (ACRe) Determination, Modelling and Prediction*, Doctor of Philosophy Thesis, Delft University of Technology, the Netherlands.
- Erkens S.M.J.G. and Poot M.R., (2000), *The Uniaxial Compression Test Asphalt Concrete Response (Acre)*, Report 7-98-117-4, Delft University of Technology, The Netherlands.
- Erkens S.M.J.G. and Poot M.R., (2001), *The Uniaxial Test Asphalt Concrete Response (ACRe)*, Report 7-01-117-7, Delft University of Technology, The Netherlands.
- Francken L. and Clauwaert C. (1987), *Characterization and Structural Assessment of Bound Materials for Flexible Road Structures*, Proceedings of the Sixth International Conference on the Structural Design of Asphalt Pavements, pp. 130 – 144, University of Michigan Ann Arbor, United States of America.
- Groenendijk J., (1998), *Accelerated Testing and Surface Cracking of Asphaltic Concrete Pavements*, Doctor of Philosophy Thesis, Delft University of Technology, the Netherlands.
- Jacobs M.M.J., (1995), *Crack Growth in Asphalt Mixes*, Ph.D. dissertation, Delft University of Technology, Faculty of Civil Engineering, Delft, The Netherlands.
- Jönsson M., Partl M.N., and Flisch A. (2002), *Comparison of Different Compaction Methods Using X-ray Tomography*, EMPA-No. FE840544, Road Engineering/Sealing Components, Highway Engineering, Swedish Royal Institute of Technology, Sweden.
- Lytton R.L., Uzan J., Fernando E.M., Roque R., Hiltunen D. and Stoffels S.M., (1993), *Development and Validation of Performance Prediction Models and Specifications for Asphalt Binders and Paving Mixes*, SHRP report A-357, SHRP/NRC, Washington DC, United States of America.
- Masad E., Jandhyala V.K., Dasgupta N., Somadevan N. and Shashidhar N. (2002), *Characterization of Air Void Distribution in asphalt Mixes Using X-ray Computed Tomography*, Journal of Materials in Civil Engineering, vol. 14, Issue 2, p122-129, Online version.

- Medani T.O., (2006), *Design Principles of Surfacing on Orthotropic Steel Bridge Decks*, Doctor of Philosophy Thesis, Delft University of Technology, The Netherlands.
- Medani, T.O., Molenaar, A.A.A. and Huurman, M., (2004), *A Single Model to Describe Several Properties of Bituminous Mixes*, 5th International PhD Symposium in Civil Engineering, pp.1411-1418, vol 2, Delft, The Netherlands.
- Molenaar, A.A.A., (1993), *Road materials Part III-Asphaltic Materials*, The Netherlands.
- MTS Manual, Rock and Concrete Testing Systems Version 6.
- Nowak A.S. and Collins K.R. (2000), *Reliability of Structures*, McGraw-Hill Higher Education, United States of America.
- Robinson, G.K. (2000), *Practical Strategies for Experimenting*, Sussex, England.
- Sayegh G. (1967), *Viscoelastic Properties of Bituminous Mixtures*, Proceedings of the Second International Conference on the Structural Design of Asphalt Pavements, University of Michigan Ann Arbor, United States of America.
- Scarpas, A., (2005), *International Course on Application of FE and Constitutive Models in Geotechnical Engineering*, Torino, Italy.
- Sinadinis C. (1999), *Servopac Operating and Maintenance Manual*, Industrial Controls Ltd.
- Tashman L., Masad E., Peterson B. and Saleh H. (2001), *Internal Structure Analysis of Asphalt Mixes to Improve the Simulation of Superpave Gyrotory Compaction to Field Conditions*, Proceedings of the Association of Asphalt Paving Technologists Technical Sessions, CD ROM.
- Tashman L., Masad E., Little D. and Lytton R. (2004), *Damage Evolution in Triaxial Compression Tests of HMA at High Temperatures*, Proceedings of the Association of Asphalt Paving Technologists Technical Sessions, CD ROM.
- Verstraeten J. (1972), *Moduli and Critical Strains in Repeated Bending of Bituminous Mixes Application to Pavement Design*, Proceedings of the Third International Conference on the Structural Design of Asphalt Pavements, pp. 729 – 738, London, England.
- Voskuilen J.L.M. and Ven M.F.C. van de (2004), *Specimen Preparation for Testing, Lab Versus Field: The Spatial Approach*, Proceedings of the 3rd Eurasphalt & Eurobitume Congress, CD ROM.
- Withana, U.T. (2001), *Investigation of Influencing Factors on Permanent Deformation of Asphalt Mixes*, Master of Science Thesis, Delft University of Technology / IHE Delft, The Netherlands.

6 Mastic and Bitumen

6.1 Introduction

In this research, the bituminous mortar or the mastic binding the aggregate skeleton together was defined in relation to the minimum size of the aggregate skeleton composition that was presented in Chapter 4. The aggregate skeleton was identified to consist of the aggregates above 0.5 mm for the PAC, 2 mm for the SMA and 0.063 mm for the DAC. For purposes of discrimination, the mortar was defined as a mixture of bitumen and any of the aggregates below the minimum aggregate skeleton size and the mastic as the mixture of bitumen and the filler. Based on this definition, the bituminous binder in the PAC and SMA consist of both mortar and mastic while the bituminous binder in the DAC is composed of the mastic only. Because of time limitations, only the DAC bituminous binder which consisted of only the mastic was investigated in this research.

The mastic was characterized by means of tensile strength. The importance of the tensile strength in the mastic/mortar was underscored by a comparison of the extent of dilation occurring in the aggregate skeleton during the DCMCC tests and in the total asphalt mixture during the DCMC tests. In order to compare the extent of dilation in the total asphalt mixture and the aggregate skeleton, the change in volume relative to the minimum volume at the point of initiation of dilation was considered. This change in volume is expressed as shown in Equation 6.1. The expression ensures that the points of initiation of dilation in all the tests commence from the same reference volume of zero. The change in volume was considered for the DCMCC tests conducted on the aggregate skeleton and the DCMC conducted on the total mixture. In the figures that follow, numbered labels will be used for the DCMCC aggregate skeleton tests and alphabet labels for the DCMC total mixture tests.

$$\text{change in volume strain} = \varepsilon_{vol} - \varepsilon_{volmin} \quad 6.1$$

Where:

$$\begin{aligned} \varepsilon_{vol} &= \text{volumetric strain [\%]}, \\ \varepsilon_{volmin} &= \text{volumetric strain at the point of initiation of dilation [\%]}. \end{aligned}$$

Figure 6.1 shows a comparison of the extent of dilation in the DCMCC tests conducted on the PAC aggregate skeleton and the DCMC tests performed on the PAC total asphalt mixture. The figure shows that despite of confinement, the extent of dilation in the PAC aggregate skeleton was higher than in the PAC total asphalt mixture. At equal axial strains, most of the DCMCC tests performed on the aggregate skeleton exhibited more dilation than the DCMC tests performed on the total asphalt mixture. 14 of the 18 tests DCMCC tests conducted on the aggregate skeleton exhibited more dilation than the DCMC tests conducted on total asphalt mixture. Two DCMCC tests (P and Q) performed at a confinement

level of 0.31 MPa and 2 DCMCC tests (M and N) performed at a confinement level of 0.187 MPa confinement exhibited less dilation than the DCMC tests.

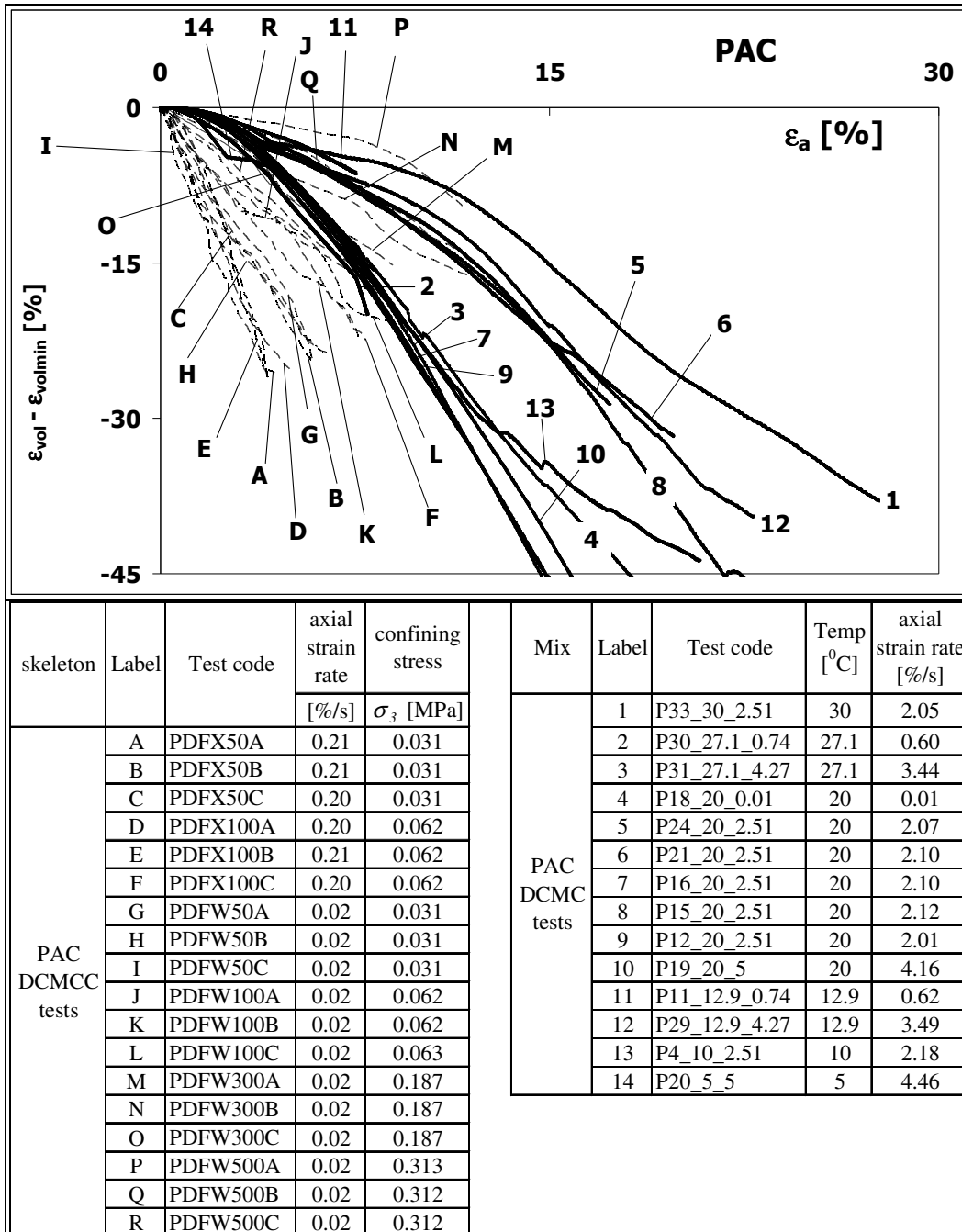


Figure 6.1 A comparison of the dilation in the DCMCC tests conducted on the PAC aggregate skeleton and the DCMC tests performed on the PAC total asphalt mixture

Figure 6.2 shows a comparison of the extent of dilation in the DCMCC tests conducted on the SMA aggregate skeleton and the DCMC tests performed on the SMA total asphalt mixture. The figure shows that despite of confinement, the SMA aggregate stone skeleton exhibited more dilation than the SMA total asphalt mixture. At equal axial strains, most of the tests performed on asphalt mixture exhibited less dilation than the tests performed on the skeleton. 14 of the 15 DCMC tests conducted on the SMA total asphalt mixture exhibited less dilation

than the DCMCC tests conducted on the aggregate skeleton. The only exception was the test (label 3) conducted at a temperature of 25°C and a strain rate of 0.01%/s. The dilation in this test is initially lower than in the aggregate skeletons. However, beyond an axial strain of about 4%, the dilation in this test becomes higher than the dilation of some of the aggregate tests conducted at 0.187 and 0.25 MPa confinement (labels E, G and I).

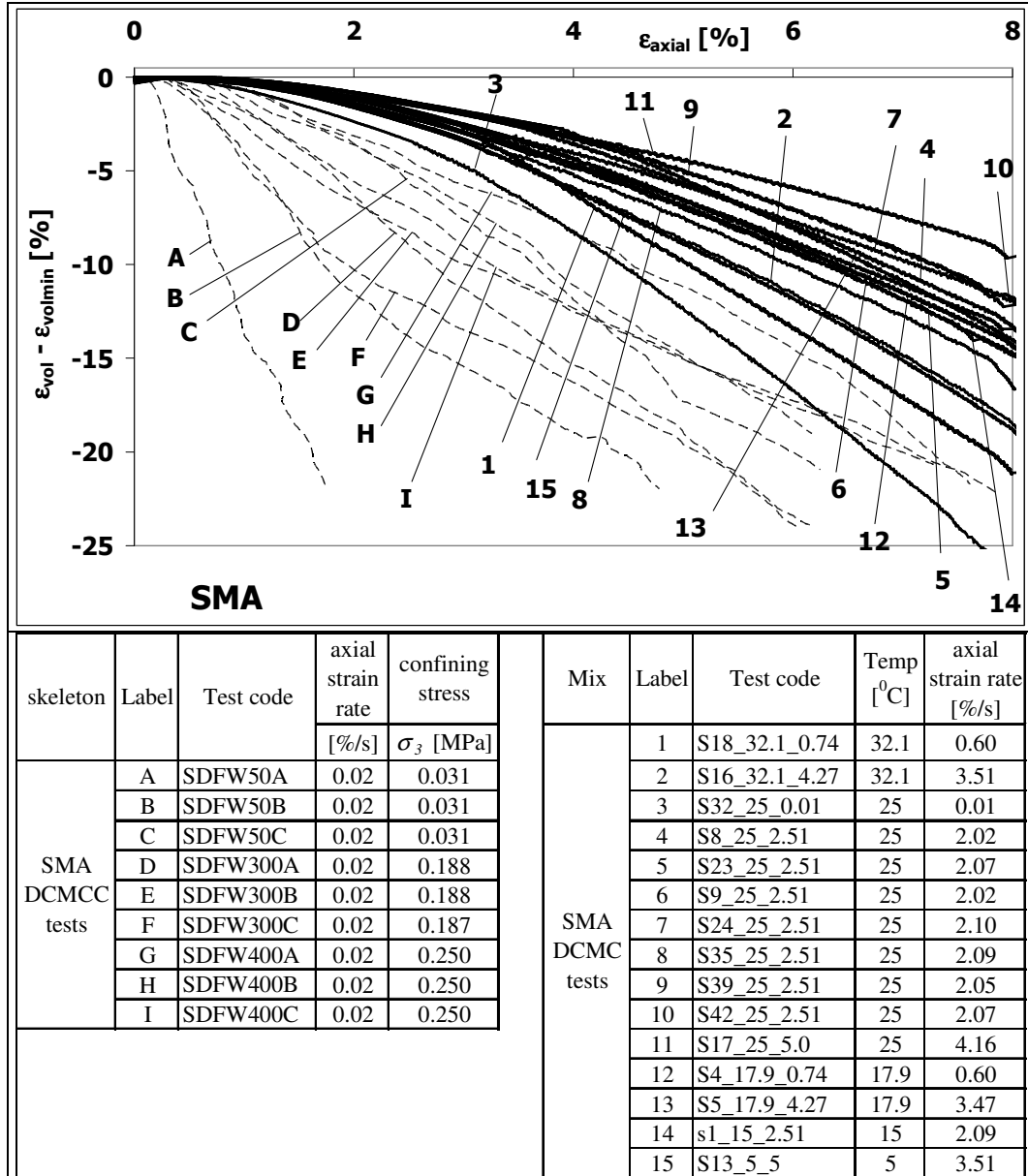


Figure 6.2 A comparison of the dilation in the DCMCC tests conducted on the SMA aggregate skeleton and the DCMC tests performed on the SMA total asphalt mixture

Figure 6.3 shows a comparison of the extent of dilation in the DCMCC tests conducted on the DAC aggregate skeleton and the DCMC tests performed on the DAC total asphalt mixture. The figure shows that despite of confinement, the DAC aggregate stone skeleton exhibited more dilation than the DAC total asphalt mixture. All the tests performed on the asphalt mixture exhibited less dilation than the tests performed on the skeleton.

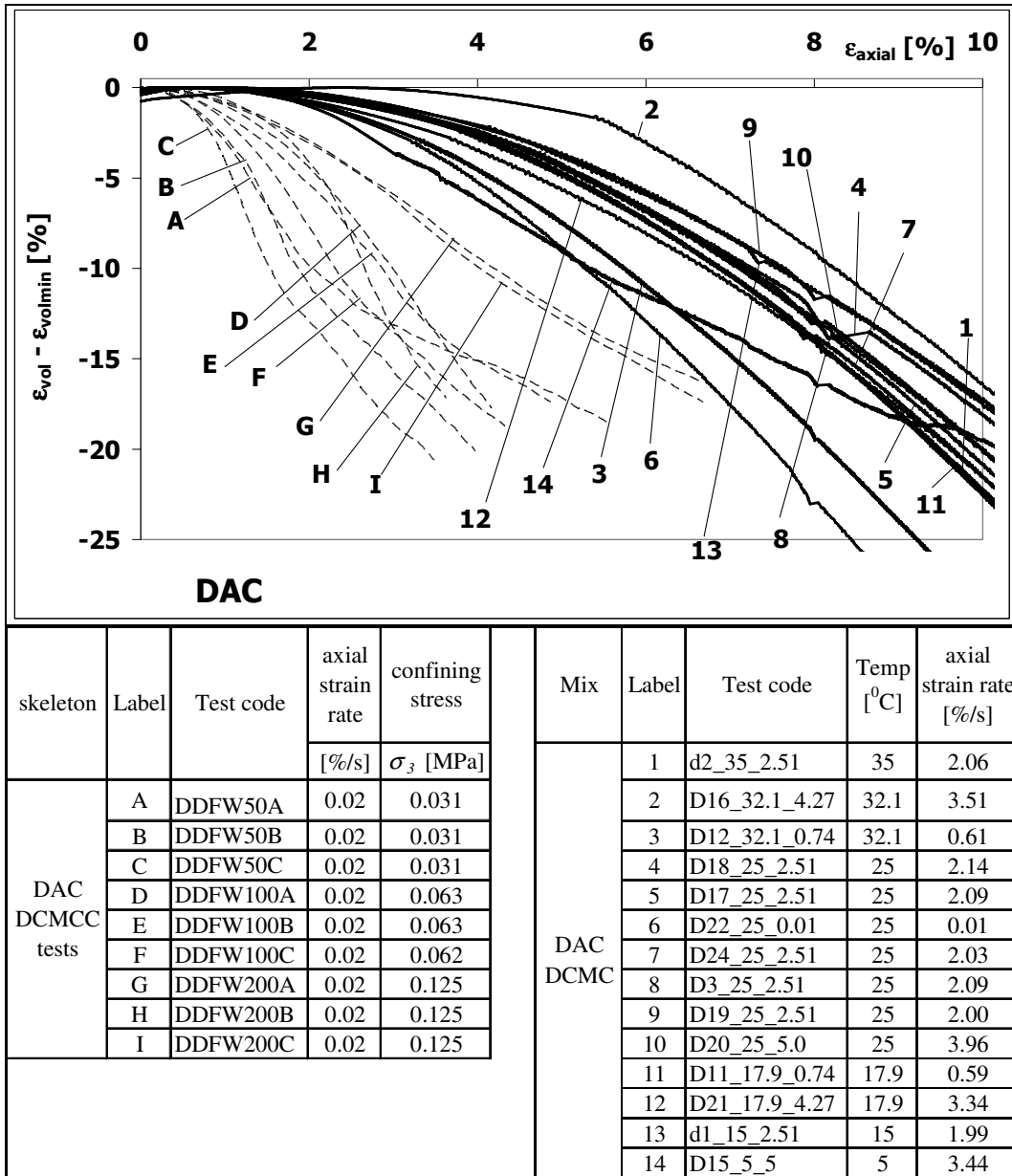


Figure 6.3 A comparison of the dilation in the DCMCC tests conducted on the DAC aggregate skeleton and the DCMC tests performed on the DAC total asphalt mixture

6.1.1 Determination Indicative Tensile Stress in the Mastic/Mortar

As discussed in the previous section, the aggregate skeleton for the PAC, SMA and DAC under confinement exhibited more dilation than the total asphalt mixture without confinement. The lower dilation in the total asphalt mixture can be attributed to the presence of the mastic/mortar in the total asphalt mixture. The mastic/mortar acts as a deterrent against dilation by holding the aggregate skeleton together. The tensile stress in the mastic/mortar holds the aggregate skeleton together thus decreasing the extent of dilation in the total asphalt mixture. The indicative tensile in the mastic/mortar was determined as follows:

1. Assume that tension initiates in the mastic/mortar at initiation of dilation in the total asphalt mixture.

2. The tensile stress in the total asphalt mixture that holds the aggregate skeleton together against dilation is comparable to some measure of equivalent confinement. This equivalent confinement can be determined by comparing the extent of dilation in total asphalt mixture to the extent of dilation in the aggregate skeleton.
3. In order to describe the extent of dilation in the aggregate skeleton and total asphalt mixture and allow consequent determination of equivalent confinement, the following relationships were used:

$$\epsilon_{aggrad} = -k_1 \epsilon_{aggax}^{k_2} \left(\frac{\sigma_3}{\sigma_{3,0}} \right)^{k_3} \quad 6.2$$

$$\epsilon_{mixrad} = -k_1 \epsilon_{mixax}^{k_2} \left(\frac{\dot{\epsilon}_0}{\dot{\epsilon}} \right)^{k_3} \exp(-k_4 [T - T_0]) \quad 6.3$$

ϵ_{aggrad}	=	radial strain in the aggregate after initiation of dilation [%],
ϵ_{mixrad}	=	radial strain in the total mixture after initiation of dilation [%],
ϵ_{aggax}	=	axial strain in the aggregate after initiation of dilation [%],
ϵ_{mixax}	=	axial strain in the total asphalt mixture after initiation of dilation [%],
σ_3	=	confining stress in the aggregate skeleton,
$\sigma_{3,0}$	=	reference confinement = 1 [MPa],
$\dot{\epsilon}$	=	axial strain rate in the total asphalt mixture [%/s],
$\dot{\epsilon}_0$	=	reference strain rate = 1 [%/s],
T	=	temperature [K],
T_0	=	reference temperature,
k_1, k_2, k_3, k_4	=	regression coefficients.

4. The equivalent confinement can be obtained as the confinement on the aggregate skeleton that leads to a similar extent of dilation in the unconfined total asphalt mixture as illustrated in Figure 6.4. This is achieved by minimizing the total absolute error between the dilation in the total asphalt mixture and the dilation in aggregate skeleton using Equation 6.4.

$$\text{tot. abs. error} = \sum \left(100 \left[\frac{|\text{tot asphalt mix dil} - \text{agg skeleton dil}|}{\text{asphalt mix dil}} \right] \right) \quad 6.4$$

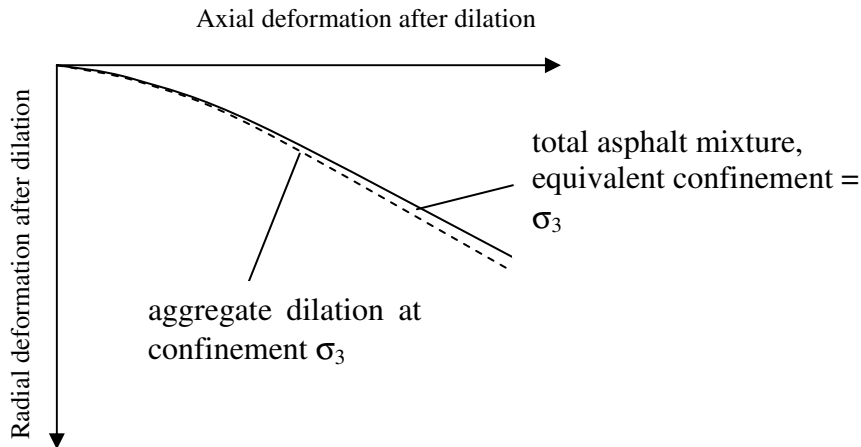


Figure 6.4 Illustration of determination of equivalent confinement

5. The tensile stress in the total asphalt mixture occurs in the mastic/mortar and is uniformly distributed in the volume of the mastic/mortar. The indicative tensile stress can be determined from Equation 6.5.

$$\sigma_{mt} = \frac{\sigma_{3eq}}{P_m} \quad 6.5$$

Where:

- σ_{mt} = indicative tensile stress in the mastic/mortar,
 σ_{3eq} = equivalent confining stress,
 P_m = mastic/mortar content by volume [-].

The regression coefficients for the radial strain for the aggregate skeleton, total asphalt mixture and the mastic/mortar content by volume in the asphalt mixtures are shown in Table 6.1. Figure 6.5, Figure 6.6 and Figure 6.7 show the model fit on the data. The negative k_3 coefficients for the three aggregate skeletons indicate that dilation increases with decrease in confinement. The positive k_3 coefficients for the total asphalt mixture in the three mixtures imply that dilation increases with decrease in strain rate and the negative k_4 coefficient indicates that dilation increases with increase in temperature.

Table 6.1 Regression coefficients

coefficient	PAC		SMA		DAC	
	skeleton	mix	skeleton	mix	skeleton	mix
k_1	0.412	0.872	0.825	0.769	0.309	0.563
k_2	1.126	1.237	1.274	1.307	1.437	1.443
k_3	-0.492	0.008	-0.324	0.052	-0.547	0.061
k_4	-	-0.022	-	-0.009	-	-0.003
T_0	-	298	-	298	-	298
P_m	0.154		0.315		0.187	

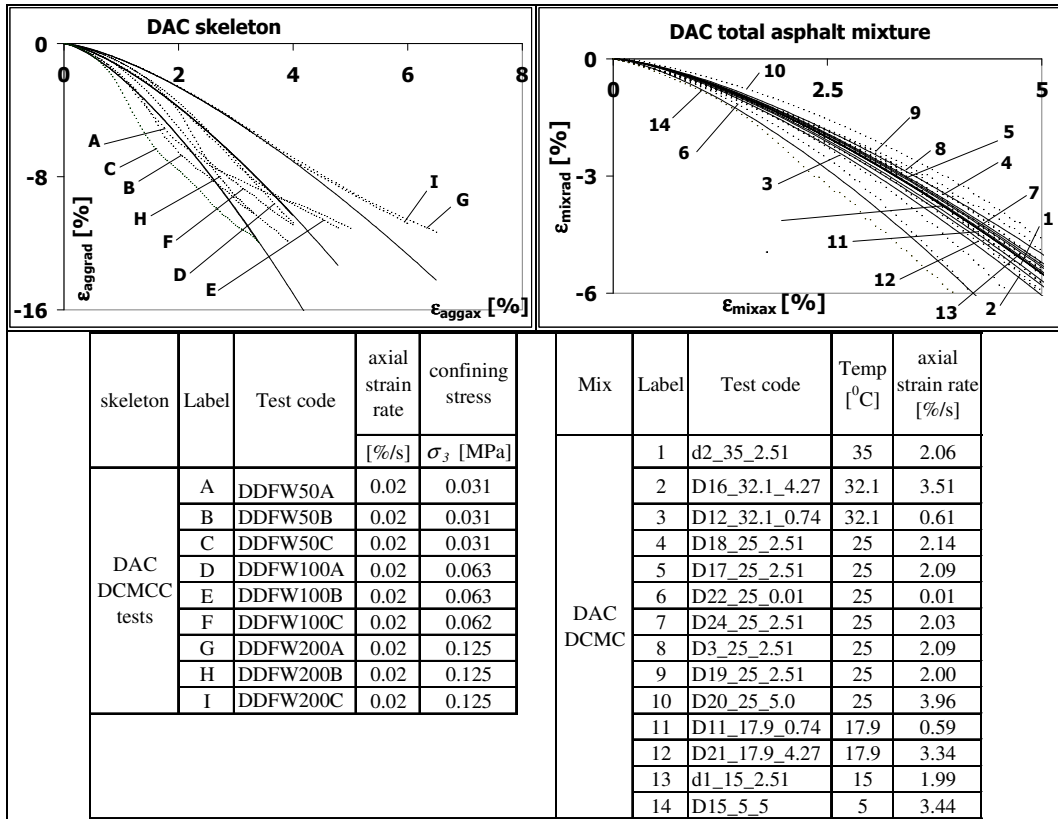


Figure 6.5 Model fit for the DAC aggregate skeleton and total asphalt mixture

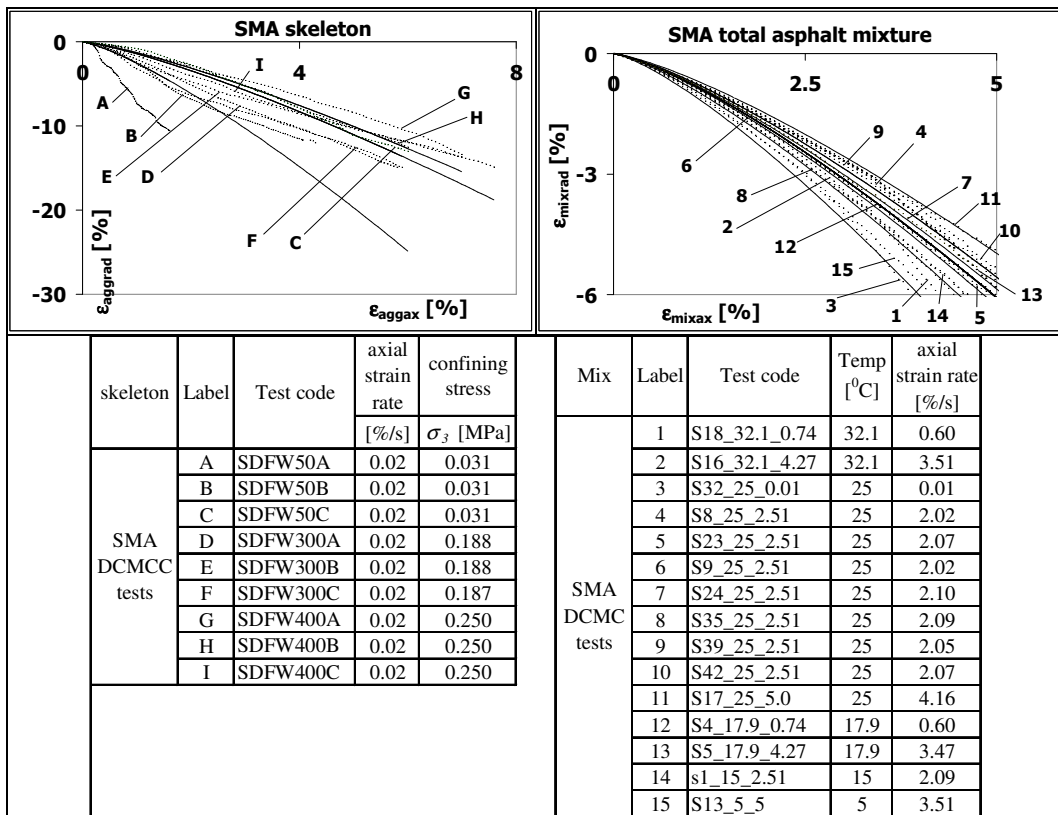


Figure 6.6 Model fit for the SMA aggregate skeleton and total asphalt mixture

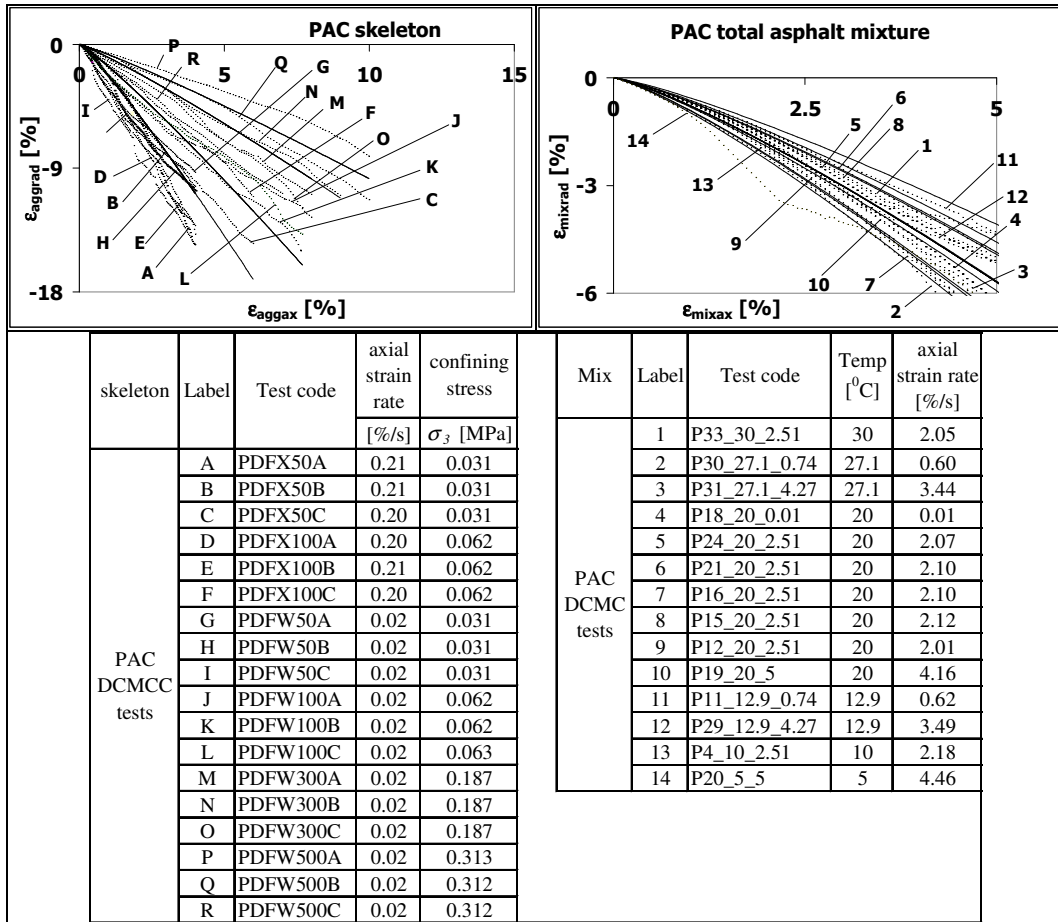


Figure 6.7 Model fit for the PAC aggregate skeleton and total asphalt mixture

6.1.2 Indicative Tensile Stress in the Mastic/Mortar

Figure 6.8 and Figure 6.9 show a plot of the indicative tensile stress and the equivalent confining stress for the mastic/mortar in the three asphalt mixtures. The reduced frequency is obtained as a product of the strain rate and the temperature shift factor determined from DCMC tests using the Unified Model in Chapter 5. The figure shows that both the indicative tensile stress and the equivalent confining stress are highest for the SMA followed by DAC and then PAC. This suggests that in order to resist permanent deformation, SMA mortar should have the highest resistance to tension followed by DAC and then PAC with the lowest. However, it should be mentioned that due to the surrounding material, the extent of dilation in the pavement is lower than the extent of dilation in laboratory.

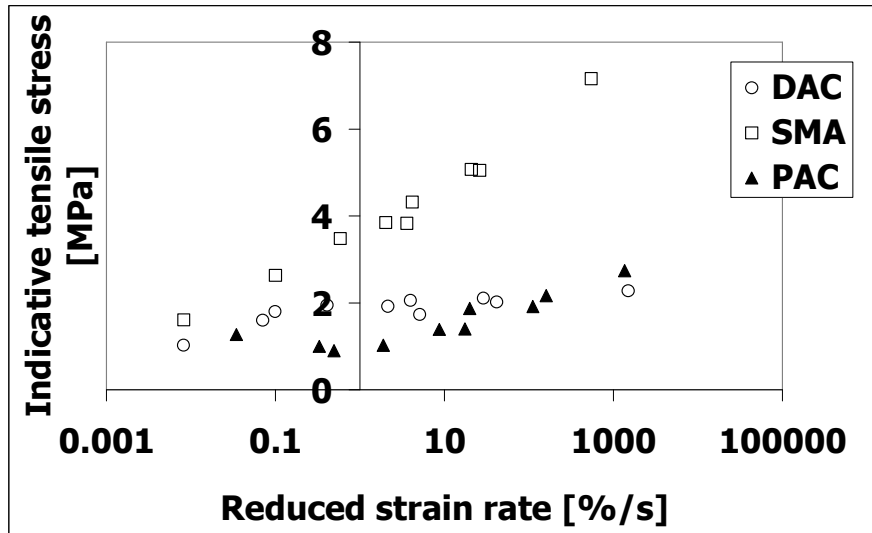


Figure 6.8 Indicative tensile stress in the mastic/mortar

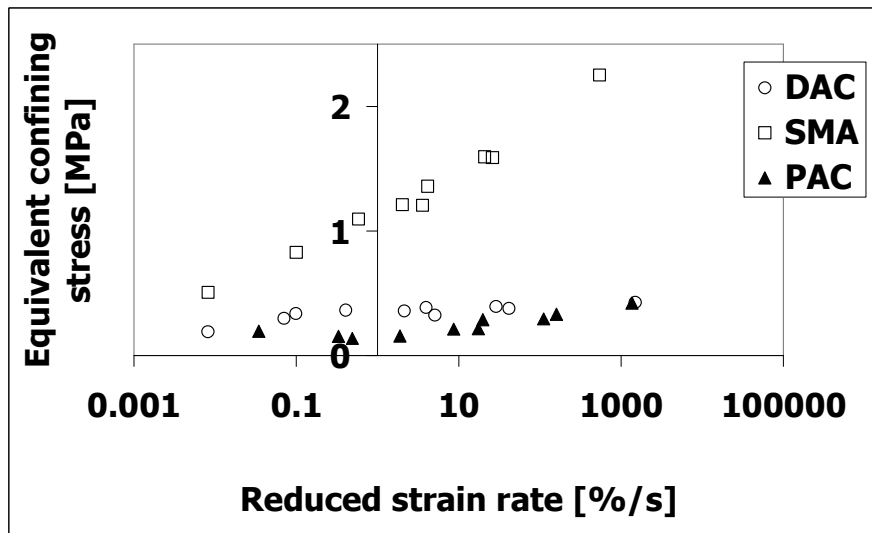


Figure 6.9 Equivalent confining stress of the mastic/mortar

6.1.3 Mastic Characterization

The foregoing discussion shows that the extent of dilation in the aggregate skeleton is higher than in the total asphalt mixture. This demonstrates the importance of the tensile strength in the bituminous binder for holding the aggregate skeleton together during deformation.

The tensile strength in the mastic was characterized using the direct tension test (DTT). The dynamic shear rheometer (DSR) test was used to determine the temperature susceptibility of the DAC mastic and the direct tension test (DTT) was used to characterise the failure behaviour of the DAC mastic. In addition to the DSR tests performed on the mastic, DSR tests were also performed on the 40/60 bitumen.

6.2 Ageing Test

Mastic specimens are fabricated at high temperatures and require longer mixing time than normal asphalt mixtures. The high temperatures are necessary to ensure sufficient workability during the mixing process. At such high temperatures and longer mixing time, the mastic may become more susceptible to ageing than normal asphalt mixtures. Since the asphalt mixtures considered in this research were mixed for three minutes, it was important to consider the extent of ageing that would occur during the mixing process of the mastic specimens.

Due to the anticipated difficulties in obtaining consistent and uniformly mixed mastic samples at the early stages of the mastic mixing process, bitumen was used to simulate the mixing process of the mastic. The ageing tests involved penetration tests performed on the 40/60 bitumen that was mixed for long time durations at high temperatures. The bitumen was mixed by means of a Hobart mixer to facilitate the flow of air into the bitumen during mixing.

The bitumen penetration tests were performed in accordance with the European specification (NEN 1426) but with a slight alteration in the sampling of bitumen. The bitumen was sampled above the recommended temperatures in NEN 1426. The purpose of the high temperatures was to simulate the mixing temperature of the mastic. In accordance with NEN 1426, unmodified bitumen should be sampled at 80 to 90⁰C above the expected softening point. This results in a temperature of 135⁰C using an average temperature above the softening point of 85⁰C and a softening point of 50⁰C that was obtained from the 40/60 bitumen certificate. However, due to poor workability it was not possible to mix the bitumen and the filler if the bitumen was heated temperatures below 135⁰C. The poor workability was as a result of rapid cooling during the mixing process.

The bitumen mixing procedure that was used to simulate the mastic mixing procedure is outlined below. In this procedure, the bitumen was mixed for more than 30 minutes with test specimens being extracted into containers (55 mm internal diameter by 35 mm internal height) after 0, 10, 20 and 30 minutes. During the sampling process after any given time duration, the temperature of the bitumen sometimes dropped by as much as 10⁰C. In order to correct for this drop in temperature during sampling, the temperature of the bitumen was raised back to the pre-sampling temperature prior to continuation of the mixing process. This procedure was carried out at time durations of 0, 10, 20 and 30 minutes with the bitumen being cooled for 1.5 hours and kept in the water bath at 25⁰C for 1.5 hours prior to the penetration test. Four specimens were sampled after each mixing duration. The adopted procedure was as follows:

1. Melt about 2 kg of bitumen at 135⁰C and extract 4 penetration test samples to represent 0 minutes mixing time.
2. Raise the temperature of the bitumen to 160⁰C and mix for 10 minutes, note the pre-sampling temperature and extract 4 penetration test samples.
3. Since the temperature of the bitumen drops during sampling, raise the temperature of bitumen back to pre-sampling temperature and mix for another time duration, note the temperature then extract 4 penetration test samples. Repeat step 3 for all the specified time durations.

4. Allow the sampled bitumen to cool for 1.5 hours at room temperature.
5. Keep the test samples in a water bath for 1.5 hours at 25⁰C then perform at least four penetration tests.

Table 6.2 and Figure 6.10 show the results of the penetration tests for the 40/60 bitumen. In accordance with NEN 1426, at least three determinations were selected in which the difference between the minimum and the maximum did not exceed a value of 2. Penetrations not meeting this criterion in a given sample were discarded. The penetration decreased with increase in mixing time as shown in Figure 6.10. Figure 6.10 shows that mixing the 40/60 bitumen at a temperature range of 140 – 160⁰C for half an hour results in no significant change in the penetration results. This shows that no significant ageing takes place after mixing the 40/60 bitumen for half an hour. Consequently it was concluded that no significant ageing would take place in the first 30 minutes during the preparation of DAC mastic specimens at temperatures in the range of 140⁰C to 160⁰C.

Table 6.2 Penetration results for 40/60 bitumen ageing tests

Mixing time [min]	Sample	Penetration [0.1 mm]					Average pen [0.1 mm]
0	01	44	45	46	43	46	45
	02	45	44	44	45	44	44
	03	46	44	46	45	44	45
	04	40	45	45	45	44	45
	Average pen before mixing						45
10	101	42	42.3	46	46	46	46
	102	45	44	48	45.3	45.5	45
	103	45	43	42	46	46.5	43
	104	44	43	43.5	45.5	45	44
	Average pen after mixing for 10 minutes						45
20	201	40	39	42	45		
	202	44	43	46	41	39	
	203	43	44	42	45	40	44
	204	48	44	45	44	43	44
	Average pen after mixing for 20 minutes						44
30	301	40	41	43	43		42
	302	41.5	43	43	42.5	45.5	43
	303	45.5	42	43.5	42	43	43
	304	42	42	40	44	43	43
	Average pen after mixing for 30 minutes						43
disregarded penetration values							

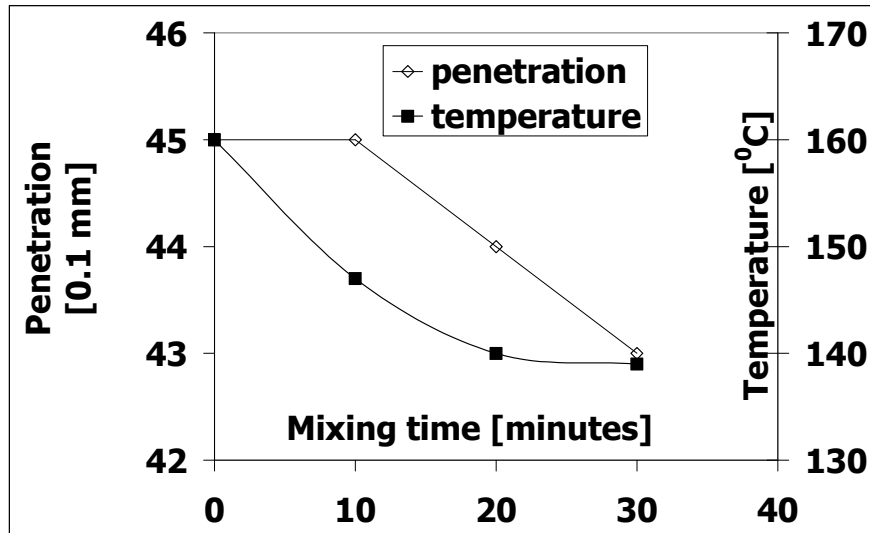


Figure 6.10 Penetration results for 40/60 bitumen ageing tests

6.3 Preparation of Mastic Specimens

The DAC mastic consisted of the fractions that were omitted from the dense aggregate skeleton. The composition of the mastic is shown in Table 6.3. The table also shows the densities of the fractions and the mastic. The volumetric composition was calculated assuming that the mastic contained no air voids and that no bitumen was absorbed by the aggregates in the mastic. The volumetric composition of different fractions was determined using the expression shown in Equation 6.6.

$$V_x = \frac{\rho_m P_x}{\rho_x} \quad 6.6$$

$$\rho_m = \frac{100}{\frac{P_{sand}}{\rho_{sand}} + \frac{P_{filler}}{\rho_{filler}} + \frac{P_{bitumen}}{\rho_{bitumen}}} \quad 6.7$$

Where:

- V_x = volumetric composition of fraction x [%],
- P_x = percentage by weight of fraction x [%],
- ρ_x = density of fraction x [kg/m^3].

Table 6.3 DAC mastic composition

fraction		sand <0.063 mm	wigro filler	bitumen 40/60	total
composition	weight	5.3	50.7	44.0	100
	volume	3.2	29.3	67.6	100
fraction		sand <0.063 mm	wigro filler	bitumen 40/60	mastic
density [kg/m^3]		2677	2750	1035	1589

The mastic specimen preparation involved manual mixing of the aggregate fractions and the bitumen in a heated container using a heated spoon. The aggregates, the spoon and the container were heated to 10°C above the bitumen

EVT temperature (160⁰C) while the bitumen was heated at EVT temperature. The heated bitumen was poured into the heated container after which the bitumen was mixed together with about half of the aggregates. After the mixture was well mixed, the other half was added and mixed. The aggregates and the bitumen were mixed together for a total of 8 minutes. During this time the mixture was re-heated 3 to 4 times on a heating plate to facilitate the mixing process. The mastic was then cooled and stored in a freezer at below -20⁰C ready for DSR test or DTT specimen fabrication.

6.4 DSR Test Set Up

The DSR test set-up consisted of three sets of parallel test plates of 8, 25 and 50 mm diameter, a temperature control chamber and a data acquisition/processing system. Figure 6.11 shows the temperature control chamber and the parallel test plates. The test plates consisted of a fixed upper plate and a lower oscillating plate capable of providing a loading frequency in the range of 0.1 – 400 rad/sec. The temperature control cabinet was capable of maintaining temperatures in the range of -10 to 60⁰C. The data acquisition/processing system acquired the data and calculated the storage modulus, loss modulus, phase angle and complex modulus.

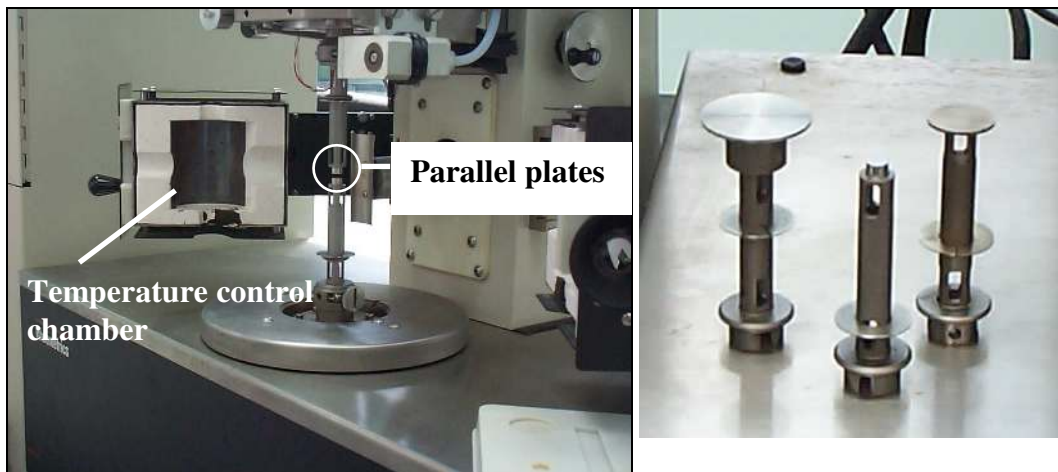


Figure 6.11 DSR Test set up and the parallel plates of 50, 8 and 25 mm diameter

6.5 DSR Test Conditions

In order to determine the temperature susceptibility of the DAC mastic and the 40/60 bitumen, DSR frequency sweep tests were performed at numerous test conditions. The frequency sweep tests were performed in the region where the complex modulus is linear and independent of the shear strain. Prior to each frequency sweep test at a given temperature, a strain sweep test was performed on the same specimen to determine the linear region of the complex modulus. The strain sweep tests were conducted up to a maximum of 10% strain. The frequency sweep tests were then conducted at strains determined in the linear region of the complex modulus from Equation 6.8 (SHRP-A-370 1994). Table 6.4 and Table 6.5 show the DSR test conditions for DAC mastic and 40/60 bitumen. The tests were conducted at -10, 0, 10, 20, 30, 40, 50 and 60⁰C with a frequency sweep test being performed at each temperature. Each frequency sweep consisted of frequencies ranging from 0.1 to 400 rad/s.

$$\text{strain [\%]} = \frac{12}{\left(\frac{G^*}{1000}\right)^{0.29}} \quad 6.8$$

Where:

strain = strain at which the frequency sweep tests were conducted,
 G^* = complex modulus determined from the strain sweep tests [Pa].

Table 6.4 DSR for DAC Mastic Test Conditions

frequency [rad/s]	400, 252.4, 159.2, 100.5, 63.4, 40, 25.2, 15.9, 10, 6.3, 4, 2.5, 1, 0.6, 0.3, 0.2, 0.1							
plate diameter [mm]	8				25			
temp [$^{\circ}$ C]	-10	0	10	20	30	40	50	60
strain [%]	0.25	0.28	0.37	0.6	1	2.1	3.5	5.5
height [mm]	2.322	2.218	2.154	2.127	2.148	0.999	1	1

Table 6.5 DSR for 40/60 Bitumen Test Conditions

frequency [rad/s]	400, 252.4, 159.2, 100.5, 63.4, 40, 25.2, 15.9, 10, 6.3, 4, 2.5, 1, 0.6, 0.3, 0.2, 0.1							
plate diameter [mm]	8				25			
temp [$^{\circ}$ C]	-10	0	10	20	30	40	50	60
strain [%]	0.32	0.43	0.62	1.1	2.5	3.5	5.5	8.5
height [mm]	2.402	2.369	2.362	2.264	2.168	1	1	1

6.6 DTT Test Set Up

The DTT test set up consisted of a lower crosshead moving with a maximum speed of 383 mm/min and a data acquisition system. The data acquisition system was capable of capturing data at low and high displacement rates above 100 mm/min. The axial specimen deformation was measured by means of two axial LVDTs that recorded the relative displacement of the lower moving crosshead as illustrated in Figure 6.12. The measuring range of the two external LVDTs was 10 and 20 mm.

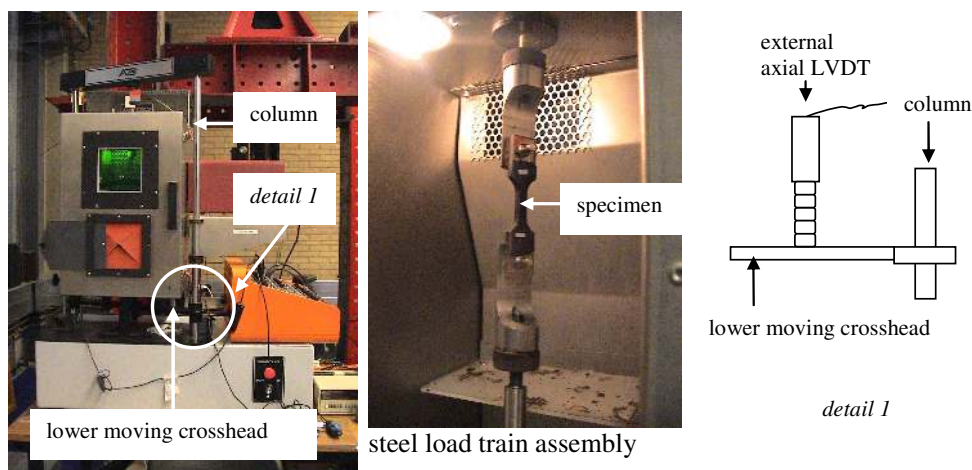


Figure 6.12 Measurement of axial deformation in the DTT test

6.7 DTT Specimen Fabrication

Table 6.6 shows a summary of four procedures that were considered in the fabrication of the DAC mastic specimens. The aim of considering these four methods was to obtain a specimen fabrication method that could be used to obtain an even surface on the upper part of the specimen. Method 3 was used in the fabrication of most of the test specimens since it resulted in a better texture on the upper surface in comparison with the other methods. However, since the cracks during testing appeared to initiate from the bottom surface and because segregation was suspected to be the cause of this crack initiation some test specimens were prepared using method 4. The specimens prepared using method 4 were observed to have a dull upper surface similar in texture to the bottom surface. It was as such concluded that the shiny upper surface observed in method 3 was not caused by segregation during cooling but by the texture of the aluminium foil.

Table 6.6 Mastic specimen fabrication procedures

Method	description	comments
1	Melt the mastic and heat the mould for 1 hr at 160 ⁰ C. Pour the mastic into the hot mould and trim with a hot knife. Cool at room temperature for 1 hr and place in the freezer. Extract from the mould and break off the excessive mastic on the edges.	Not possible to trim with one stroke. Results in a shiny rough upper surface and rough edges. Cracks seem to initiate from the dull bottom surface.
2	Melt the mastic and heat the mould and a steel plate for 1 hr at 160 ⁰ C (140 ⁰ C for some). Pour the mastic into the hot mould and place a silicon paper on the upper surface followed by the hot steel plate. Cool at room temperature for 1 hr and place in the freezer. Extract from the mould and file the excessive mastic on the edges.	Results in a specimen with smooth edges and shiny smooth upper surface with holes that were probably caused by the release of trapped air during cooling. The cracks during testing appeared to initiate from these holes. The workability of the specimens prepared by heating the moulds and the mastic at a temperature of 140 ⁰ C was insufficient to properly fill the cavities of the mould.
3	Melt the mastic and heat the mould and a glass plate for 1 hr at 150 ⁰ C. Pour the mastic into the hot mould and place an aluminium foil on the upper surface followed by the hot glass plate. Cool for 1 hr. in the cold room at 14 ⁰ C and place in the freezer. Extract from the mould and file the excessive mastic on the edges.	Specimens cooled in the cooling room to minimise and control any segregation that may occur during cooling. Results in a specimen with sufficient workability, smooth edges and shiny smooth upper surface with relatively smaller holes in comparison to the other methods.
4	Melt the mastic and heat the mould and, glass plate and a piece of rubber for 1 hr at 150 ⁰ C. Pour the mastic into the hot mould and place the hot rubber on the upper surface followed by the hot glass plate. Cool for 1 hr. in the cold room at 14 ⁰ C and place in the freezer. Extract from the mould and file the excessive mastic on the edges.	Upper surface and bottom surface appear to have similar textures. Shiny surface observed in method 2 and 3 was not caused by segregation during cooling but by the texture of the silicon paper and the aluminium foil.

6.7.1 DTT specimen Fabrication Summary

Method 3 was used to fabricate most of the DAC mastic specimens. The mastic specimens were fabricated using a rubber mould, steel plate, aluminium foils, a glass plate and a steel mixing spoon. Figure 6.13 shows the file, aluminium foils, rubber mould and steel plate that were used in the DTT specimen fabrication. Prior to specimen fabrication, the mastic, rubber mould, glass plate and the mixing spoon were heated together for one hour at 150°C. The mastic was then remixed and poured into the mould placed on the steel plate after which the aluminium foils were placed on the mastic followed by the glass plate. The poured mastic was then cooled in a cold room at 14°C for one hour prior to being placed in a freezer. The specimens were then extracted and filed to remove the excessive mastic on the edges. The mastic was cooled in a cold room in order to minimise and control any segregation that may have occurred during the cooling process. The purpose of the glass plate and the aluminium foils was to create a smooth top surface without using a knife edge as in standard DTT preparation procedure for bitumen since the mastic surface could not be trimmed at one go.

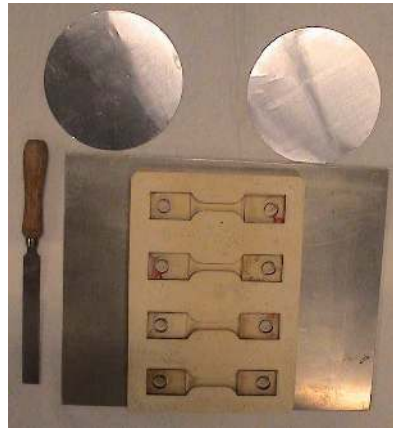


Figure 6.13 File, aluminium foils, rubber mould and steel plate used in the DTT specimen fabrication

6.8 DTT Test Conditions for DAC Mastic

Since permanent deformation occurs at high temperatures, the idea behind DTT test conditions was to characterize the mastic failure behaviour in tension at the highest possible temperatures within the limits of the DTT set up. These limits included both the displacement range and rate of displacement of the lower moving crosshead. The maximum displacement rate was 383 mm/min and the maximum displacement range was about 18 mm. The lowest displacement rate for each temperature was identified after which the tests were performed at displacement rates within the minimum and the maximum possible rate of displacement. The target test conditions of the DTT mastic specimens are shown in Table 6.7.

Table 6.7 DTT test conditions

Label	Test code	Temp [°C]	Target strain rate [%/s]	Label	Test code	Temp [°C]	Target strain rate [%/s]
1	M1301-006_5_25	5	1.23	17	M2112-008_10_100	10	4.93
2	M2601-001_5_25	5	1.23	18	M2112-007_10_100	10	4.93
3	M1301-001_5_50	5	2.47	19	M2112-006_10_200	10	9.86
4	M2001-001_5_100	5	4.93	20	M2112-005_10_200	10	9.86
5	M2601-002_5_100	5	4.93	21	M2112_004_10_200	10	9.86
6	M1301-003_5_150	5	7.40	22	M2112-003_10_383	10	18.89
7	M2301-002_7.5_50	7.5	2.47	23	M2112-002_10_383	10	18.89
8	M2601-004_7.5_50	7.5	2.47	24	M2112-001_10_383	10	18.89
9	M2301-001_7.5_100	7.5	4.93	25	M1201-002_12.5_150	12.5	7.40
10	M2001-004_7.5_150	7.5	7.40	26	M1201-003_12.5_200	12.5	9.86
11	M2301-004_7.5_150	7.5	7.40	27	M1201-004_12.5_250	12.5	12.33
12	M2001-003_7.5_200	7.5	9.86	28	M1201-005_12.5_300	12.5	14.79
13	M2601-003_7.5_200	7.5	9.86	29	M1201-006_12.5_350	12.5	17.26
14	M2001-002_7.5_250	7.5	12.33	30	M1201-007_12.5_383	12.5	18.89
15	M2212-007_10_100	10	4.93	31	M2012-006_15_383	15	18.89
16	M2112-009_10_100	10	4.93	32	M2012-005_15_383	15	18.89
				33	M2012-004_15_383	15	18.89

6.9 DSR Test Results

The complex modulus and the phase angle as obtained from the DSR test results for the 40/60 bitumen and the DAC mastic are shown in Figure 6.14 and Figure 6.15 respectively. The tabulated values can be found in Table 6.8, Table 6.9, Table 6.10, Table 6.11, Table 6.12 and Table 6.13. Figure 6.14 and Figure 6.15 show that the complex modulus of the bitumen and the mastic decreases with increase in temperature and increases with increase in frequency especially at high temperatures. At low temperatures of 20°C and below, the complex modulus increases with frequency but the rate of increase decreases with increase in frequency. Figure 6.14 and Figure 6.15 also show that the phase angle increases with increase in temperature but above 40°C and at frequencies below 1 rad/s, the phase angle remains more or less the same. In general, the phase angle decreases with increase in frequency. However, at temperatures below 0°C and frequencies above approximately 300 rad/s for the bitumen and at temperatures below 10°C and above approximately 100 rad/s for the mastic, the phase angle reaches some limiting value after which it seems to increase with increase in frequency. This apparent increase of the phase angle could be due to the generation of heat at high frequencies.

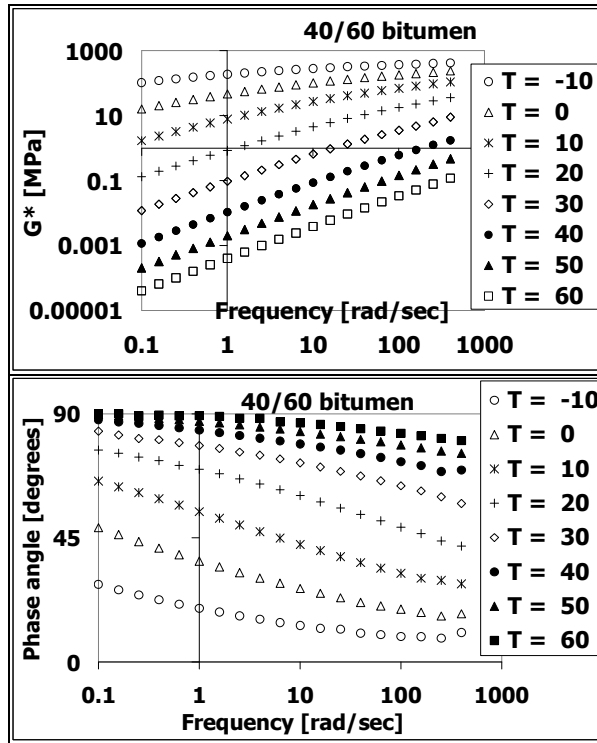


Figure 6.14 Complex modulus and phase angle DSR test results for the 40/60 bitumen

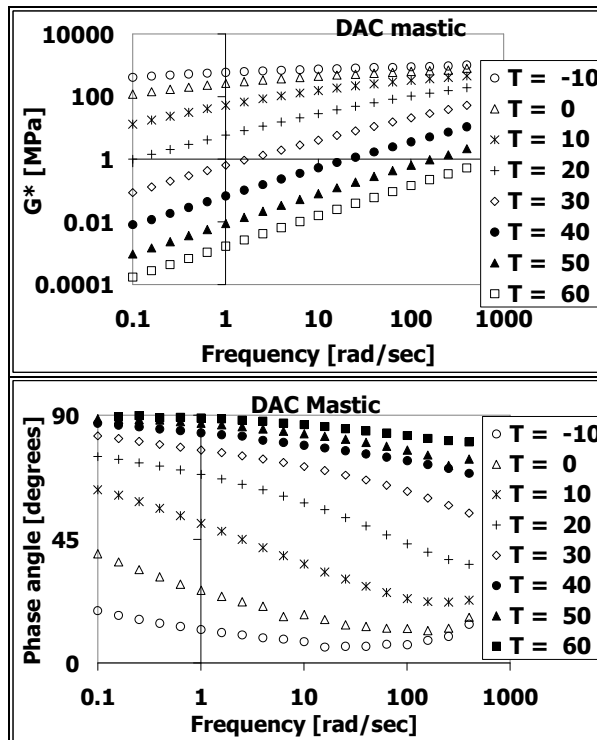


Figure 6.15 Complex modulus and phase angle DSR test results for the DAC mastic

Table 6.8 DSR test results for 40/60 bitumen at -10, 0 and 10°C

Temp [°C]	Freq [rad/s]	G* [MPa]	Phase angle [°]	Temp [°C]	Freq [rad/s]	G* [MPa]	Phase angle [°]	Temp [°C]	Freq [rad/s]	G* [MPa]	Phase angle [°]
-10	400	420	11	0	400	237	17	10	400	108.2	28
	252.4	402	9		252.4	214	17		252.4	94.9	30
	159.2	382	9		159.2	197	18		159.2	80.8	30
	100.5	367	9		100.5	180	19		100.5	69.2	32
	63.4	350	10		63.4	163	20		63.4	58.8	34
	40.0	334	10		40.0	147	22		40.0	49.3	36
	25.2	323	12		25.2	131	23		25.2	40.8	38
	15.9	299	12		15.9	116	25		15.9	33.4	40
	10.0	281	13		10.0	102	27		10.0	27.0	43
	6.3	261	14		6.3	88	29		6.3	21.6	45
	4.0	243	16		4.0	76	30		4.0	17.1	47
	2.5	224	17		2.5	65	32		2.5	13.3	50
	1.6	205	18		1.6	55	34		1.6	10.2	52
	1.0	187	19		1.0	46	37		1.0	7.8	54
0.6	170	21	0.6	38	39	0.6	5.9	57			
0.4	152	23	0.4	31	41	0.4	4.4	59			
0.3	135	24	0.3	25	44	0.3	3.2	61			
0.2	119	26	0.2	20	46	0.2	2.4	63			
0.1	104	28	0.1	16	49	0.1	1.7	66			

Table 6.9 DSR test results for 40/60 bitumen at 20, 30 and 40°C

Temp [°C]	Freq [rad/s]	G* [MPa]	Phase angle [°]	Temp [°C]	Freq [rad/s]	G* [MPa]	Phase angle [°]	Temp [°C]	Freq [rad/s]	G* [MPa]	Phase angle [°]
20	400	36.1	42	30	400	9.03	57	40	400	1.739	70
	252.4	28.6	44		252.4	6.41	60		252.4	1.253	69
	159.2	22.7	47		159.2	4.76	62		159.2	0.880	71
	100.5	17.9	49		100.5	3.56	64		100.5	0.613	73
	63.4	14.0	51		63.4	2.61	66		63.4	0.421	74
	40.0	10.8	53		40.0	1.88	67		40.0	0.286	76
	25.2	8.2	56		25.2	1.35	69		25.2	0.194	77
	15.9	6.1	58		15.9	0.95	71		15.9	0.130	78
	10.0	4.5	60		10.0	0.66	72		10.0	0.087	79
	6.3	3.3	63		6.3	0.45	74		6.3	0.057	80
	4.0	2.4	65		4.0	0.31	75		4.0	0.038	81
	2.5	1.7	66		2.5	0.21	76		2.5	0.025	82
	1.6	1.2	68		1.6	0.14	77		1.6	0.016	83
	1.0	0.9	70		1.0	0.10	78		1.0	0.011	84
0.6	0.6	71	0.6	0.06	79	0.6	0.007	85			
0.4	0.4	73	0.4	0.04	81	0.4	0.004	86			
0.3	0.3	74	0.3	0.03	81	0.3	0.003	87			
0.2	0.2	76	0.2	0.02	82	0.2	0.002	87			
0.1	0.1	77	0.1	0.01	84	0.1	0.001	88			

Table 6.10 DSR test results for 40/60 bitumen at 50 and 60°C

Temp [°C]	Freq [rad/s]	G* [MPa]	Phase angle [°]	Temp [°C]	Freq [rad/s]	G* [MPa]	Phase angle [°]
50	400	0.470	76	60	400	0.1187	80
	252.4	0.319	76		252.4	0.0784	81
	159.2	0.215	78		159.2	0.0517	82
	100.5	0.144	79		100.5	0.0340	83
	63.4	0.096	80		63.4	0.0222	84
	40.0	0.064	81		40.0	0.0145	85
	25.2	0.042	82		25.2	0.0093	85
	15.9	0.028	83		15.9	0.0060	86
	10.0	0.018	84		10.0	0.0039	87
	6.3	0.012	84		6.3	0.0024	87
	4.0	0.008	85		4.0	0.0016	88
	2.5	0.005	86		2.5	0.0010	88
	1.6	0.003	87		1.6	0.0006	89
	1.0	0.002	87		1.0	0.0004	89
0.6	0.001	88	0.6	0.0003	89		
0.4	0.001	88	0.4	0.0002	90		
0.3	0.001	89	0.3	0.0001	89		
0.2	0.0003	89	0.2	0.0001	90		
0.1	0.0002	90	0.1	0.00004	90		

Table 6.11 DSR test results for DAC mastic at -10, 0 and 10°C

Temp [°C]	Freq [rad/s]	G* [MPa]	Phase angle [°]	Temp [°C]	Freq [rad/s]	G* [MPa]	Phase angle [°]	Temp [°C]	Freq [rad/s]	G* [MPa]	Phase angle [°]
-10	400	1011	14	0	400	789	17	10	400	449.0	23
	252.4	941	10		252.4	692	13		252.4	403.9	22
	159.2	892	8		159.2	658	12		159.2	366.7	22
	100.5	884	7		100.5	638	13		100.5	328.6	23
	63.4	845	7		63.4	587	13		63.4	289.1	26
	40.0	834	6		40.0	552	13		40.0	252.5	28
	25.2	804	6		25.2	516	14		25.2	219.4	30
	15.9	764	6		15.9	483	16		15.9	185.2	33
	10.0	746	8		10.0	444	18		10.0	155.1	36
	6.3	715	9		6.3	403	17		6.3	129.0	39
	4.0	689	9		4.0	370	21		4.0	105.1	42
	2.5	655	10		2.5	332	22		2.5	84.6	45
	1.6	624	11		1.6	297	24		1.6	67.2	48
	1.0	589	12		1.0	262	26		1.0	52.6	51
0.6	554	13	0.6	229	29	0.6	40.7	54			
0.4	519	14	0.4	198	31	0.4	31.2	56			
0.3	482	16	0.3	169	34	0.3	23.6	59			
0.2	447	17	0.2	142	37	0.2	17.8	61			
0.1	410	19	0.1	118	40	0.1	13.2	63			

Table 6.12 DSR test results for DAC mastic at 20, 30 and 40°C

Temp [°C]	Freq [rad/s]	G* [MPa]	Phase angle [°]	Temp [°C]	Freq [rad/s]	G* [MPa]	Phase angle [°]	Temp [°C]	Freq [rad/s]	G* [MPa]	Phase angle [°]
20	400	189.8	36	30	400	52.58	54	40	400	10.743	69
	252.4	156.4	38		252.4	38.52	57		252.4	7.268	71
	159.2	127.9	40		159.2	28.59	60		159.2	5.104	72
	100.5	103.2	43		100.5	21.04	62		100.5	3.566	74
	63.4	81.8	47		63.4	15.34	65		63.4	2.464	75
	40.0	63.6	50		40.0	11.12	67		40.0	1.697	76
	25.2	49.0	53		25.2	8.00	68		25.2	1.158	77
	15.9	37.2	56		15.9	5.69	70		15.9	0.784	78
	10.0	28.0	58		10.0	4.01	71		10.0	0.526	79
	6.3	20.9	61		6.3	2.80	73		6.3	0.352	80
	4.0	15.4	63		4.0	1.94	74		4.0	0.232	81
	2.5	11.2	65		2.5	1.34	75		2.5	0.154	82
	1.6	8.1	67		1.6	0.92	76		1.6	0.102	83
	1.0	5.8	69		1.0	0.63	77		1.0	0.067	84
0.6	4.1	70	0.6	0.43	78	0.6	0.044	84			
0.4	2.9	72	0.4	0.29	79	0.4	0.029	85			
0.3	2.0	73	0.3	0.20	80	0.3	0.018	86			
0.2	1.4	74	0.2	0.13	82	0.2	0.012	86			
0.1	1.0	75	0.1	0.09	83	0.1	0.008	87			

Table 6.13 DSR test results for DAC mastic at 50 and 60°C

Temp [°C]	Freq [rad/s]	G* [MPa]	Phase angle [°]	Temp [°C]	Freq [rad/s]	G* [MPa]	Phase angle [°]
50	400	2.145	74	60	400	0.5234	80
	252.4	1.376	72		252.4	0.3385	81
	159.2	0.959	76		159.2	0.2208	82
	100.5	0.643	77		100.5	0.1424	83
	63.4	0.426	79		63.4	0.0922	84
	40.0	0.282	80		40.0	0.0597	84
	25.2	0.185	81		25.2	0.0386	85
	15.9	0.121	82		15.9	0.0249	86
	10.0	0.080	83		10.0	0.0159	87
	6.3	0.052	84		6.3	0.0102	87
	4.0	0.033	85		4.0	0.0065	88
	2.5	0.022	86		2.5	0.0042	88
	1.6	0.014	87		1.6	0.0026	89
	1.0	0.009	87		1.0	0.0017	89
0.6	0.006	88	0.6	0.0011	89		
0.4	0.004	88	0.4	0.0007	89		
0.3	0.002	88	0.3	0.0004	90		
0.2	0.0015	88	0.2	0.0003	89		
0.1	0.0009	89	0.1	0.00017	90		

6.9.1 Modelling of Complex Modulus and Phase Angle

The Unified Model has been applied in the modelling of properties that were determined from the DCMC and DCMT tests conducted on the total mixture. However, it was not possible to describe the DSR test results using the Unified Model. This was due to the following reasons:

1. The temperature susceptibility function in the Unified Model could not describe the temperature susceptibility observed in the DSR tests.
2. The expression of the S-curve in the Unified Model could not describe the complex modulus observed in DSR test results. More parameters in the expression for the S-curve were necessary in order to describe the complex modulus obtained from the DSR tests.

The complex modulus test results were consequently modelled based on a relationship developed by Bahia et al (2001) given in Equation 6.9 while the phase angle test results were modelled based on a modified version of the Unified Model given in Equation 6.10. The temperature susceptibility for the complex modulus and phase angle test results was described by Arrhenius type of Equation (Verstraeten 1972) shown in Equation 6.12.

$$G^* = G_e^* + \frac{G_g^* - G_e^*}{\left[1 + \left(\frac{f_c}{f'}\right)^k\right]^{\frac{m_e}{k}}} \quad 6.9$$

$$\delta = \delta_{\min} + (\delta_{\max} - \delta_{\min}) \left\{ \exp \left(- \left[\left(\frac{f'}{u_0} \right)^\lambda \right] \right) \right\} \quad 6.10$$

$$f' = a_T f \quad 6.11$$

$$a_T = e^{\left[c \left(\frac{1}{T} - \frac{1}{T_0} \right) \right]} \quad 6.12$$

Where:

G^*	=	complex modulus [MPa],
G_e^*	=	complex modulus as $f \rightarrow 0$ [MPa],
G_g^*	=	complex modulus as $f \rightarrow \infty$ [MPa],
f	=	loading frequency [rad/s],
f_c	=	location parameter [rad/s],
f'	=	reduced frequency [rad/s],
m_e, k	=	shape parameters [-],
δ	=	phase angle [degrees],
δ_{\max}	=	phase angle as $f \rightarrow 0$ point of inflexion [degrees],
δ_{\max}	=	phase angle as $f \rightarrow \infty$ [degrees],

u_0	=	a reference frequency [rad/s],
a_T	=	temperature shift factor,
T	=	temperature [K],
T_0	=	reference temperature [K],
λ	=	model parameter [-],
C	=	temperature susceptibility factor [K].

Table 6.14 shows the model coefficients for the complex modulus, phase angle and the Arrhenius equation. Figure 6.16, Figure 6.17 and Figure 6.18 show the model fit for the DSR test results for the 40/60 bitumen and the DAC mastic respectively. The figures show that the models described the data reasonably well.

Table 6.14 Model coefficients for the complex modulus and phase angle that were used in the construction of the master curves

Type of mixture	G*					Phase angle			Arrhenius		
	G* _g	G* _e	f _c	k	m _e	δ_{\max}	δ_{\min}	u_0	λ	C	T ₀
	[MPa]	[MPa]	[rad/s]	[-]	[-]	[degrees]	[degrees]	[rad/s]	[-]	[-]	[°C]
40/60 bitumen	569	0.0	4196	0.273	0.869	90.0	10.4	1335	0.217	23661	298
DAC mastic	1022	0.0	780	0.324	0.895	90.0	6.7	782	0.230	24360	298

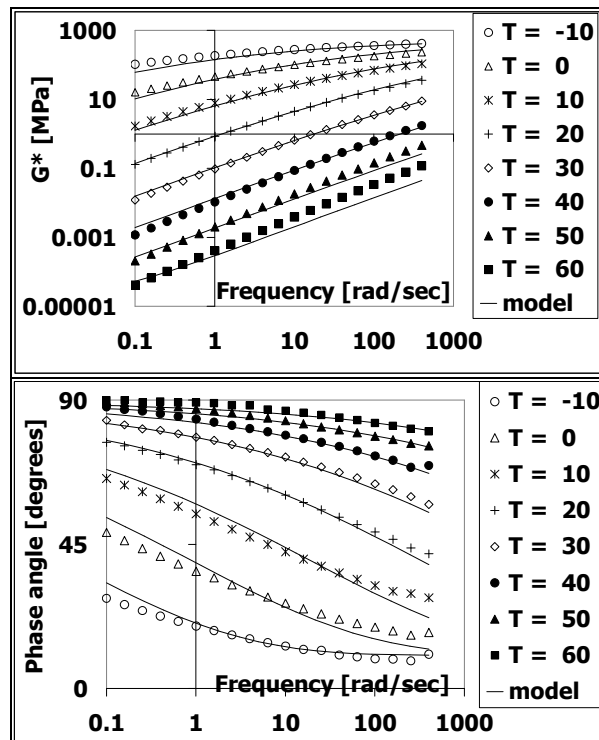


Figure 6.16 Model fit for the Complex modulus and phase angle test results of the 40/60 bitumen

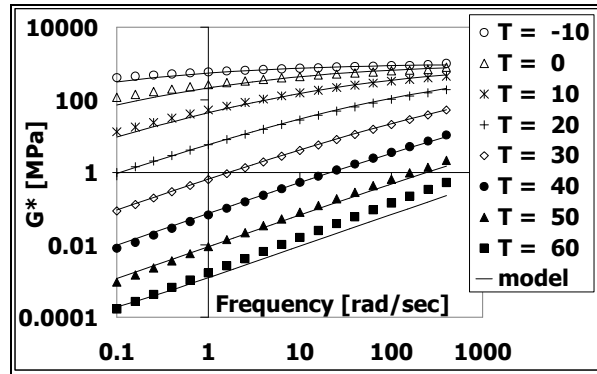


Figure 6.17 Model fit for the Complex modulus test results of the DAC mastic

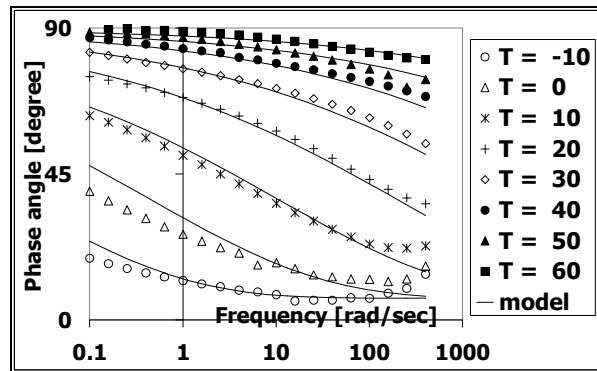


Figure 6.18 Model fit for the phase angle test results of the DAC mastic

Figure 6.19 shows the master curves for the complex modulus and phase angle. The figure shows that the complex modulus of the mastic was higher than that of the bitumen irrespective of the frequency. This shows that addition of filler to the bitumen increases the stiffness. The relative magnitude of the mastic phase angle in comparison to that of the bitumen depends on the frequency. At low frequencies and high temperatures, the phase angle of the mastic and bitumen are similar and close to the maximum phase angle of 90 degrees. On the other hand, the phase angle of the mastic is lower at high frequencies and low temperatures.

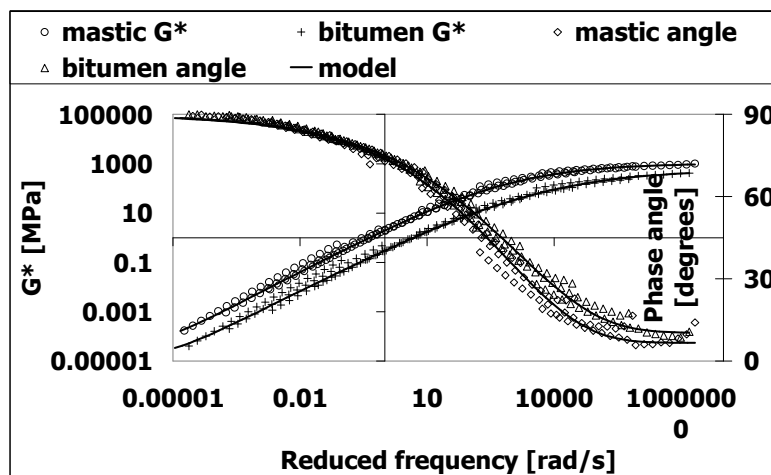


Figure 6.19 Shifted data and master curve for the complex modulus and the phase angle measured in the DSR tests at a reference temperature of 25°C

6.9.2 Comparison of the Measured Complex Modulus to the Shell Relationship for Dynamic Stiffness

Figure 6.20 and Figure 6.21 show the complex modulus of the DAC mastic as a function of the complex modulus of the bitumen. The figures include a comparison of the complex modulus measured in the DSR test and the complex modulus calculated using the Shell relationship for dynamic stiffness shown in Equation 6.13. The figure shows that the Shell relationship reasonably predicts the upper range of the mastic complex modulus at -10°C but underestimates the complex modulus at the other test temperatures of 0 to 60°C . The difference calculated from Equation 6.15 was less than 20% in tests conducted at -10°C and at frequencies in the range of 1 to 400 rad/s. The difference at all the other temperatures and frequencies was higher than 20%. This comparison shows that the relationship developed by Shell researchers 34 years ago seems less relevant to the mastic investigated in this research. This is not surprising since the Shell relationship does not account for the effect of the type of filler which is known to have a significant effect on the stiffness.

$$\frac{S_{mix}}{S_{bit}} = \left(1 + \frac{2.5}{n} \left[\frac{C_v}{1 - C_v} \right] \right)^n \quad (\text{Heukelom and Wijga, 1973}) \quad 6.13$$

Where:

$$n = 0.83 \log \left(\frac{4 \times 10^{10}}{S_{bit}} \right) \quad 6.14$$

$$\begin{aligned} S_{bit} &= \text{dynamic stiffness of the bitumen [Pa],} \\ S_{mix} &= \text{dynamic stiffness of the mixture [Pa],} \\ C_v &= \frac{\text{volume of minerals}}{\text{volume of minerals + bitumen}} = 0.324. \end{aligned}$$

$$\text{difference [\%]} = 100 \frac{|\text{DSR data} - \text{value calculated using Shell formula}|}{\text{DSR data}} \quad 6.15$$

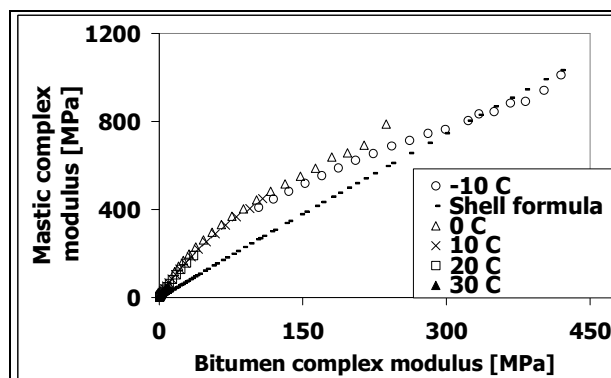


Figure 6.20 Mastic complex modulus as a function of bitumen complex modulus and a comparison of the complex modulus measured in the DSR test and the complex modulus calculated using the Shell formula for dynamic stiffness at 0 , 10 , 20 and 30°C

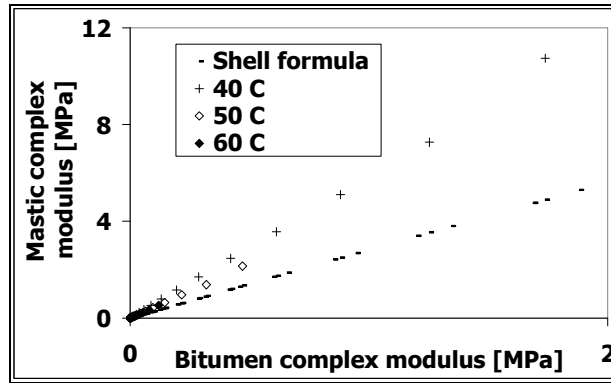


Figure 6.21 Mastic complex modulus as a function of bitumen complex modulus and a comparison of the complex modulus measured in the DSR test and the complex modulus calculated using the Shell formula for dynamic stiffness at 40, 50 and 60°C

6.10 DTT Test Results

Figure 6.23 and Figure 6.24 show the DTT test results for the DAC mastic conducted at 5, 7.5, 10, 12.5 and 15°C. The strain rates shown in these figures represent the actual strain rates during the test. The actual strain rate and the tangent stiffness from the DTT tests results were processed as illustrated in Figure 6.22. The stress and the strain in the DTT tests were calculated from Equation 6.16 and Equation 6.17 respectively. Table 6.15 and Table 6.16 show the target strain rates, actual strain rate, maximum tensile stress and the tangent stiffness that were processed from the DTT tests conducted on the DAC mastic.

$$\text{stress} = \frac{F}{A} = \left(\frac{F}{1000000w \times t} \right) \quad 6.16$$

$$\text{strain [\%]} = 100 \left(\frac{\delta L}{L_e} \right) \quad 6.17$$

Where:

δ	=	change in length [mm],
L_e	=	effective length = 33.8 mm,
F	=	axial force [MN],
w	=	average width of the necked section [mm],
t	=	thickness of the specimen = 6 mm.

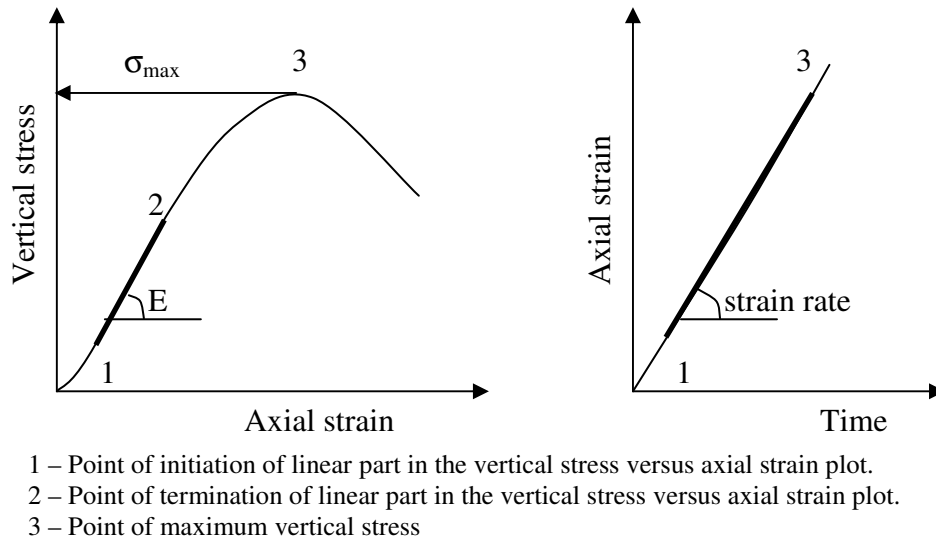


Figure 6.22 An illustration of the determination of the actual strain rate and the tangent stiffness in the DTT tests

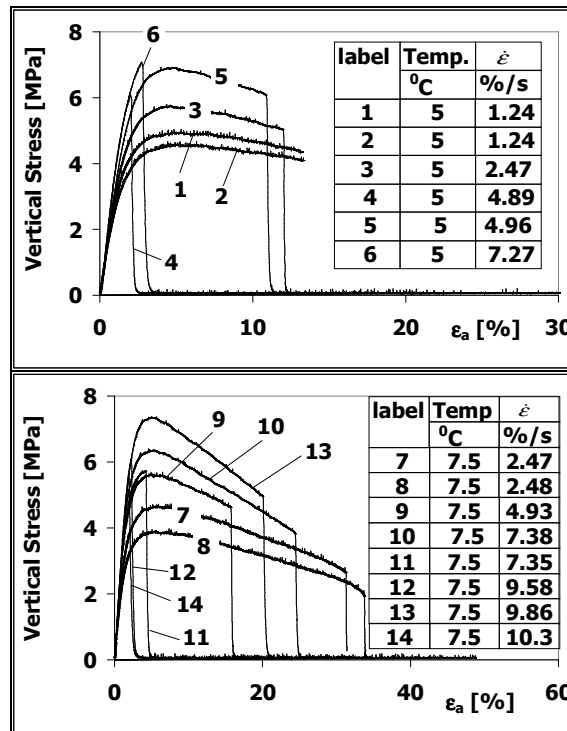


Figure 6.23 DTT Test Results for DAC mastic at 5 and 7.5^oC

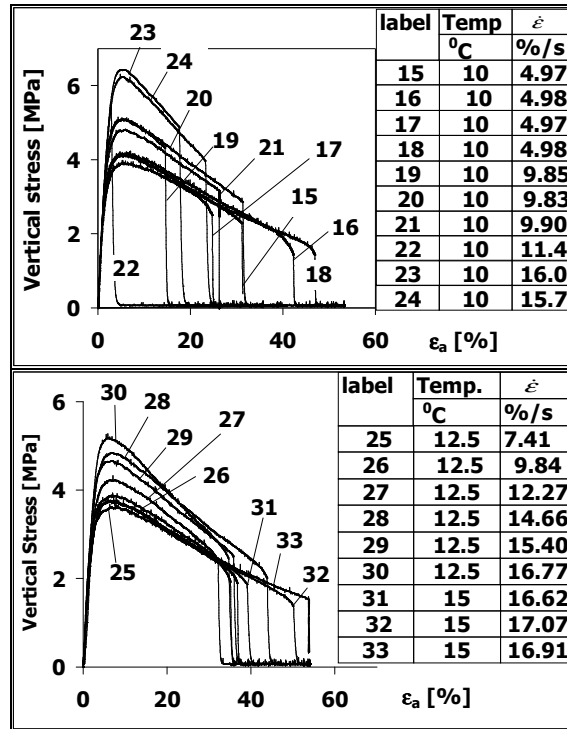


Figure 6.24 DTT Test Results for DAC mastic at 10, 12.5 and 15°C

Table 6.15 DTT Test Results for the DAC mastic at 5, and 7.5°C

Label	Test code	Temp [°C]	Target strain rate [%/s]	Actual strain rate [%/s]	f _i [MPa]	E _{tm} [MPa]
1	M1301-006_5_25	5	1.23	1.24	4.9	316
2	M2601-001_5_25	5	1.23	1.24	4.5	294
3	M1301-001_5_50	5	2.47	2.47	5.6	336
4	M2001-001_5_100	5	4.93	4.89	6.0	415
5	M2601-002_5_100	5	4.93	4.96	6.8	352
6	M1301-003_5_150	5	7.40	7.27	6.9	383
7	M2301-002_7.5_50	7.5	2.47	2.47	4.6	277
8	M2601-004_7.5_50	7.5	2.47	2.48	3.8	260
9	M2301-001_7.5_100	7.5	4.93	4.93	5.5	356
10	M2001-004_7.5_150	7.5	7.40	7.38	6.2	356
11	M2301-004_7.5_150	7.5	7.40	7.35	5.6	325
12	M2001-003_7.5_200	7.5	9.86	9.58	6.0	339
13	M2601-003_7.5_200	7.5	9.86	9.86	7.2	327
14	M2001-002_7.5_250	7.5	12.33	10.28	5.5	323

Table 6.16 DTT test results for the DAC mastic at 10, 12.5 and 15°C

Label	Test code	Temp [°C]	Target strain rate [%/s]	Actual strain rate [%/s]	f _t [MPa]	E _{tm} [MPa]
15	M2212-007_10_100	10	4.93	4.97	4.1	258
16	M2112-009_10_100	10	4.93	4.98	4.1	284
17	M2112-008_10_100	10	4.93	4.97	4.1	250
18	M2112-007_10_100	10	4.93	4.98	3.9	261
19	M2112-006_10_200	10	9.86	9.85	5.0	253
20	M2112-005_10_200	10	9.86	9.83	5.0	247
21	M2112_004_10_200	10	9.86	9.90	4.7	231
22	M2112-003_10_383	10	18.89	11.36	5.4	254
23	M2112-002_10_383	10	18.89	16.03	6.3	260
24	M2112-001_10_383	10	18.89	15.70	6.1	248
25	M1201-002_12.5_150	12.5	7.40	7.41	3.6	207
26	M1201-003_12.5_200	12.5	9.86	9.84	3.8	192
27	M1201-004_12.5_250	12.5	12.33	12.27	4.2	164
28	M1201-005_12.5_300	12.5	14.79	14.66	4.8	177
29	M1201-006_12.5_350	12.5	17.26	15.40	4.6	191
30	M1201-007_12.5_383	12.5	18.89	16.77	5.1	187
31	M2012-006_15_383	15	18.89	16.62	3.7	145
32	M2012-005_15_383	15	18.89	17.07	3.7	158
33	M2012-004_15_383	15	18.89	16.91	3.7	158

6.11 Modelling of DTT Test Results

The maximum tensile stress determined from the DTT tests were modelled using the modified version of the Unified Model shown in Equation 6.18. In this modified version the temperature susceptibility was described using the Arrhenius type of equation similar to the DSR test results. As mentioned in the introduction (section 6.1), the purpose of the DSR test conducted on the mastic was to characterise the temperature susceptibility of the DAC mastic. The temperature susceptibility determined from the mastic DSR tests was used in the modelling of the DTT maximum tensile stress. The tangent stiffness was modelled using the strain rate independent linear expression shown in Equation 6.22. The linear expression was used since the tangent stiffness was observed to be independent of the strain rate.

$$f_{tm} = f_{tmhigh} + S(f_{tmlow} - f_{tmhigh}) \quad 6.18$$

Where:

$$S = e^{(-[u, \beta]^2)} \quad 6.19$$

$$u_r = \frac{u}{u_0} \quad 6.20$$

$$\beta = a_T = e^{\left[c \left(\frac{1}{T} - \frac{1}{T_0} \right) \right]} \quad 6.21$$

$$E_{tm} = k_1 - k_2 T \quad 6.22$$

Where:

f_{tm}	=	maximum tensile stress [MPa],
f_{tmhigh}	=	maximum tensile stress as the strain rate approaches infinity [MPa],
f_{tmlow}	=	minimum tensile stress as the strain rate approaches zero [MPa],
u_0	=	a reference value for the strain rate [%/s],
u	=	strain rate [%/s],
C	=	temperature susceptibility factor from DSR modelling [K],
T_0	=	a temperature reference [K],
T	=	temperature [K],
λ	=	model parameter,
E_{tm}	=	tangent stiffness [MPa],
k_1, k_2	=	model coefficients.

Table 6.17 shows the model parameters for the mastic tensile strength and the tangent stiffness. Figure 6.25 shows the model fit on mastic tensile strength and Figure 6.26 shows the model fit on the tangent stiffness. These figures show that the models fitted the data reasonably well.

Table 6.17 Model parameters for the DAC mastic tensile strength and stiffness

Property	symbol	λ	C	T_0	μ_0	f_{tmhigh}	f_{tmlow}	k_1	k_2
DAC mastic tensile strength	f_{tm}	0.449	24360	298	998	9.46	0.0	-	-
DAC mastic tangent stiffness	E_{tm}	-	-	-	-	-	-	6099	20.7

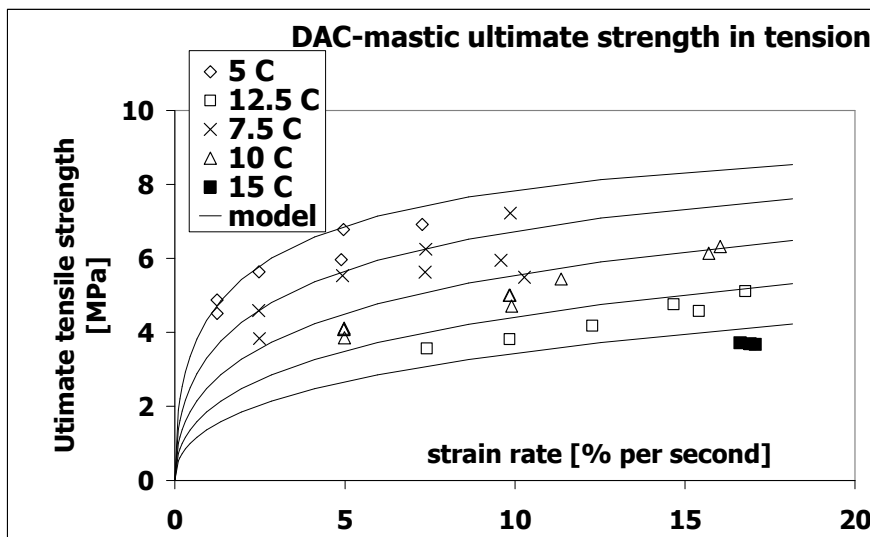


Figure 6.25 Model fit on the DAC mastic tensile strength

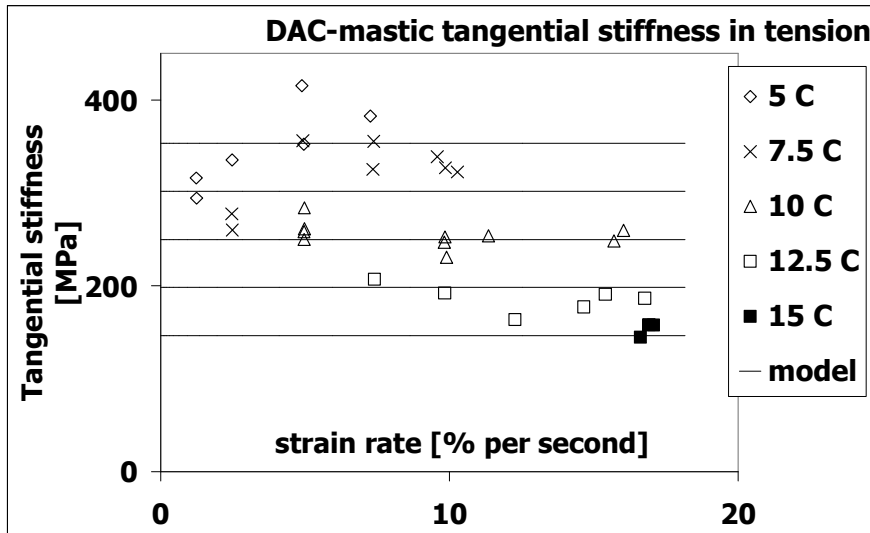


Figure 6.26 Model fit on the DAC mastic stiffness

6.12 Conclusions

The importance of the tensile strength in the mastic/mortar was underscored by a comparison of the extent of dilation occurring in the aggregate skeleton during the DCMCC tests and in the total asphalt mixture during the DCMC tests. Because of time limitations, the DAC bituminous binder which consisted of only the mastic was chosen for tensile strength characterization. The tensile strength in the DAC mastic was characterized using the DTT test. The temperature susceptibility of the DAC mastic was determined using the DSR test. Further DSR tests were conducted on the 40/60 bitumen. The following conclusions were reached:

- Despite of the application of confinement during the aggregate skeleton tests, the extent of dilation in the aggregate skeleton was higher than in the total asphalt mixture tests that were conducted without confinement. 14 of the 18 DCMCC tests conducted on the PAC aggregate skeleton exhibited more dilation than the DCMC tests conducted on the PAC total asphalt mixture. 14 of the 15 DCMC tests conducted on the SMA total asphalt mixture exhibited less dilation than the DCMCC test conducted on SMA aggregate skeleton. All the DCMC tests performed on DAC total asphalt mixture exhibited less dilation than the DCMCC tests performed on the DAC aggregate skeleton.
- The indicative tensile stress required to hold the aggregates together is highest for the SMA followed by DAC then PAC. This suggests that in order to resist permanent deformation, SMA mortar should have the highest resistance to tension followed by DAC then PAC with the lowest. However, it should be mentioned that due to the surrounding material, the extent of dilation in the pavement is expected to be lower than the extent of dilation in the laboratory tests.
- In order to evaluate the extent of ageing that took place during the mixing of the DAC mastic, the mastic mixing process was simulated using 40/60 bitumen. The simulation showed that no significant ageing took place in the 40/60 bitumen in the first 30 minutes during mixing at temperatures in the range of 140 to 160°C. Consequently it was concluded that no significant ageing would take place in the first 30 minutes during the

preparation of DAC mastic specimens at temperatures in the range of 140°C to 160°C.

- Method 3 was most suitable for the fabrication of the DAC mastic specimens for DTT tests in comparison to the other specimen fabrication methods. In this method, the mastic was poured into a hot mould after which an aluminium foil and a hot glass plate were placed on the upper surface of the mastic. The purpose of the aluminium foil and the glass plate was to obtain an even texture on the upper surface of the mastic. After cooling, the mastic was extracted and excess mastic removed.
- The temperature susceptibility determined from the DSR complex modulus provided reasonably good data fit for the phase angle and the maximum tensile stress.

6.13 References

- Bahia H.U., Hanson D.I., Zeng M., Zhai H., Khatri M.A. and Anderson R.M. (2001), *Characterization of Modified Asphalt Binders in Superpave Mix Design*, NCHRP report 459, Transportation Research Board-National Research Council, Web version (http://onlinepubs.trb.org/onlinepubs/nchrp/nchrp_rpt_459-a.pdf), United States of America.
- Heukelom W. and Wijga P.W.O. (1973), *Bitumen Testing*, Koninklijke/Shell – Laboratorium, Amsterdam, The Netherlands.
- NEN 1426 (en) (199), *Bitumen and Bituminous Binders – Determination of Needle Penetration*.
- SHRP-A-370 (1994), *Binder Characterization and Evaluation Volume 4: Test Methods*, Strategic Highway Research Program, Washington DC, United States of America.
- Verstraeten J. (1972), *Moduli and Critical Strains in Repeated Bending of Bituminous Mixes Application to Pavement Design*, Proceedings of the Third International Conference on the Structural Design of Asphalt Pavements, pp. 729 – 738, London, England.

7 Failure and Permanent Deformation of the Components and Asphalt Mixtures

7.1 Introduction

This chapter presents the behaviour of the different components in the asphalt mixture and the total asphalt mixture in the context of the test results obtained in this research. The components of the asphalt mixture include the aggregate skeleton and the mastic. The implication of the test results on the permanent deformation of actual pavements is also presented in this chapter.

In order to demonstrate the implication of the test results obtained in this research on pavement engineering, the two tests sections that were analyzed in section 2.5 were considered. The top layer of the second and the third test pavements were composed of DAC and PAC respectively. Since these layers were composed of materials different from those considered in this research, the pavements were only used as an example to illustrate the implications of the test results. It is important to note that these test sections represented realistic pavement sections as constructed on a particular highway in the Netherlands and that they were subjected to test conditions that are prone to permanent deformation. The temperature of the top layer was approximately 40°C and the loading wheel travelled at a speed of 20 km/h.

7.2 Pavement Strains

The stresses and strains in these test sections were determined at the mid-depth of the top layer using the manually fitted Burger's parameters presented in Annex 1 as input in the VEROAD package. These manually fitted Burger's parameters were used since they were fitted on the measured strains and measured rut depths occurring in the two test pavements. Owing to the complexity of the stresses and strains occurring in the pavement, the volumetric and deviatoric invariants for stresses and strains were used to determine the comparable laboratory test conditions from pavement stresses and strains. For purposes of consistent terminology, the comparable laboratory test conditions will be referred to as triaxial test conditions in the sections to follow. Figure 7.1 shows an illustration of the calculated strains at the middle of the top layer along the wheel path of the second test pavement. The figure illustrates that the strains occurring in the pavement are three dimensional and vary depending on the position of the point under consideration with respect to the wheel.

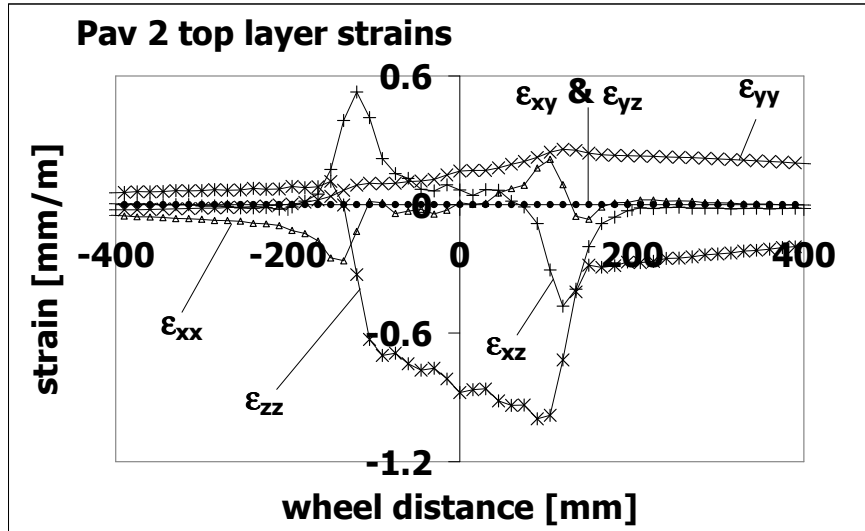


Figure 7.1 Calculated pavement strains in the top layer of the second test pavement

7.3 Triaxial Stress and Strain Conditions

The triaxial stress conditions were determined from the volumetric and deviatoric stress invariants occurring in the pavement using the expressions shown in Equations 7.1 to 7.5. The triaxial strain conditions were determined using a similar approach as illustrated in Equations 7.6 to 7.11.

pavement stress

$$I_1 = \sigma_{xx} + \sigma_{yy} + \sigma_{zz} \quad 7.1$$

$$J_2 = \frac{1}{6} \left[(\sigma_{xx} - \sigma_{yy})^2 + (\sigma_{yy} - \sigma_{zz})^2 + (\sigma_{zz} - \sigma_{xx})^2 \right] + \tau_{xy}^2 + \tau_{yz}^2 + \tau_{xz}^2 \quad 7.2$$

triaxial stress

$$\sigma_h = \frac{1}{3} (I_1 - \sqrt{3J_2}) \quad 7.3$$

$$\sigma_v = \frac{1}{3} (I_1 + 2\sqrt{3J_2}) \quad 7.4$$

$$\text{pulse duration} = \frac{D}{v} \quad 7.5$$

Where:

- | | | |
|--|---|--|
| I_1, J_2 | = | first and second deviatoric stress invariants, |
| σ_h | = | triaxial horizontal stress, |
| σ_v | = | triaxial vertical stress, |
| $\sigma_{xx}, \sigma_{yy}, \sigma_{zz}, \tau_{xy}, \tau_{yz}, \tau_{xz}$ | = | stresses in the test pavement, |
| D | = | distance in the direction of wheel movement in which both the triaxial vertical to 6% of the maximum stress occurring at the mid-depth of the top layer, |

$$v = \text{wheel velocity} = 5.56 \text{ m/s.}$$

pavement strain

$$\epsilon_{vol} = \epsilon_{xx} + \epsilon_{yy} + \epsilon_{zz} \quad 7.6$$

$$\epsilon_{dev} = \sqrt{\frac{2}{9} \left[(\epsilon_{xx} - \epsilon_{yy})^2 + (\epsilon_{yy} - \epsilon_{zz})^2 + (\epsilon_{zz} - \epsilon_{xx})^2 + \frac{4}{3} (\epsilon_{xy}^2 + \epsilon_{yz}^2 + \epsilon_{xz}^2) \right]} \quad 7.7$$

triaxial strain

$$\epsilon_{vol} = \epsilon_v + 2\epsilon_h \quad 7.8$$

$$\epsilon_{dev} = \frac{2}{3}(\epsilon_v - \epsilon_h) \quad 7.9$$

Hence:

$$\epsilon_v = \frac{1}{3}(\epsilon_{vol} + 3\epsilon_{dev}) \quad 7.10$$

$$\epsilon_h = \frac{1}{3} \left(\epsilon_{vol} - \frac{3}{2} \epsilon_{dev} \right) \quad 7.11$$

Where:

ϵ_{vol}	=	volumetric strain [%],
$\epsilon_{xx}, \epsilon_{yy}, \epsilon_{zz}, \epsilon_{xy}, \epsilon_{yz}, \epsilon_{xz}$	=	strains in the pavement [%],
ϵ_{dev}	=	deviatoric strain [%],
ϵ_v	=	triaxial vertical strain [%],
ϵ_h	=	triaxial horizontal strain [%].

7.3.1 Determination of Vertical Triaxial Strain Rate

A vertical triaxial strain rate was determined to obtain pavement strain rates that could be applied on the test results. In the pavement strain calculation output, positive normal strains (ϵ_{xx} , ϵ_{yy} and ϵ_{zz}) indicate tensile strains while negative normal strains signify compressive strains. In order to derive logical triaxial strains, the output normal strains are made positive by multiplying by -1. The effect of this multiplication is to make the volumetric strain positive, thus making compressive normal strains positive and tensile normal strains negative. This is logical since the triaxial horizontal strain expressed in Equation 7.11 becomes tensile or compressive depending on the magnitude of the volumetric strain and the deviatoric strain in the pavement. If the volumetric strain in the pavement is taken as negative, the triaxial horizontal strain resulting from Equation 7.11 is always negative or compressive which is illogical.

The vertical triaxial strain rates were determined from the profile of the vertical triaxial strain along the wheel path. The vertical triaxial strains rates were

estimated by dividing the profile into different intervals depending on the slope of the profile. The first interval was taken to initiate at the point of initialization of the triaxial vertical stress pulse that was determined from Equation 7.5. Further explanation on the calculation of the vertical stress pulse duration can be found in section 4.5.2. The slope in these linear intervals was then determined using a linear fit. Figure 7.2, Figure 7.3 and Figure 7.4 show the triaxial strains and the linear intervals in the top layer of the second and the third test pavement. The time durations in Figure 7.2 and Figure 7.4 are calculated starting from a wheel position 1.8 m away from the point under consideration along the wheel path. The positions of the linear intervals in relation to the distance from the point under consideration along the wheel path are shown in Figure 7.3. These figures illustrate that the triaxial strain rate in the pavement is not constant but varies depending on the position of the wheel from the point under consideration. The estimated triaxial vertical strain rates and the average triaxial confinement in these layers are shown in Table 7.1. The strain rates and the average confinement in the second and the third intervals of the second test pavement were used as representative conditions to illustrate the effect of pavement conditions on test results in sections 7.5, 7.6 and 7.7.

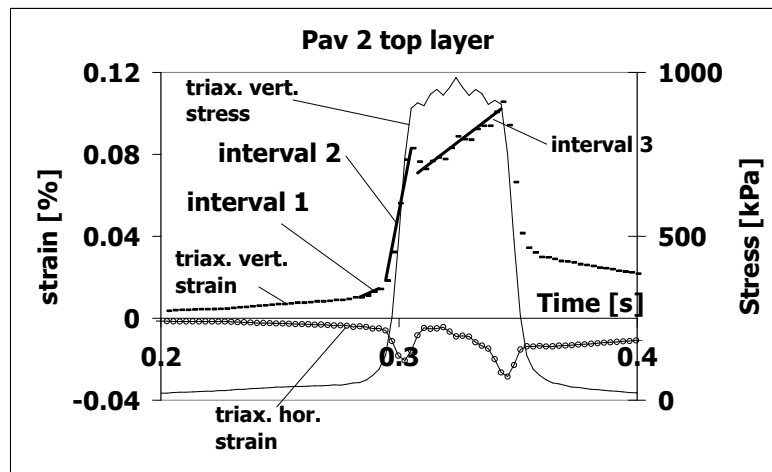


Figure 7.2 Triaxial strains in the top layer of the second test pavement in relation to time

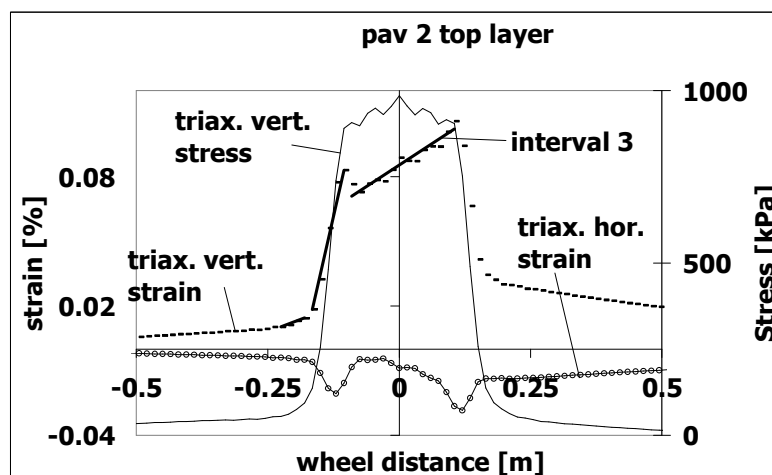


Figure 7.3 Triaxial strains in the top layer of the second test pavement in relation to distance along the wheel path

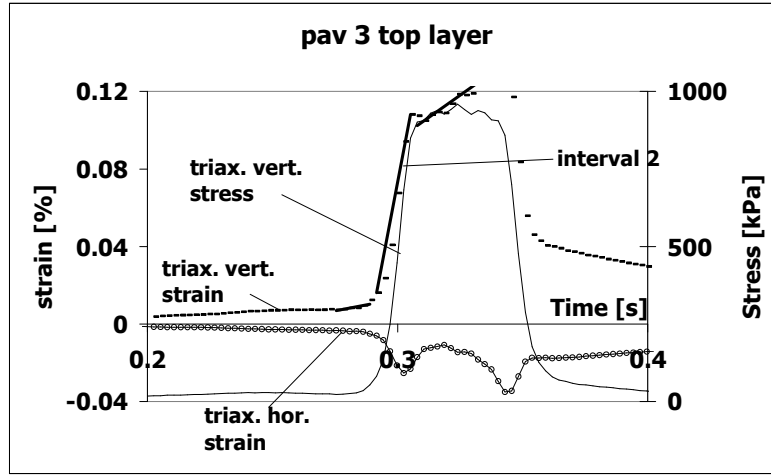


Figure 7.4 Triaxial strains in the top layer of the third test pavement

Table 7.1 Triaxial vertical strain rates and average confinement in the top layer of the second and third test pavement

test pavement	second			third		
interval	1	2	3	1	2	3
triaxial vertical strain rate [%/s]	0.52	5.98	0.89	0.23	6.81	0.91
average triaxial confinement [MPa]	0.01	0.11	0.49	0.01	0.09	0.45

7.4 Equivalency Principle to Analyze Permanent Deformation

The DCMC, DCMT and DTT test results can be compared using equivalent strain rate. The equivalent strain rate can be obtained as a product of the strain rate and the temperature shift factor as shown in the following expressions.

$$P = P_{high} + (P_{low} - P_{high})S \quad 7.12$$

Where:

$$S = e^{(-[u, \beta]^k)} \quad 7.13$$

$$u_r = \frac{u}{u_0} \quad 7.14$$

$$\beta = e^{(-\tau_s [T - T_0])} \text{ for DCMC and DCMT tests} \quad 7.15$$

$$\beta = e^{\left[c \left(\frac{1}{T} - \frac{1}{T_0} \right) \right]} \text{ for DTT tests}$$

- P = strength [MPa],
- P_{high} = strength as the strain rate approaches infinity [MPa],
- P_{low} = strength as the strain rate approaches zero [MPa],
- u_0 = a reference value of the strain rate [%/s],
- u = strain rate [%/s],

- T_s = temperature susceptibility factor in DCMC and DCMT tests [K⁻¹],
- T_0 = reference temperature [K],
- T = temperature [K],
- C = temperature susceptibility factor for DTT tests [K],
- λ = model parameter,
- β = temperature shift factor.

reduced strain rate = βu 7.16

The equivalency principle was employed to obtain the reduced strain rate at a reference temperature of 40⁰C for the compression and tension test results. The strain reference parameter, u_0 , in model parameters for the total asphalt mixture presented in Chapter 5 and in Chapter 6 for the mastic was adjusted to fit the models to the data at the new reference temperature of 40⁰C while the other parameters were kept constant. Table 7.2 shows the new u_0 parameters at a reference temperature of 40⁰C and the other model parameters.

Table 7.2 Model parameters at a reference temperature of 40⁰C

Mix	Test	symbol	λ	T_s	T_0	u_0	P_{high}	P_{low}
PAC	maximum stress in compression	f_c	0.346	0.286	313	152703.9	24	0
	tangent stiffness in compression	E_c	0.453	0.286	313	204420.5	9102	0
	maximum stress in tension	f_t	0.628	0.286	313	797.3	2	0
	tangent stiffness in tension	E_t	0.382	0.286	313	34573.5	9999	0
	stress at initiation of dilation	σ_{dm}	0.499	0.286	313	21024.8	15	0
	stress at initiation of plasticity	σ_{pm}	0.597	0.286	313	9981.0	10	0
SMA	maximum stress in compression	f_c	0.402	0.252	313	14458.0	30	0
	tangent stiffness in compression	E_c	0.475	0.252	313	26412.3	10000	0
	ultimate strength in tension	f_t	0.696	0.252	313	581.7	4	0
	tangent stiffness in tension	E_t	0.391	0.252	313	31005.3	12988	0
	stress at initiation of dilation	σ_{dm}	0.650	0.252	313	3661.3	20	0
	stress at initiation of plasticity	σ_{pm}	0.580	0.252	313	6190.0	19	0
DAC	maximum stress in compression	f_c	0.316	0.304	313	68989.6	57	0
	tangent stiffness in compression	E_c	0.446	0.304	313	7257.8	8055	0
	ultimate strength in tension	f_t	0.551	0.304	313	258.4	6	0
	tangent stiffness in tension	E_t	0.480	0.304	313	1256.5	8500	0
	stress at initiation of dilation	σ_{dm}	0.405	0.304	313	14568.2	39	0
	stress at initiation of plasticity	σ_{pm}	0.479	0.304	313	16109.4	36	0
Property		symbol	λ	C	T_0	u_0	f_{tmhigh}	f_{tmlow}
DAC mastic tensile strength		f_{tm}	0.449	24360	313	69657	9.46	0

7.5 Compressive and Tensile Strengths of the PAC, SMA and DAC Total Asphalt Mixtures

Figure 7.5 shows the compressive and tensile strengths of the PAC, SMA and DAC total asphalt mixtures at a reference temperature of 40⁰C and the representative triaxial strain conditions selected from the second test pavement.

The compressive strengths and tensile strengths were obtained from the DCMC tests and DCMT tests respectively. The figure shows that both the compressive as well as the tensile strengths can be ranked in order of decreasing strength as DAC, SMA and PAC. However, at high temperatures and low strain rates the tensile strength of the SMA is closer to the tensile strength of the PAC than at low temperatures and high strain rates. It is interesting to note that the measured tensile strength for the three asphalt mixtures at high equivalent strain exhibits a tendency to decrease after a certain limit. Because permanent deformation was the main concern in this research, this tendency was not considered further.

The figure also shows that irrespective of the temperature or strain rate, the compressive strength of any of the three asphalt mixtures is higher than the tensile strength. In addition, the figure shows that the triaxial strain rates occurring in the pavement are lower than most of the equivalent strain conditions in the tests. However, the properties associated with the triaxial strain rates in the pavement can be determined from the equivalent strain rates in the test conditions.

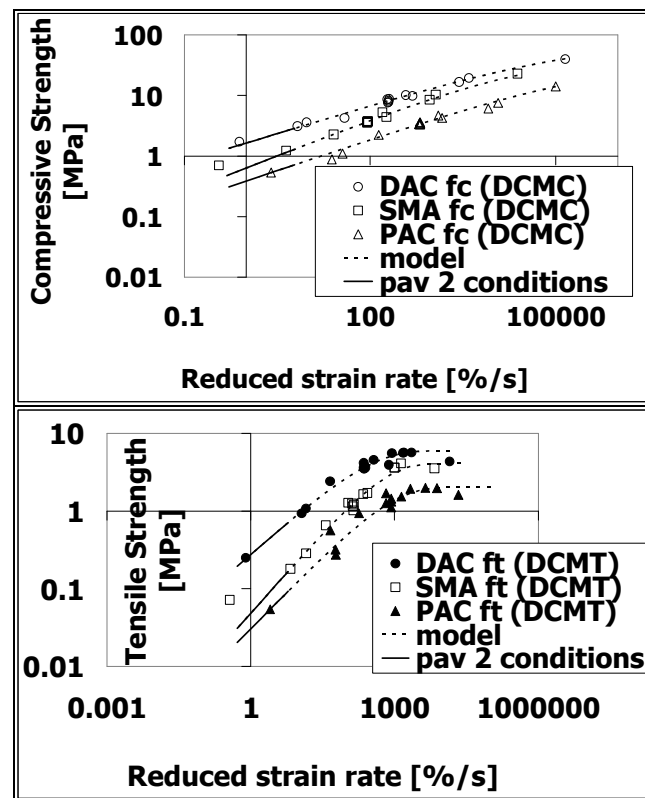


Figure 7.5 Compressive and tensile strengths of the total asphalt mixtures at a reference temperature of 40°C

7.6 Compressive Strength and Stress at Initiation of Dilation of the PAC, SMA and DAC Total Asphalt Mixtures

Figure 7.6 shows the compressive strength and the stress at initiation of dilation for the PAC, DAC and SMA total asphalt mixtures. The labels fc and sd refer to the compressive strength and the stress at initiation of dilation respectively. The figure shows that irrespective of the asphalt mixture, the difference between the

compressive strength and the stress at initiation of dilation decreases with increase in reduced strain rate. In other words, the compressive strength is closer to the stress at initiation of dilation at low temperatures and high strain rates than at high temperatures and low strain rates. This can be attributed to the behaviour of the tensile strength of the mastic. The tensile strength of the mastic increases with reduced strain rates as discussed in section 7.7.

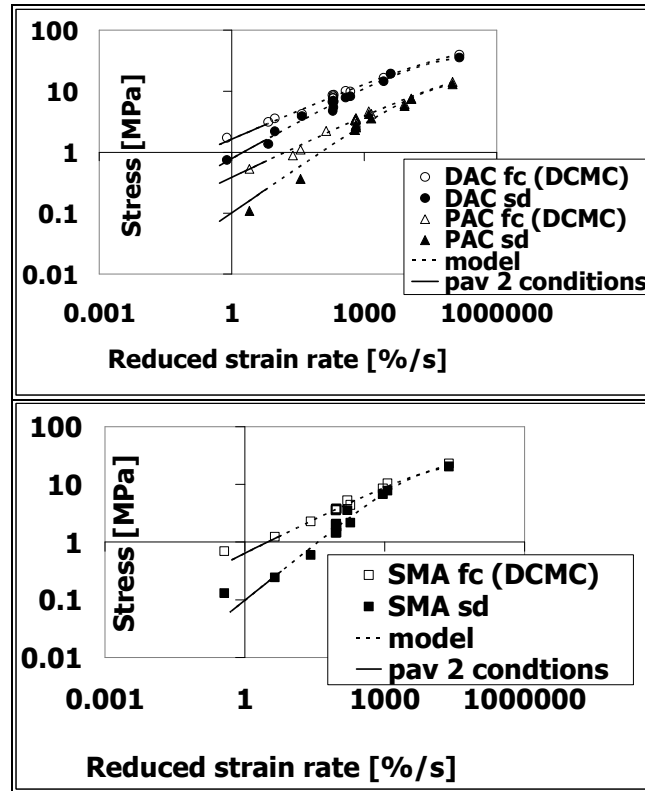


Figure 7.6 Compressive strength and stress at dilation of the total asphalt mixtures at a reference temperature of 40°C

7.7 Strength at Failure of DAC Total mixture and Tensile Strength of the DAC Mastic

Figure 7.7 shows a comparison of the DCMC, DCMT and DTT tests results for the DAC on an equivalent strain rate scale. Several observations can be made from this figure:

1. Irrespective of the temperature or the strain rate, the compressive strength of the DAC total asphalt mixture is always higher than the tensile strength.
2. At low temperatures and high strain rates, the strength of the mastic is within a comparable range to the tensile strength of the DAC total asphalt mixture. This suggests that at low temperatures and high strain rate, the resistance to tensile failure in the DAC total asphalt mixture is to a large extent dependent on the tensile strength of the mastic.
3. The aggregate skeleton has little capacity to provide the tensile strength in the DAC total asphalt mixture. Consequently it is logical to conclude that most of the observed tensile strength of the DAC total asphalt mixture at high temperatures and low strain rates is as a result of the tensile strength

of the mastic. It is also possible that some of the tensile strength of the total asphalt mixture may also be as a result of the interface between the skeleton and the mastic. However, since the interface was not part of this research, this was not considered any further.

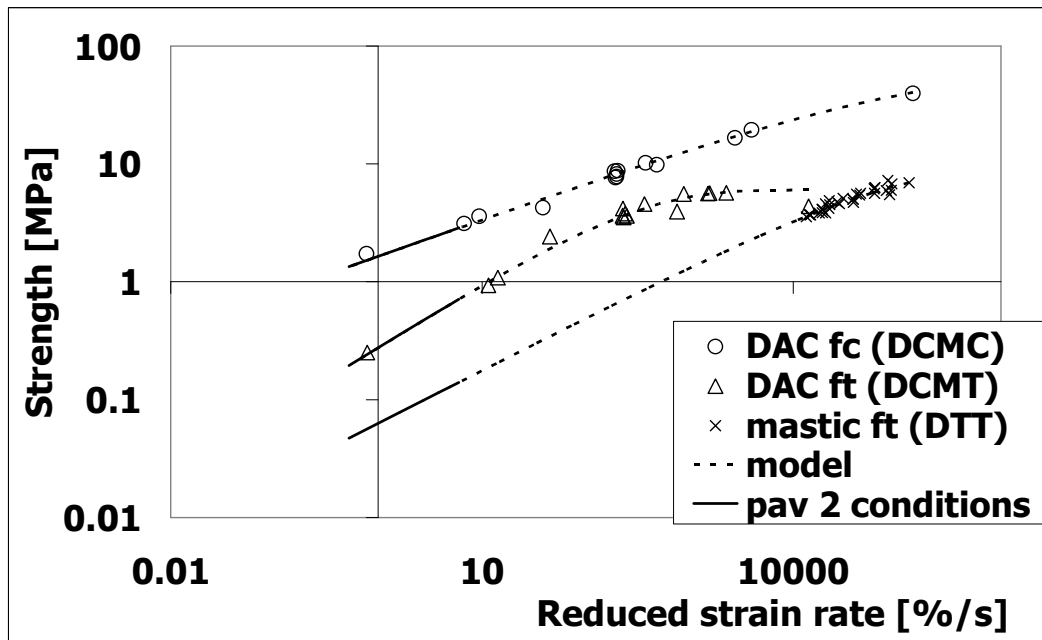


Figure 7.7 Comparison of the DCMC, DCMT and DTT tests results for DAC at a reference temperature of 40°C

7.8 Ultimate Surfaces of the Total Asphalt Mixture and the Aggregate Skeleton

The ultimate surfaces of total asphalt mixtures and the aggregate skeletons are compared at 40°C and at the representative strain rate and average confinement determined from the second test pavement. The two intervals were selected to demonstrate the effect of low and high strain rates and a high confinement on the ultimate surfaces. In order to limit the scale, the ultimate surfaces are plotted with the upper point being the modelled compressive failure strength.

Figure 7.8 shows the ultimate surfaces for the PAC asphalt mixture and the PAC aggregate skeleton. Figure 7.9 shows the ultimate surfaces for the SMA asphalt mixture and the SMA aggregate skeleton. These figures show that the ultimate surfaces of aggregate skeleton of the two stone skeleton mixtures are only slightly lower than the ultimate surface of the asphalt mixtures. This indicates that the stone skeleton of PAC and SMA play a very important role in building resistance to combinations of normal compressive stresses and shear stresses that are so typical for pavement wearing courses. Since the aggregate skeleton has no capacity to offer resistance in tension, most of the tension capacity observed in the total asphalt mixture can be attributed to the mortar. The contribution of the mortar at high temperatures becomes more important at high strain rates as evident from the ultimate surface of the PAC and SMA mixtures at a strain rate of 5.98%/s. This demonstrates that the effect of the confinement on the aggregate skeleton plays a significant role in the resistance against compressive failure in the

PAC and SMA asphalt mixtures at high temperatures. It is also clear from Figure 7.8 and Figure 7.9 that the PAC and SMA asphalt mixtures have little or no capacity to resist tension at high temperatures.

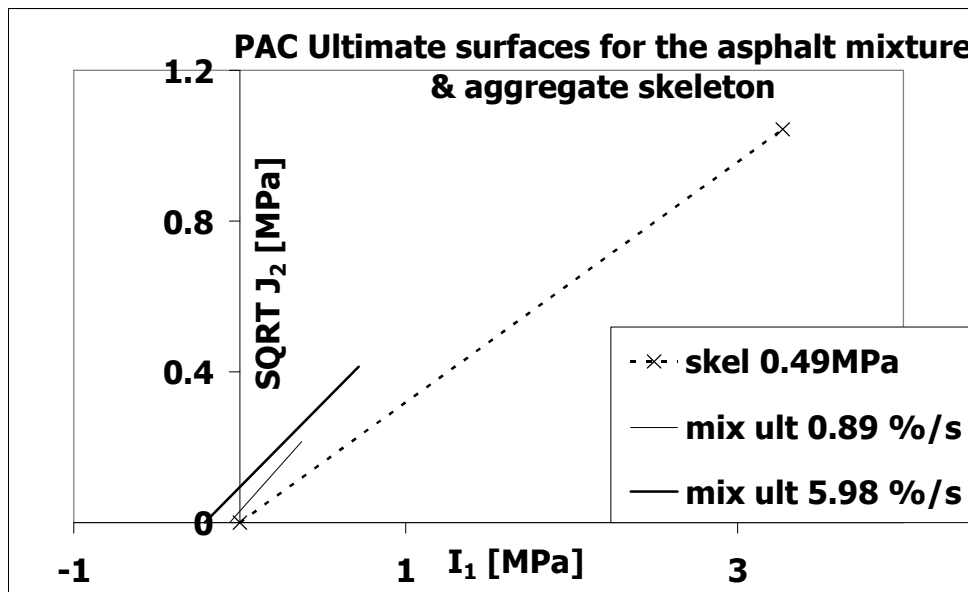


Figure 7.8 Ultimate surfaces for the PAC aggregate skeleton and PAC asphalt mixture at a reference temperature of 40°C

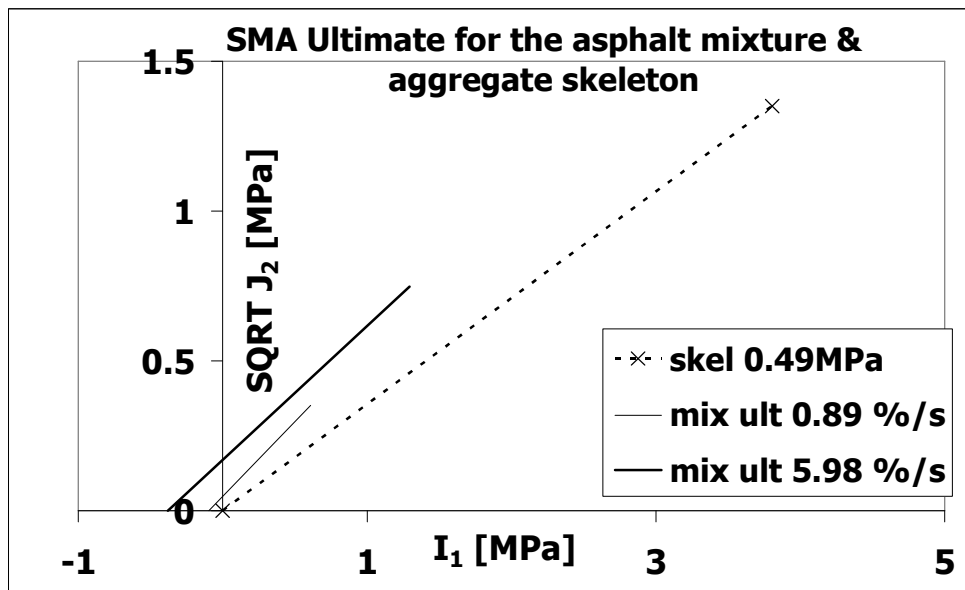


Figure 7.9 Ultimate surfaces for the SMA aggregate skeleton and SMA asphalt mixture at a reference temperature of 40°C

Figure 7.10 shows the ultimate surfaces for the DAC asphalt mixture and the DAC aggregate skeleton. This figure shows a significant difference between the ultimate surface of DAC aggregate skeleton and the ultimate surface of the asphalt mixture. The surface of the DAC mixture at both the high and the low strain rate exhibit considerable strength in tension. Since little or no tensile strength can be

expected from the aggregate skeleton, this observation suggests that the mastic offers resistance to tensile failure even at high temperatures and low strain rates.

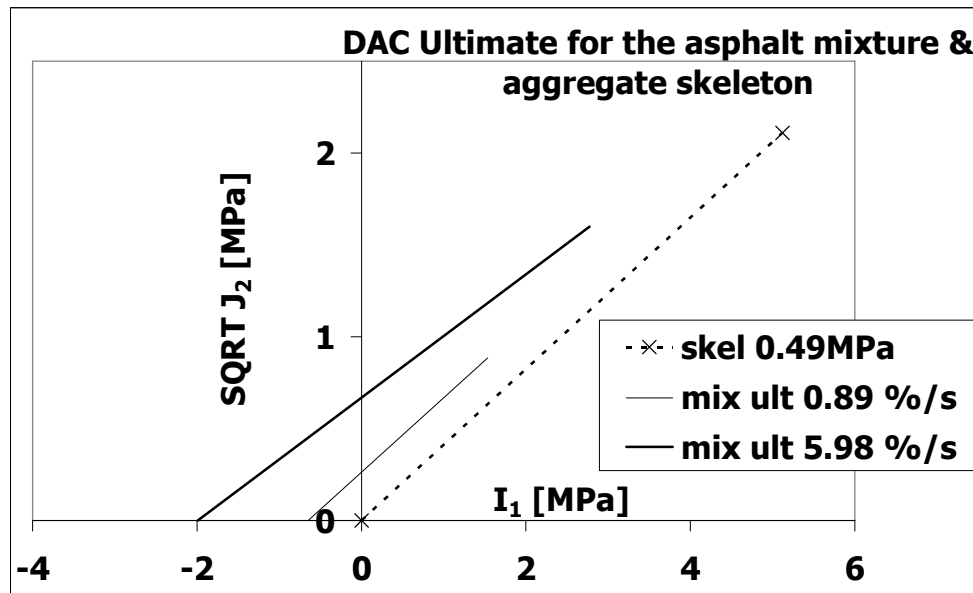


Figure 7.10 Ultimate surfaces for the DAC aggregate skeleton and DAC asphalt mixture at a reference temperature of 40°C

Figure 7.11 shows an illustration of the ultimate surfaces for the total asphalt mixture and aggregate skeleton of the PAC, SMA and DAC. The figure shows that the DAC total asphalt mixture has a bigger tension resistance than SMA and PAC total asphalt mixtures. This observation suggests that the contribution of the mastic in the DAC asphalt mixture towards resistance to tensile failure is larger than that of the mortar in PAC and SMA. The figure also shows that the ultimate surface of the DAC aggregate skeleton is bigger than the ultimate skeleton of the SMA and PAC. It is also evident from this figure that the contribution of the mastic towards resistance against failure and in extension permanent deformation is more important in the DAC skeleton than in the PAC and SMA stone skeleton mixtures.

At first sight this may seem to imply that DAC aggregate is more resistant to permanent deformation than the SMA and PAC aggregate skeletons. However, this is not the case. Figure 7.12 shows a comparison of the ultimate stress at failure in the DCMCC tests and the stress conditions leading to a permanent deformation of $\geq 10\%$ after 20 000 load repetitions for the PAC, SMA and DAC aggregate skeleton. The figure shows that the PAC and SMA aggregate skeleton can be loaded close to failure conditions while still providing a reasonable resistance to permanent deformation. In addition, the DAC aggregate skeleton offers the least resistance to permanent deformation. This is evident from the results in Figure 7.13 which shows the PD tests stress conditions for a high axial permanent deformation of more than 10% and 1%. The figure also indicates that the SMA aggregate skeleton provides excellent resistance to permanent deformation even at high stress levels but failure occurs almost immediately when the stresses are too high.

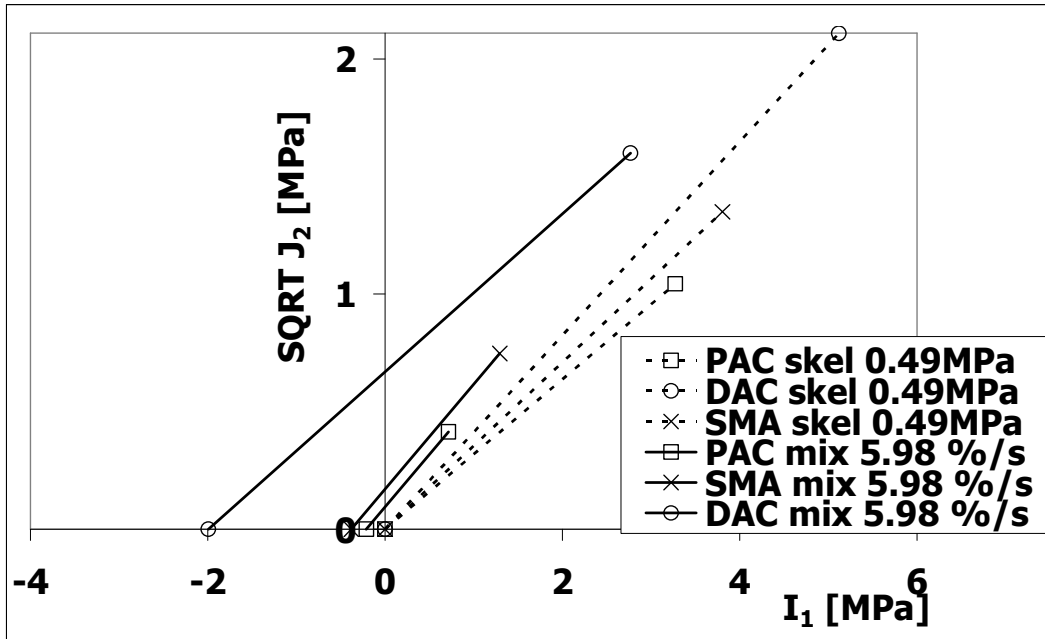


Figure 7.11 Surfaces for the aggregate skeleton and total asphalt mixture of PAC, SMA and DAC at a reference temperature of 40°C

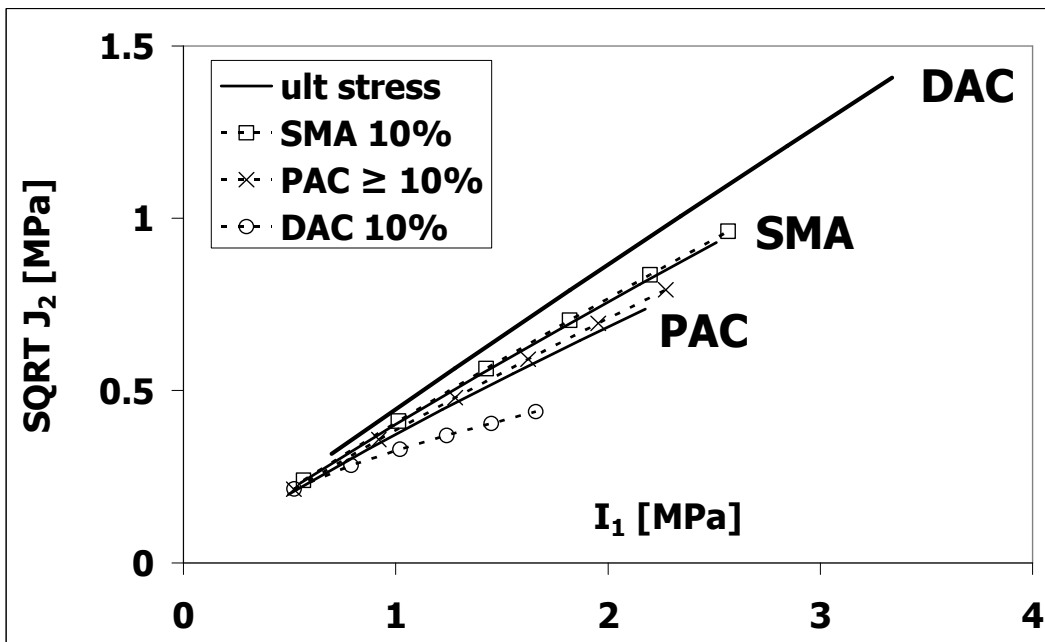


Figure 7.12 Ultimate stress and the stress conditions leading to a permanent deformation of $\geq 10\%$ after 20 000 load repetitions for the PAC, SMA and DAC aggregate skeleton

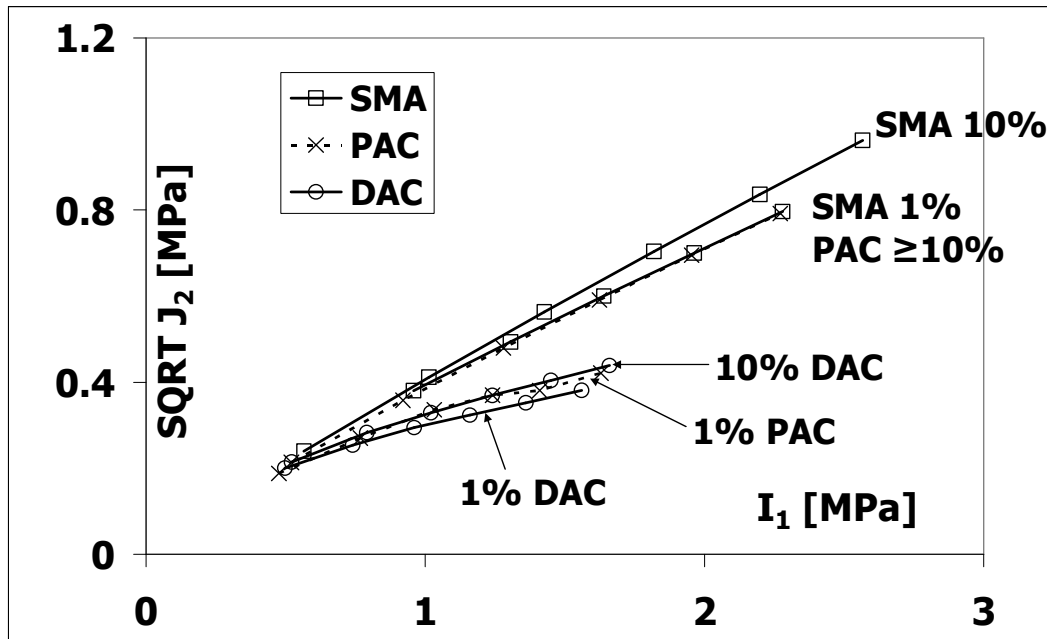


Figure 7.13 PD stress conditions leading to permanent deformation of 1 and $\geq 10\%$ after 20 000 load repetitions for the PAC, SMA and DAC aggregate skeleton

7.9 Comparison of the Test Results to Pavement Stress and Strain Conditions

Since the top layer of the second and third test pavements was composed of DAC and PAC respectively, the test results of the PAC and DAC total asphalt mixtures were compared to the stress conditions in the top layer of the second and third test pavement respectively. The ultimate and initiation of plasticity surfaces of the total asphalt mixture for PAC and DAC were determined at the vertical triaxial strain rates occurring in the three intervals and compared to the stress conditions in the pavement.

7.9.1 PAC (Third) Test Pavement

Figure 7.14, Figure 7.15 and Figure 7.16 show the ultimate and initiation of plasticity surfaces at the three intervals in comparison to the pavement stress conditions in the third test pavement. The figures show that most of the pavement stresses are beyond the PAC surface at initiation of plasticity. This suggests that a linear elastic or a linear visco-elastic approach cannot be used to predict the permanent deformation in the third test pavement. The figures also imply that a plasticity approach would be more appropriate.

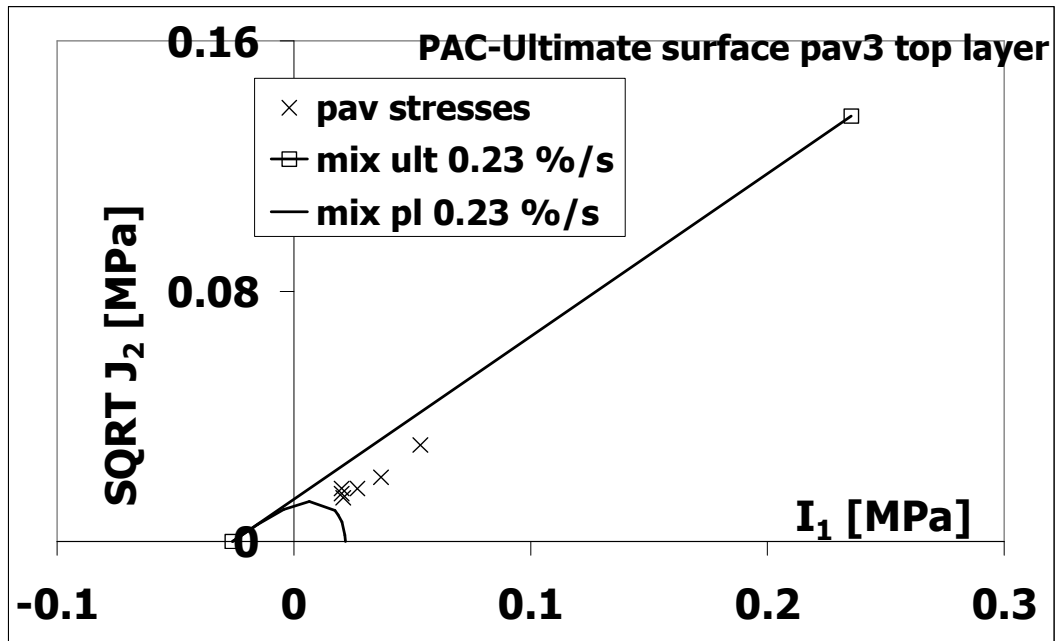


Figure 7.14 PAC third test pavement interval 1

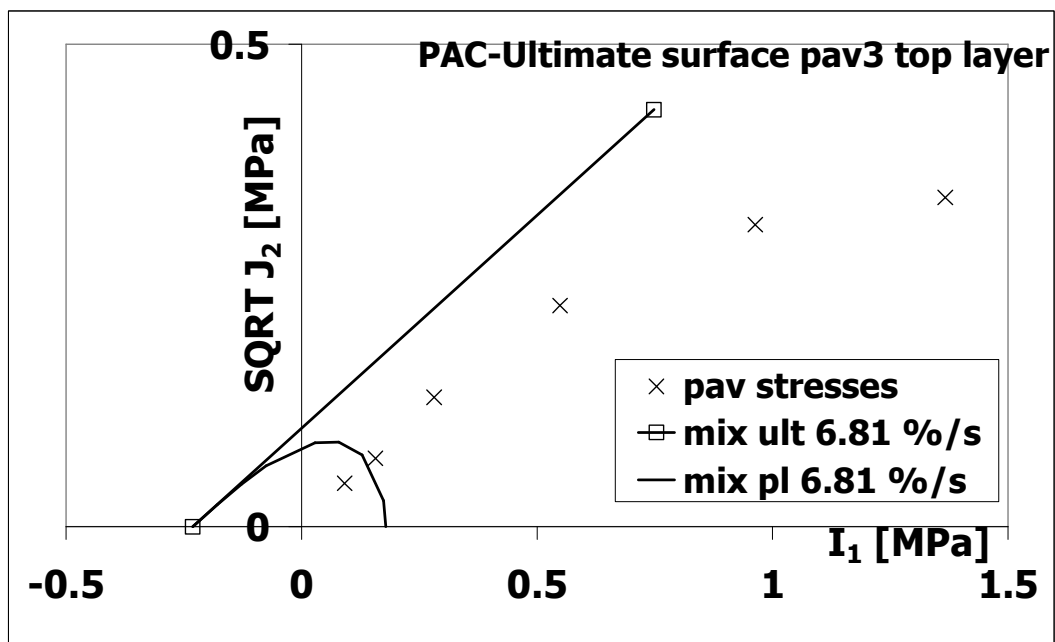


Figure 7.15 PAC third test pavement interval 2

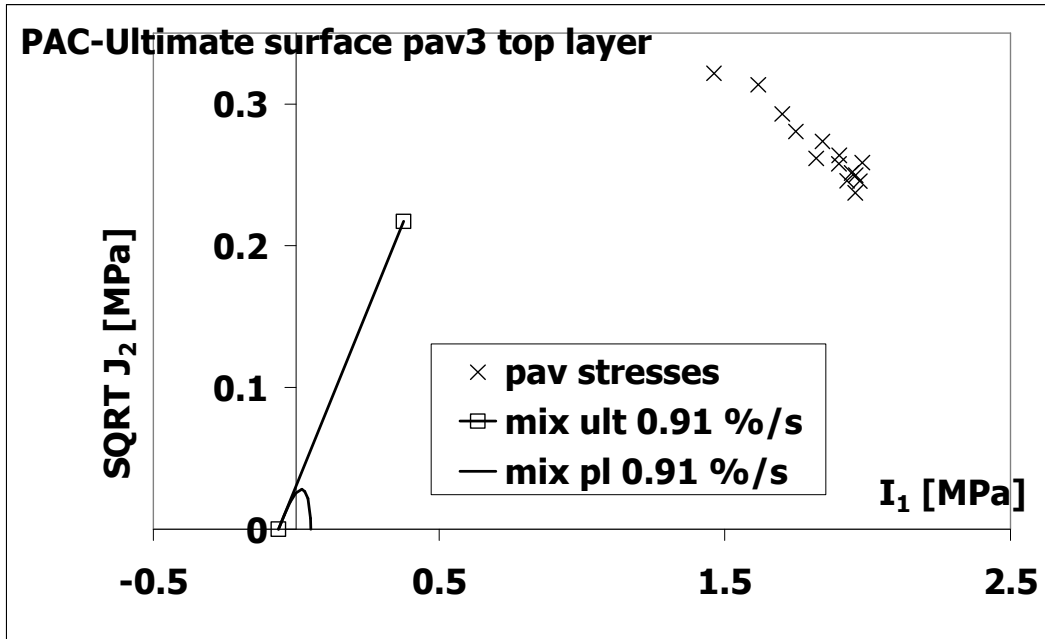


Figure 7.16 PAC third test pavement interval 3

7.9.2 DAC (Second) Test Pavement

Figure 7.17, Figure 7.18 and Figure 7.19 show the ultimate and initiation of plasticity surfaces at the three intervals in comparison to the pavement stress conditions in the second test pavement. These figures show that most of the pavement stresses especially in intervals two and three are beyond the DAC surface at initiation of plasticity. Similar to the third test pavement, this suggests that a linear elastic or a linear visco-elastic approach cannot be used to predict the permanent deformation in the second test pavement. The stresses beyond the plasticity surface also indicate that a plasticity approach would be more appropriate.

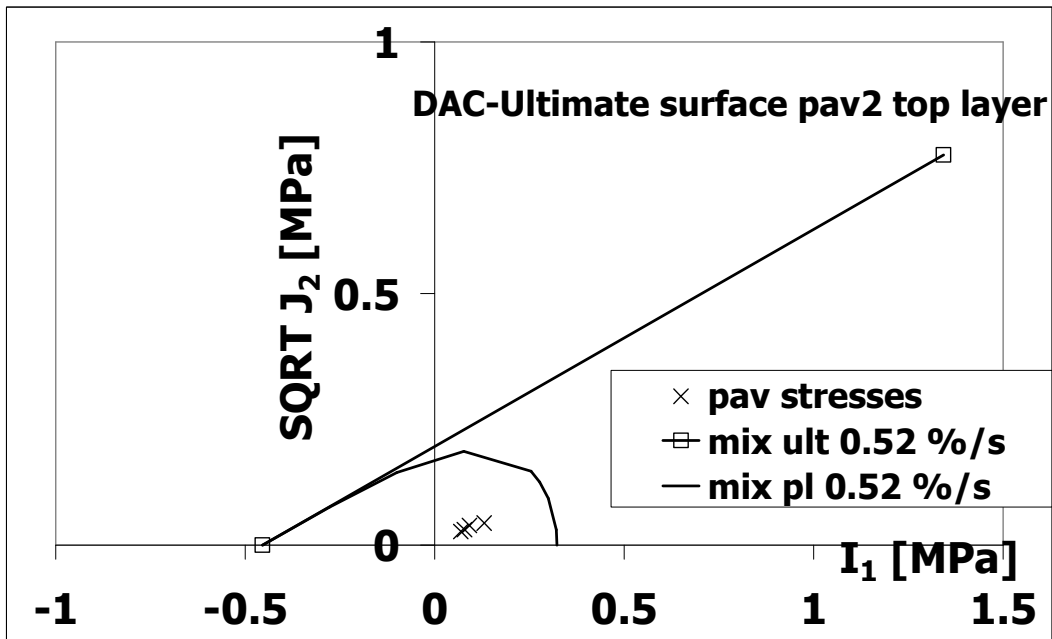


Figure 7.17 DAC second test pavement interval 1

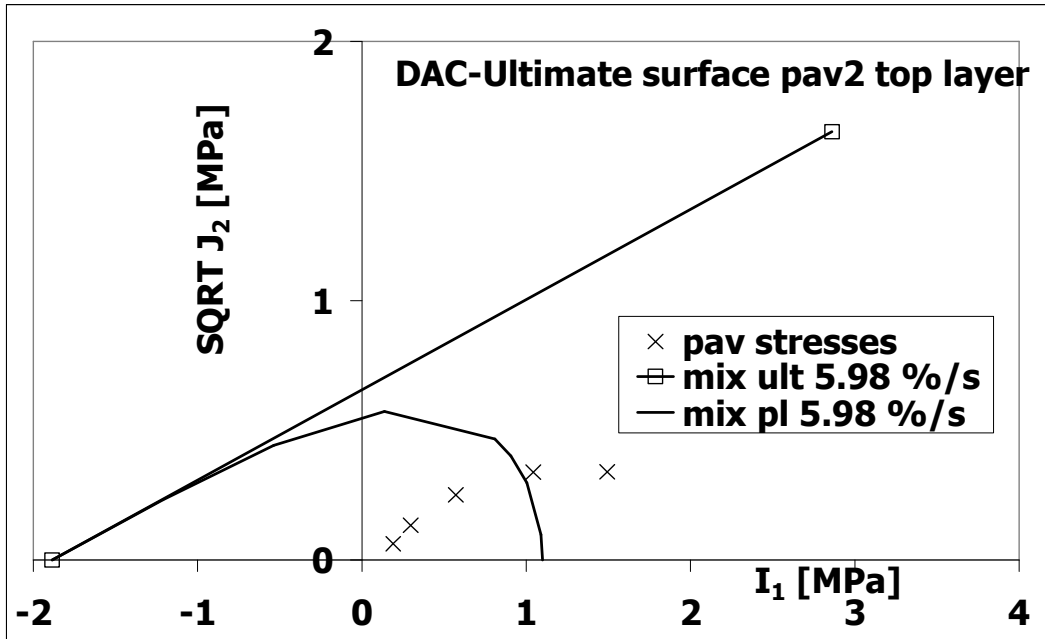


Figure 7.18 DAC second test pavement interval 2

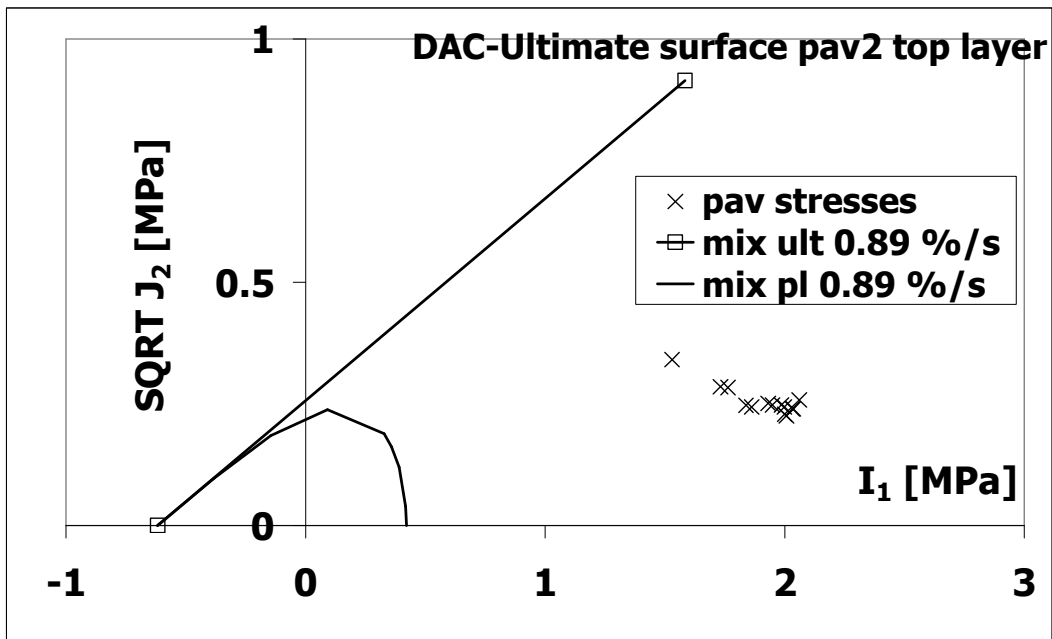


Figure 7.19 DAC second test pavement interval 3

7.10 Comparison of PD Tests to Pavement Stress Conditions

From the previous section, it may seem that the relatively severe pavement stress conditions in the PAC top layer of the third test pavement may cause higher permanent deformation in comparison to DAC top layer in the second test pavement. However, this is not the case. The practical rut depths of the DAC top layer pavement (second test pavement) and PAC top layer test pavement (third test pavement) were practically the same (refer to Figure 2.21). The similarity between the rut depths in two test pavements may to some extent be explained by

behaviour of the aggregate skeleton. Figure 7.20 and Figure 7.21 show the stress conditions leading to 1% and $\geq 10\%$ axial permanent deformation for the PAC and the DAC aggregate skeletons after 20 000 load repetitions that were determined from PD tests. The figures show that the pavement stress conditions are more severe for the DAC aggregate skeleton in comparison to the PAC aggregate skeleton. The PAC aggregate skeleton is more resistant to permanent deformation than the DAC aggregate skeleton.

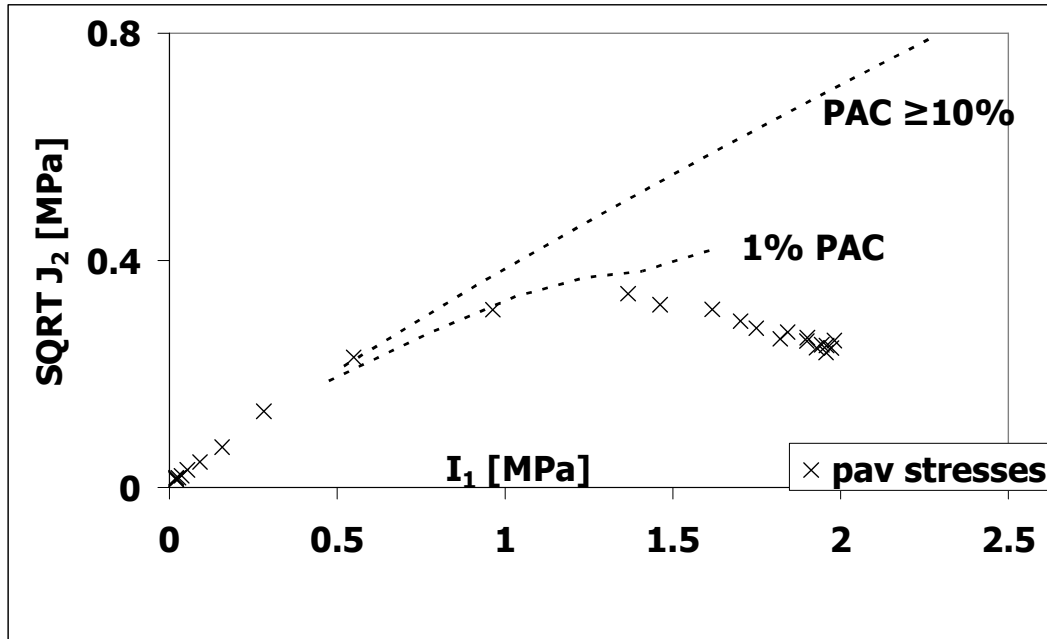


Figure 7.20 Stress conditions leading to 1 and $\geq 10\%$ axial permanent deformation for the PAC aggregate skeleton and the stress conditions in the third test pavement

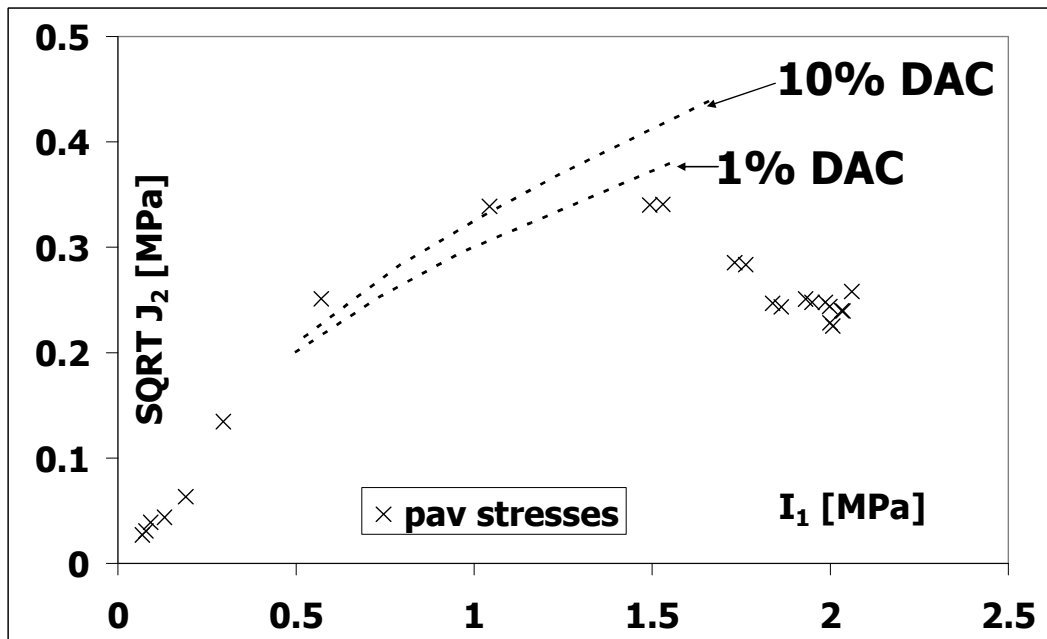


Figure 7.21 Stress conditions leading to 1 and 10% axial permanent deformation for the DAC aggregate skeleton and the stress conditions in the third test pavement

7.11 Conclusions

- The triaxial strain rate in the pavement is not constant but varies depending on the position of the wheel from the point under consideration.
- Irrespective of the asphalt mixture, the difference between the compressive strength and the stress at initiation of dilation decreases with increase in strain rate and decrease in temperature. This can be attributed to the behaviour of the tensile strength of the mastic. The tensile strength of the mastic was observed to increase with increase in strain rate and decrease in temperature.
- The resistance of the PAC and SMA asphalt mixtures against failure in compression at high temperatures is to a large extent dependent on the effect of the confinement on the aggregate skeleton.
- PAC and SMA asphalt mixtures have little or no capacity to resist tension at high temperatures. Since the aggregate skeleton has no capacity to offer resistance in tension, the tension capacity observed in the total asphalt mixture can be attributed to the mortar. The contribution of the mortar at high temperatures becomes more important at high strain rates.
- The contribution of the mastic in the DAC asphalt mixture towards resistance against failure in tension at high temperatures is larger in comparison to the contribution of the mortar in PAC and SMA.
- The contribution of the mastic towards resistance to permanent deformation is more important in the DAC mixture than the contribution of the mortar in the PAC and SMA stone skeleton mixtures.
- In the two test pavements, most of the pavement stress conditions were beyond the surface at initiation of plasticity. This implies that a linear elastic or a linear visco-elastic approach cannot be used to predict the permanent deformation occurring in asphalt pavements. A non-linear elasto visco-plasticity can offer a better approach.

8 Conclusions and Recommendations

In order to move forward, we must learn from our experience in the past. Conclusions represent lessons learnt from experience and the recommendations are a pointer to the way forward.

The aim of this research was to identify and characterize the contribution of the components in an asphalt mixture towards resistance to permanent deformation. In this research, the components of the asphalt mixture and the total mixture were identified and separately characterized. In the previous chapters the different aspects involved in the identification and separate characterization were discussed. This chapter offers the main highlights in the various chapters and the conclusions related to practice.

8.1 Conclusions

8.1.1 Main Highlights

8.1.1.1 Related to Background, Literature Review and Test Program (Chapter 2)

- The skeleton and the mortar components in an asphalt mixture play distinct roles in the resistance to permanent deformation. It is therefore important to understand and characterize the separate contribution of the components of an asphalt mixture.
- Elastic/hybrid and linear visco-elastic models are not sufficient for purposes of describing the permanent deformation in asphalt mixtures. The permanent deformation calculated for the two test pavements was much smaller than the measured permanent deformation.
- Plasticity models can be used to describe the roles played by the components of an asphalt mixture towards resistance to permanent deformation.

8.1.1.2 Related to the Aggregate Skeleton (Chapter 4)

- In order to achieve realistic laboratory based material characterization, sufficient attention should be paid to the method of testing. The pavement analysis performed on the LINTRACK test pavements showed that cyclic confinement in triaxial tests may provide a better stress simulation for the upper part of the pavement in comparison to other triaxial test methods that involve a constant confinement.
- The triaxial tests performed on the aggregate skeleton showed that the permanent deformation under cyclic confinement was higher than the permanent deformation under constant confinement.
- In relation to the DCMCC tests, the aggregate skeleton of the three asphalt mixtures can be ranked in order of decreasing vertical stress at failure as DAC, SMA and PAC. However, in relation to the cyclic PD tests, the three aggregate skeletons can be ranked in order of decreasing resistance to permanent deformation as SMA, PAC followed by DAC. Severe permanent deformation in the PAC and SMA aggregate skeletons takes

place at stress conditions close to the DCMCC failure stresses while severe permanent deformation in the DAC skeleton occurs at much lower stress conditions. This difference can be attributed to the better post-peak stability exhibited by the PAC and SMA aggregate stone skeletons.

8.1.1.3 Related to the Total Asphalt mixture (Chapter 5)

- The degree of compaction within gyratory specimens varies considerably. In order to produce homogeneous tests specimens, it is necessary to core the test specimens from the middle part of gyratory compacted specimens and to remove the upper and lower parts of the specimen.
- The hot density of gyratory compacted specimens can be used as an effective means of achieving desired density in the extracted test specimens.
- In this research, it was not possible to use the number of gyrations as a compaction control parameter.
- The strength of the three asphalt mixtures is higher in compression than in tension and the three mixtures can be ranked in order of decreasing maximum compression or tension as DAC, SMA and PAC.
- The three asphalt mixtures can be arranged in order of decreasing size of ultimate failure surface as DAC, SMA and PAC.

8.1.1.4 Related to Mastic and Bitumen (Chapter 6)

- Despite of the application of confinement during the aggregate skeleton tests, the extent of dilation in the aggregate skeleton was higher than in the total asphalt mixture tests that were conducted without confinement.
- The indicative tensile stress required to hold the aggregates together is highest for the SMA followed by DAC and then PAC. This suggests that in order to resist permanent deformation, SMA mortar should have the highest resistance to tension followed by DAC and then PAC. However, it should be mentioned that due to the surrounding material, the extent of dilation in the pavement is expected to be lower than the extent of dilation in the laboratory tests.

8.1.1.5 Related to Failure and Permanent Deformation Behaviour of the Components of Asphalt mixture (Chapter 7)

- The resistance of the PAC and SMA asphalt mixtures against failure in compression is to a large extent dependent on the effect of confinement on the aggregate skeleton.
- The contribution of the mastic towards resistance to permanent deformation is more important in the DAC aggregate skeleton than in PAC and SMA stone skeletons.
- The triaxial strain rate in the pavement is not constant but varies depending on the position of the wheel from the point under consideration.
- Most of the pavement stress conditions were beyond the surface at initiation of plasticity in the two test pavement. This implies that a linear elastic or a linear visco-elastic approach cannot be used to predict the permanent deformation occurring in asphalt pavements.

8.1.2 Related to Practice

- The aggregate skeleton of the PAC and SMA mixtures can be loaded close to failure, while still providing reasonable resistance to permanent deformation if a permanent deformation of 10% is allowed.
- SMA provides excellent resistance to permanent deformation even at very high stress levels but failure occurs almost immediately when the stress levels are too high.
- Stone skeleton of PAC and SMA play a very important role in building resistance to combinations of normal compressive stresses and shear stresses that are so typical for pavement wearing courses.
- The stress conditions for the SMA total asphalt mixture at initiation of dilation and at initiation of plasticity are almost the same. In practice this implies that SMA is a very rut resistant mixture because damage or plasticity initiates at initiation of dilation. However, dilation in the pavement does not occur in the same way as in the laboratory. In reality it is hindered by the surrounding material. This means that in practice high confining stresses develop and counteract the development of permanent deformation. Almost the same phenomenon occurs in PAC where the stress at initiation of dilation is close to the stress at initiation of plasticity. This makes a PAC mixture rut resistant as well.
- Since dilation contributes significantly to the permanent deformation of PAC and SMA mixtures, ample consideration should be given to the design of stone skeleton mixtures as well as to the degree of compaction. A well designed stone skeleton which is well compacted is prone to have a high tendency to dilate which helps the resistance to permanent deformation.
- Although the effect of binder content was not investigated in this research, caution should be exercised on the binder content in SMA. A high binder content will have a negative effect on the resistance to permanent deformation.
- In summary it can be stated that the results from this research have clearly emphasized the importance of the gradation as well as the degree of compaction on the resistance to permanent deformation of stone asphalt mixtures such as PAC and SMA.
- The test results in this research indicate that the resistance to permanent deformation of stone skeleton mixtures PAC and SMA can be evaluated by means of monotonic tension and compression tests.
- The results obtained on DAC indicate quite a different trend in comparison to the PAC and SMA. The ultimate surfaces of the DAC mixture suggested that the mastic has a significant contribution to the strength of the mixture. In addition, the PD tests performed on the aggregate skeleton showed that significant permanent deformation develops at stress levels well below the failure stresses. The results of the tests performed on the DAC total mixture indicated that initiation of plasticity takes place at stress levels below the initiation of dilation. This means that in reality, development of plastic deformation is not counteracted immediately by increased confinement that occurs due to dilation. Given the fact that the mastic plays an important role in resistance against failure and by extension in resistance to permanent deformation, ample attention should

be paid on the tensile characteristics of the mastic since they have a large effect on the location of the failure envelope in the $I_1-\sqrt{J_2}$ space.

8.2 Recommendations

8.2.1 Related to Chapter 2 and 4

- An extensive visco-elastic analysis was performed using the VEROAD visco-elastic model with the main aim of evaluating the application of a visco-elastic model in the prediction of the permanent deformation. In addition the applicability of a hybrid model was also considered. The permanent deformation determined using these methods was much lower than the permanent deformation occurring in the test pavements. One of the causes of this discrepancy was the method of specimens testing which involved constant confinement. This was confirmed by the permanent deformation tests performed on the aggregate skeleton. The triaxial tests performed on the aggregate skeleton showed that cyclic confinement was more realistic and that the permanent deformation under cyclic confinement was higher than the permanent deformation under constant confinement. The implication of this is that triaxial characterization of the asphalt mixtures in the top part of the pavement should be conducted using cyclic confinement. In addition unequal pulse durations in the vertical and confining stress should also be explored.

8.2.2 Related to Chapter 5

- During the preparation of test specimens for the asphalt mixture, a fabrication technique was developed. The fabrication technique demonstrated that hot density can be used as effective means of achieving desired density in extracted cores. The technique also showed that it was not possible to use the number of gyrations as a compaction control parameter. It is the recommendation of this research that hot density should be used as a compaction control parameter in gyratory compaction rather than the number gyrations.
- The tangent stiffness and Poisson's ratios for the total asphalt mixture determined from the tension tests (DCMT) were higher than those determined from the compression tests (DCMC). This was most likely caused by the gluing of the end caps to the specimen in the DCMT tests. In order to minimize this problem, the axial deformation should be measured at the middle part of specimen away from the end caps.

8.2.3 Related to Chapter 2 and 7

- The pavement analysis presented in Chapter 2 and Chapter 7 underscored the fact that linear elastic and linear visco-elastic models are inappropriate in the prediction of permanent deformation of asphalt pavements. For purposes of modeling permanent deformation a non-linear elasto visco-plasticity model should be developed. With such a model the permanent deformation in stone skeleton mixtures and mixtures such as DAC can be predicted.

Annex 1 - VEROAD Visco-Elastic Analysis

As part of this research an extensive visco-elastic analysis was performed for two LINTRACK test pavements namely second and third test pavements (Muraya et al 2002, Muraya et al 2003, Muraya and Van Dommelen, 2004). The analysis was performed using VEROAD (Visco Elastic ROad Analysis Delft) linear multilayer visco-elastic pavement analysis model. In the VEROAD program, the material behaviour is described by the Burger's model shown in Figure A1.1. Each of the asphalt pavement layers is characterised by the four rheological Burger's parameters i.e. E_1 , E_2 , η_1 , η_2 and a Poisson's ratio while each of the non-asphaltic layers is characterised by Young's modulus and Poisson's ratio. The permanent deformation calculation in VEROAD is performed in two phases. The first phase consists of a stress calculation from a given set of Burger's parameters, after which the permanent deformation is calculated from the stresses and the η_1 parameter in the second stage (Hopman 2000).

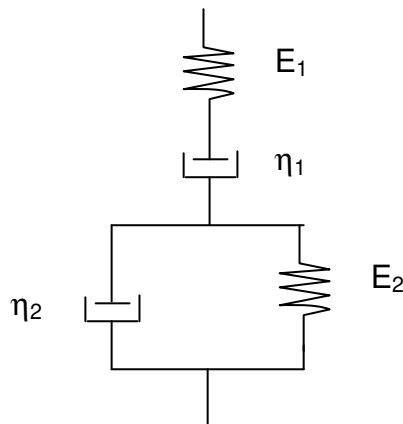


Figure A1.1 Burger's model

A1.1 Test Pavements

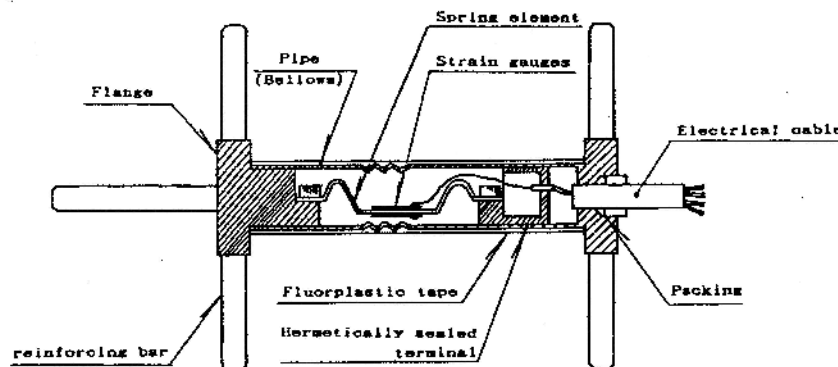
Table A1.1 shows the pavement structure and test conditions of the two test pavements. The two test pavements consisted of four asphalt layers and a cement bound asphalt granulate base layer constructed on a well compacted sand subgrade. During testing, the test section was sheltered from climatic influences such as rain and sunshine by a housing hall measuring 23 m long, 6 m wide and 5 m high, which covers the entire installation. The temperature of the test pavement is controlled through an infrared heating system.

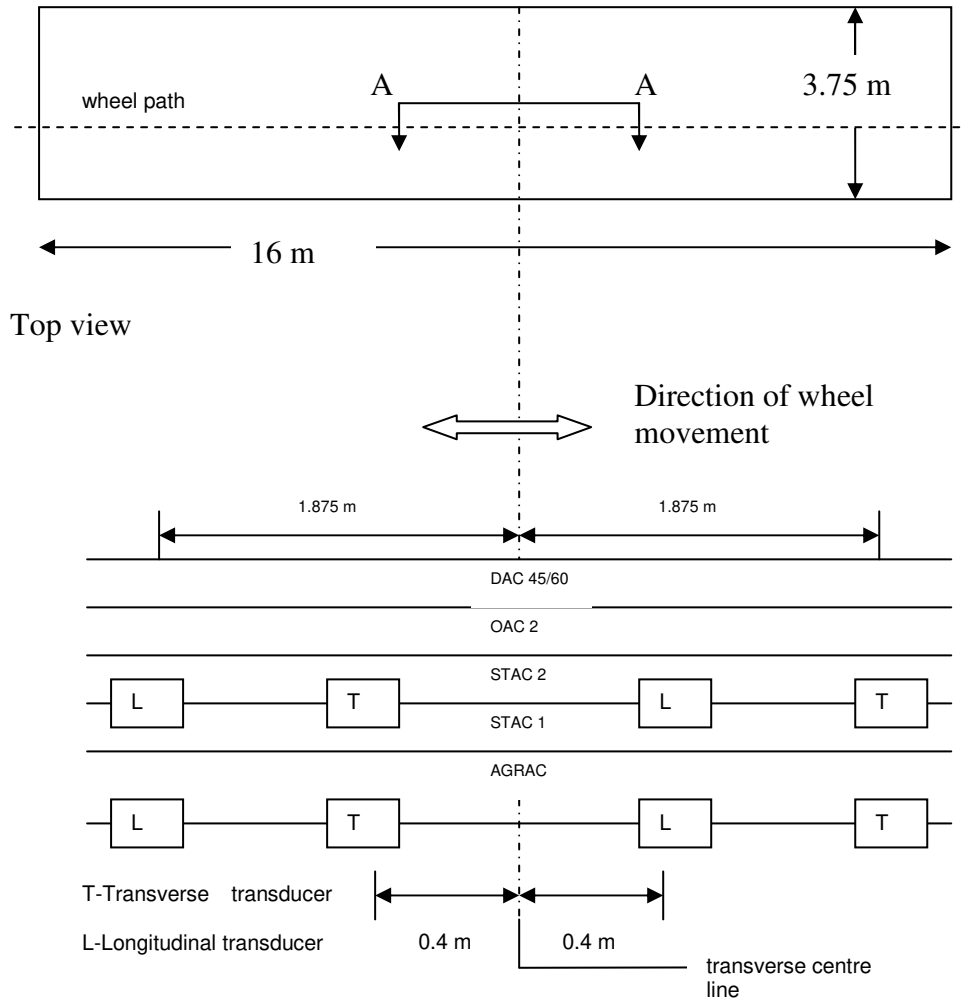
Table A1.1 Second and third LINTRACK test pavements

Layer	Test pavement	
	second	third
top layer	DAC-45/60 40 mm thick	PAC 50 mm thick
second layer	OAC2 60 mm thick	STAC3 60 mm thick
third layer	STAC2 80 mm thick	
fourth layer	STAC1 90 mm thick	
fifth layer	AGRAC 250 mm thick	
subgrade	WCS over 5 m thick	
wheel load characteristics	standard wide based tyre 45 kN load, 0.9 MPa tyre pressure, 0.123 m contact radius, 20 km/h speed	
temperature	between 38 - 40°C at the top of the pavement and 32 - 34°C at the top of the base	
abbreviation	Material description	
DAC-45/60	Dense asphalt concrete	
OAC2	Open asphalt concrete	
STAC1,2,3	Stone asphalt concrete	
AGRAC	Cement bound asphalt aggregate base	
WCS	well compacted sand	

A1.2 Measurement of Pavement Response

The deformation in the tests pavements during the wheel passage was measured by means of strain transducers while the permanent deformation on the pavement surface was measured using a transverse profilometer. The deformation in the pavement during the wheel passage was measured using eight Tokyo Sokki KM-100HAS strain transducers placed at two different depths beneath the wheel path and symmetrically with respect to the transverse centre line of both the second and the third test pavement as illustrated in Figure A1.3. The transducers were composed of a resistance foil type strain gauge glued on a tiny bending beam mounted between two flanges in a copper tube as shown in Figure A1.2. The copper tube is constructed in such a way to protect the gauge and to permit a low longitudinal stiffness (40 MPa) thus allowing the flanges to move with the layer materials even at low material stiffness.

**Figure A1.2 Tokyo Sokki KM-100HAS strain transducers**



Section A-A

Figure A1.3 Placement of the strain transducers in second test pavements

During the test runs, the rutting profile in both test pavements was regularly measured by means of a transverse profilometer. Figure A1.4 shows a typical rutting profile in the test pavements. The typical rutting profile consisted of heaves and depressions indicating the presence of shear failure. The practical rut depth and the depression rut depth were determined from the rutting profile. The practical rut depth is defined as the maximum height between the rutting profile and a straight edge laid over the peaks of the rutting profile and the depression rut depth is defined as the height between the depression and the original pavement level. The definition of the practical and the depression rut depths and the measured practical rut depth is shown in Figure A1.4.

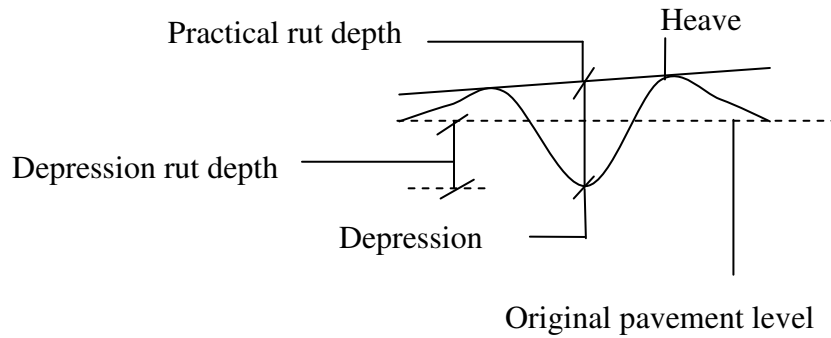


Figure A1.4 Typical rutting profile in the test pavements

A1.3 Laboratory Characterization of the Pavement Materials

In the course of the LINTRACK research, extensive triaxial tests were carried out on specimens cored from material sections that were constructed at the same time and in the same manner as the actual LINTRACK test pavements (Houben et al, 2003). All test samples had a diameter of 101.6 mm and a height between 110 and 120 mm. The triaxial tests consisted of resilient and permanent deformation tests that were performed using a vertical haversine stress signal and constant confinement as illustrated in Figure A1.5.

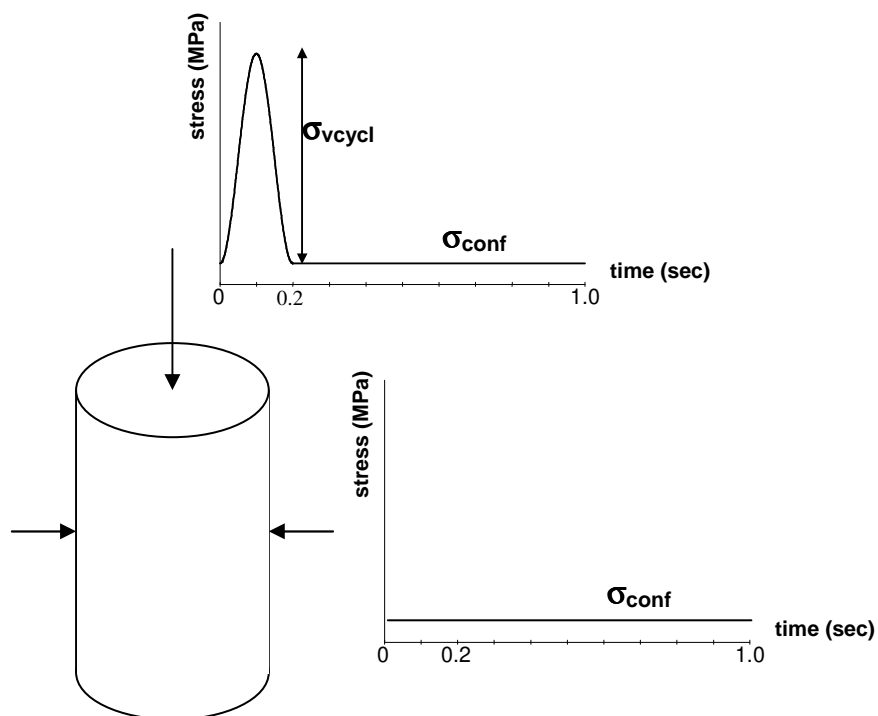


Figure A1.5 Triaxial stress signals

A1.3.1 Resilient Deformation Tests

Resilient modulus and Burger's parameters were determined from resilient deformation tests that were conducted at numerous combinations of temperature,

stresses and loading frequencies. Further information regarding these tests can be obtained from Antes (2002) and Parajuli (2002).

The results from the resilient deformation tests showed that the Burger's parameters were highly non-linear and were dependent on temperature, stress conditions and loading duration. The Burger's parameters and the resilient modulus were then modelled to reflect this observed dependency (Muraya et al, 2002). The models used to model this observed dependency were based on relationships developed by Pellinen and Witczak (2002). Equation A1.1 was applied to model the Burger's spring parameters (E_1 and E_2) and the resilient modulus. Equations A1.1 and A1.2 were used to model the η_1 and η_2 respectively. Table A1.2 to Table A1.5 show the regression coefficients and the correlation coefficients for the Burger's parameters and the resilient moduli. The correlation coefficients for η_1 and E_2 were lower than the correlation coefficients of the other Burger's parameters and those of the resilient moduli in all the asphalt mixtures.

$$\log_{10} E = k_1\alpha + k_{13}\alpha\mu + k_{14}\mu \quad \text{A1.1}$$

Where:

$$\begin{aligned} E &= E_1, E_2 \text{ or } M_r \text{ [MPa]}, \\ k_n &= \text{regression coefficients}, \\ \alpha &= k_2 \log_{10} \left(\frac{\sigma_1}{\sigma_3 + k_7} \right) + k_3 \log_{10} (\sigma_3^{k_9} + k_4) + k_{10} \log_{10} (k_{11} + \sigma_{cyc}^{k_{12}}), \\ \mu &= 1 - e^{-\beta}, \\ \beta &= \left(\frac{k_8 + \log_{10}(sf)}{k_5} \right)^{k_6}, \\ sf &= a_t \cdot freq \\ a_t &= e^{c \left(\frac{1}{T+273} - \frac{1}{T_{ref}+273} \right)}, \\ \sigma_1 &= \text{vertical stress [kPa]}, \\ \sigma_3 &= \text{confining stress [kPa]}, \\ \sigma_{cyc} &= \text{cyclic stress [kPa]}, \\ freq &= \text{frequency [Hz]}, \\ c &= \text{constant}, \\ T &= \text{temperature [}^\circ\text{C]}, \\ T_{ref} &= \text{reference temperature [}^\circ\text{C]}. \end{aligned}$$

$$\log_{10} \eta_1 = k_1\alpha + k_{14}(1-\alpha) + k_{13}\mu \quad \text{A1.2}$$

Where:

$$\begin{aligned} k_n &= \text{regression coefficients}, \\ \alpha(pac) &= k_2 \log_{10} \left(\frac{\sigma_1}{\sigma_3 + k_7} \right) + k_3 \log_{10} (\sigma_3^{k_9} + k_4) + k_{10} \log_{10} (\sigma_{cyc}), \\ \alpha(\text{other materials}) &= k_2 \log_{10} \left(\frac{\sigma_1}{\sigma_3 + k_7} \right) + k_3 \log_{10} (\sigma_3^{k_9} + k_4) + k_{10} \log_{10} (k_{11} + \sigma_{cyc}^{k_{12}}). \end{aligned}$$

$$\log_{10} \eta_2 = k_1 \alpha + k_{10} (1 - \alpha) + k_{11} \mu$$

A1.3

Where:

$$\alpha = k_2 \log_{10} \left(\frac{\sigma_1}{\sigma_3 + k_7} \right) + k_3 \log_{10} (\sigma_3^{k_9} + k_4),$$

$$\mu = e^{-\beta},$$

$$\beta = \left(\frac{k_8 + \log_{10}(sf)}{k_5} \right)^{k_6}.$$

Table A1.2 DAC 45/60 regression coefficients

Coefficient	Parameter				
	η_1	η_2	E_1	E_2	M_r
k_1	5.659	3.633	5.154	4.670	1.368
k_2	1.184	0.043	0.000	0.000	0.045
k_3	0.314	0.098	0.118	0.253	0.096
k_4	1688.581	1786.025	869.569	871.483	1352.295
k_5	641.560	313.132	2.761	2.562	4.424
k_6	104.570	184.892	2.776	23.504	2.014
k_7	96.121	10.826	1.967	1.000	1.000
k_8	642.408	312.648	0.999	1.113	1.400
k_9	2.331	1.579	1.094	1.097	1.745
k_{10}	-1.384	0.000	1.623	-0.713	4.954
k_{11}	-15.982	2.608	0.681	0.143	2.177
k_{12}	0.824	-	-0.045	0.059	-4.830
k_{13}	7.989	-	0.561	0.150	0.545
k_{14}	3.537	-	0.832	0.269	0.660
C	-	-	-	-	25447.885
r^2	0.918	0.982	0.965	0.727	0.984

Table A1.3 OAC 2 regression coefficients

Coefficient	Parameter				
	η_1	η_2	E_1	E_2	M_r
k_1	5.914	3.613	5.068	5.085	3.455
k_2	0.000	0.070	0.015	0.016	0.034
k_3	0.352	0.077	0.138	0.208	0.109
k_4	1744.416	1786.025	869.572	864.646	1312.504
k_5	316.173	313.159	2.786	2.597	119.681
k_6	35.811	184.895	3.293	20.226	85.217
k_7	99.590	10.830	2.325	1.000	1.000
k_8	317.457	312.618	0.734	1.161	117.443
k_9	1.158	1.637	1.171	1.158	1.549
k_{10}	-0.865	0.000	1.681	-0.653	2.270
k_{11}	5.761	2.859	0.645	-0.008	1.382
k_{12}	0.319	-	-0.076	0.052	-0.545
k_{13}	10.584	-	0.806	0.175	-3.093
k_{14}	-0.914	-	1.233	0.106	4.106
C	-	-	-	-	25491.450
r^2	0.755	0.830	0.977	0.744	0.990

Table A1.4 STAC 1&2 regression coefficients

Coefficient	Parameter				
	η_1	η_2	E_1	E_2	M_r
k_1	6.640	3.457	4.345	4.955	2.850
k_2	0.102	0.126	0.001	0.000	0.003
k_3	0.103	0.092	0.173	0.253	0.174
k_4	1722.910	1784.858	867.433	872.647	1892.430
k_5	312.519	313.446	3.015	2.702	42.866
k_6	28.172	191.894	3.670	24.969	22.455
k_7	96.618	45.731	1.000	1.000	1.000
k_8	313.955	312.714	0.806	1.000	40.812
k_9	2.100	1.558	1.187	1.113	1.245
k_{10}	-0.735	0.000	2.367	-0.449	0.477
k_{11}	1.838	2.817	0.698	0.326	5.068
k_{12}	0.423	-	-0.091	0.080	-0.497
k_{13}	13.865	-	0.703	0.002	-2.226
k_{14}	1.504	-	1.019	0.004	3.832
C	-	-	-	-	20641.736
r^2	0.859	0.917	0.982	0.742	0.949

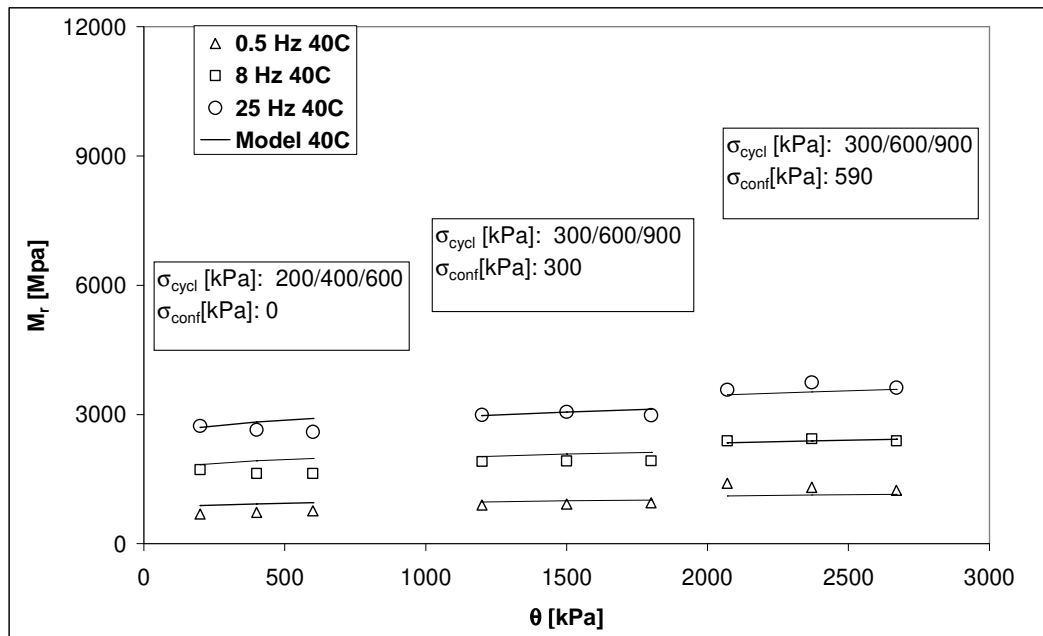
Table A1.5 PAC regression coefficients

Coefficient	Parameter				
	η_1	η_2	E_1	E_2	M_r
k_1	2.196	3.114	4.048	4.413	4.709
k_2	-2.463	0.094	0.001	0.000	0.039
k_3	0.090	0.099	0.026	0.322	0.154
k_4	1561.933	1787.711	0.500	433.817	779.597
k_5	316.018	312.479	11.601	2.484	25.887
k_6	77.291	185.963	19.750	198.865	12.674
k_7	73.374	9.500	3.330	1.000	35.195
k_8	314.692	312.812	9.994	1.055	17.240
k_9	6.950	1.746	1.952	1.037	1.248
k_{10}	-0.824	0.000	2.757	-1.225	0.785
k_{11}	-	3.772	1.035	0.218	0.897
k_{12}	-	0.000	-0.058	0.041	-0.175
k_{13}	8.089	0.000	0.267	0.097	-111.854
k_{14}	1.569	0.000	0.723	0.140	96.447
C	-1111.358	173.765	8239.889	641.720	13916.770
r^2	0.540	0.877	0.868	0.854	0.975

Table A1.6 STAC 3 regression coefficients

Coefficient	Parameter				
	η_1	η_2	E_1	E_2	M_r
k_1	16.313	2.572	4.814	5.088	6.259
k_2	0.000	0.117	0.012	0.007	0.035
k_3	0.001	0.139	0.067	0.275	0.062
k_4	4819.647	1786.700	1149.414	1133.733	1280.072
k_5	229.109	311.406	5.784	13.216	34.508
k_6	162.707	200.168	2.224	40.728	16.691
k_7	444.180	6.154	1.000	0.453	0.700
k_8	229.235	312.198	1.974	11.197	31.978
k_9	50.291	1.936	1.546	1.161	1.978
k_{10}	-0.269	0.020	1.948	-1.348	0.732
k_{11}	0.000	4.558	1.461	0.424	1.385
k_{12}	0.430	-	-0.325	0.034	-0.520
k_{13}	2.282	-	-5.018	-3.857	-7.122
k_{14}	6.042	-	5.609	3.803	4.820
C	-2623.820	8.569	19233.424	8679.174	25297.231
r^2	0.840	0.951	0.928	0.892	0.978

Figure A1.6 and Figure A1.7 show an example of the modelled Burger's parameter, E_1 , and the resilient modulus, M_r , both at 40°C for the DAC 45/60 material respectively. The figures show that the E_1 parameter was higher than the resilient modulus and that the E_1 parameter decreases with increase in the vertical load while the resilient modulus remains more or less constant. The two figures also show that both the E_1 parameter and the M_r increase with increase in confinement.

Figure A1.6 M_r Modelling for DAC 45/60 at 40°C

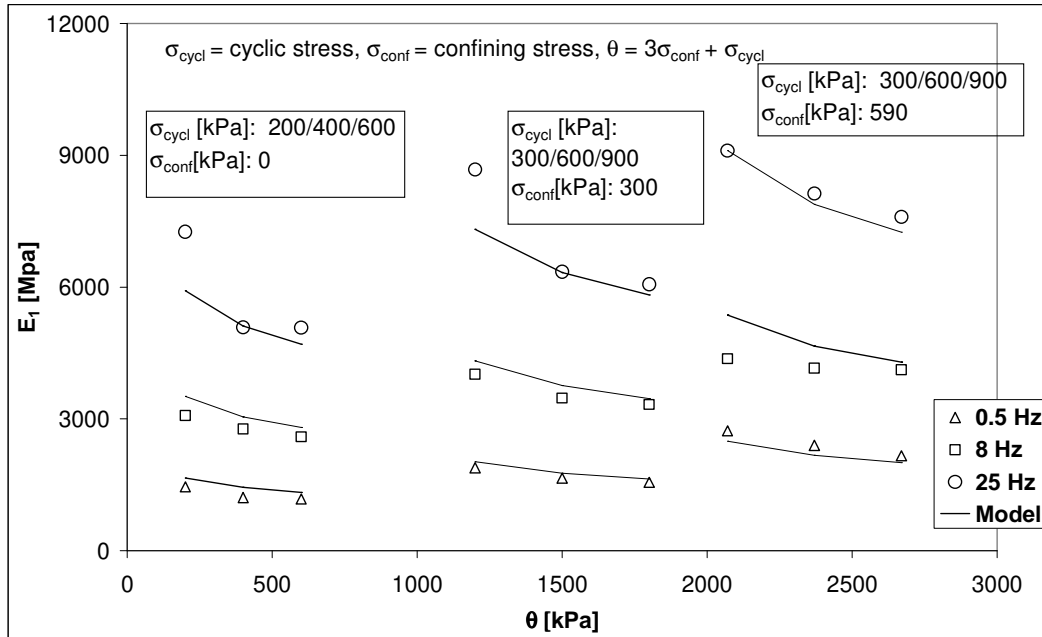


Figure A1.7 E_1 modelling for DAC 45/60 at 40°C

A1.3.2 Permanent Deformation Tests

The permanent deformation tests were conducted at 40°C under short (0.05 seconds) and long (0.2 seconds) haversine load durations. The axial permanent deformation was modelled in terms of the deviator stress, bulk stress, and the number of load repetitions as in Equation A1.4 (Dommelen et al 2001, Houben et al 2003). The regression coefficients are given in Table A1.7 and Table A1.8. Apart from the PAC material for which some short loading duration data was available, the short loading duration data for the other materials is not available. The short loading duration for the OAC 2, STAC 2 and STAC1 was adopted from materials with similar gradations. The permanent deformation for DAC 45/60 at short loading durations was estimated by multiplying the deformation at the long loading durations by factor of 0.76, which was the average reduction in deformation that was obtained during the short loading durations.

$$\varepsilon = a \frac{Q^b}{P^c} N^d \quad \text{A1.4}$$

Where:

ε	=	permanent deformation [%],
Q	=	deviator stress [MPa],
P	=	bulk stress [MPa],
N	=	number of load repetitions,
a, b, c, d	=	regression coefficients.

Table A1.7 Permanent deformation regression coefficients for long loading duration (0.2 seconds)

Test pavement	Material	Regression coefficient				r^2
		a	b	c	d	
Second	DAC 45/60	0.119	2.109	1.575	0.236	0.934
	OAC 2	0.227	2.036	-0.396	0.468	0.658
	STAC 2	0.124	2.034	1.329	0.242	0.954
	STAC 1	0.149	2.300	1.579	0.229	0.908
Third	PAC	0.278	1.471	1.120	0.127	0.942
	STAC 3	0.164	1.692	1.358	0.192	0.948
	STAC 2	0.124	2.034	1.329	0.242	0.954
	STAC 1	0.149	2.300	1.579	0.229	0.908

Table A1.8 Permanent deformation regression coefficients for short loading duration (0.05 seconds)

Test pavement	Material	Regression coefficient				r^2
		a	b	c	d	
Second	DAC 45/60	0.091	2.109	1.575	0.236	0.934
	OAC 2	0.207	1.113	0.484	0.277	0.693
	STAC 2	0.261	2.855	1.581	0.188	0.890
	STAC 1	0.261	2.855	1.581	0.188	0.890
Third	PAC	0.144	1.471	1.447	0.160	0.804
	STAC 3	0.261	2.855	1.581	0.188	0.890
	STAC 2	0.261	2.855	1.581	0.188	0.890
	STAC 1	0.261	2.855	1.581	0.188	0.890

A1.4 Visco-Elastic Analysis

The visco-elastic analysis for the two test pavements was performed using the multi-layer linear visco-elastic analysis program, VEROAD. The analysis involved the calculation of the pavement response in two stages at the load axis using the material behaviour as characterized in the triaxial tests. In the first phase, the strains in the pavement were calculated and in the second phase the permanent deformation was calculated. The Burger's parameters in the first phase were calculated from the models of Burger's parameters through an iterative approach. In this iterative approach, the parameters were calculated in relation to stresses, temperatures occurring at the middle of each layer and the frequency of the vertical stress.

The Burger's parameters are frequency, temperature and stress dependent. The loading frequency and the temperature for a given layer in the LINTRACK test pavements remain constant since the wheel speed and the pavement temperature are controlled during testing. VEROAD determines the pavement response based on constant values of the Burger's parameters irrespective of the position of the wheel. This means that the effect of temperature and frequency can effectively be accounted since they are independent of the position of the wheel. However, it is difficult to account for the stress dependency in using constant Burger's parameters owing to the dependency of the stress conditions on the position of the wheel.

In order to obtain representative Burger's parameters for each layer, the point of load symmetry was chosen. This point was chosen since the maximum rut depth in the test pavements occurred within a close vicinity to this point. The triaxial vertical and triaxial confining stresses at this point were determined as a function of the bulk stress and the deviator stress as shown in Equations A1.5 to A1.8. Equation A1.9 gives the relationship that was used to determine the loading frequency in a given layer.

$$P = \frac{\sigma_{xx} + \sigma_{yy} + \sigma_{zz}}{3} \quad \text{A1.5}$$

$$Q = \sqrt{3} \left\{ \frac{1}{6} \left[(\sigma_{xx} - \sigma_{yy})^2 + (\sigma_{yy} - \sigma_{zz})^2 + (\sigma_{zz} - \sigma_{xx})^2 \right] + \sigma_{xy}^2 + \sigma_{xz}^2 + \sigma_{yz}^2 \right\}^{0.5} \quad \text{A1.6}$$

$$\sigma_h = P - \frac{Q}{3} \quad \text{A1.7}$$

$$\sigma_v = P + \frac{2Q}{3} \quad \text{A1.8}$$

Where:

- σ_h = triaxial confining stress,
- σ_v = triaxial vertical stress,
- P = bulk stress,
- Q = deviator stress.

$$freq = \frac{1}{T_{\text{pulse time}}} = \frac{v}{D} \quad \text{A1.9}$$

Where:

- $freq$ = frequency [Hz],
- v = wheel velocity [m/s],
- D = Distance in which the vertical stress falls to 5% of the maximum triaxial vertical stress occurring at the mid-point of a given layer [m],
- $T_{\text{pulse time}}$ = pulse time for the vertical stress.

The determination of the Burger's parameters at the point of load symmetry involved two consecutive iterative stages. In the first iterative stage, the stresses and frequencies occurring at mid-depth of each layer were determined using the BISAR linear-elastic multi-layer computer programme. The stresses and frequencies calculated in the first stage using BISAR were used to calculate the initial Burger's parameters for the second iterative stage involving the VEROAD programme. This approach is described in more detail below.

The initial resilient modulus was roughly estimated from the resilient modulus charts at assumed frequencies, temperatures, cyclic stresses and confining stresses at the point of load symmetry. The purpose of this initial assumption is to enable

the determination of the initial moduli values directly from the charts. The initial moduli values together with the wheel load characteristics were then used in BISAR to calculate the stresses from which the frequencies were obtained. These stresses, frequencies and the measured layer temperatures were then applied in the resilient modulus model to estimate the next set of resilient moduli for the different pavement layers. This process was repeated until the change in resilient moduli was less or equal to 5%. The final resilient moduli and other input parameters in this first stage are given in Table A1.9. The final stresses and frequencies calculated in this first stage were used to calculate the initial Burger's parameters for the second iterative stage involving the VEROAD programme.

Figure A1.8 shows the second iterative involving VEROAD. The first estimate of the Burger's parameters acted as the initial input in the VEROAD stress analysis programme to determine the new stresses. The stresses were then processed to obtain the loading frequencies occurring in each of the pavement layers. The next set of Burger's parameters was determined from these stresses, frequencies and layer temperatures using the Burger's models. This process was repeated until the change in Burger's parameters was less or equal to 5%. The final values of the Burger's parameters following this approach are given in Table A1.10 and Table A1.11.

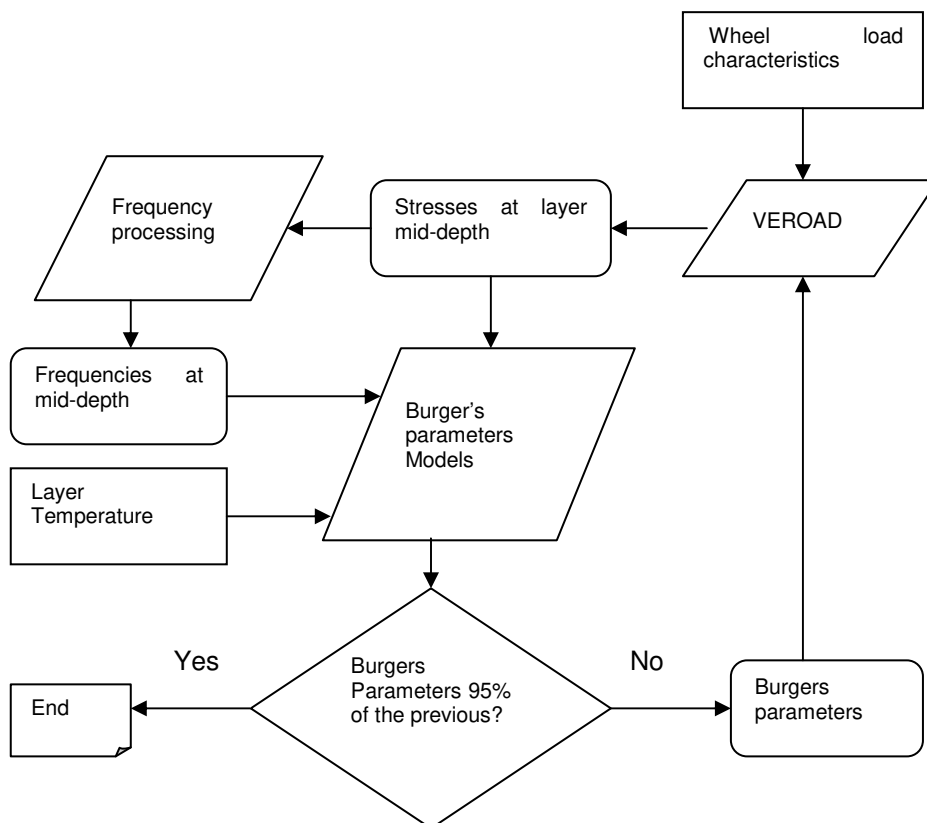


Figure A1.8 Second iterative involving VEROAD

Table A1.9 Final BISAR input

Test Pavement	Layer	Thickness [m]	Elastic Modulus [MPa]	Poisson ratio [-]
Second	DAC 45/60	0.04	3160	0.35
	OAC 2	0.06	2540	0.35
	STAC 2	0.08	3030	0.35
	STAC 1	0.09	3300	0.35
	AGRAC	0.25	3170	0.35
	Subgrade	-	153	0.45
Third	PAC	0.05	2100	0.35
	STAC 3	0.06	2430	0.35
	STAC 2	0.08	3020	0.35
	STAC 1	0.09	3300	0.35
	AGRAC	0.25	3170	0.35
	Subgrade	-	153	0.45

Table A1.10 Burger's parameters based on triaxial resilient deformation tests for the second test pavement

layer material	η_1 [MPa.s]	η_2 [MPa.s]	E_1 [MPa]	E_2 [MPa]
DAC 45/60	37107	133	9412	2730
OAC 2	5520	67	6397	1389
STAC 2	3859	161	5572	1410
STAC 1	2432	199	6877	1186

Table A1.11 Burger's parameters based on triaxial resilient deformation tests for the third test pavement

layer material	η_1 [MPa.s]	η_2 [MPa.s]	E_1 [MPa]	E_2 [MPa]
PAC	21864	72	5354	3178
STAC 3	6912	99	5132	1516
STAC 2	3506	162	5342	1353
STAC 1	2581	198	5510	1199

A1.4.1 Comparison of Stresses Calculated using BISAR and VEROAD

Figure A1.9 and Figure A1.10 show the stresses determined using the BISAR and the VEROAD analysis in top two layers of the second and the third test pavements. The figures show that the stresses in the top layers calculated using the linear elastic approach in BISAR and the linear visco-elastic analysis in VEROAD compare reasonably well. They are virtually the same.

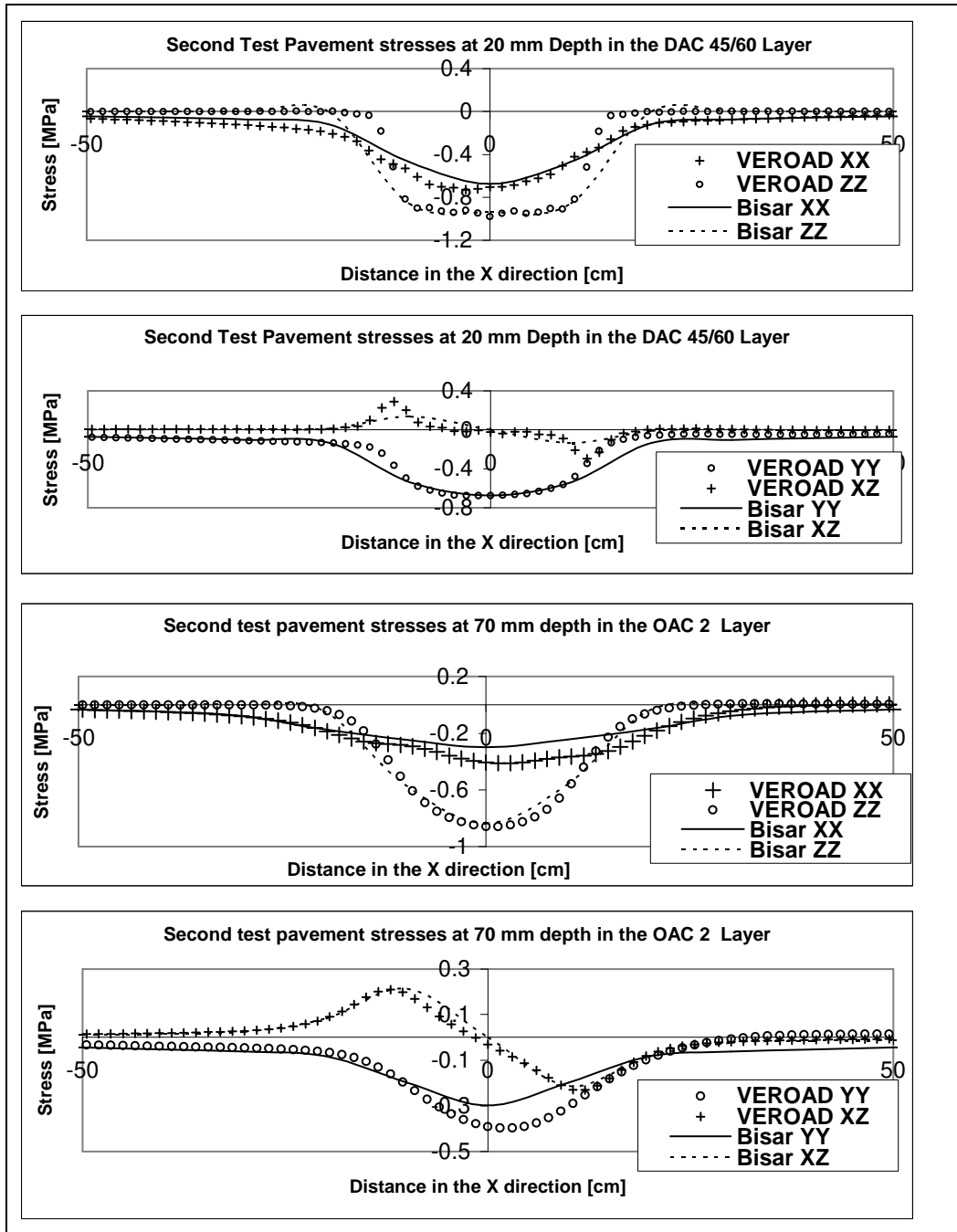


Figure A1.9 BISAR and VEROAD Stresses in the top two layers of the second test pavement (DAC 45/60 and OAC 2)

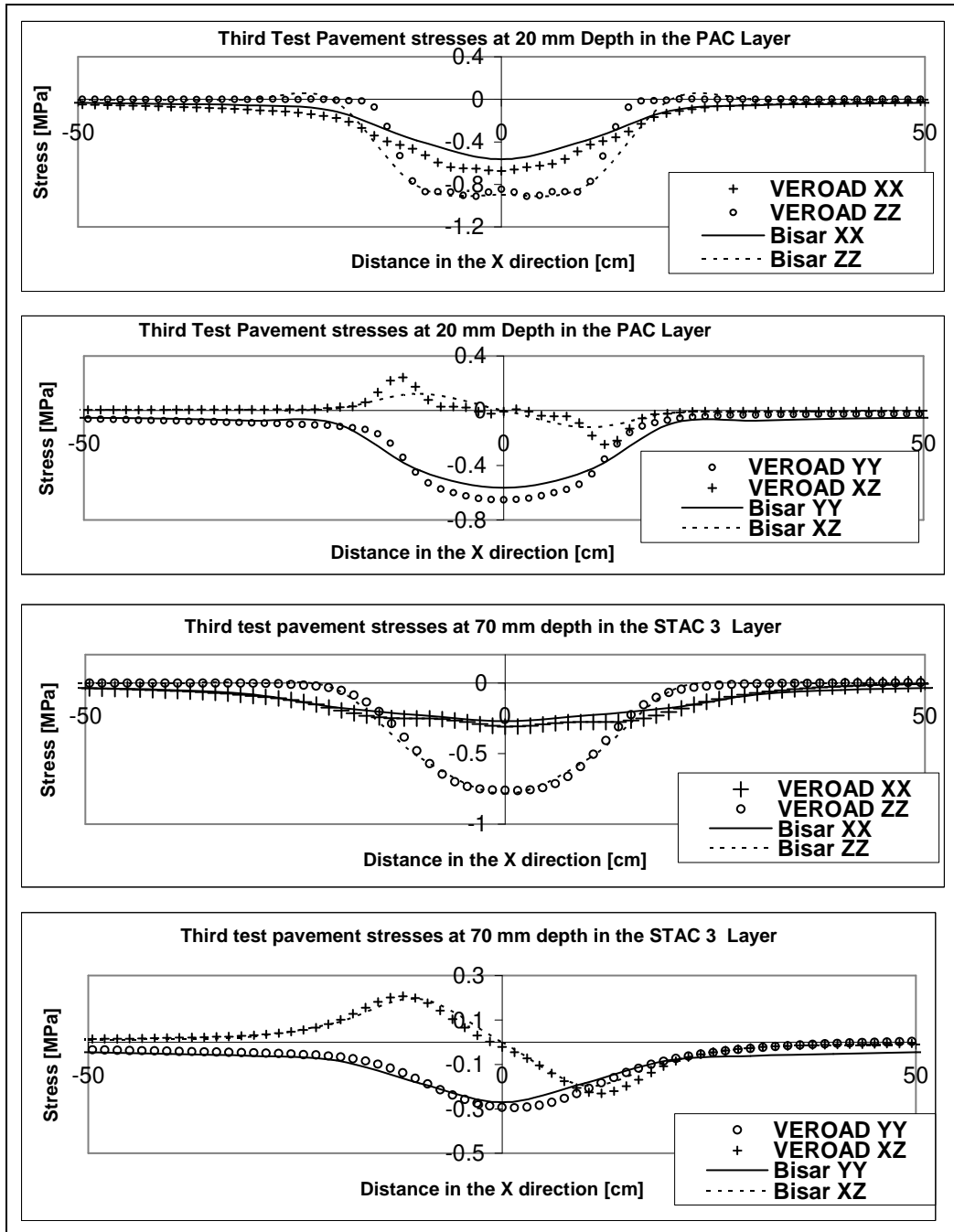


Figure A1.10 BISAR and VEROAD Stresses in the top two layers of the third test pavement (PAC and STAC 3)

A1.4.2 Comparison of Measured and Calculated Strains

The Resilient modulus and Burger's parameters determined using this process resulted in strains that were much lower in comparison to the measured strains. Figure A1.11 and Figure A1.12 show the measured strains at $N = 100$ and calculated strains in the asphalt layer at 180 mm depth and at 190 mm depth for the second and the third test pavement respectively. These figures show that the calculated strains using both BISAR and VEROAD were much lower and out phase relative to the measured strains. The figures also show that both the transverse and longitudinal VEROAD strains were of the same shape as the measured strains. On the other hand, the shape of the longitudinal BISAR strain

and the measured longitudinal strain was similar but the shape of the BISAR transverse strain was different to the measured transverse strain.

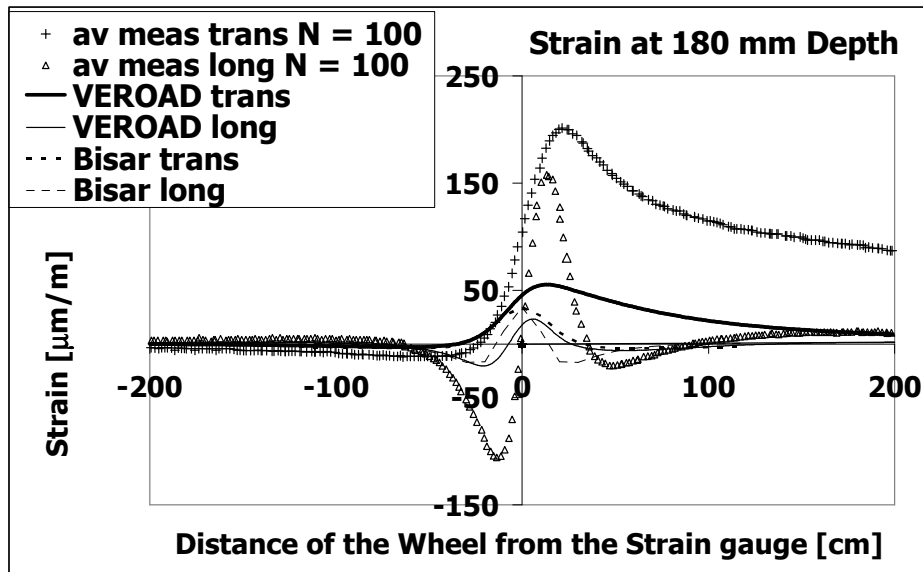


Figure A1.11 Measured strain signals at $N = 100$ and calculated strains (based on triaxial resilient deformation tests) in the asphalt layer for the second test pavement at 180 mm depth

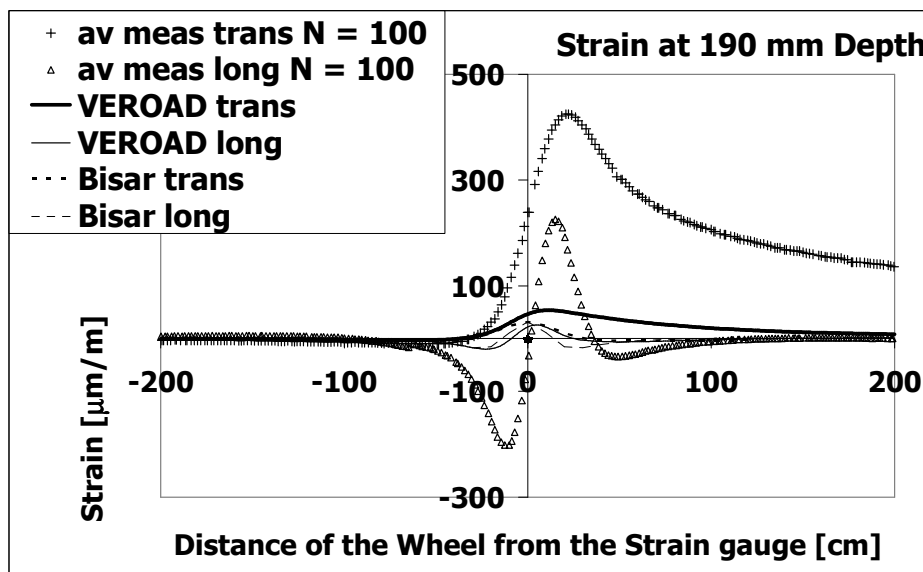


Figure A1.12 Measured strain signals at $N = 100$ and calculated strains (based on triaxial resilient deformation tests) in the asphalt layer for the third test pavement at 190 mm depth

A1.5 Manual Fitting of the Burger's Parameters

An alternative manual process was therefore adopted to fit the Burger's parameters on the measured pavements strain, in order to achieve more realistic stresses for the permanent deformation analysis. In this manual process, the η_1

was first fitted on the measured practical rut depth while accounting for the effect of lateral wander through the Twinwheels computer program (Van Dommelen 2000). This was followed by the fitting of the other Burger's parameters on the measured strains. The manually fitted Burger's parameters were then used to calculate the stresses occurring in the test pavements. The triaxial vertical and triaxial confining stresses in the two test pavements calculated from the fitted Burger's parameters exhibited little variation irrespective of the number of load repetitions. Consequently representative Burger's parameters and pavement stresses were adopted from load repetition #4000 in the second test pavement and from load repetition #3000 in the third test pavement. Table A1.12 shows the laboratory based and manually fitted Burger's parameters for the two test pavements. The table shows that the manually fitted Burger's parameters were much lower than the laboratory based Burger's parameters. The representative stresses and pulse durations for the second and the third test pavements at the load axis are given in Table A1.13.

Table A1.12 Laboratory based and representative manually fitted Burger's parameters for the two test pavements

Pavement	Type of parameters	Layer material	η_1 [MPa.s]	η_2 [MPa.s]	E_1 [MPa]	E_2 [MPa]
Second	Laboratory	DAC 45/60	37107	133	9412	2730
		OAC 2	5520	67	6397	1389
		STAC 2	3859	161	5572	1410
		STAC 1	2432	199	6877	1186
	Manually fitted	DAC 45/60	9557	38	868	384
		OAC 2	1799	28	391	200
		STAC 2	1953	48	616	145
		STAC 1	1683	55	764	131
Third	Laboratory	PAC	21864	72	5354	3178
		STAC 3	6912	99	5132	1516
		STAC 2	3506	162	5342	1353
		STAC 1	2581	198	5510	1199
	Manually fitted	PAC	6280	31	662	261
		STAC 3	1947	41	604	114
		STAC 2	1356	49	659	114
		STAC 1	2318	38	873	119

Table A1.13 Representative stresses and pulse durations

Test pavement	Load repetition N	Material	Pulse time [s]	σ_1 [kPa]	σ_3 [kPa]	P [kPa]	Q [kPa]
Second	4000	DAC 45/60	0.059	953	541	678	412
		OAC 2	0.076	872	284	480	588
		STAC 2	0.097	604	97	266	507
		STAC 1	0.113	375	95	188	280
Third	3000	PAC	0.059	905	495	632	410
		STAC 3	0.081	796	164	375	631
		STAC 2	0.103	584	145	291	439
		STAC 1	0.113	403	209	274	193

A1.5.1 Rut Depth Calculation

The rut depth calculation was based on the representative stresses at the load axis and the permanent deformation behaviour of the test pavement materials as characterized in the permanent deformation triaxial tests. The calculation involved two methods. In the first method (direct method) Equation A1.4 was

directly applied to the pavement layers and in the second method (η_1 method), the rut depth was calculated using the VEROAD permanent deformation package with η_1 values derived in relation to Equation A1.4 and representative pulse durations in the pavement layers.

A1.5.1.1 η_1 method

The purpose of the η_1 method was to determine the rut depth at loading times equivalent to those in the test pavements. The triaxial tests were carried out at a loading pulse time of 0.2 seconds and 0.05 seconds while the loading duration in the pavement varied depending on the depth of the layer below the pavement surface. The rate of permanent deformation can be expressed in terms of viscosity and stresses using the following expression:

$$\frac{\partial \varepsilon}{\partial t} = \frac{1}{\eta_1} [\sigma_v - \nu(\sigma_h + \sigma_h)] \quad \text{A1.10}$$

Where:

ε	=	permanent axial strain,
η_1	=	Viscosity = series dashpot Burger's parameter,
σ_v	=	vertical stress,
σ_h	=	horizontal stress.

In the VEROAD programme, the permanent deformation is calculated after the wheel passage and with the wheel being at an infinite distance from the point under consideration. At infinity distance, the frequency is zero and the material model is such that the Poisson's ratio becomes 0.5 (Hopman 2000). As such Equation A1.10 can be written in terms of the deviator stress, Q as in Equation A1.11 using a Poisson's ratio of 0.5.

$$Q = \eta_1 \frac{\partial \varepsilon}{\partial t} \Rightarrow \eta_1 = Q \frac{\partial t}{\partial \varepsilon} = Q \frac{\Delta t}{\Delta \varepsilon}, \quad \frac{\Delta t}{\Delta \varepsilon} \approx \frac{T}{\varepsilon} \Rightarrow \eta_1 = Q \frac{T}{\varepsilon} \quad \text{A1.11}$$

Where:

T	=	cumulative loading time,
Q	=	deviator stress.

At equal cumulative loading time in the triaxial tests and in a given pavement layer, the number of load repetitions, N can be expressed in terms of the equivalent block pulse time in the triaxial tests, t_{Btriax} , and the cumulative loading time as in Equation A1.12. The final expression for η_1 can then be obtained in terms of the total cumulative loading time as shown in Equations A1.13 and A1.14.

$$T = N t_{Btest} \Rightarrow N = \frac{T}{t_{Btriax}} \quad \text{A1.12}$$

$$\varepsilon [\%] = a \frac{Q^b}{P^c} N^d \Leftrightarrow \varepsilon [-] = a \frac{Q^b \left(\frac{T}{t_{Btriax}} \right)^d}{100 P^c} = \left(\frac{a}{t_{Btriax}^d} \right) \frac{Q^b}{100 P^c} T^d \quad A1.13$$

$$\eta_1 = \frac{100 Q^{(1-b)} T^{(1-d)} t_{Btriax}^d P^c}{a} \quad A1.14$$

Where

t_{Btriax} = equivalent to block pulse time in the triaxial test,
 = half the pulse duration in the triaxial test.

The calculated η_1 values were then used in the VEROAD programme to calculate the rut depths. VEROAD permanent deformation calculation provides a rut-depth cross-section profile with heaves and a trough. This profile made it possible to incorporate the lateral wander effect on the rut depth using the Twinwheels package (Van Dommelen 2000). Table A1.14 shows the lateral wander effect for long loading durations in the second and the third test pavements. The lateral wander (LW) factor was calculated as the ratio between the rut depth after the lateral wander and before the lateral wander. The average of the lateral wander factor determined from the η_1 method was used to estimate the effect of the lateral wander in the direct method.

Table A1.14 Lateral wander effect in the η_1 method for long loading durations in the two test pavements

N		0	100	500	1000	2000	3000	4000	5000	6000	Average LW factor
Test Pavement	Second	-	0.48	0.47	0.47	0.46	0.45	0.45	0.45	0.45	0.45
	Third	-	0.45	0.46	0.46	0.46	0.46	0.46	0.46	0.46	0.46

A1.5.1.2 Direct Method

In the direct method the rut depth is determined by directly applying Equation A1.4 and the stresses occurring at the axis of load symmetry in the pavement layers. The effect of lateral wander in the rut depths was incorporated by a constant factor adopted from the η_1 method. This method assumes that the permanent deformation is a function of the number of load repetitions and is independent of the loading time.

A1.6 Measured and Calculated Rut Depths

Figure A1.13 shows the results of the visco-elastic analysis. As evident from this figure, the rut depths calculated in the visco-elastic analysis were much smaller than the measured rut depths.

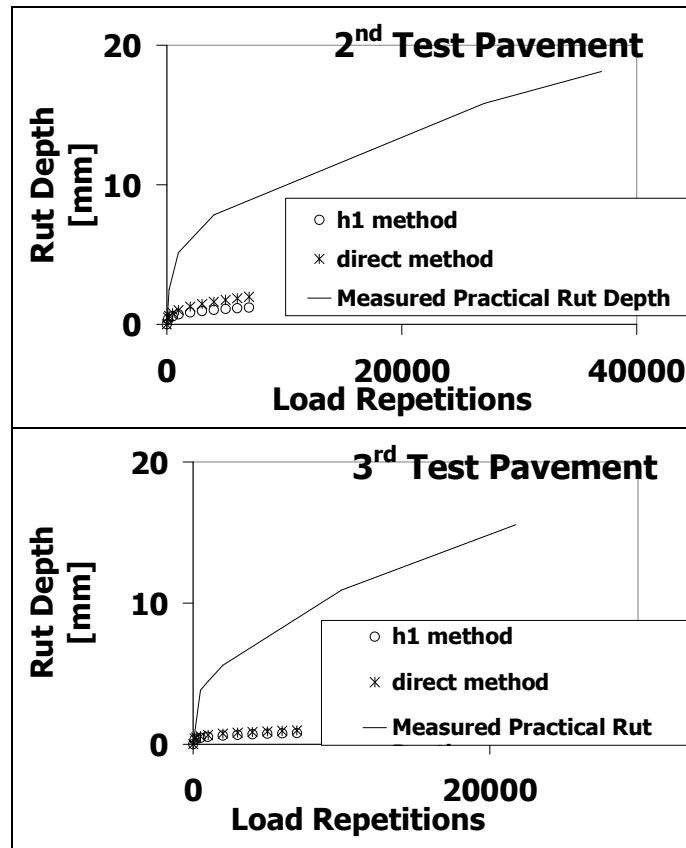


Figure A1.13 A comparison of rut depths calculated using VEROAD and measured rut depths in the second and the third LINTRACK test pavements

The inability by the VEROAD analysis and hybrid models in predicting the permanent deformation could be attributed to following reasons:

- The Burger's parameters and resilient modulus were determined from constant confinement tests. However, the stresses in the pavement vary depending on the position of the wheel load. This approach of measuring the Burger's parameters and resilient modulus may not be sufficient and variation of the confinement during laboratory tests may be necessary.
- The shear failure observed in the rut depths profiles suggests the need for shear strength tests. This type of deformation cannot be explained by means of a linear visco-elastic or the linear elastic approach.
- The Burger's parameters and resilient moduli were highly non-linear and dependent on stress conditions and loading duration. VEROAD and BISAR are linear models that do not incorporate non-linearity in stress dependency or in loading durations.

A1.7 References

- Antes P.W., (2002), *Onderzoek naar Spanningsafhankelijk Gedrag van STAB en ZOAB*, Msc. Thesis, Delft University of Technology, Delft, the Netherlands (In Dutch).
- Dommelen A.E. van, (2000), *Twinwheels Manual*.

- Dommelen, A.E. van, Houben, L.J.M. and Miradi, A., (2001), *Analysis of triaxial test results at 40°C on asphalt samples from LINTRACK test section with DAC 80/100 wearing course* Report 7-01-200-36M, Road and Railroad Research Laboratory, Delft University of Technology, Delft, The Netherlands.
- Muraya, P.M., Houben, L.J.M and Dommelen, A.E. van, (2002), *LINTRACK research into Rutting of Asphalt Concrete Test Pavement*, Report 7-02-200-43M, Road and Rail Research Laboratory, Delft University of Technology, The Netherlands.
- Muraya P.M. & Molenaar A.A.A. & Dommelen A.E. van., (2003), *Visco-elastic Analyses of Test Pavements from LINTRACK ALT Rutting Research*, Third International Symposium on Maintenance and Rehabilitation of Pavements and Technological Control, University of Minho, Guimarães, Portugal.
- Muraya P.M. & Dommelen A.E. van., (2004). *APT Testing and Visco-elastic Analysis of Asphalt Motorway Pavements*, 2nd International Conference on Accelerated Pavement Testing, Minnesota, United States of America.
- Parajuli U., (2002), *Stress dependent Analysis of Asphalt Concrete*, Msc. Thesis, Delft University of Technology/IHE, Delft, The Netherlands.
- Pellinen T.K. and Witczak M.W., (2002), *Stress Dependent Master Curve Construction for Dynamic (Complex) Modulus*. Proceedings of the Association of Asphalt Paving Technologists Technical Sessions, vol. 71, CD-ROM.

Annex 2 - Influence of Model Parameters on the Desai Model and Unified Model

In this annex a brief description of the influence of the model parameters on the Desai and Unified model will be offered.

A2.1 Desai Model

A2.1.1 Parameter α

Figure A2.1 shows an illustration a typical stress-strain response of an asphalt mixture or unbound granular material in a monotonic strain controlled test and the influence of parameter α on the size of the flow surface. The stress-strain figure shows that the material response can be divided in to elastic, non-linear or hardening and post-peak regions. The figure also shows that the size of the flow surface increases with decrease in α . By defining α as a constant in the elastic region and as a decreasing function that becomes zero at the peak, the material response in the three regions can be described. The size of the flow surface remains constant in the elastic region and increases as α decreases in non-linear or hardening region. At the peak when α becomes zero, the ultimate size of the flow surface is reached.

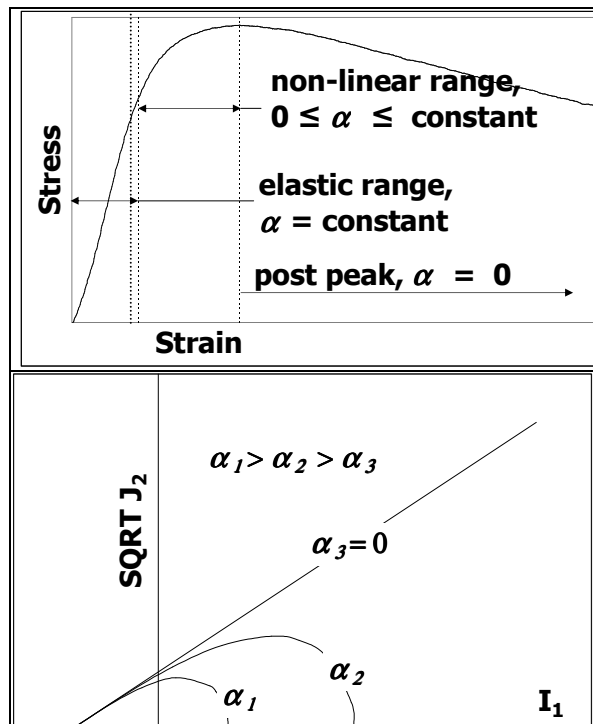


Figure A2.1 Typical stress-strain relationship of an asphalt mixture or unbound granular material in a monotonic strain controlled test and the influence of Parameter α on size of the flow surface

A2.1.2 Parameter n

The apex of the flow surface in the I_1 -SQRT J_2 space corresponds to the point at which dilation initiates. The model parameter n is determined by equating the partial derivative of equation at the apex of the flow surface to zero as shown in Figure A2.2. The model parameter n determines the state of stress at which dilation is initiated. The size of the surface increases with decrease in n values.

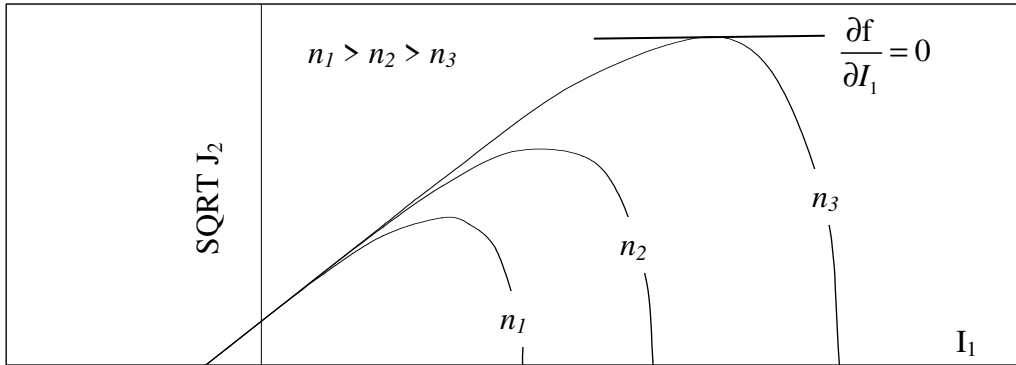


Figure A2.2 Influence of parameter n on the flow surface

A2.1.3 Parameter R

In the I_1 -SQRT J_2 space, parameter R is the intercept of the flow surface on the I_1 axis. It is an indication of cohesion. In cohesion-less materials the value of R is zero. If tensile stresses are taken to be negative and compressive stresses positive, then the R values or the intercept occurs on the negative side of I_1 axis as shown in Figure A2.3. In this case, R becomes more negative increase in cohesion. The cohesion increases with increase in the absolute value of R .

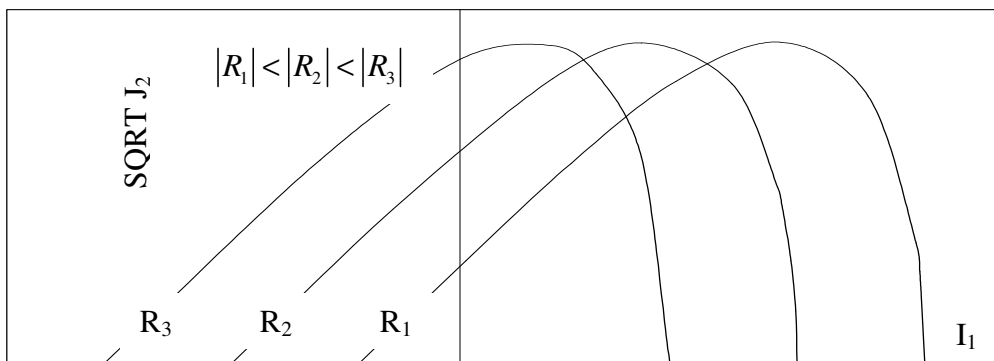


Figure A2.3 Influence of parameter R on the flow surface

A2.1.4 Parameter γ

Parameter γ defines the slope of the ultimate surface as illustrated in Figure A2.4. The slope of the ultimate surface increases with increase in γ . Similar to the slope in the Mohr-Coulomb criterion, γ is an indicator of the internal angle of friction for the material under consideration. The internal angle of friction increases with increase in γ values.

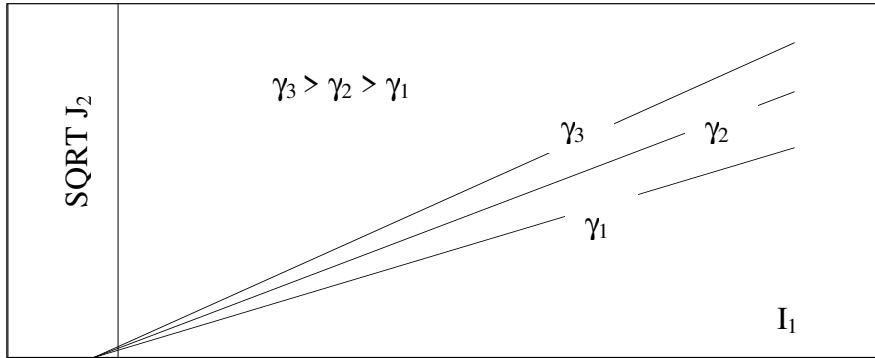


Figure A2.4 Influence of Parameter γ on the ultimate surface

A2.2 Unified Model

The parameters in this model govern different aspects of the overall model. As an example, the influence of the model parameters will be discussed in relation to the time derivative domain and for cases where $P_{high} > P_{low}$.

A2.2.1 Parameter λ

Parameter λ controls the slope of the middle part of the curve and the approach of the curve towards the minimum and maximum limits as illustrated in Figure A2.5. The slope at the middle part of the curve increases with increase in λ . The curve also approaches the minimum and maximum limits faster at higher λ values than at lower values.

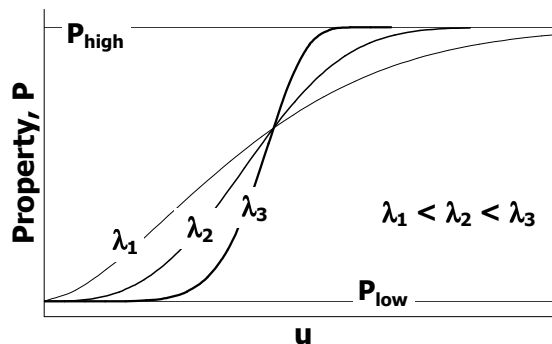


Figure A2.5 Influence of Parameter λ in the range $\lambda \geq 1$

A2.2.2 Parameter β and T_s

Parameter β is a function of the change in temperature relative to the reference temperature and the temperature susceptibility factor T_s . At the reference temperature, the value of β becomes 1. β values relatively higher or lower than 1 result in significant temperature susceptibility. High temperature susceptibility factors, T_s , indicate significant change in the property under consideration as a result of change in temperature. On the other hand low temperature susceptibility

factors, T_s , are a sign of insignificant change in the property under consideration with respect to change in temperature.

Parameter β is used to relate the time derivative at a reference temperature to the time derivative at other temperatures. Parameter β shifts the time derivative at a given temperature to an equivalent time derivative at the reference temperature as illustrated in Figure A2.6. The figure illustrates the time-temperature superposition principle for temperatures above (T_2) and below (T_1) the reference temperature (T_0). The equivalent time derivative is considered to be the time derivative at the reference temperature which results in the same property value as the as the time derivative at another temperature. Or, the reference temperature time derivative at which a test can be performed to obtain the same property value as in another temperature and time derivative.

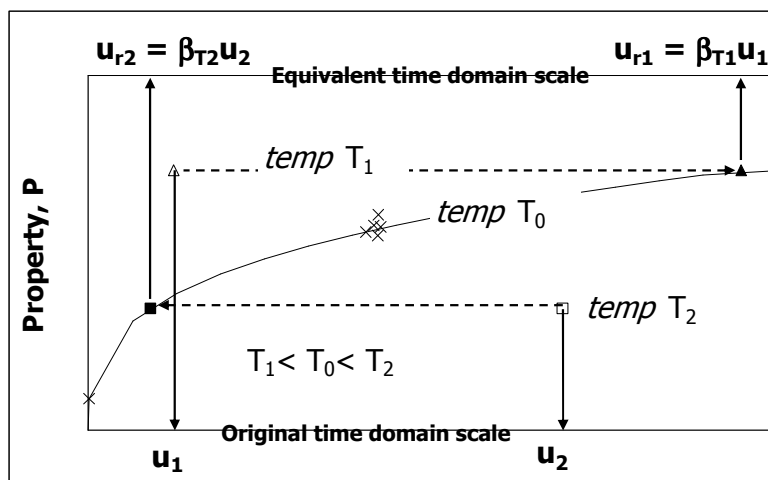


Figure A2.6 Application of Parameter β in the time-temperature super position principle

Annex 3 - MATLAB Code

A3.1 Step 1: Sorting Out the Slides

For some reason, the DICOM slides were always mixed up. The mix up was such that the DICOM slides were not arranged in order and consecutive slides did not necessarily belong to the same specimen. As such the slides belonging to a particular specimen were first identified and sorted out in order. The slides for a given specimen were identified through the use of image comments field entered by the operator during the scanning of each specimen while the instance number field was used to sort out the order. The slides were then arranged in order using the slide name which is a number recorded in the A.FileName field. In order to avoid any mix up, each bunch of consecutive numbered slides were manually stored in separate sub-folders a, b, c, etc. as shown in Table A3.1.

Code for viewing the order of slides and specimen name

```
ctpath=cd;d=dir([ctpath '\7*']);
for ii=1:length(d)
A=dicominfo(d(ii).name);
D1=A.FileName
D2=A.SeriesTime
D3=A.InstanceNumber
D4=A.ImageComments
D5=A.AcquisitionTime
end
```

A3.2 Step 2: Exclusion of Empty Slides

In this step the specimens were visually inspected for empty slides at the top and the bottom. After identification, the empty slides were manually segregated from the other slides and stored in the top empty or bottom empty folder as illustrated in Table A3.1. The arrangement of the slides was then verified in each of the folders excluding the top empty and bottom empty folders.

Code for viewing the top and bottom part of the specimen

Top part of the specimen

```
ctpath = cd;d = dir([ctpath '\2*']);
V=im2uint16(zeros(512,512,10));
for ii=1:10
V(:, :,ii)=dicomread(d(ii).name);
end
```

```
figure,imshow(V(:, :,1),[]);figure,imshow(V(:, :,2),[])
figure,imshow(V(:, :,3),[]);figure,imshow(V(:, :,4),[])
figure,imshow(V(:, :,5),[]);figure,imshow(V(:, :,6),[])
figure,imshow(V(:, :,7),[]);figure,imshow(V(:, :,8),[])
figure,imshow(V(:, :,9),[]);figure,imshow(V(:, :,10),[])
```

```

Bottom part of the specimen
ctpath = cd;d = dir([ctpath '\2*']);
h=length(d);
V=im2uint16(zeros(512,512,h));
for ii=1:h
V(:, :,ii)=dicomread(d(ii).name);
end

```

```

figure,imshow(V(:, :,h),[])
figure,imshow(V(:, :,h-1),[]);figure,imshow(V(:, :,h-2),[])
figure,imshow(V(:, :,h-3),[]);figure,imshow(V(:, :,h-4),[])
figure,imshow(V(:, :,h-5),[]);figure,imshow(V(:, :,h-6),[])
figure,imshow(V(:, :,h-7),[]);figure,imshow(V(:, :,h-8),[])
figure,imshow(V(:, :,h-9),[]);figure,imshow(V(:, :,h-10),[])

```

Table A3.1 *Sorting out of slides and exclusion of empty slides*

folder name	final order excluding empty slides	slide name or A.Filename	Instance number	Image comments	
top empty	-	24122076	1	PA30G	
		.	.	.	
		.	.	.	
		.	.	.	
a	1	24122166	6	PA30G	
		24122184	7	PA30G	
		.	.	.	
		.	.	.	
b	3	24122220	9	PA30G	
		4	24118587	10	PA30G
		.	.	.	
		.	.	.	
c	103	24120369	109	PA30G	
		104	24116695	110	PA30G
		.	.	.	
		.	.	.	
bottom empty	-	173	24117937	179	PA30G
		.	24117955	180	PA30G
		.	.	.	
		.	.	.	
bottom empty	-	24118153	191	PA30G	
		.	.	.	

Codes for the verification of order of slides in the folders

Create I matrix, read folder and check if the slides are arranged in order

```

I=im2uint16(zeros(512,512,173));
ctpath = cd;
d = dir([ctpath '\2*']);
for ii=1:length(d)

```

```
A=dicominfo(d(ii).name);
A.InstanceNumber
I(:,ii)=dicomread(d(ii).name);
end
```

Read folder a and check if the slides are arranged in order

```
ctpath = cd;
d = dir([ctpath '\2*']);
for ii=1:3
iii=ii;
A=dicominfo(d(ii).name);
A.InstanceNumber
I(:,iii)=dicomread(d(ii).name);
end
```

Read folder b and check if the slides are arranged in order

```
ctpath = cd;
d = dir([ctpath '\2*']);
for ii=1:100
iii=ii+3;
A=dicominfo(d(ii).name);
A.InstanceNumber
I(:,iii)=dicomread(d(ii).name);
end
```

read set c in d directory and check if the slides are arranged in order

```
ctpath = cd;
d = dir([ctpath '\2*']);
for ii=1:70
iii=ii+103;
A=dicominfo(d(ii).name);
A.InstanceNumber
I(:,iii)=dicomread(d(ii).name);
end
```

A3.3 Step 3: Location of Centre of Area

In order to interpolate the location of centre of area in the other slides, the position centre of area of the specimen in a slide close to the top and in another slide close to the bottom was located. The uppermost and the lowest slide containing a significant area of the specimen were first visually identified. After which the centre of area in the uppermost and lowest slides was located.

Code for identifying the uppermost and lowest slide

```
figure,imshow(I(:,1),[]);figure,imshow(I(:,2),[])
figure,imshow(I(:,3),[]);figure,imshow(I(:,4),[])
figure,imshow(I(:,5),[]);figure,imshow(I(:,6),[])
figure,imshow(I(:,173),[]);figure,imshow(I(:,172),[])
figure,imshow(I(:,171),[]);figure,imshow(I(:,170),[])
```

```
figure,imshow(I(:,:,169),[]);figure,imshow(I(:,:,168),[])
```

A3.4 Step 4: Determination of Material Boundaries

This step involved the determination of the intensity values for the aggregate/bitumen, (aggregate/cellulose, cellulose/bitumen for SMA specimen) and bitumen/air boundaries for each specimen. These boundaries were based on the actual volumetric composition of the specimens. The boundaries were located by means of trial and error in such a way that the aggregate, cellulose and bitumen volume determined in the analysis was similar to that in the actual specimens. An illustration of the intensities determined for a PAC specimen is given in Figure A3.1. The air void content in the PAC was based on `bwarea` command while that of SMA and DAC was based on the `regionprops-Area` command. An example a code for the `regionprops` commands is given in this section.

Note: `aggvol` = aggregate volume in the specimen (mm^3), `LA2` = pixel intensity at the upper aggregate boundary, `cet` = aggregate area calculated from the image = volume of aggregates in the image since the height of the slide = 1 mm, `LB2` = pixel intensity at the aggregate/bitumen boundary, `bitvol` = aggregate volume in the specimen (mm^3), `AV` = trial value for the pixel intensity at the aggregate/bitumen, `BV` = trial value for the pixel intensity at bitumen/air boundary.

Code for generating an array of boundary intensity and the difference between aggregate volume in the specimen and the volume calculated from image using the `bwarea` command

```
LA2=5500;aggvol=19115019;iv=0;ll=2020;st=1;ed=2050;
rws=((ed-ll)/st+1);
AGG=zeros(rws,2);
for AV=ll:st:ed
for j=1:N
XL=(I(:,:,j)<=LA2 & I(:,:,j)>=AV);
BW=bwarea(XL);
TA(j,1)=BW;
end
cet=sum(TA) ;
iv=iv+1 ;
AGG(iv,1)=AV ;AGG(iv,2)=aggvol-cet ;
end
```

Code for generating an array of boundary intensity and the difference between bitumen volume in the specimen and the volume calculated from image using the `bwarea` command

```
LB2=2045;bitvol=2193663;iv=0;ll=1300;st=1;ed=1350;
rws=((ed-ll)/st+1);
BIT=zeros(rws,2);
for BV=ll:st:ed
for j=1:N
XL=(I(:,:,j)<=LB2 & I(:,:,j)>=BV);
```



```

BW=bwarea(XL);
TB(j,1)=BW;
end
cet=sum(TB) ;
iv=iv+1 ;
BIT(iv,1)=BV ;BIT(iv,2)=bitvol-cet ;
end

```

Example of code for generating an array of boundary intensity and the difference between bitumen volume and the volume calculated from the image using the regionprops command

```

LB2=2045;bitvol= 2193663;iv=0;ll=1300;st=2;ed=1350;
rws=((ed-ll)/st+1);
BIT=zeros(rws,2);
for BV=ll:st:ed
for j=1:N
XL=(K(:,j)<=LB2 & K(:,j)>=AV); LB=bwlabeln(XL);
ST=regionprops(LB);A=zeros(length(ST),1);
for i=1:length(ST)
A(i)=ST(i).Area;
end
TA(j,1)=sum(A);
end
cet=sum(TA) ;
iv=iv+1 ;
BIT(iv,1)=BV ;BIT(iv,2)=bitvol-cet ;
end

```

A3.5 Step 5: Elimination of the Air Surrounding the Specimen

At first, the highest value of the pixels in the specimen was obtained from the DICOM data by means of a frequency distribution plot. This was followed by the segregation of the air in the square cross-section surrounding the circular specimen cross-section. The air was identified and segregated by setting these surrounding pixels to intensity values that were much higher than those in the specimen. The surrounding air was identified based on the specimen radius and the centre of a given slide.

Note: N = number of slides, (grt, gct) = row and column coordinates of the centre of area of the uppermost slide, (grb, gcb) = row and column coordinates of the centre of area of the lowest slide, RS = specimen radius in pixels = measured specimen radius (mm)/0.332, u = pixel intensity value for the surrounding area, gr = interpolated radius of the specimen for a given slide.

Frequency distribution code

```
[freq,pix]=imhist(I(:),65535);
```

Code for air elimination

```
grt=261;grb=260;gct=248;gcb=244.5;N=173;
```

```

RS=225.4;u=6000;
mr=(grb-grt)/(N-1);cr=(grt-mr);
mc=(gcb-gct)/(N-1);cc=(gct-mc);
K(:,:,:)=I(:,:,:);
for j=1:N
gr=mr*j+cr;gc=mc*j+cc;
for r=1:512
for c=1:512
rd=((gr-r)^2+(gc-c)^2)^0.5;
if (rd>RS)
K(r,c,j)=u;
end
end
end
end

```

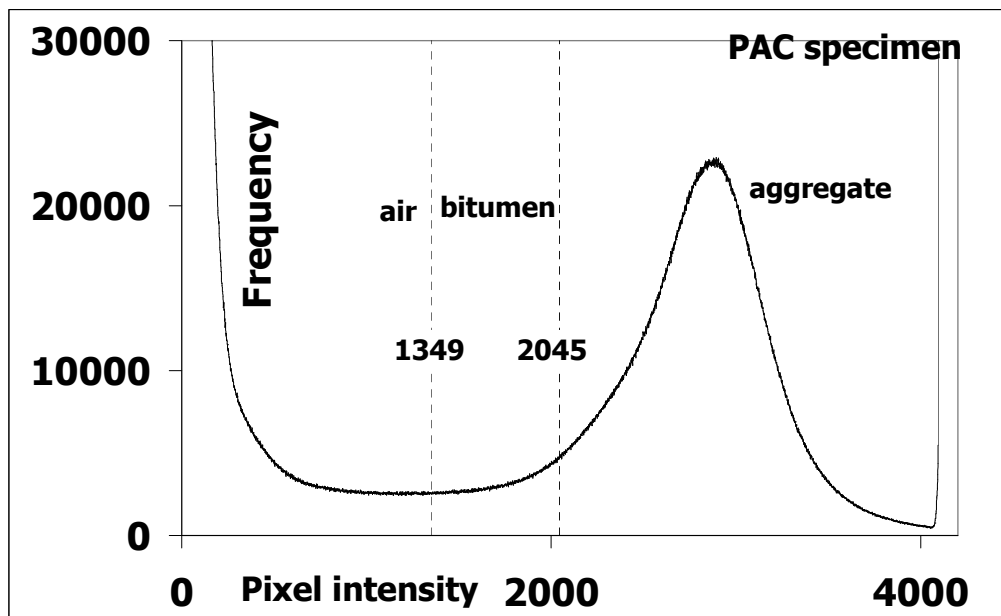


Figure A3.1 An illustration of the boundaries determined for a PAC specimen

A3.6 Step 6: Coring and Determination of Air Content in the Cores

The X, Y and Z cores were electronically cored after which the air void content was determined. The coring was based on geometry (external and internal radius). The air void content was then obtained as a ratio between the areas of the pixels less than the pixel intensity at the bitumen/air boundary for each slide and the total cross-section area of the core. The codes used for the `bwarea` command and the `regionprops` command are given in this section.

Note: `xext` = external radius of the X-core (pixels), `LB1` = pixel intensity at the bitumen/air boundary, `yext` = external radius of the Y-core (pixels), `yint` = internal radius of the Y-core (pixels), `zint` = internal radius of the Z-core (pixels).

Code for electronic coring of X, Y and Z cores

```
xext= 75.1;
MX(:,:,:)=K(:,:,:);
for j=1:N
gr=mr*j+cr;gc=mc*j+cc;
for r=1:512
for c=1:512
if ((gr-r)^2+(gc-c)^2)^0.5>xext
MX(r,c,j)=u;
end
end
end
end
```

```
yint= 85.6; yext= 149.5;
MY(:,:,:)=K(:,:,:);
for j=1:N
gr=mr*j+cr;gc=mc*j+cc;
for r=1:512
for c=1:512
rd=((gr-r)^2+(gc-c)^2)^0.5;
if (rd<yint | rd>yext)
MY(r,c,j)=u;
end
end
end
end
```

```
zint= 161.5;
MZ(:,:,:)=K(:,:,:);
for j=1:N
gr=mr*j+cr;gc=mc*j+cc;
for r=1:512
for c=1:512
rd=((gr-r)^2+(gc-c)^2)^0.5;
if (rd<zint)
MZ(r,c,j)=u;
end
end
end
end
```

Code for calculating the area of air voids in the X, Y and Z cores using the bwarea command

```
for j=1:N
XL=(MX(:,:,j)<LB1);
BW=bwarea(XL);
TA(j,1)=BW;
end
```

```

for j=1:N
XL=(MY(:,:,j)<LB1);
BW=bwarea(XL);
TA(j,1)=BW;
end

```

```

for j=1:N
XL=(MZ(:,:,j)<LB1);
BW=bwarea(XL);
TA(j,1)=BW;
end

```

Code for calculating the total area of the X, Y and Z cores using the bwarea command

```

for j=1:N
XL=(MX(:,:,j)<LA2);
BW=bwarea(XL);
TA(j,1)=BW;
end

```

```

for j=1:N
XL=(MY(:,:,j)<LA2);
BW=bwarea(XL);
TA(j,1)=BW;
end

```

```

for j=1:N
XL=(MZ(:,:,j)<LA2);
BW=bwarea(XL);
TA(j,1)=BW;
end

```

Code for calculating the area of air voids in the X-core using the regionprops command

```

for j=1:N
XL=MX(:,:,j)<LB1; LB=bwlabeln(XL);
ST=regionprops(LB);A=zeros(length(ST),1);
for i=1:length(ST)
A(i)=ST(i).Area;
end
TA(j,1)=sum(A);
end

```

```

for j=1:N
XL=MY(:,:,j)<LB1; LB=bwlabeln(XL);
ST=regionprops(LB);A=zeros(length(ST),1);
for i=1:length(ST)
A(i)=ST(i).Area;
end
TA(j,1)=sum(A);

```

```

end

for j=1:N
XL=MZ(:,j)<LB1; LB=bwlabeln(XL);
ST=regionprops(LB);A=zeros(length(ST),1);
for i=1:length(ST)
A(i)=ST(i).Area;
end
TA(j,1)=sum(A);
end

```

Code for calculating the total area of the X-core using the regionprops command

```

for j=1:N
XL=MX(:,j)<LA2; LB=bwlabeln(XL);
ST=regionprops(LB);A=zeros(length(ST),1);
for i=1:length(ST)
A(i)=ST(i).Area;
end
TA(j,1)=sum(A);
end

```

```

for j=1:N
XL=MY(:,j)<LA2; LB=bwlabeln(XL);
ST=regionprops(LB);A=zeros(length(ST),1);
for i=1:length(ST)
A(i)=ST(i).Area;
end
TA(j,1)=sum(A);
end

```

```

for j=1:N
XL=MZ(:,j)<LA2; LB=bwlabeln(XL);
ST=regionprops(LB);A=zeros(length(ST),1);
for i=1:length(ST)
A(i)=ST(i).Area;
end
TA(j,1)=sum(A);
end

```


Annex 4 - Determination of Tangent Stiffness and Poisson's Ratios

The Tangent stiffness and the Poisson's ratio were determined as illustrated in Figure A4.1 using the procedure explained below.

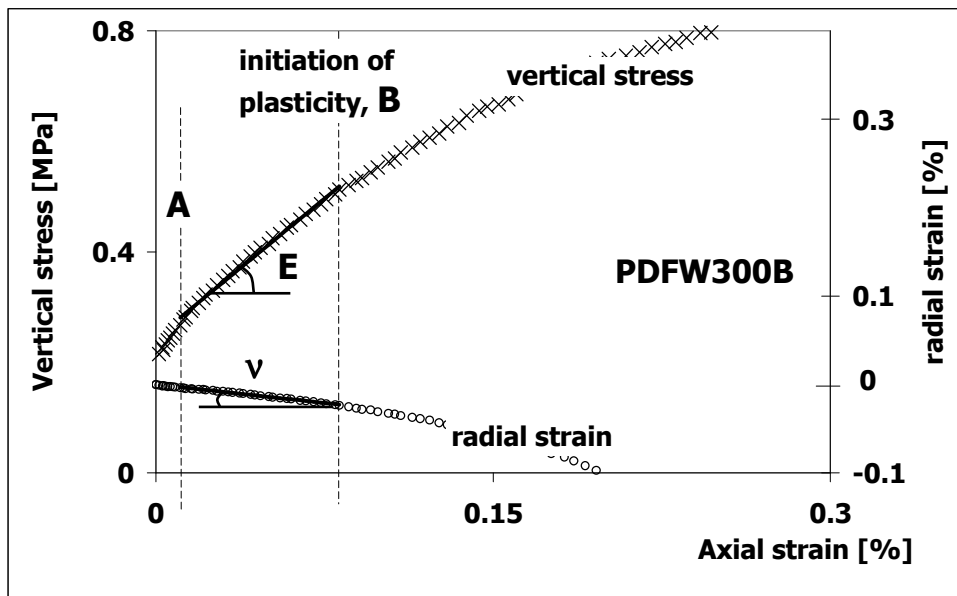


Figure A4.1 An illustration of the determination of tangent modulus and Poisson's ratio in the DCMCC test

1. Determine the point of initiation of the linear part in the vertical stress versus axial strain plot, A, and the point of initiation of plasticity, B. In the DCMCC, DCMC and DCMT tests points A and B were represented by the points shown in Table A4.1.

Table A4.1 Points A and B in the DCMCC, DCMC and DCMT tests

Test	A	B
DCMCC	Point of initiation of linear part in the vertical stress versus axial strain plot.	Point of termination of linear part in the radial strain versus axial strain plot.
DCMC and DCMT		Point of termination of linear part in the vertical stress versus axial strain plot.

2. Obtain the straight line that best fits the data between point A and B using the LINEST function in EXCEL. The tangent stiffness, E is given by the slope of the straight line in the vertical stress versus the axial strain plot. The Poisson's ratio, ν is given by the negative slope of the straight line in the radial strain versus axial strain plot.

CURRICULUM VITAE

Name Patrick Mwangi Muraya
Date of birth 24th September 1966

Educational background

1998-2000 MSc in Transport and Road Engineering at Delft University of Technology/ International Institute for Infrastructural, Hydraulics and Environmental Engineering in The Netherlands. Attained MSc. degree with distinction in road engineering.

1987-1990 BSc in civil engineering at the University of Nairobi in Kenya. Graduated with BSc Honours in civil engineering.

1984-1985 High school education at St. Patrick's High School, Iten.

1980-1983 Secondary school education at Njabini Secondary School.

Work Experience

2002-2007 PhD research in road engineering at the Delft University of Technology. Central to this research was the characterization and analysis of the contribution of the aggregate skeleton and the bituminous binder to the permanent deformation characteristics of the total asphalt mixture.

1991-1998 & 2000-2002 Taught structural analysis, structural design and soil mechanics at the Kenya Polytechnic in Kenya.

2001 Drainage Engineer at Wanjohi Consulting Engineers in Kenya.

2001 Taught road engineering at Jomo Kenyatta University of Technology in Kenya.

1996-1997 Road/Structural Engineer at Engiconsult Consulting Engineers in Kenya.

PROPOSITIONS

Witty sayings are the salt with which words are eaten. – Chinua Achebe

1. Permanent deformation of asphalt mixtures cannot be predicted without accounting for plasticity.
2. In well compacted asphalt mixtures, the tension strength of the mastic/mortar is one of the most important factors contributing towards resistance to permanent deformation.
3. In order to achieve appropriate laboratory based material characterization, sufficient attention should be paid to the method of testing. Too often material models are based on tests that are performed in the wrong way.
4. The gyrator should be rejected as a compaction equipment for mix design purposes since it results in specimens with non-uniform compaction density.
5. The test conditions in the European norm for triaxial test should be revised to compel the application of cyclic confinement in permanent deformation tests of asphalt mixtures.
6. In order to increase efficiency in research projects, universities should consider increasing the ownership stake of their employees in the projects.
7. Although transport planners from other countries can learn a lot from the innovative Dutch bicycle infrastructure, caution should be exercised in adopting such an infrastructure. One should keep in mind that it is a Dutch solution to a Dutch problem.
8. The Dutch tax system is a marvellous application of deduction and addition. It strives to ensure that everybody can afford the basic needs irrespective of the level of income.
9. The problem with the Dutch immigration laws is not that they are harsh but they are applied without respect to the immigrants.
10. Donor aid does not help to alleviate poverty in Africa.

STELLINGEN

1. Blijvende vormverandering van asfaltmengsels kan niet worden voorspeld zonder rekening te houden met plasticiteit.
2. In goed verdichte asfaltmengsels is de treksterkte van de mastiek/mortel één van de belangrijkste factoren die bijdragen tot de weerstand tegen blijvende vormverandering.
3. Voor een juiste karakterisering van materialen in het laboratorium is het nodig dat veel aandacht wordt gegeven aan een correcte manier van beproeven. Te vaak zijn materiaalmodellen gebaseerd op onjuist uitgevoerde proeven.
4. Omdat met de gyrator proefstukken met een ongelijkmatige verdichting worden geproduceerd moet het gebruik ervan voor het mengselontwerp worden ontraden.
5. De Europese norm voor het uitvoeren van triaxiaalproeven moet worden herzien zodanig dat het gebruik van een herhaald aangebrachte steunspanning bij proeven ter bepaling van de weerstand tegen blijvende vormverandering kan worden afgedwongen.
6. Teneinde de efficiëntie te verhogen zouden universiteiten moeten overwegen het gevoel van “eigenaarschap” bij hun medewerkers te verhogen.
7. Alhoewel verkeerskundigen uit andere landen veel kunnen leren van de innovatieve Nederlandse fietsinfrastructuur, moeten ze voorzichtig zijn bij het overnemen daarvan. Men moet er rekening mee houden dat het een Nederlandse oplossing is voor een Nederlands probleem.
8. Het Nederlandse belastingstelsel is een schitterende toepassing van “aftrekken en optellen”. Het beoogt zeker te stellen dat iedereen in zijn basisbehoeften kan voorzien ongeacht de hoogte van zijn inkomen.
9. Het probleem van de Nederlandse immigratiewetgeving is niet dat ze streng is maar dat ze zonder respect voor immigranten wordt toegepast.
10. Donorhulp zal de armoede in Afrika niet verlichten.